Western Australian
Geothermal
CENTRE OF EXCELLENCE

Perth Basin Assessment Program

Project 3: HYDROTHERMAL MODELLING IN THE PERTH BASIN, WESTERN AUSTRALIA

Authors:
L. B. Reid, S. Corbel, T. Poulet,
L. P. Ricard, O. Schilling,
H. A. Sheldon and J. F. Wellmann

March 2012

CSIRO
Curtin University
The University of Western Australia
Achieving International Excellence
Government of Western Australia

Enquiries should be addressed to:

Dr Heather Sheldon
CSIRO Earth Science and Resource Engineering

Australian Resources Research Centre
26 Dick Perry Avenue, Kensington WA 6151
heather.sheldon@csiro.au

ISBN 978-0-643-10907-0

Report 4

Project 3: Hydrothermal Modelling in the Perth Basin, Western Australia,
L. B. Reid, S. Corbel, T. Poulet, L. P. Ricard, O. Schilling, H. A. Sheldon and J. F. Wellmann - PRINT

Copyright and Disclaimer

© 2012 WAGCoE To the extent permitted by law, all rights are reserved and no part of this publication covered by copyright may be reproduced or copied in any form or by any means except with the written permission of WAGCoE.

Important Disclaimer

WAGCoE advises that the information contained in this publication comprises general statements based on scientific research. The reader is advised and needs to be aware that such information may be incomplete or unable to be used in any specific situation. No reliance or actions must therefore be made on that information without seeking prior expert professional, scientific and technical advice. To the extent permitted by law, WAGCoE (including its partners, employees and consultants) excludes all liability to any person for any consequences, including but not limited to all losses, damages, costs, expenses and any other compensation, arising directly or indirectly from using this publication (in part or in whole) and any information or material contained in it.

CSIRO

Curtin University

The University of Western Australia
Achieving International Excellence

Government of Western Australia

CONTENTS

EXECUTIVE SUMMARY IX

PREFACE X

ACKNOWLEDGEMENTS XI

1. INTRODUCTION 1

2. RESEARCH BACKGROUND 3

2.1 Previous Geothermal Investigations in Western Australia 3

2.2 Geothermal Investigations in the Rhine Graben 5

3. GEOTHERMAL POTENTIAL OF WESTERN AUSTRALIA 8

3.1 Geothermal Prospectivity in Western Australia 9

3.1.1 Methods 9

3.1.2 Results 13

3.1.3 Conclusions 16

3.2 Potential for Electricity Generation in the North Perth Basin 18

3.2.1 Methods 18

3.2.2 Results 20

3.2.3 Conclusions 28

3.3 Identifying Advective Heat Transport in the Perth Metropolitan Area 28

3.3.1 Introduction 28

3.2.2 Background 29

3.3.3 Methods and Results 31

3.3.4 Conclusions 37

3.4 Potential for Convection in the Perth Basin 38

3.4.1 Convection theory 39

3.4.2 Hydrogeology of the Perth Basin 41

3.4.3 Evidence for convection: Temperature 42

3.4.4 Evidence for convection: Salinity 45

3.4.5 Rayleigh number analysis of the Yarragadee Aquifer 46

3.4.6 Numerical models 48

3.4.7 Discussion 49

3.4.8 Conclusions 50

4. DETAILED HYDROTHERMAL MODELS 53

4.1 Use of Public Data: Canning Basin Workflow 53

4.1.1 Introduction 53

4.1.2 Workflow and results 54

4.1.3 Conclusions 58

4.2 Conductive Heat Transport Model of the Perth Basin 59

4.2.1 Introduction 59

4.2.2 Methods 59

4.2.3 Results 64

4.2.4 Discussion 75

4.2.5 Conclusions 82

4.3 Hydrothermal Model of the Perth Metropolitan Area 82

4.3.1 Introduction 82

4.3.2 Model geometry, properties and boundary conditions 82

4.3.3 Mesh generation and modelling workflow 85

4.3.4 Results 86

4.3.5 Discussion 92

4.3.6 Conclusions 93

5. COMPUTATIONAL METHODS FOR INVESTIGATING HYDROTHERMAL RESOURCES 94

5.1 Thermodynamic Reactive Transport Simulations: *escriptRT* 94

5.1.1 Introduction 94

5.1.2 Reactive transport formulation 95

5.1.3 Reactive transport solvers 97

5.1.4 Computer platforms compatibility 98
5.1.5 Benchmarks 99
5.1.6 Conclusions 115
5.2 Thermal-Hydrological-Mechanical-Chemical (THMC) coupling of geological processes 116
5.2.1 Introduction 116
5.2.2 Constitutive model 117
5.2.3 Application to albitisation 119
5.2.4 Conclusions 122
5.3 Incorporation of Uncertainty in the Simulation Workflow 123
5.3.1 Introduction 123
5.3.2 System-based measures of uncertainty 124
5.3.3 Structural uncertainty workflow 128
5.3.4 Case study: North Perth Basin, Western Australia 132
5.3.5 Conclusions 135

6. DISCUSSION 137
6.1 Synthesis of research results 137
6.2 Future directions 138

REFERENCES 139

APPENDIX A. LISTING OF STUDENTS 153

APPENDIX B. CONFERENCE AND WORKSHOP CONTRIBUTIONS 154
Appendix B.1 Conference Presentations and Attendance 154
Appendix B.2 Short Courses 154
Appendix B.2.1 Direct Use Applications for Hot Sedimentary Aquifers 155
Appendix B.2.2 Geothermal Energy Systems 155
Appendix B.2.3 Geothermal Energy Resources 156
Appendix B.2.4 SPICE 156

APPENDIX C. SCIENTIFIC PUBLICATIONS 157

EXECUTIVE SUMMARY

The Western Australian Geothermal Centre of Excellence (WAGCoE) conducted scientific and engineering research into WA's geothermal resources, principally Hot Sedimentary Aquifer (HSA) resources in the Perth Basin. Project 3 of the Perth Basin Assessment Program focused on geothermal data analysis and hydrothermal simulations. Three-dimensional computer models of basin- to local-scale conditions have been developed to predict temperature regimes, test hypotheses, estimate parameters, provide modelling tools, and quantify uncertainty. This work has supported the training and development of 7 undergraduate Honours students, 2 MSc students, and 7 doctoral candidates at Australian and international universities. Several educational and industry workshops were held to encourage direct use geothermal applications.

In this report, several hydrothermal modelling projects are presented and significant research outputs are identified. Section 2 summarises thermal modelling research in Western Australia that existed by 2009, the founding date of WAGCoE. An overview of current research into HSA modelling is provided with a focus on studies in the European Rhine Graben.

Section 3 examines the geothermal potential in Western Australia, through analysis of new and existing temperature data and theoretical models. A state-wide survey of deep petroleum exploration data indicates regions of WA which are prospective for HSA geothermal projects, based on the depth, thickness and temperature of aquifers. A more detailed study of the North Perth Basin highlights the Yarragadee and Eneabba Formations as potential HSA geothermal prospects. A temperature logging campaign in the Perth Metropolitan Area (PMA) provided data for analysis of advective subsurface heat movement in the shallow aquifers, highlighting the influence of advection on the subsurface thermal regime. The potential for density-driven heat transport (i.e. convection) in the Perth Basin was also analysed. Temperature maps, theoretical considerations, salinity data, and numerical models suggest that convection may be possible within the Yarragadee Aquifer, depending on its thickness, geothermal gradient and permeability.

Detailed hydrothermal models are presented in Section 4. A workflow for geothermal resource modelling using limited publically-available data is demonstrated for the Canning Basin. The first geothermal model of conductive heat transport in the entire Perth Basin is presented, revealing large-scale thermal features that can be used to guide subsequent detailed studies. A smaller-scale study addresses coupled heat transport and fluid flow in the PMA, highlighting the potential influence of convection and advection in permeable aquifers and the influence of faults on subsurface heat flow.

The final section presents work performed by the WAGCoE team on developing tools for hydrothermal modelling, including a new flexible modelling package, *escriptRT*, and a scientific workflow which incorporates geologic uncertainty using thermodynamic considerations.

This report highlights significant progress in hydrothermal modelling of geothermal systems in Western Australia. WAGCoE has developed a strong team with geothermal modelling expertise capable of providing leadership in both research and industrial areas.

PREFACE

The Western Australian Geothermal Centre of Excellence (WAGCoE) was established in 2009 for an initial three year term with a $2.3M grant from the Western Australian Department of Commerce. WAGCoE operated as an unincorporated joint venture between CSIRO, University of Western Australia, and Curtin University, with CSIRO as the Centre agent. The remit of WAGCoE was to assist the Western Australian Government to provide a foundation for a sustainable geothermal industry by conducting advanced scientific and engineering research into WA's geothermal resources, principally HSA resources in the Perth Basin, and to develop and transfer to industry innovative new technologies for direct heat use.

In order to deliver on this task, WAGCoE was structured into three mutually supportive research Programs:

- Perth Basin Assessments (Program 1)
- Above-Ground Engineering (Program 2)
- Deep Heat and Future Resources (Program 3)

The Perth Basin Assessments Program contained the following four research Projects:

- WAGCoE Data Catalog (Project 1)
- Perth Basin Geomodel (Project 2)
- Hydrothermal Simulations (Project 3)
- Reservoir Productivity and Sustainability (Project 4)

This document is the final research report of Project 3 within Program 1 of WAGCoE. The format of the document is that of a summary report; detailed tabulations of technical data and results are to be found in the supporting research reports, papers and theses cited herein.

ACKNOWLEDGEMENTS

WAGCoE was funded by the Western Australian government and the partners of CSIRO, the University of Western Australia, and Curtin University of Technology. We also received financial support from our industry associates, Green Rock energy and GT Power.

Considerable amounts of data were provided by the Western Australian Department of Mines and Petroleum (DMP) and the Western Australian Department of Water (DoW). The DoW also provided access to observation bores throughout the PMA and allowed publication of results. Geoscience Australia loaned temperature logging equipment and provided training.

Much of the work presented here was performed with the assistance of people employed outside of WAGCoE. Honours students Sarah Glasson, Gemma Bloomfield and Chris Botman provided results for this report. Ph.D. student Brendan Florio was a large contributor. Other students involved with hydrothermal modelling are acknowledged in Appendix A. Collaborations with Lutz Gross from the University of Queensland, Brett Harris from Curtin University, and Ali Karrech from CSIRO led to extensive new research results.

The numerical simulations described in this report were performed on computers ranging from standard desktops to supercomputers. We are grateful to the information technology divisions of the partners in providing hardware and support for the machines. We particularly acknowledge the support of iVEC and the generous provision of time on the computers cognac, cortex, and epic.ivec.org. Essential external software included FEFLOW, by DHI-Wasy; GoCad/SKUA by Paradigm, ArcGIS by ESRI; and Tempest MORE by Roxar.

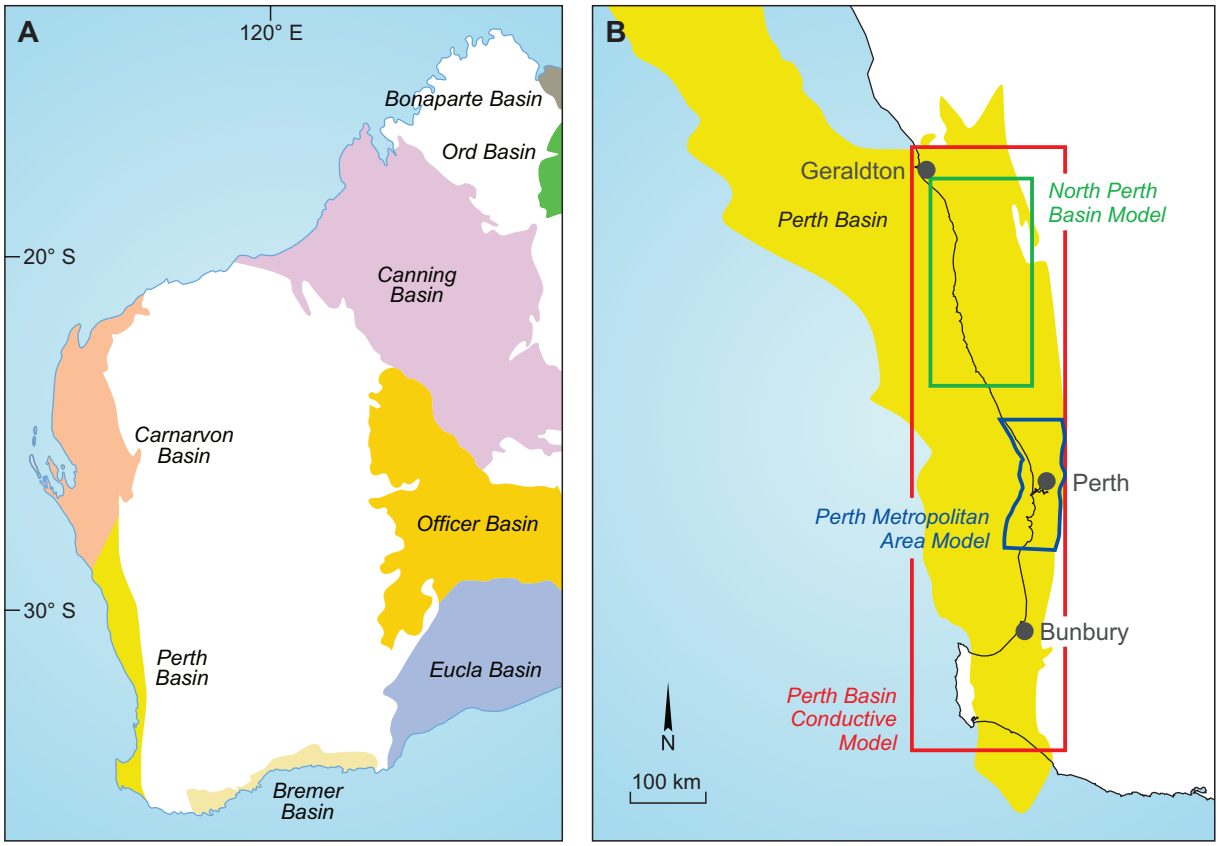

Figure 1.1: Location maps. (A) Onshore sedimentary basins in Western Australia. (B) Location of study areas in the Perth Basin.

1. INTRODUCTION

The Western Australian Geothermal Centre of Excellence [Regenauer-Lieb et al., 2009] was formed, in part, to lead the exploration for geothermal prospects in the state of Western Australia. A geothermal prospect is an area with anomalous subsurface temperature (either high or low) and easy accessibility to the heat resource contained in the rock. Successful exploration for geothermal energy involves many disciplines and requires the input of many specialists, including geologists, geochemists, geophysicists, mechanical engineers, and economists. Subsurface exploration in any field, however, is always hampered by the paucity of data and the high cost of gathering data. It is important to integrate the available knowledge with the perspectives of the entire research team, along with the underlying physics of the problem, to best form a conceptual understanding of conditions and processes which cannot be easily observed.

In this report we focus on developing new understandings of hydrothermal processes in the Perth Basin (Fig. 1.1), i.e. the movement of heat by conduction, advection and convection within the sedimentary sequence of the Perth Basin. Figure 1.1 shows the location of study areas described in this report. Our horizontal scales of study range from the full basin scale (thousands of kilometres) to regional scale (tens to hundreds of kilometres). We consider vertical scales from several kilometres to the entire thickness of the crust, thereby investigating macroscale thermal processes of interest to geothermal resource planners. In performing these studies we employ a quantitative modelling approach to assist with the integration of disparate data and process information. This effort culminates in numerical models of hydrothermal domains and processes, which themselves represent quantitative summaries of the available structural, material property, and physical process data, and which are suitable for use in subsequent predictive analysis.

Numerical modelling provides a tool to assess geothermal opportunities through simulation of heat transport processes in the subsurface. The conceptual model of how heat moves below ground drives the choice of relevant physical processes to include in the simulations and the boundary and initial conditions to be imposed. The model results describe the movement of heat and detail the various influences on the system state, for example the effect of thermal conductivity variations or advective heat transport by moving groundwater. Numerical modelling provides several key advantages to geothermal exploration:

- Modelling integrates knowledge of physical principles and direct measurements obtained from various sources. For example, gravity measurements may help define the shape of the basin, which is reflected in the model layering.
- Modelling leads to general-purpose scientific conclusions by the use of hypothesis testing. For example, the influence of fault hydraulic conductivity on temperature distributions can be tested with models representing various fault permeability scenarios.
- Modelling provides spatial predictions of conditions which are difficult to observe directly. For example, linear interpolation of scattered borehole temperature measurements does not account for known variations in thermal properties, whereas conductive modelling does.
- Modelling provides temporal predictions forward or backward in time from the current

observable state. For example, the sustainability of a reservoir system can be predicted by a numerical model including a pumping doublet.

- Modelling allows determination of physical properties that are consistent with observed data, using inverse methodologies. For example, detailed temperature log analysis can allow determination of thermal conductivity variations or identification of regions of moving groundwater.
- Modelling allows the investigation of risk through uncertainty analysis by the testing of alternative hypotheses and a range of input parameters.

All of the benefits of hydrothermal numerical modelling are applicable to geothermal exploration in the Perth Basin and throughout Western Australia. The aim of this project within WAGCoE is to model the hydrothermal systems of the Perth Basin and to assess opportunities for exploiting the most prospective of these geothermal resources. Because of the data-intensive and computationally-demanding nature of this task, significant progress is only possible with the help of major computing facilities and a multidisciplinary team of researchers. Three-dimensional computer models of basin- to local-scale conditions have been developed to predict temperature regimes, test hypotheses, estimate parameters, and quantify uncertainty. WAGCoE has developed a strong team with geothermal modelling expertise capable of providing leadership in both research and industrial areas.

This report is structured in five main areas. In Section 2, we first present a summary of hydrothermal modelling research in Western Australia which existed by 2009, the founding date of WAGCoE. We also include reviews of relevant work done in the Perth Basin by research teams outside of WAGCoE since that time. The next three sections report on research performed by WAGCoE in the field of hydrothermal modelling from 2009 to 2012. Section 3 groups work relating to the geothermal potential in Western Australia, in particular focusing on the integration of scattered data, and exploring conceptual models of heat transport that include advection and convection as well as conductive heat transport. Section 4 presents four detailed hydrothermal modelling studies in Western Australia. These include broad scale studies using limited publically-available data, an example of how precise geothermal data collection can aid hydrogeologic modelling studies, the first conductive geothermal model of the entire Perth Basin, and a smaller scale study addressing coupled heat transport and fluid flow in the PMA. Section 5 presents work performed by the WAGCoE team on developing tools for hydrothermal modelling. A new flexible modelling package, *escriptRT*, is presented along with benchmarks of its solution performance and an application to thermal, hydrological, mechanical, and chemical coupling processes. Finally, a scientific workflow which incorporates geologic uncertainty using thermodynamic considerations is presented, with an application to the North Perth Basin. Section 6 provides a synthesis of the research presented in this report, and suggests future directions which build on the WAGCoE-generated capability for geothermal modelling in Western Australia.

2. RESEARCH BACKGROUND

Hydrothermal modelling has a broad background in the mathematical and geological sciences. The basic equations of heat transport are provided in Sections 3.3.2 and more complex reactive equations in Section 5.1.2. In the context of geothermal exploration, research initially focused on one-dimensional studies. With the advent of inexpensive computers, research into two- and three-dimensional geothermal characterisation has blossomed. In all these efforts, the focus has been on the description of subsurface temperature regimes. Because predictive numerical modelling requires knowledge of rock properties, measurements of fundamental thermal properties are a pre-requisite to advanced hydrothermal simulations. Geothermal modelling has progressed through several stages:

1. Interpolation of borehole temperature measurements to produce one-dimensional vertical temperature gradient estimates
2. Measurement of thermal rock properties such as thermal conductivity and radiogenic heat production.
3. One-dimensional estimation of heat-flow, the product of thermal conductivity and temperature gradient.
4. Spatial interpolation of heat-flow values to produce two-dimensional maps.
5. Multidimensional modelling of heat movement, beginning with conduction and subsequently incorporating advection and convection.

In all these cases, applicability and accuracy has been held back by the lack of reliable measurements of both temperature and rock properties. Research progress has been hampered by the lack of easy-to-use numerical tools and the difficulty of integrating different research backgrounds into a coherent workflow. WAGCoE aimed to incorporate local knowledge with state-of-the-art tools to provide comprehensive assessment of geothermal opportunities in Western Australia.

2.1 Previous Geothermal Investigations in Western Australia

Geothermal investigations in Western Australia have been performed since the 1950s. In general, they follow the stages described above. Early studies were primarily focused on heat flow calculations through the measurement of temperature gradients and thermal conductivities [e.g. Hyndman et al., 1968]. Bestow [1982] summarised this geothermal knowledge in all of Western Australia through 1982 by collating surveyed data from individual basins, from the small Eucla and Officer Basins to the Carnarvon, Canning, and Perth Basins. Bestow concluded that prospects for direct-use projects exist and further studies were warranted. The early studies showed that heat-flow values ranged from approximately 25 to 67 mW m^{-2}, with the highest values in the Fitzroy Trough of the Canning Basin and the lowest values over Precambrian shield areas.

These results were echoed by temperature estimates at depth compiled by Chopra and Holgate [2007] into AUSTHERM, a GIS database. They analysed subsurface temperature measurements from deep geothermal wells, estimated true formation temperatures, and estimated the depth of the 200 °C isotherm. They produced Australia-wide maps with estimates of surface heat flow and

temperatures at depth. A similar Australia-wide study was performed by Goutorbe et al. [2008]. They compiled temperature data from oil exploration wells and estimated thermal conductivity profiles and radiogenic heat production in depth from geophysical well logs. Their derived heat-flow values were discussed in relation to the relative contributions of heat from the mantle and basement rocks and the overlying sediments. Note that there have been many studies of heat flow [e.g. Matthews and Beardsmore, 2008, Matthews, 2009] in the south-east of Australia, particularly in the basins underlying the Great Artesian Basin.

Crostella and Backhouse [2000] focused on the Perth Basin. They mapped the geothermal gradient and pointed out low values due to the high thermal conductivity of Middle Triassic to Upper Jurassic sediment units of the North and Central parts of the Perth Basin, and high thermal conductivities of the entire stratigraphic section in the southern part of the Perth Basin. The Crostella and Backhouse study indicates that many thermal studies in Western Australia [e.g. Ghori et al., 2005, He and Middleton, 2002] are driven by petroleum prospectivity and the desire to estimate a thermal history to determine if petroleum generation could have taken place in geologic history.

These studies indicated a lack of rock property data for the Perth Basin. The Western Australian Geological Survey sponsored Hot Dry Rocks Pty Ltd (HDRPL) to measure thermal conductivity from core samples from formations within the several basins in Western Australia [Hot Dry Rocks Pty Ltd, 2008, 2009, 2010a, 2010b, 2010c]. These reports provide summary tables of representative thermal conductivities by formation. In addition, HDRPL estimated radiogenic heat production rates of the sedimentary basins' basement rocks throughout Western Australia by using data from Geoscience Australia's geochemical data base Ozchem [Geoscience Australia, 2011]. Their summary tables of this parameter are more general, and include only rock types representative of basement lithologies (rather than samples of actual basement lithologies) due to the difficulties of sampling.

The HDRPL studies [Hot Dry Rocks Pty Ltd, 2008, 2009, 2010a, 2010b, 2010c] also estimated vertical conductive heat flow using the measured thermal conductivities and temperature gradients from deep petroleum wells. They produced spatial maps of heat flow for each of the basins studied.

The first model which considered the influence of convective forces in Western Australia was produced by Swift et al. [Swift, 1991, Swift et al., 1992]. He studied heat flow values estimated from offshore wells in the Exmouth Plateau of the Carnarvon Basin, and postulated that a small region of relatively very low heat flow could not be produced by conductive heat transport alone. He developed a two-dimensional cross-sectional model and concluded that lateral variations of thermal conductivity produce high horizontal temperature gradients which drive natural convection in the region.

The Geological Survey of Western Australia (GSWA) sponsored the generation of a three dimensional geological model in the North Perth Basin [Geological Survey of Western Australia, 2011a, Gibson et al., 2011], derived from an extensive array of petroleum prospecting wells in the region. Conductive temperature estimates and heat flows were calculated based on the geologic structure and the average thermal conductivity values measured by HDRPL [2008]. Unfortunately, the software

utilised in the modelling study was incapable of considering non-conductive heat transport and hence the influence of groundwater flow or convective heat transport was not considered in this region. However, the reports by Gibson et al. did point out the important disconnect between areas of high modelled surface heat flow (where basement rocks were not covered by insulating sediments) and zones of high temperature anomalies, which emphasises the need to focus on the fundamental parameter of temperature (rather than heat flow) in geothermal modelling.

2.2 Geothermal Investigations in the Rhine Graben

It is informative to compare the progress of geothermal investigations in Western Australia with those of the Rhine Graben in Western Europe, where interest in renewable energy sources has boomed in recent years due to government incentives [Runci, 2005, Quaschning and Jourdan, 2010, Oschmann, 2010]. Western Europe has considerably more resources to tackle the problem of geothermal exploration in terms of population and therefore funding, and a considerably smaller land area than Western Australia. Nonetheless, the excellent techniques utilised by research groups in Western Europe provide a guideline to compare work performed here by the Western Australian Geothermal Centre of Excellence. This review focuses on hydrothermal modelling studies in the Rhine Graben, which has been compared in a geothermal context to the Perth Basin [Larking and Meyer, 2010]. The Rhine Graben is a north-northeast trending basin formed in the late Eocene, with a width of approximately 40 km and a length of approximately 300 km. Total vertical offset of the basin sediments is approximately 4500 m and the basin is strongly faulted.

Identification of prospective geothermal regions has been performed both in the Rhine Graben and within the larger European context. Hurter and Schellschmidt [2003] compiled a European atlas of geothermal resources in Europe by investigating the thickness of potential reservoirs and average geothermal gradients. A more detailed Germany wide system was described by Agemar et al. [2007] and made available on-line through the GeoITS project [Pester et al., 2010]. Analysis of shallow borehole heat exchanger potential was provided by Ondreka et al. [2007]. Similar investigations have been performed by WAGCoE. The WAGCoE geothermal data catalogue, described in a companion report [Poulet and Corbel, 2012], is an attempt to collate relevant hydrologic, petrophysical, and temperature data across the entire state. Geothermal prospectivity across Western Australia is detailed in Section 3.1 below, and a more detailed analysis of the North Perth Basin is provided in Section 3.2 of this report.

One of the first major hydrothermal modelling studies was performed by Christoph Clauser as his Ph.D. thesis and presented in a paper by Clauser and Villinger [1990]. This landmark work identified and quantified the conductive and convective components of heat transfer in the basin using three different data sets and means of analysis. First, energy budgets were calculated from shallow thermal profiles disturbed by groundwater flow. Second, thermal data in deep boreholes was analysed by Peclet number considerations to investigate the ratio of convective versus conductive heat transfer. Finally, a two-dimensional cross-section numerical model of water and heat flow confirmed the more local analyses. Similar research in the Western Australian context is provided both in this

report (Sections 3.3, 3.4, 4.3, and 4.4) and within the associated WAGCoE report by Ricard et al. [2012], which presents shallow temperature data. In this report, Section 3.3 investigates the effect of advection on temperature profiles. Section 3.4 uses analytical and numerical analyses to determine whether convective hydrothermal flow is likely to be occurring in the Perth Basin. Sections 4.3 presents a conductive model of the Perth Basin, and Section 4.4 a more detailed hydrothermal convective model of the PMA.

The more recent hydrothermal models developed in the Rhine Graben region are made more accurate by the enormous amount of measurements of subsurface temperatures and hydrothermal rock properties. Pribnow and Schellschmidt [2000] detail a database of over 52 000 temperature values measured from 10 000 boreholes. They provide detailed maps of horizontal and vertical temperature variability across the Rhine Graben. In Western Australia, temperature measurements from petroleum wells are available online [Western Australian Department of Mines and Petroleum, 2012, CSIRO, 2011], but no comprehensive survey of the data is available. The temperature logging performed by WAGOCE and detailed in Reid et al. [2011a] and the associated report by Ricard et al. [2012] is a first step, as is the analysis performed in Section 3.2 below. For rock properties, several studies [Clauser, 2009, Sass and Götz, 2012] detail extensive measurements of thermal conductivity, radiogenic heat production, and porosity and permeability. The equivalent level of detail simply does not exist for Western Australian sediments, despite useful initial studies funded by the GSWA [Hot Dry Rocks Pty Ltd, 2008, 2009, 2010a, 2010b, 2010c].

Within the Rhine Graben, additional modelling studies investigated the influence of geologic structure on fluid and heat flow. Clauser et al. [2002] studied the chemical composition of mineral waters, helium signatures in springs, and the subsurface temperature distribution in the Rhine Graben. They created multiple two-dimensional generic models to investigate the effects of anisotropy, faulting, sediment cover, and the transition from a conductive thermal regime to an advection-dominated one. Bächler et al. [2003] showed that thermal anomalies in the Rhine Graben followed north-south striking faults by using a three-dimensional convective numerical model. That study pointed out that these convective features would not be noticed in a two-dimensional analysis. A similar analysis for the PMA is shown here in Section 4.3.

Heat as a groundwater tracer was utilised by Zschocke et al. [2005] to determine Darcy flow velocities from temperature logs. A similar analysis is provided in Section 3.3 below, which investigates the disturbance of conductive temperature profiles by advective groundwater movement.

Similar to the Driscoll studies detailed in section 2.1 [Geological Survey of Western Australia, 2011a, Gibson et al., 2011], a purely conductive model of the Rhine Graben was performed by Dezayes et al. [2008]. They investigated geothermal potential across the entire Rhine Graben by modelling reservoir thickness and estimating a regional geothermal gradient. From these building blocks, the study provided estimates of heat-in-place density and exploitable heat, although a full three-dimensional temperature field was not modelled. A more extensive whole-of-basin analysis is provided in Section 4.2 below for the Perth Basin, and heat-in-place methodology was developed by WAGCoE student Florian Wellman [Wellmann et al., 2009].

Although geothermal development is only at a research stage in Western Australia, active geothermal projects utilise subsurface heat in the Rhine Graben and throughout Germany. Blöcher et al. [2010] describe hydrothermal modelling at a geothermal power plant. They detail the changes in fluid and rock properties caused by hydraulic stimulation and the operation of a production and injection doublet. This reservoir scale modelling is further addressed in WAGCoE work in the related report by Ricard et al. [2012] and also in this report in Section 5.2, where the theoretical and computational coupling of thermal, hydrological, mechanical, and chemical processes is described.

In addition to case studies, the European research groups also focus on numerical analysis techniques. One example is provided by Rath et al. [2006], which performs joint inversion of heat transfer and fluid flow using sophisticated optimisation techniques. Similar fundamental numerical development has been performed by WAGCoE, as detailed in Section 5.1 describing the *escriptRT* code and in Section 5.2 showing an application of the new methodology. Similarly, Section 5.3 details a process which allows the incorporation of uncertainty into the entire hydrothermal modelling workflow, and concludes with a case study in the North Perth Basin.

3. GEOTHERMAL POTENTIAL OF WESTERN AUSTRALIA

Humanity has been benefiting from geothermal resources for thousands of years. Since the Iron Age, and probably much earlier, geothermal uses were based on opportunistic surface expressions, including hot springs, geysers etc. Geothermal waters were used for medicinal purposes, for cooking and for heating. With the advent of the industrial revolution an energy economy was established and geothermal resources were viewed in a new light. It was seen that tectonically/volcanically active areas circulate hot geofluids close to the Earth's surface, allowing easy construction of turbine systems to generate electrical power such as those in Italy, New Zealand, or Iceland.

Of course, not all locations on the Earth's surface are regions of intense volcanic/tectonic activity, so steam-driven technologies are not widely applicable. Nevertheless, the Earth's average thermal emission defines a temperature gradient within the subsurface, i.e. soil/rock temperature tends to increase with depth with a gradient of very approximately 30 °C per kilometre of depth into the subsurface. This gradient can be quite variable with location, according to presence/absence of radiogenic/plutonic rocks, the effects of groundwater flows, and geostructural faults and insulating formations, etc. If we assume the mean surface temperature is 20 °C and that the mean thermal gradient at the surface applies at depth, we can easily see that rock temperatures of the order of 50 °C are achievable at 1 km depth, and that 170 °C is achievable at 5 km depth. In practice, exploitation of geothermal resources is only viable where the geothermal gradient is above average; identifying locations of anomalous geothermal gradient can significantly reduce capital investment requirements in developing geothermal resources by reducing drilling and pumping costs.

This section details four studies performed by WAGCoE to search for geothermal prospects in Western Australia. Section 3.1 provides a state-wide overview of geothermal prospectivity for hot sedimentary aquifers, using publically available data from petroleum wells. Based on these results, Section 3.2 focuses on a much smaller region in the North Perth Basin and considers whether electricity generation would be feasible from geothermal reservoirs. Section 3.3 investigates the effects of groundwater flow on the temperature distribution in the PMA. Finally, Section 3.4 considers the likelihood of convective heat flow occurring in the Perth Basin.

3.1 Geothermal Prospectivity in Western Australia

For any technology or type of resource, potential accessible geothermal power can be defined [Muffler and Cataldi, 1978] by the thermal energy contained in the fluid pumped from a system per unit time:

$$\text{Power} = Q * C_w * (T_w - T_a) \qquad 3.1\text{-}1$$

Here, the fluid (usually water) properties are represented by the heat capacity C_w. The rock properties are represented by the flow rate Q and the temperature differential available for work. The available flow rate Q from a well is dependent upon the rock permeability and storativity, the aquifer thickness, and properties of the well and pump [de Marsily, 1986]. In sediments, the permeability is a well defined porous media concept, while EGS projects in granite depend upon fractures to provide the available water. The temperature differential is always defined by the temperature available at the well T_w, and some reference temperature T_a. T_a may represent the ambient temperature at the ground, or perhaps the outflow temperature of a mechanical heat exchanger. As long as the definition is consistent by application [AGRCC, 2010], the relative value of a geothermal resource can be quantified in these terms.

Hence, to search for areas where geothermal energy is easily exploited, we look for regions with high flow rates, high temperatures, and preferably both. In Western Australia, the best prospects lie in deep sedimentary basins such as the Perth Basin. Since the Perth Basin is at least 10 km deep in most locations, the sedimentary sequence accesses high temperature zones and also has physical properties conducive to drilling and water circulation.

The Western Australian Geothermal Centre of Excellence [Regenauer-Lieb et al., 2009] was formed, in part, to search for good geothermal prospects in the state of Western Australia. For deep sedimentary basins such as those found in Western Australia, the most important prospectivity parameters are the aquifer permeability and porosity, and the temperatures at depth.

This section focuses on evaluating the relative geothermal prospectivity across the state by surveying previously existing data and integrating the results into a Geographical Information System (GIS). Results are presented for four major basins (Fig. 1.1A), with recommendations for further exploration.

3.1.1 Methods

The aim of the project was to make easily accessible overviews of geothermal prospectivity for the entire State. A GIS provides ease of use and allows simple computations such as those described below. The final results have been published online through the WAGCoE Data Catalogue [Corbel and Poulet, 2010] and are disseminated easily to end users.

GIS background

The prospectivity maps were made with the GIS package ArcGIS. As ArcGIS is widely used in the geoscientific world, the maps will be easily accessible for any community interested in the results. All the data, temperatures and reservoir quality information are available in an ArcGIS database, for

query or update if requested. The data were obtained with permission from the Department of Mines and Petroleum (DMP).

Petroleum prospectors in Western Australia must provide data to the DMP, which generally becomes publically available five years after submission. Petroleum companies submit information from their drilled wells, including sedimentary formation tops and base elevations, petrophysical data from core samples obtained while drilling, and geophysical logs. The DMP compiles this information into professional overview reports on the petroleum prospectivity, and also provides associated spreadsheets containing the raw data. Data relevant to geothermal resource and reservoir analysis was included in the WAGCoE database.

Basin selection

This study focused on onshore sedimentary basins, as geothermal projects are unlikely to be executed offshore. There are eight sedimentary basins with onshore components in Western Australia (Fig. 1.1A). The Ord and Bonaparte Basins were not mapped for this study as they are primarily located in the Northern Territory, with only a small proportion of each basin lying within Western Australia. We make a threshold assumption to define resources of significance: sedimentary basins have to be deep enough to have temperatures greater than 60 °C, as this is a minimum temperature for economic direct use of geothermal energy for district heating or air conditioning applications. On this basis the Eucla and Bremer Basins are too shallow to support significant geothermal resources and were therefore excluded from this study. The four remaining onshore basins are the Officer, Canning, Carnarvon and Perth Basins.

For each basin, a well data spreadsheet was obtained from DMP. The number of applicable wells in each basin varies depending on petroleum exploration interest. For example, the Officer Basin contains only 33 exploration wells, while the Canning Basin has over 250 wells available in public data, with many more still in confidential status due to active exploration projects. Not all wells had the data required for this study. Temperatures were only available for a subset of the wells, as temperature logging is not a routine procedure for petroleum exploration.

Reservoir selection

Reservoirs were determined using the Summary of Petroleum Prospectivity report [Geological Survey of Western Australia, 2011b] from DMP. Although the focus of this report is on possible petroleum reservoirs, the rock qualities are still applicable to the geothermal context. Again, reservoirs too shallow to reach suitable temperatures were excluded from this study. This depth cut-off is also applied in the Geothermal Reporting Code [AGRCC, 2010], as shallow aquifer heat usage is usually not regulated in Australia. Reservoirs below the city of Perth have not been considered here either, this particular study being limited to remote regions. In each basin, wells crossing the remaining reservoirs were extracted from the relevant DMP spreadsheets.

Reservoir Thickness

Reservoir thickness is important for two aspects of HSA prospectivity. First, the depth, lithological unit thickness, and geothermal gradient control the maximum temperature found in any location. Second, the reservoir thickness contributes to the amount of flow available, as the transmissivity of the reservoir is vertical integral of the hydraulic conductivity over the reservoir interval. For a given permeability, a thicker reservoir will provide a higher potential transmissivity, and hence potentially greater flow rate.

The thickness of each reservoir was determined in each well by subtracting the stratigraphic base from the top of the reservoir. For wells that did not extend deep enough to determine the base of the reservoir, the total well depth was subtracted from the reservoir top to find a minimum thickness of the reservoir.

Reservoir Quality: Porosity and Permeability

Reservoir quality was also assessed by looking at the petrophysical properties of the reservoir. The most basic parameters, and those most commonly measured by petroleum companies, are porosity and permeability. Permeability directly affects the available flow from a geothermal well. Porosity describes the water available in the rock pores, and determines the bulk heat capacity of the rock/pore matrix.

The DMP spreadsheets contain laboratory measurements of porosity and permeability from small cores sampled from the well during drilling. Although these measurements are taken at a small scale under unloaded conditions, and are not applicable to the entire reservoir, it is generally assumed that they are directly correlated to the large scale reservoir behaviour.

To classify the reservoir quality, permeability was used as the primary criterion. Core permeability was averaged over the reservoir thickness of the well to yield the effective well permeability for the reservoir. A reservoir was classified as good if its effective permeability was greater than 5 mD and poor with less than that cutoff. If permeability measurements were not available, then similarly, porosity was arithmetically averaged over the reservoir formation to yield the effective well porosity for the reservoir. The reservoir was classified as good with greater than 5% porosity and poor with less than 5%. In some wells, core data are not available if the reservoirs were of no interest for petroleum purposes.

Combining into Reservoir Quality

The reservoir quality parameter was obtained by combining the metrics from reservoir petrophysics and thickness. Four categories of reservoir quality were defined, from Poor to Very Good, as shown in Table 3.1.

Thickness (m)	Permeability[mD] ≥ 5mD and ≥ 5%	Porosity (%) < 5mD and < 5%
≥ 200 m	Very good	Average
< 200 m	Good	Poor

Table 3.1: Reservoir quality classification.

Temperature

Temperatures were extracted from several reports commissioned by DMP [Chopra and Holgate, 2007, Hot Dry Rocks Pty Ltd, 2008, 2010c, 2010b, 2009, 2010a]. Temperature is often measured in petroleum wells to provide information about the possibility of useable hydrocarbons within the formation. However, there are different ways of collating temperature measurements. Most common temperature data from petroleum wells are Bottom Hole Temperatures (BHT). When geophysical logging is performed in an exploration well, a point value of temperature is usually measured at the deepest logging location. Temperatures are also quite often measured while performing Drill Stem Tests (DST) [Horne, 1997] on specific units in the wells. DSTs are designed to determine the productive capacity, permeability or pressure of a reservoir. Unfortunately, continuous temperature logs are rarely measured for the sole purpose of petroleum exploration.

Temperature Measurement Quality

In their report, Chopra and Holgate [2007] defined a borehole temperature quality-ranking scheme which they applied to all the temperatures they gathered. The highest quality data, of type A, were determined from BHT measurements performed more than seven days after the completion of drilling, or from DSTs. Lower quality data of type B were obtained from Horner-corrected BHT measurements [Beardsmore and Cull, 2001] with three or more data points in time. Quality data of type C were corrected from BHT measurements with two temporal data points. Temperature measurements of quality D, E and F were discarded in this work, being judged as unreliable. Similar quality assessment was applied to the temperature extracted for the other reports and only temperatures of good quality, therefore A, B or C were kept.

Temperature Estimates

To estimate temperatures at depth at the well locations, a synthetic temperature log with a constant average geothermal gradient was calculated. Piecewise linear interpolation was applied between the surface Mean Annual Surface Temperature (MAST) and point temperatures at depth. If the base of the formation was below the lowest measured temperature, the temperature estimate was occasionally extrapolated in depth. However, this extrapolation was uncommon because the petroleum exploration wells usually completely crossed permeable reservoirs.

This simple linear interpolation is equivalent to an assumption of subsurface formations with isotropic and constant thermal conductivity, together with purely conductive one-dimensional (i.e. vertical) heat flow. Although a true temperature log in these wells is unlikely to be linear with depth, the average gradient so derived gives a simple indication of the variation of subsurface temperature with depth.

Combining data to form maps

Within each sedimentary basin, pointwise estimates at petroleum wells were combined to make a map of geothermal potential in the sedimentary aquifers.

Temperature estimates at depth along each well were combined with the reservoir quality indices

to produce the overview maps. The reservoir quality is used to determine the size of the point estimate, so that very good reservoirs plot with larger symbols than poor reservoirs or those with no petrophysical data.

If multiple reservoirs were located in the same well, both potential estimates were plotted at the same point. The hottest reservoir was prioritised and plotted above any shallower reservoirs.

3.1.2 Results

Results from the analysis are shown in Figures 3.1 to 3.4 for remote regions in the Officer, Canning, Perth, and Carnarvon Basins. In all cases, the geothermal prospectivity map is overlain onto a reference map showing population density and nearby towns or cities. The sedimentary basin outline is also shown on the maps, indicating the extent of deep water-bearing formations. Figure 3.1 shows the legend applicable to all four maps.

The maps provide an easily assimilated overview of the available public data, geographic proximity to population centres or engineering projects, estimates of reservoir quality, and useable temperature ranges. Regions with significant amounts of data, usually in currently producing petroleum reservoirs, show up as locations with large numbers of data circles. Nonetheless, due to the size of Western Australia, even the densest data is widely scattered and lateral interpolation is difficult. Basins with little exploration data, such as the Officer Basin, can only provide hints of subsurface conditions. Individual basins are discussed below with regards to their prospectivity and data quality.

Officer Basin

The Officer Basin (Fig. 3.1) contains only four exploration wells with public data. They indicate good reservoir quality but temperatures below 80 °C. These low-enthalpy resources could be utilised by shallow aquifer projects such as geothermally heated swimming pools. However, the Officer Basin does not contain large mining, petroleum, or industrial projects and therefore the small population is unlikely to have the economic resources for targeted utilisation of geothermal heat. However, a project combining remote water supply and geothermal energy usage, such as exists at Birdsville, Queensland [Chopra, 2005], may be applicable to the Officer Basin if water quality is adequate.

Canning Basin

The Canning Basin contains several active petroleum producing fields; many more are located offshore but are not indicated on the map. This extensive amount of deep data provides a good estimate on maximum available temperatures. However, where data is available the reservoir quality is generally only “good” or less; note that petroleum production generally requires lower pumping rates than those needed by geothermal systems. Because petroleum production generally also produces unwanted water, this co-produced hot fluid could be very economically utilised in geothermal schemes. This prospectivity is particularly likely to the southeast of Derby where many petroleum producers exist.

In other locations, for example to the southwest of Broome, exploration wells indicate high temperatures but there is insufficient information on reservoir quality. This situation can occur in

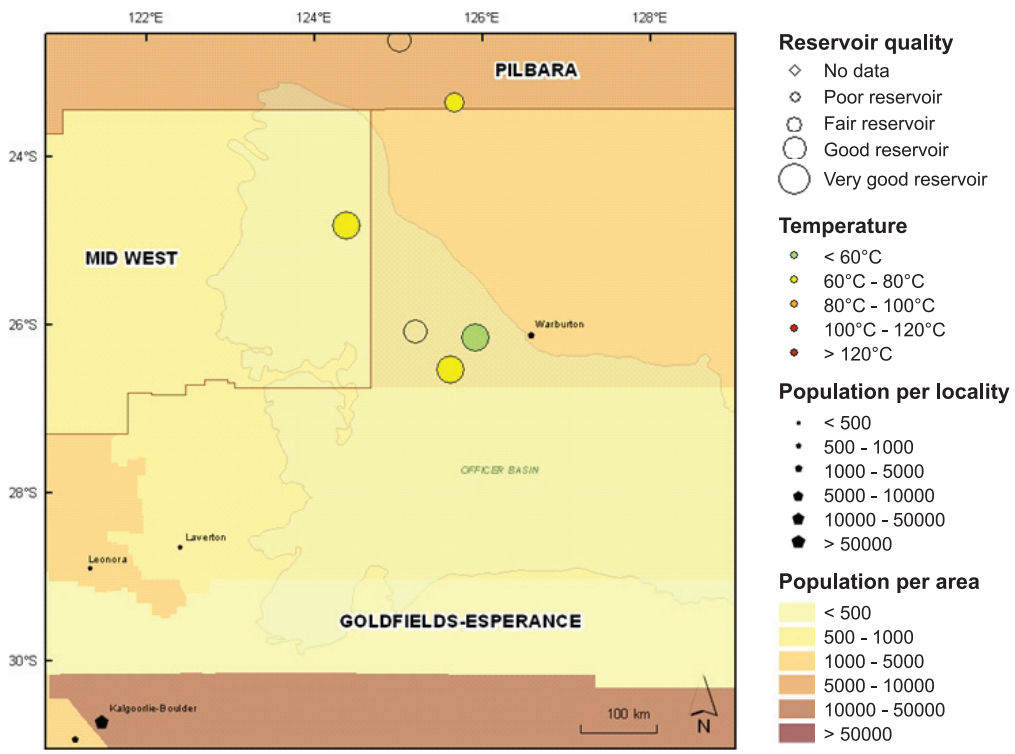

Figure 3.1: Officer basin geothermal prospectivity.

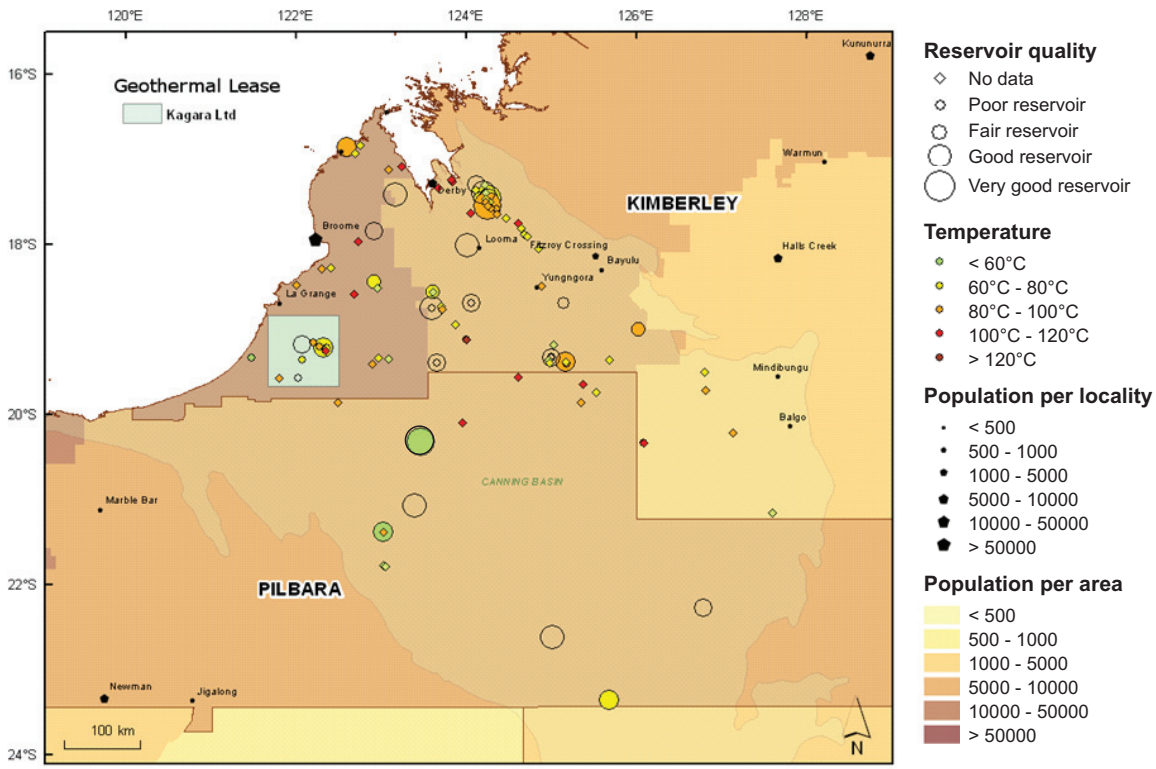

Figure 3.2: Canning Basin geothermal prospectivity.

petroleum exploration when no signs of oil or gas are present in the exploration well – in these cases the exploration company does not spend additional resources on characterising a reservoir with core plug analyses. However, alternate sources of information about reservoir quality could be obtained by investigating, for example, geophysical logs. Sufficient data exists to perform desktop explorations study such as was performed by Corbel et al. [2011] and described in Section 4.1 of this report.

Carnarvon Basin

Data coverage in the large Carnarvon Basin is more sparse. Some locations indicate good to very good reservoir quality, but do not have temperature information in the same well. Figure 3.3 differs from the other maps as it contains information about industrial locations onshore and offshore. Because multiple reservoirs are shown in this figure (witness the overlapping circles north of Kalbarri), it is difficult to determine the lateral extent of reservoirs and extrapolate either temperature or formation data. However, reservoir quality is very good east of Shark Bay. This resource could be targeted to generate geothermal schemes which would significantly enhance the tourist status of this World Heritage Location.

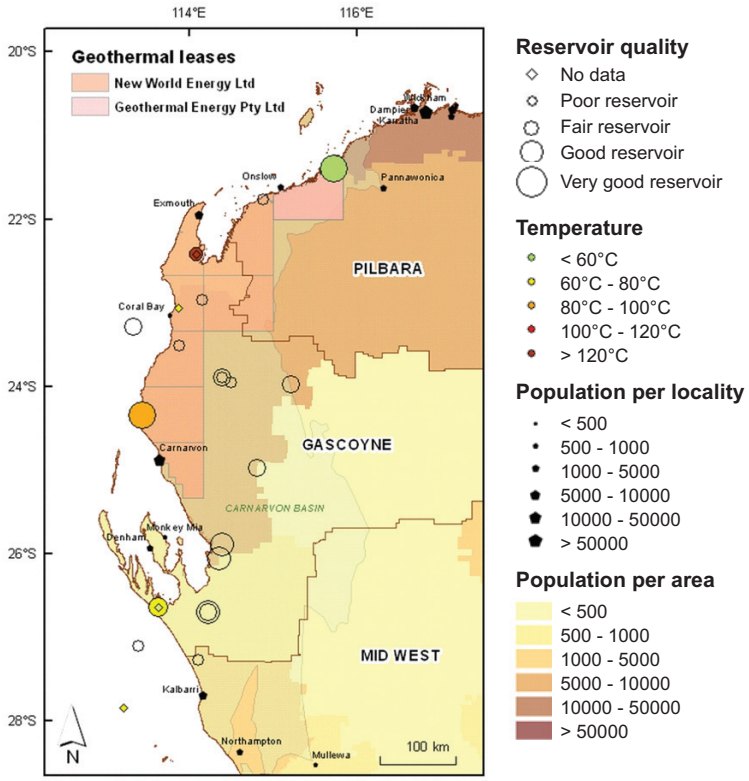

Figure 3.3: Carnarvon Basin geothermal prospectivity.

Perth Basin

The Perth Basin covers the largest longitudinal range of any of the basins and has considerably different quantities of regional data. In the North Perth Basin (see inset map in Figure 3.4) there is considerable data on reservoir quality and high temperatures above 120 °C have been recorded. In addition, there is considerable infrastructure for industries, resource projects, and energy transport. The region appears to have good prospectivity for HSA systems, and this is reflected in the number of geothermal leases taken up by geothermal companies. One difficulty with this type of data mapping is that it is difficult to determine whether the highly permeable rocks are located in the same reservoir or rock formation as the high temperature measurements.

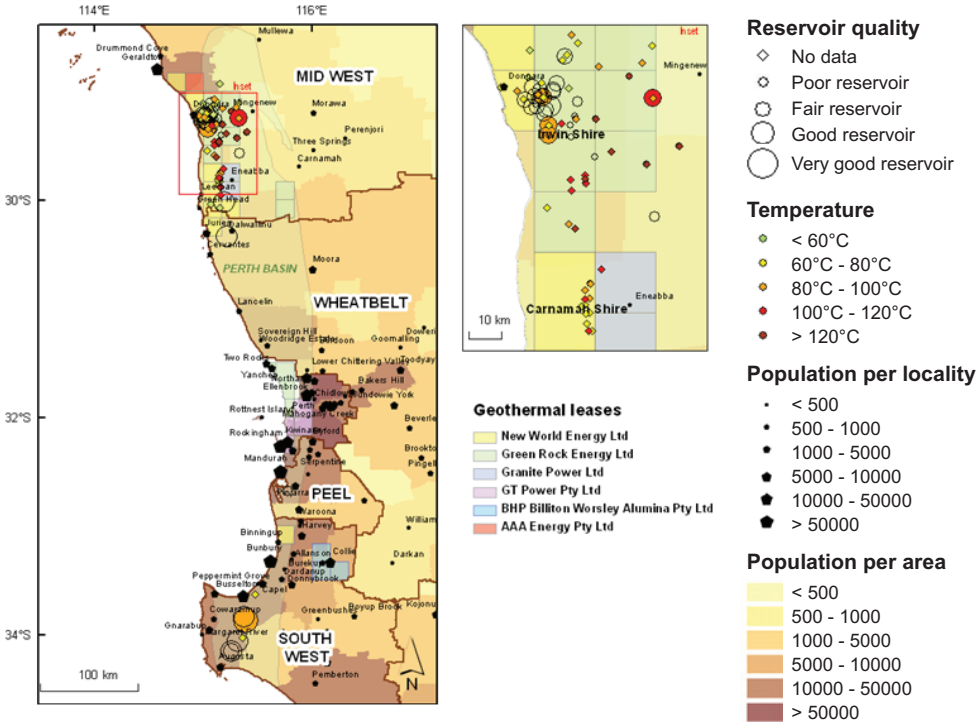

Figure 3.4: Perth Basin geothermal prospectivity, with inset of the North Perth Basin.

This mapping analysis has not been performed in the Central Perth Basin because of the proximity to large population centres. However, because of the metropolitan nature, neither are there many petroleum wells which would provide data.

In the South Perth Basin, there is sufficient data indicating both good quality reservoirs and temperatures up to 100 °C. These resources should be further investigated for low enthalpy (direct use) applications in this region of the state.

3.1.3 Conclusions

A larger overview of Western Australia is provided in Figure 3.5. Here, the relative quality of data can be compared across the different basins. High temperatures in the North Perth Basin and the Western Canning Basin are immediately obvious; these would be good regions to consider projects generating electricity with geothermal heat. Good reservoir quality is clear in the South Perth Basin, the Carnarvon Basin, the Officer Basin, and the Western Canning Basin. These areas should be investigated for geothermal projects requiring high flow rates, even if the available temperatures are in the low enthalpy range.

Insufficient data on reservoir quality exists in the Eastern Canning Basin to determine whether the high temperatures can be utilised easily. Similarly, areas in the Carnarvon Basin have insufficient temperature data to make straightforward predictions of geothermal feasibility. For both of these areas, further study would clarify the geothermal prospectivity. The targeted formation could be identified by querying the underlying database which generated these prospectivity maps. Location

within a particular formation would allow horizontal extrapolation of reservoir quality and give an idea of the geothermal gradient within the formation. For reservoir quality, alternative geophysical data such as gamma ray and electrical resistivity logs could be utilised to provide approximate predictions of formation permeability and porosity.

This study provides a general overview of hot sedimentary geothermal prospectivity in Western Australia using publically available data. It suggests regions which could be further investigated with site-specific studies, and can provide a useful input to consideration of projects under the Royalties for Regions program. A cost-effective initial step would be to perform a desk-top modelling study using public data [Reid et al., 2010], initially with a conductive heat flow analysis and, if warranted, with a complete hydrothermal model such as is presented in Section 4.1 of this report. Three-dimensional temperature estimates either from simple interpolated temperature models (e.g. Section 3.2) or from more complex models in which the mechanisms of heat transport are explicitly considered (e.g. Sections 4.1, 4.2 and 4.3) can allow determination of the technical viability and long-term sustainability of geothermal schemes. The studies could be integrated with regional data on resource projects or industrial infrastructure to best predict the economic viability of any geothermal project in these remote regions.

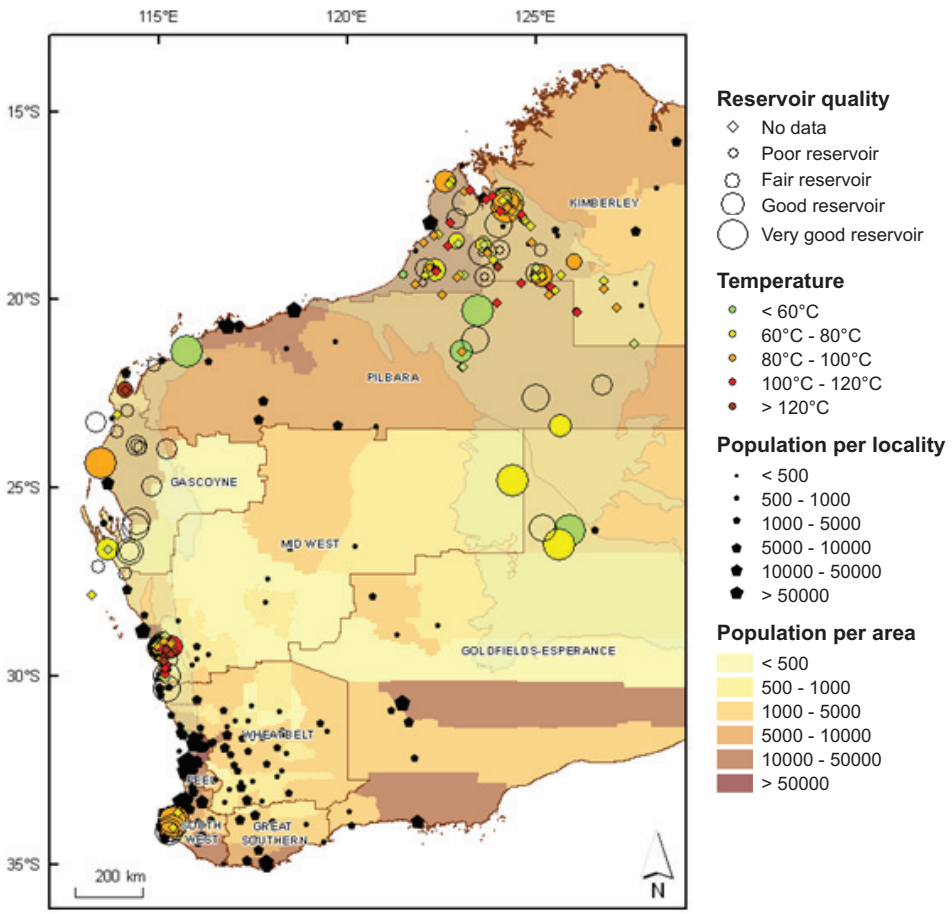

Figure 3.5: Geothermal prospectivity across Western Australia.

3.2 Potential for Electricity Generation in the North Perth Basin

The North Perth Basin (Fig. 1.1B) has been identified as a region with good potential for geothermal energy usage, as discussed in the previous section. In addition, several geothermal companies have taken up tenements with the intention of future geothermal development. Recently, a high-capacity data transmission line has been laid between Geraldton and Bentley, which will use the transmission links being built under the Australian Government's Regional Backbone Blackspots Programme (RBBP) [Nextgen Networks, 2011]. Power would ideally be provided along the route of the RBBP transmission lines to minimize on-the-ground disruption and assist with construction and maintenance.

In this pilot study, the WAGCoE has identified preliminary target locations where a geothermally powered electricity generation plant could be constructed. Previous research into the geothermal potential within the onshore Perth Basin identified high heat flow in the northern areas near Dongara [Hot Dry Rocks Pty Ltd, 2008]. Elevated temperatures are not the only ingredient for a geothermal power plant. The availability of groundwater and, in particular, high subsurface permeabilities are paramount for geothermal electricity production. WAGCoE therefore focused on quantifying the temperature regime south of Geraldton, and near the RBBP transmission line.

A power plant utilising geothermal energy could produce hot water using either an Enhanced Geothermal System (EGS) or a HSA reservoir. In the EGS case, low-permeability rocks are artificially fractured to produce permeability. Cold water is pumped down into the fractured zone, where it is heated by the surrounding rock and then extracted from another well nearby. In the HSA case, naturally permeable sediments host the hot water forming subsurface aquifers, obviating the need for an external water sources (as required for the EGS case). Because of the thick permeable sediments present in the North Perth Basin, this report focuses on HSA geothermal schemes.

3.2.1 Methods

To estimate the likelihood of obtaining suitable subsurface temperatures for geothermal electricity production, temperatures were interpolated from data measured in the North Perth Basin. The study area is shown in Figure 1.1B.

The analysis was based on data described in Mory and Iasky [1997]. Their study covers a region which is primarily onshore between 29° and 31° South, approximately between Geraldton and Lancelin, with an east-west extent between 114° 75' and 116° East. In this area, the on-shore ground surface ranges from sea level to approximately 300 m AHD.

From their analysis of 82 petroleum exploration wells and geophysical surveys of gravity, magnetic and seismic data, Mory and Iasky determined a consistent set of sedimentary formation tops and isopach maps for the major sedimentary units. Six cross-sections were also produced from this data. WAGCoE integrated the structural model described by Mory and Iasky into a three-dimensional subsurface geologic model. From this model, elevations were determined for the top of three major aquifers located in the model area: the Yarragadee Formation, the Eneabba Formation, and the Lesueur Formation. Isopach thicknesses of these formations were determined by subtracting the modelled surfaces.

Mory and Iasky list corrected BHTs and surface temperatures for 93 petroleum and 33 water wells in the North Perth Basin [Mory and Iasky, 1997], Appendix 9. These wells were geolocated onto the geological model. The extent of the Mory and Iasky model area, the well locations, local towns, and the transmission line are shown in Figure 3.6.

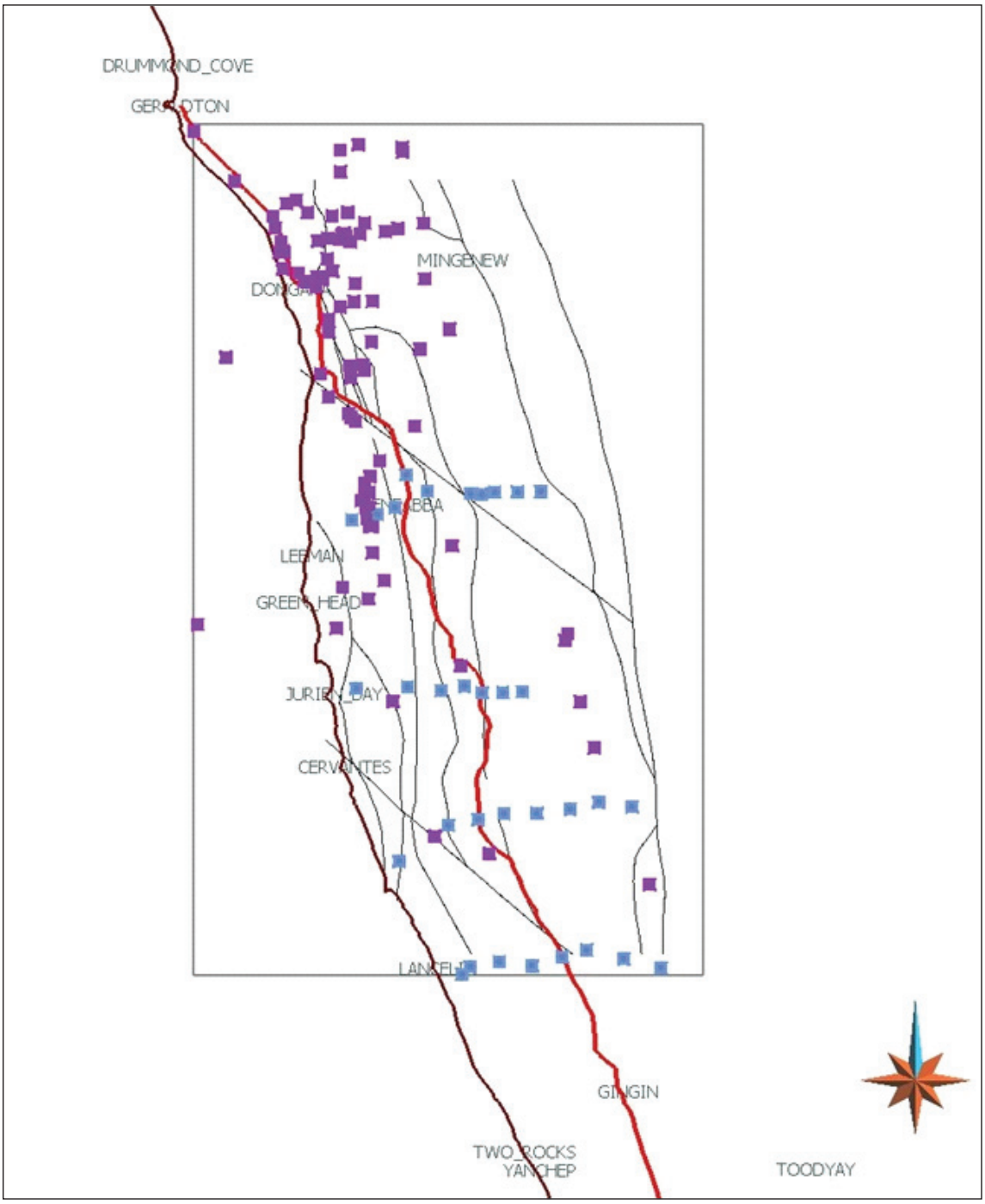

Figure 3.6: Location of Mory and Iasky [1997] model area in the North Perth Basin, with towns and additional features shown: coastline (brown), transmission line (red), deep petroleum wells (purple), shallower groundwater wells (blue), faults (black).

Temperatures were linearly interpolated from the base of the well to the ground surface to form a synthetic temperature log with a constant average geothermal gradient. This simple linear interpolation is equivalent to an assumption of subsurface formations with isotropic and constant thermal conductivity. Although a true temperature log in these wells is unlikely to be linear with depth, the average gradient so derived gives a reasonable first estimate of the vertical variation of subsurface temperature [Thomas, 1984]. The vertical temperature logs were then interpolated horizontally between wells with an inverse distance algorithm. The radius of influence of each well was assumed to extend no further than 50 km in the horizontal plane, while the interpolation grid was spaced at 25 km horizontally and 20 meters vertically.

3.2.2 Results

The interpolated temperatures and gradients can be shown in several different ways. Figure 3.7 shows the temperature at -2000 m AHD, the lowest depth where extensive temperature measurements are available. The depth to 100 °C is shown in Figure 3.8. High temperatures are

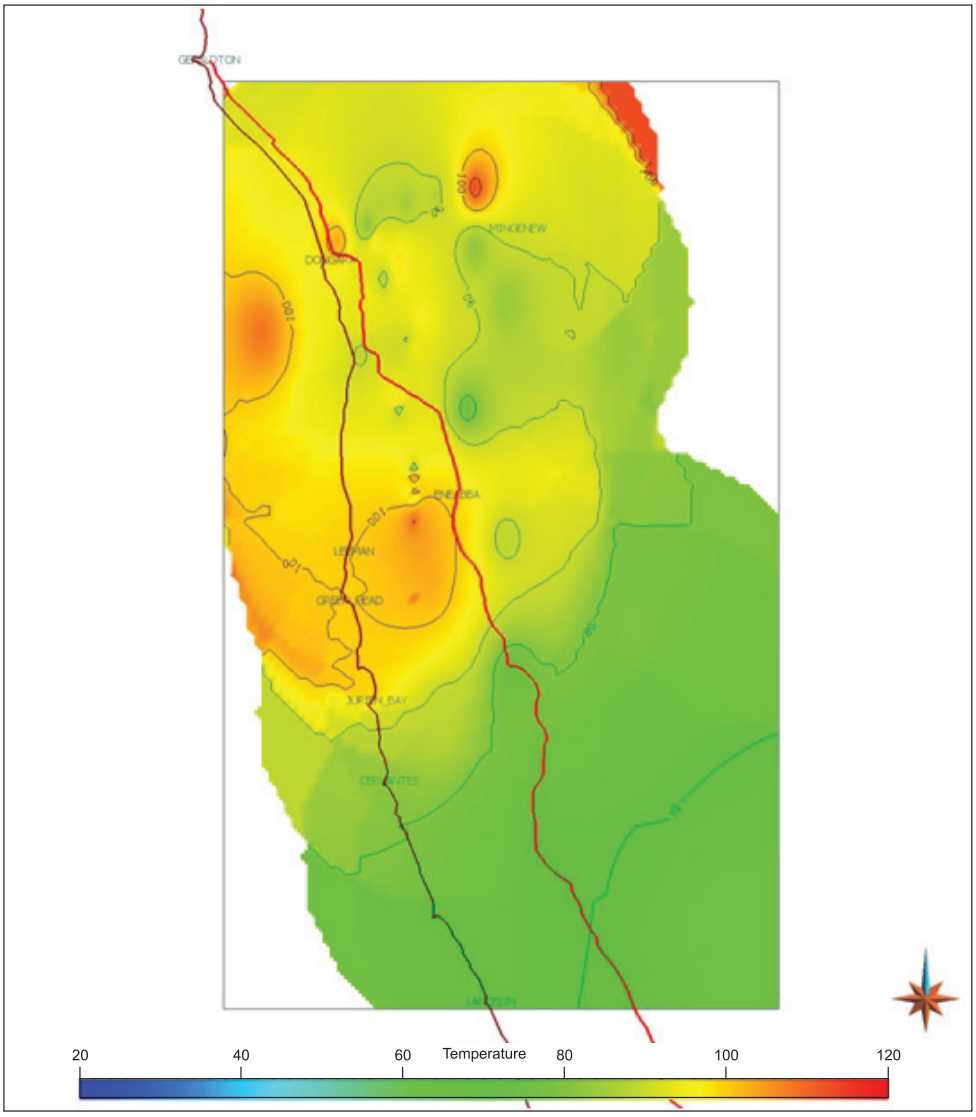

Figure 3.7: Temperature [°C] at -2000 m AHD in the North Perth Basin derived by interpolation between wells.

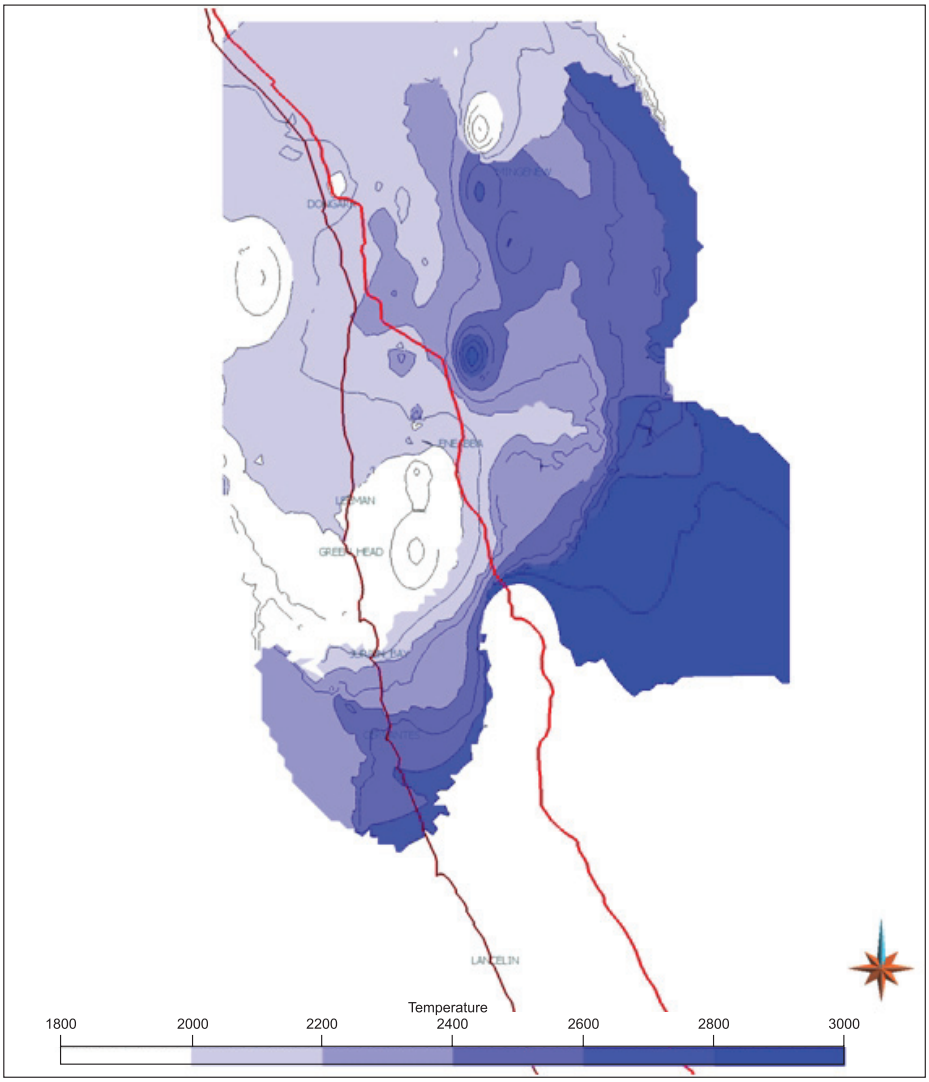

Figure 3.8: Depth [m] below AHD to 100 °C in the North Perth Basin derived by interpolation between wells.

found near Green Head and Jurien Bay. However, these elevated subsurface temperatures are primarily found in Precambrian basement rocks located along the Beagle Ridge rather than in the basin sediments [Thomas, 1984]. Figures 3.9, 3.10, and 3.11 show temperatures at the top of three formations which form significant aquifers in the region, namely the Yarragadee, Eneabba, and Lesueur Formations. In these figures, depths where temperature data does not exist are shaded in grey. Note that the Yarragadee Formation in Figure 3.9 does not exist in many locations west of the transmission line route due to faulting and erosion. Finally, the geothermal gradient calculated from this simple BHT interpolation is shown in Figure 3.12 at -500 m AHD, where significant data exists.

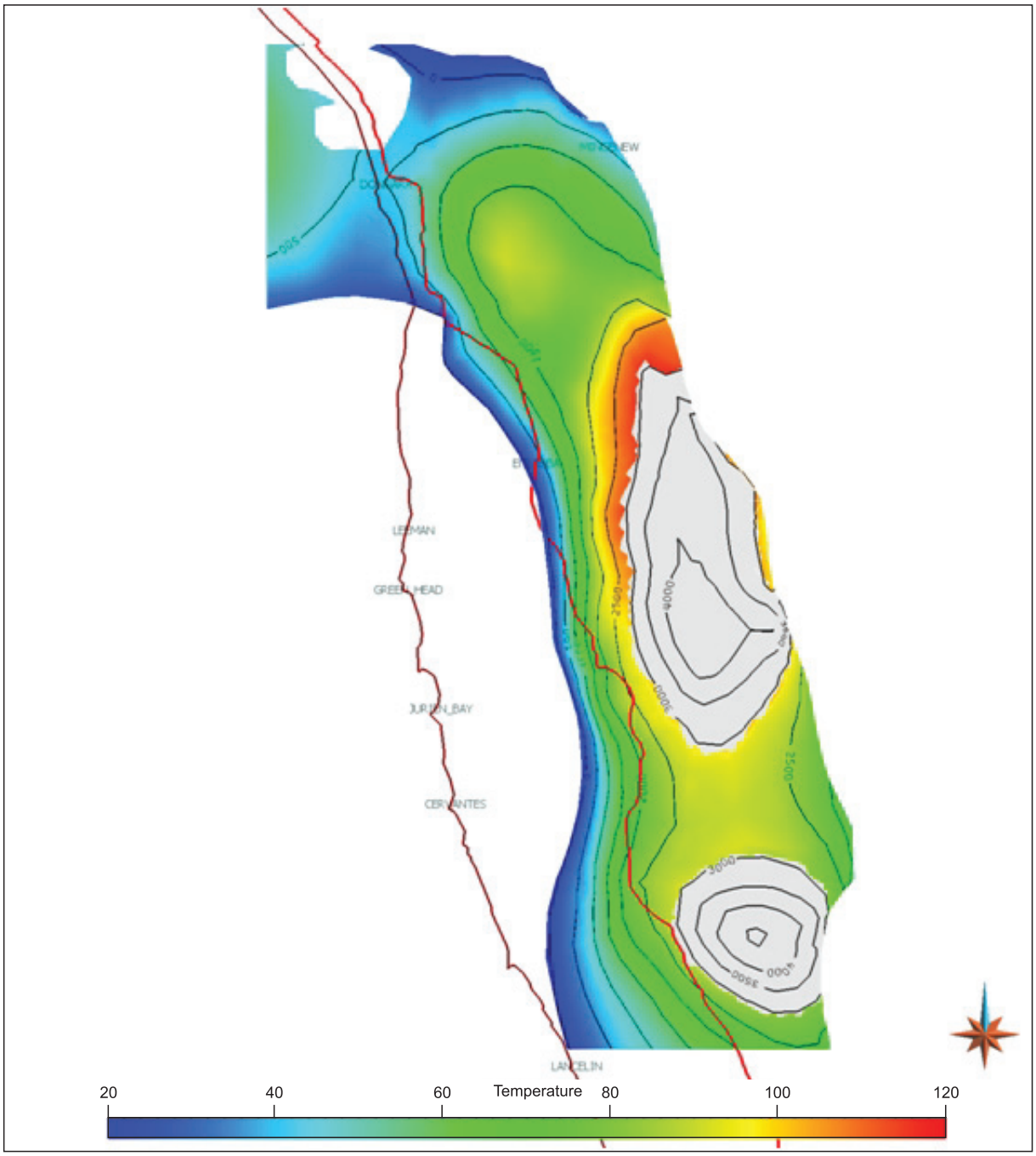

Figure 3.9: Temperature [°C] at the top of the Yarragadee Formation in the North Perth Basin derived by interpolation between wells. Contour lines show depth of the top of the formation (m below AHD). Grey shading indicates no temperature data available at those depths. White indicates the formation does not exist in these areas.

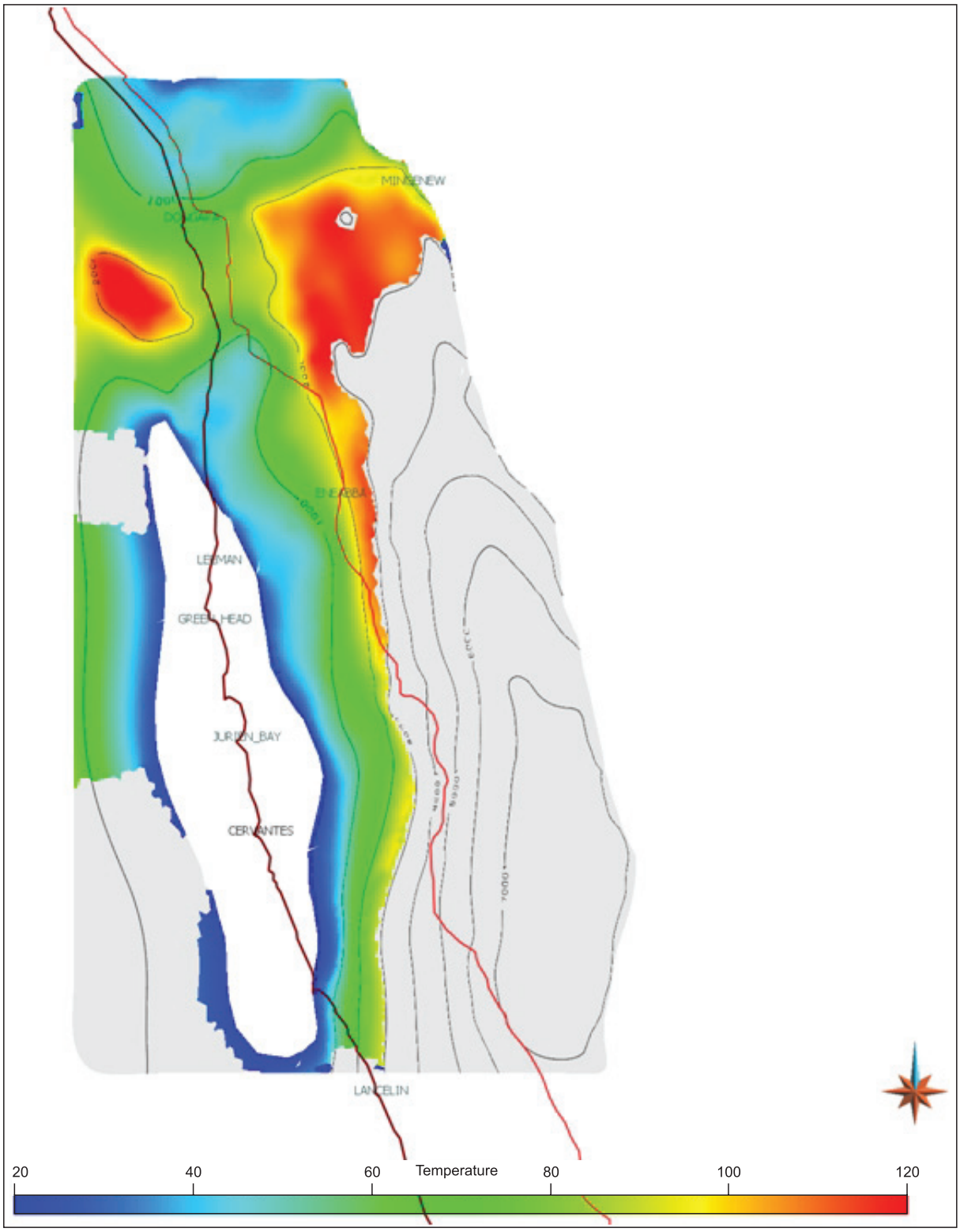

Figure 3.10: Temperature [°C] at the top of the Eneabba Formation in the North Perth Basin derived by interpolation between wells. Contour lines show depth of the top of the formation (m below AHD). Grey shading indicates no temperature data available at those depths. White indicates the formation does not exist in these areas.

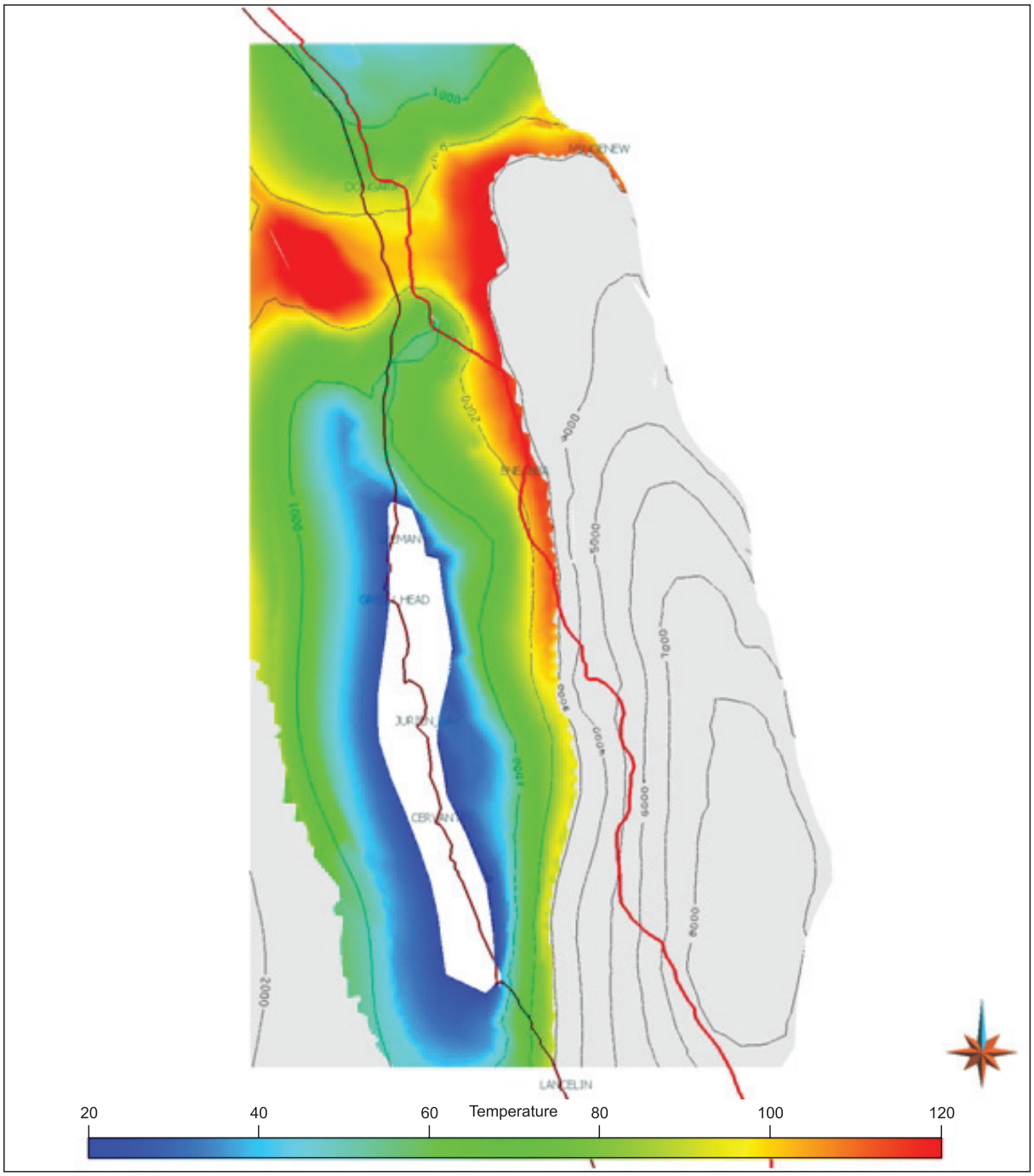

Figure 3.11: Temperature [°C] at the top of the Lesueur Formation in the North Perth Basin derived by interpolation between wells. Contour lines show depth of the top of the formation (m below AHD). Grey shading indicates no temperature data available at those depths. White areas indicate formation does not exist at that location.

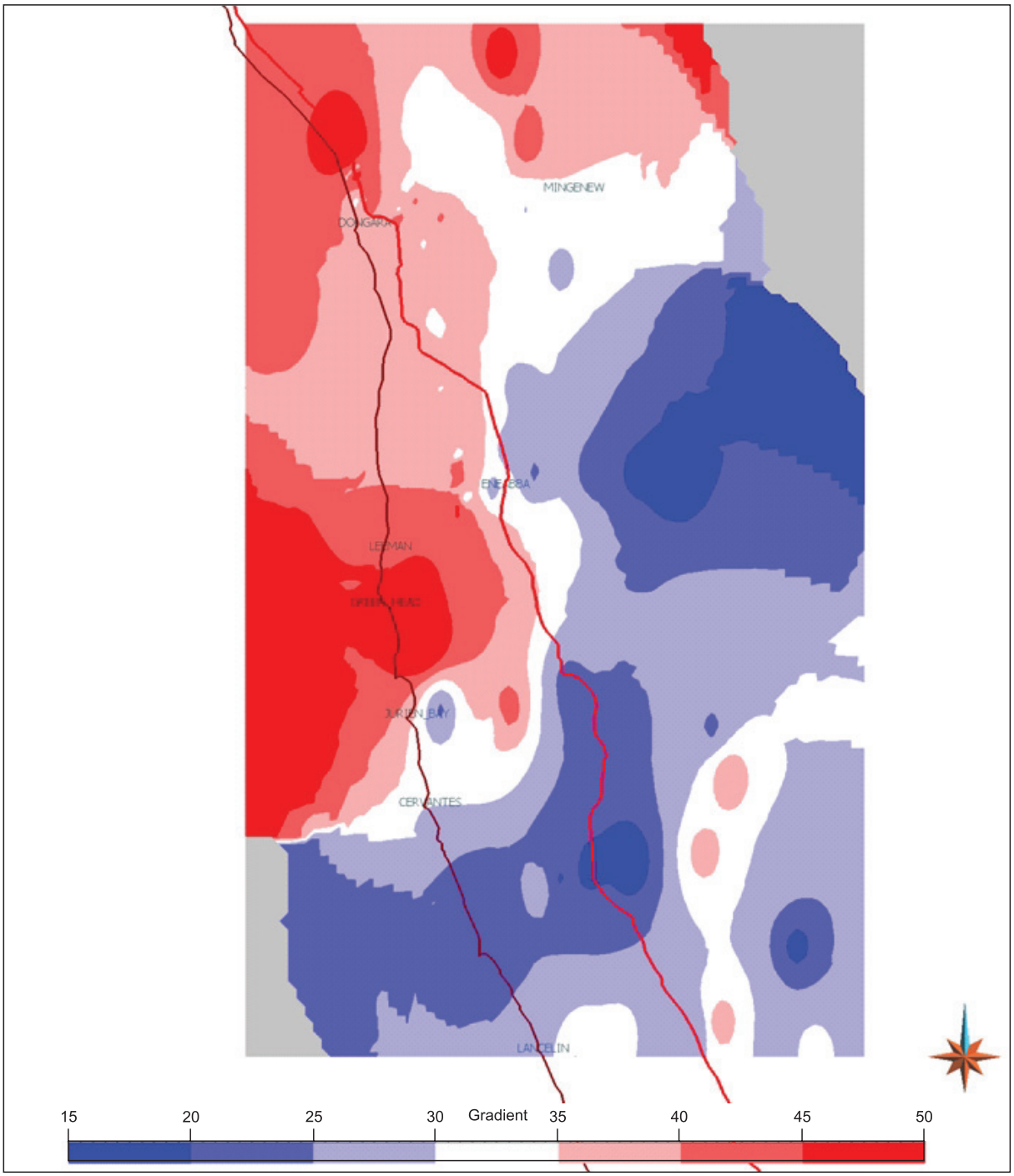

Figure 3.12: Geothermal gradient in °C km^{-1} at -500 m AHD in the North Perth Basin derived by interpolation between wells.

Geothermal power plants require a significant quantity of hot water, which in the HSA case comes from aquifers. The thickness, porosity, and permeability of the available aquifers control the amount of water naturally available. Figures 3.13 and 3.14 show the thickness of the Yarragadee and Eneabba Formations in the studied area. The Yarragadee Formation reaches over 2000 m thick in the southern part of the study area. The Eneabba Formation ranges between 80 and 1000 m thick. The Lesueur Formation is up to 400 m thick in the area.

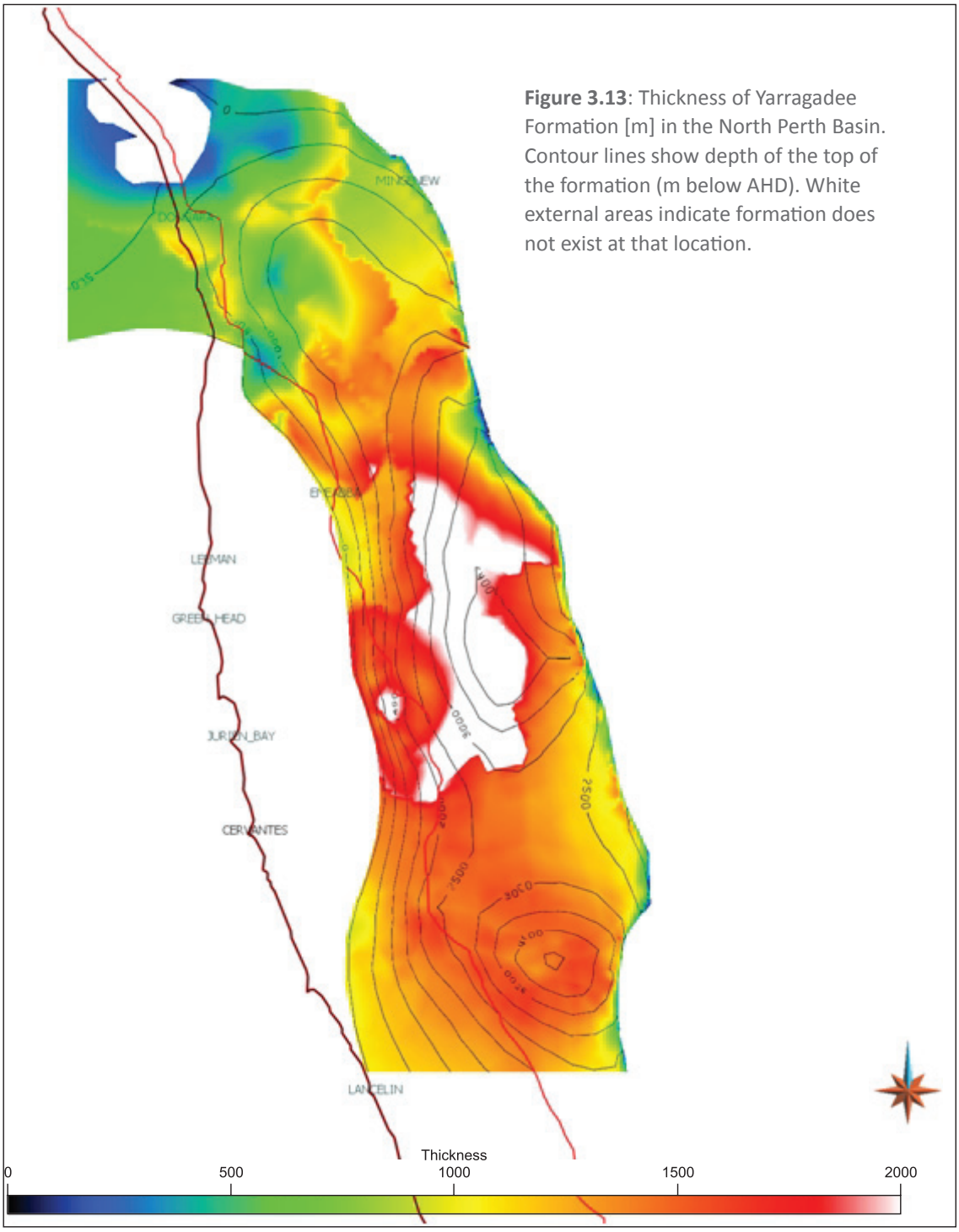

Figure 3.13: Thickness of Yarragadee Formation [m] in the North Perth Basin. Contour lines show depth of the top of the formation (m below AHD). White external areas indicate formation does not exist at that location.

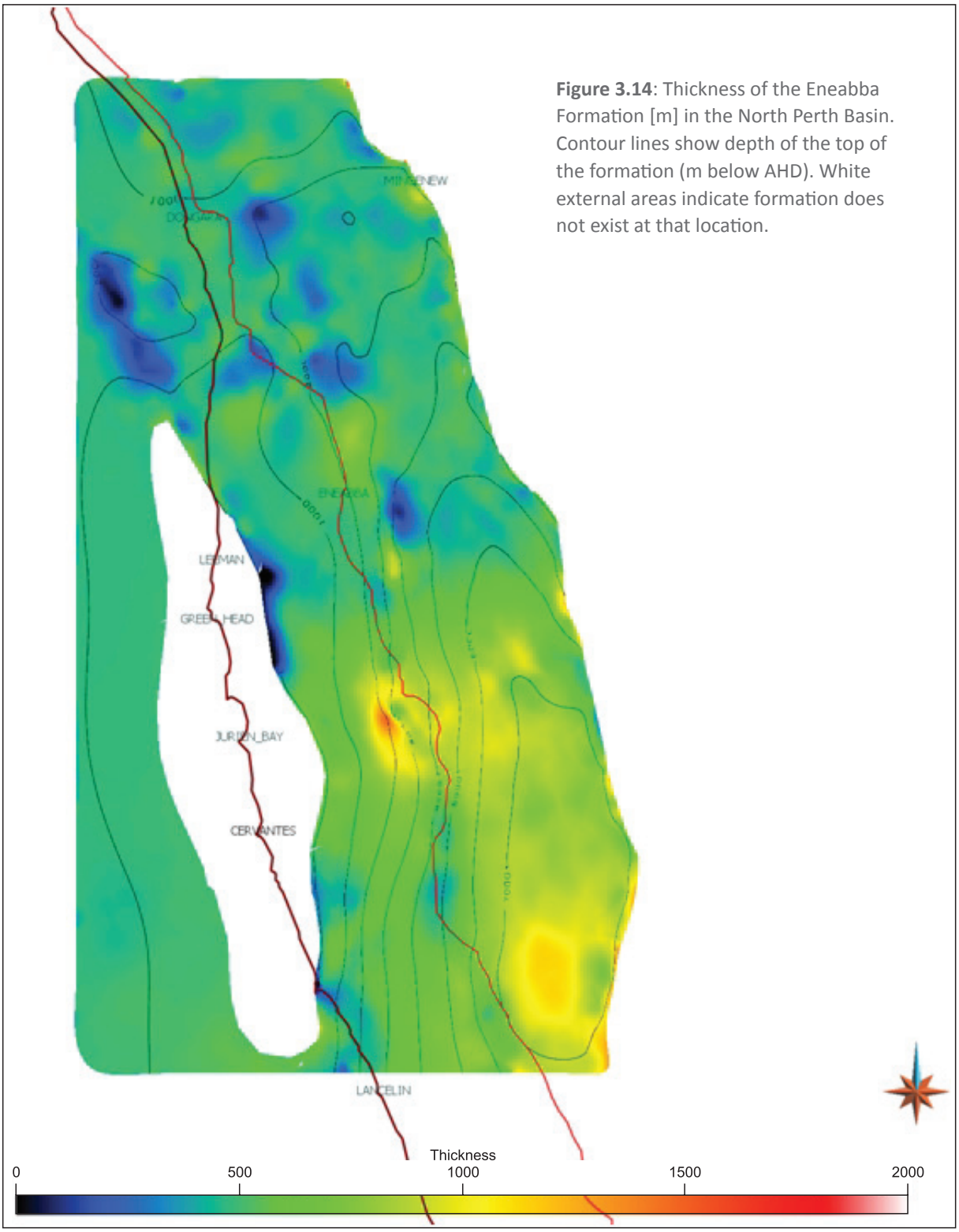

Figure 3.14: Thickness of the Eneabba Formation [m] in the North Perth Basin. Contour lines show depth of the top of the formation (m below AHD). White external areas indicate formation does not exist at that location.

Permeability and porosity data for local formations are available from testing performed in the large numbers of petroleum exploration wells nearby. The Yarragadee Formation is interbedded fine to coarse sandstone, siltstone, and claystone with minor amounts of conglomerate and coal [Crostella, 1995]. The Eneabba formation is a fine- to coarse-grained sandstone interbedded with siltstones and claystones. The Lesueur Sandstone is made up of coarse to very coarse sandstone with minor siltstone and conglomerate. Crostella [1995] notes that all of these formations have excellent water-yielding properties.

3.2.3 Conclusions

For a successful HSA geothermal application, naturally occurring aquifers must supply sufficient hot water to support electricity generation for the plant lifetime. In the North Perth Basin, the Yarrragadee, Eneabba and Lesueur Formations form aquifers with adequate temperatures. The Yarragadee and Eneabba Formations additionally provide sufficient thickness for large quantities of water production, and their reservoir properties are good.

Based on the maps shown in this section, the most promising areas for HSA geothermal electric power plants near the RBBP transmission network lie near Dongara. This statement is based on only a very preliminary analysis of the available data and does not constitute professional advice on the feasibility of any such electricity generation initiatives. Additional work in this area should focus on characterising the geologic structures in more detail, quantifying the aquifer properties, building a much more comprehensive hydrothermal understanding of local reservoirs and formations, and identifying local infrastructure essential for the geothermal power plant.

3.3 Identifying Advective Heat Transport in the Perth Metropolitan Area

3.3.1 Introduction

In this section, continuous downhole temperature logs from Artesian Monitoring (AM) wells in the Perth Metropolitan Area (PMA) are examined for evidence of advection. Advection is transport of heat by groundwater that is moving due to external forces such as topographic head or groundwater extraction. Advection causes the temperature-depth profile to depart from the piecewise linear form that is expected if heat is transported purely by conduction.

The concept of using subsurface heat as a tracer for groundwater flow was established in the 1960s; however interest in this field waned and research became scarce. Anderson [2005] provides a comprehensive review of the body of work on heat as a groundwater tracer. In her work, Anderson highlights the difficulties of using hydraulic head measurements to calibrate a groundwater flow model, and explains how temperature data can be used to generate independent estimates of groundwater fluxes instead. Several works address the issue of identifying groundwater flow from perturbations in geothermal profiles [e.g. Drury et al., 1984] and subsequently estimating groundwater velocities from said thermal profiles [e.g. Zschocke et al., 2005, Reiter, 2001].

Verdoya [2008] focuses on the coupling of hydraulic and thermal properties to estimate the

Darcy velocity and infer an aquifer hydraulic conductivity, based on analysis of artesian wells and boreholes drilled in unconfined aquifers. This work matched thermal logs to analytical models which incorporated both heat and fluid transfer. Several models and underlying assumptions were tested, and models assuming non-conductive heat flow fitted the data best. Verdoya also noted that by taking into account the shape of the thermal profile as a quality descriptor of the type of flow (for example, a concave-down profile representing a horizontal influx of warmer water), reliable estimates of the flow components can be determined.

A more recent overview of coupled groundwater and heat transfer studies is found in Saar [2011]. This paper focuses on using geothermal heat as a tracer in large scale groundwater systems and utilizes this feature to determine aquifer flow systems and permeabilities.

Our work takes place in the PMA within the Perth Basin (Fig. 1.1), a 1000 km long sedimentary rift basin in the southwest of Western Australia, extending between the latitudes 27°00'S and 34°00'S in a north-northwesterly orientation. Its upper layers comprise three major sedimentary aquifers of Early Permian to Late Cretaceous age; the Superficial Aquifer, the Leederville Aquifer and the Yarragadee Aquifer. This study focuses on the Leederville Aquifer, a semi-confined aquifer comprising the Henley Sandstone Member of the Osborne Formation and the Pinjar Member, Wanneroo Member and Mariginiup Member of the Leederville Formation [Davidson, 1995]. This aquifer typically lies between 10 and 360 m below ground in the PMA and is an important source of drinking water for Perth's northern suburbs. The study area is shown in Figures 1.1B and 3.15.

The purpose of this study is to identify regions of advection in the Leederville Aquifer by analyzing detailed temperature logs. Portions of this research have been published as reports [Bloomfield, 2010, Reid et al., 2011a, Reid et al., 2011b] and this work is being further developed into a journal publication [Reid et al., 2012].

3.2.2 Background

The primary source of geothermal heat is the decay of radionuclides and heat released by crystallization in the outer core of the Earth [Beardsmore and Cull, 2001]. This heat can then be transported by conduction through adjacent rock and water-filled pores or by water movement within the rocks by advection or convection [Haenel and Stegena, 1988].

Conduction is described by Fourier's Law, where heat flows from the higher temperatures, usually at greater depth, to the lower temperatures at the Earth's surface. In a one-dimensional, vertical case steady-state conductive heat transfer is determined using the following equation:

$$Q_z = -\lambda \cdot \frac{\partial T}{\partial z} \qquad 3.3\text{-}1$$

where Q_z is the conductive vertical heat flow (Wm^{-2}), λ is the thermal conductivity of the local lithology ($W\ m^{-1}\ K^{-1}$) and $\partial T/\partial z$ is the thermal gradient within the formation ($K\ m^{-1}$). Note that this equation ignores the contribution of internal heat generation, which is usually negligible in sedimentary rocks [Beardsmore and Cull, 2001]. From this equation, if thermal conductivity is constant within each formation, then a temperature profile exhibiting conductive heat flow will have

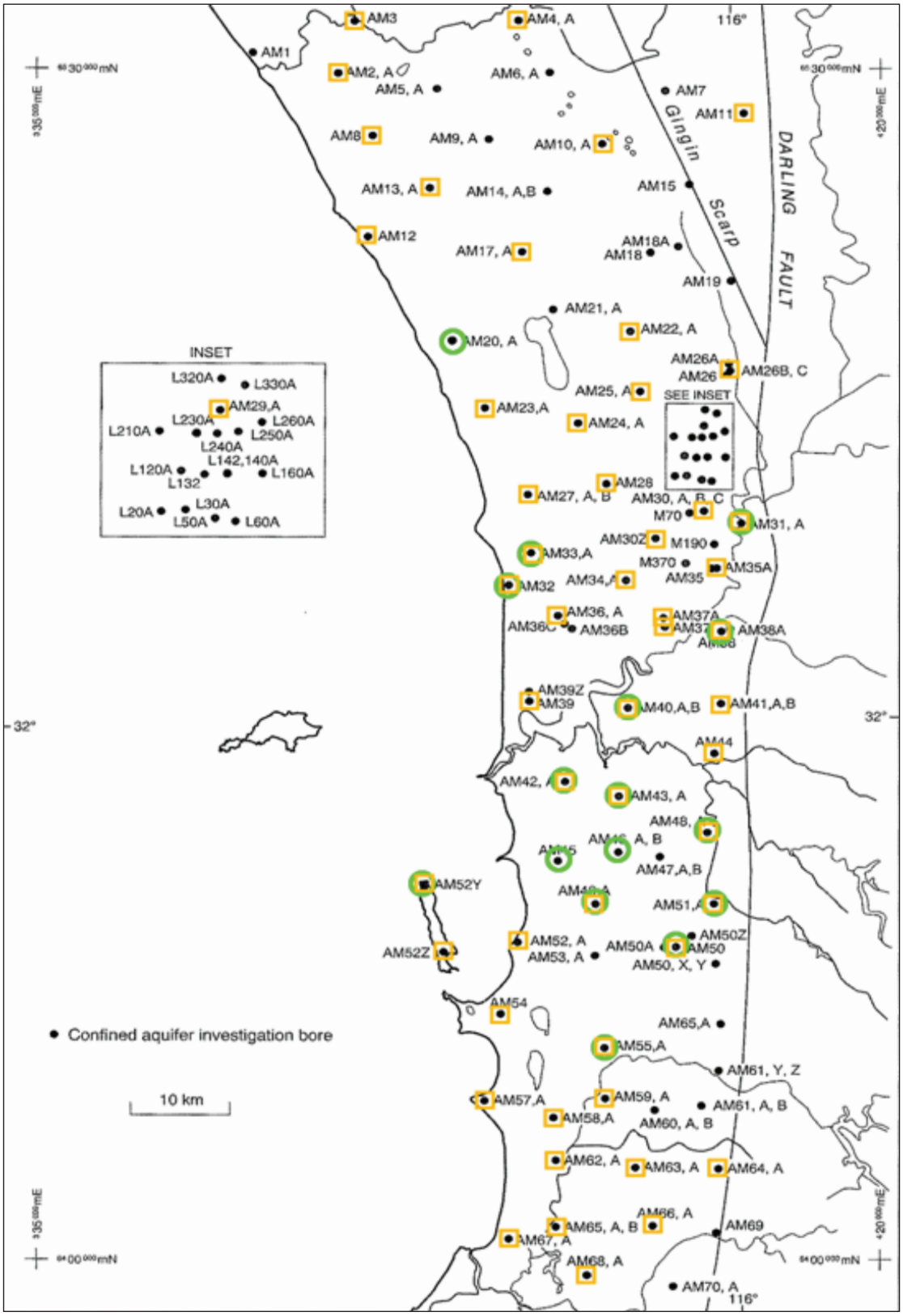

Figure 3.15: Locations of logged (green circles) and digitized (yellow squares) WA DoW AM wells (after Davidson, 1995).

linear segments by formation within the well. Variable thermal conductivities may generate non-linear temperature profiles.

When heat movement by water is significant, the heat transfer equation involves the water flow rate v (m s^{-1}):

$$(\rho c)_m \frac{\partial T}{\partial t} = \lambda_m \left(\frac{\partial^2 T}{\partial x^2} + \frac{\partial^2 T}{\partial y^2} + \frac{\partial^2 T}{\partial z^2} \right) - (\rho c)_f \left(v_x \frac{\partial T}{\partial x} + v_y \frac{\partial T}{\partial y} + v_z \frac{\partial T}{\partial z} \right) + A \qquad 3.3\text{-}2$$

where ρ is density (kg m^{-3}), c is specific heat (J kg^{-1} K^{-1}), subscript m refers to the combined rock and fluid medium, subscript f the fluid only, and the dimensional subscripts (x, y and z) define the direction of flow [Jessop and Majorowicz, 1994]. The first term on the right-hand side of Equation 3.3-2 describes the conductive component of heat flow, whilst the second term describes the advective component of heat flow and A is the rate of heat generation (W m^{-3}). As with Equation 3.3-1, the rate of heat generation in sediments is considered negligible, and thus A is often ignored. In this equation, the thermal conductivity of the rock and fluid medium λ_m is assumed constant and the transfer of heat between liquid and solid phases is assumed to be instantaneous.

In general, the water flow rate v may be imposed by external conditions (advection) or may be caused by buoyancy effects due to density gradients (convection) [Clauser, 2009]. In formations where water flow represents a significant source of heat movement, the vertical thermal profiles deviate from straight-line segments and assume non-linear shapes within these formations. Here, we demonstrate this effect in Perth's Leederville Aquifer.

3.3.3 Methods and Results

Data collection and quality control

Temperature profiles were obtained from Artesian Monitoring (AM) wells owned by the WA Department of Water (DoW). Detailed geophysical logging was performed in 17 wells during 2010 to obtain temperature and gamma ray profiles. Additional data were obtained by digitizing 52 wells logged in the 1980s. The work was performed by members of WAGCoE and Honours students from the University of Western Australia and Curtin University of Technology.

The analysis in this section utilizes field data which are never as tidy as theoretical considerations would assume. Before analysis could commence, several quality control issues needed to be addressed. First, the influence of measurement drift was removed. Second, the depth interval of valid data was determined. Finally, bad data were identified and discarded. Detailed information on the logging, digitization and quality control of the data can be found in an extensive technical report [Reid et al., 2011a], here we mention only the types of necessary corrections.

The digitized wells sometimes suffered from poor data quality throughout the depth profile. The mechanical logger utilized in the 1980s could sometimes introduce spurious spikes or flat areas in the log recorded on paper. In addition, the digitization procedure was by necessity much coarser in resolution, yielding smaller quantities of more approximate data.

Conductive analysis

In order to isolate the effects of advective heat transport in the aquifer, the simple conductive assumption of heat flow is first applied to the data. Discrepancies between the conductive temperature profile and the measured data can then be investigated for possible advective influences.

The first step of the analysis was to assume that vertical conduction as given by Equation 3.3-1 is the only form of heat transport in the well. The thermal profiles and stratigraphy data were loaded into the GeoTemp software package [Ricard et al., 2011]. The point temperatures at the top and base of each formation were used to determine an average thermal gradient for each formation in each well. This technique is a simple way to ensure the modeled profile is continuous along the depth of the well. Formation boundaries were provided by Davidson [1995] and in some cases adjusted by WAGCoE after analysis of the recent gamma ray logs. As an example, Figure 3.16 illustrates the range of calculated geothermal gradients in the Mariginiup Member of the Leederville Formation; Reid et al. [2011a] provides similar plots for each formation. The average geothermal gradient in the Leederville Aquifer ranges from a low of 23.9 °C m^{-1} in the Henley Member to a high of 31.8 °C m^{-1} in the Mariginiup Member.

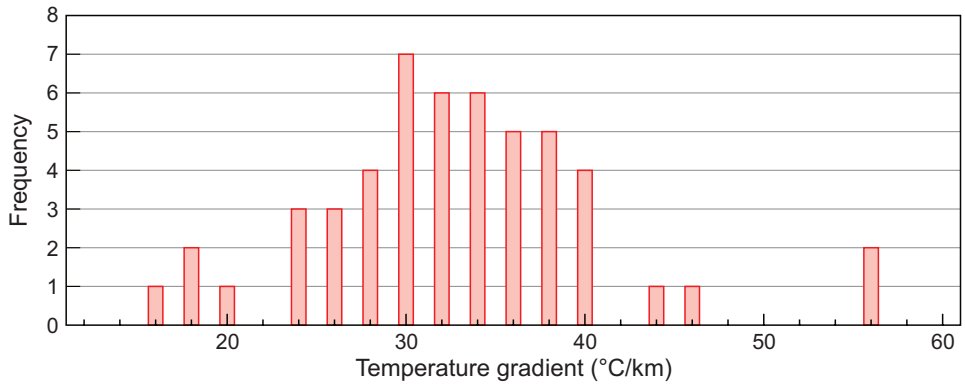

Figure 3.16: Histogram showing the distribution of the calculated thermal gradients in the Mariginiup Member.

Under the conductive assumption, Equation 3.3-1 implies that for a constant vertical heat flux, the geothermal gradient and the thermal conductivity are inversely related. Using the global average crustal heat flow of Q = 64 mW m^{-2} [Beardsmore and Cull, 2001] and the geothermal gradients calculated in GeoTemp, thermal conductivities were calculated for each formation. These calculated thermal conductivities are compared to thermal conductivities measured from core samples in the Perth Basin by HDRPL [Hot Dry Rocks Pty Ltd, 2008]. Table 3.2 details the ranges of thermal conductivities calculated from the conductive assumption in the Leederville Aquifer.

Formation	Calculated range of thermal conductivities (W m^{-1} K^{-1})	Harmonic mean of measured thermal conductivities by HDRPL (W m^{-1} K^{-1})
Henley Sandstone Member (Osborne Formation)	1.48 - 5.25	1.13
Pinjar Member (Leederville Formation)	1.52 - 15.61	2.56
Wanneroo Member (Leederville Formation)	1.58 - 7.71	2.56
Mariginiup Member (Leederville Formation)	1.14 - 4.00	2.56

Table 3.2: Range of thermal conductivities in the members of the Leederville Aquifer calculated from a purely conductive assumption, and the corresponding measured values from HDRPL [2008]

Measured thermal conductivities in clastic sedimentary rocks generally range from 1.5 to 4.0 W m^{-1} K^{-1} worldwide [Clauser, 2009]. The wide spread in the data calculated from the conductive assumption implies that the inherent assumptions of Equation 3.3-1 and the constant heat flow are violated. The most obvious violations are that the vertical heat flow or thermal conductivity is not spatially homogeneous, and/or water movement plays a significant part in moving heat.

Advective analysis

The influence of coupled heat and fluid flow was determined by first identifying locations where non-conductive heat flow is significant. The horizontal thermal gradient is then quantified.

To determine whether a section of the thermal profile in each formation was advective or conductive, the relative quadratic error between the conductive model and the observed data was calculated in each formation as shown in Equation 3.3-3.

$$e = \frac{\sqrt{\sum_i \left(\left| T_{O(i)} - T_{M(i)} \right|^2 \right)}}{\Delta z} \qquad 3.3\text{-}3$$

Here, e is error per unit depth (°C m^{-1}), T_O is the observed temperature (°C), T_M is the modelled temperature (°C), and Δz is formation thickness (m). Errors greater than 5% are deemed to indicate formations influenced by advection. Figure 3.17 illustrates the visualization of conduction and advection in a thermal profile and the relative error.

Table 3-3 lists the wells that exhibit advective behavior in the members of the Leederville Aquifer. Wells exhibiting advection in the Leederville are dispersed relatively evenly across the study region. Proximity to major surface water expressions, such as rivers and lakes, appears to have little influence on the occurrence of advection. For example, Figure 3.18 shows that AM38A is located near a tributary to the Swan River and shows advection in the Leederville Aquifer, whilst AM31, located on a similar tributary, does not. Thermal profiles also appear to be largely unaffected by proximity to the coast.

AM49 is located near the Jandakot area where the Water Corporation has several active pumping bores, suggesting that advection may be related to a well's proximity to other bores. It is likely that the other wells categorized as advective are being influenced by local pumping as the potentiometric surface in the Leederville Aquifer is heavily disturbed by pumping [Davidson and Yu, 2008]. Unfortunately, pumping bore locations were unavailable during this study to investigate this hypothesis. Advection may also be caused by regional groundwater flow.

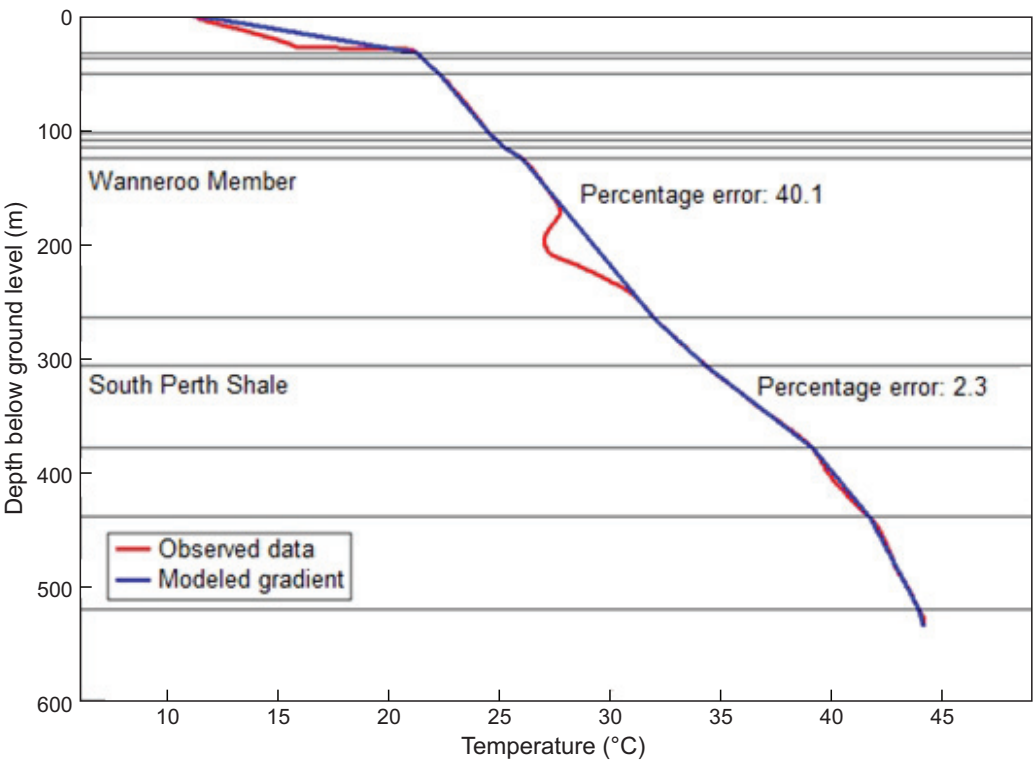

Figure 3.17: Thermal profile from WA DoW AM well AM33A showing evidence of advection in the Wanneroo Member and conductive behaviour in the South Perth Shale.

Well	Henley Sandstone Member (Osborne Formation)	Pinjar Member (Leederville Formation)	Wanneroo Member (Leederville Formation)	Mariginiup Member (Leederville Formation)
AM2	-	no	yes	no
AM4A	-	no	yes	no
AM22	-	no	yes	-
AM33A	no	no	yes	no
AM35A	yes	no	no	no
AM37A	no	no	no	yes
AM38A	yes	yes	yes	no
AM41	yes	-	no	no
AM49	no	yes	yes	no
AM55	-	yes	no	yes

Table 3.3: Members of the Leederville Aquifer which exhibit advective behaviour, based on a mismatch of 5% or more between the observed temperature and the modelled linear vertical temperature gradient. Wells that intersect the Leederville Aquifer but do not exhibit advective behavior are not listed.

Vertical recharge and discharge regions to the Leederville Aquifer may play a role in the temperature fluctuations. Figure 3.18 shows the advective locations overplotted onto groundwater recharge/discharge zones of the Leederville Aquifer as determined by Davidson [1995] in 1992. The majority of the advective perturbations in the thermal profiles are negative (i.e. the perturbed temperature is lower than that of the conductive profile at the same depth), implying that colder water is entering

the Leederville Aquifer, which is likely to come from above the depth of the perturbation. This trend is consistent with a more recent groundwater modelling study [Davidson and Yu, 2008] which noted that recharge areas are increasing westward because of declining aquifer heads.

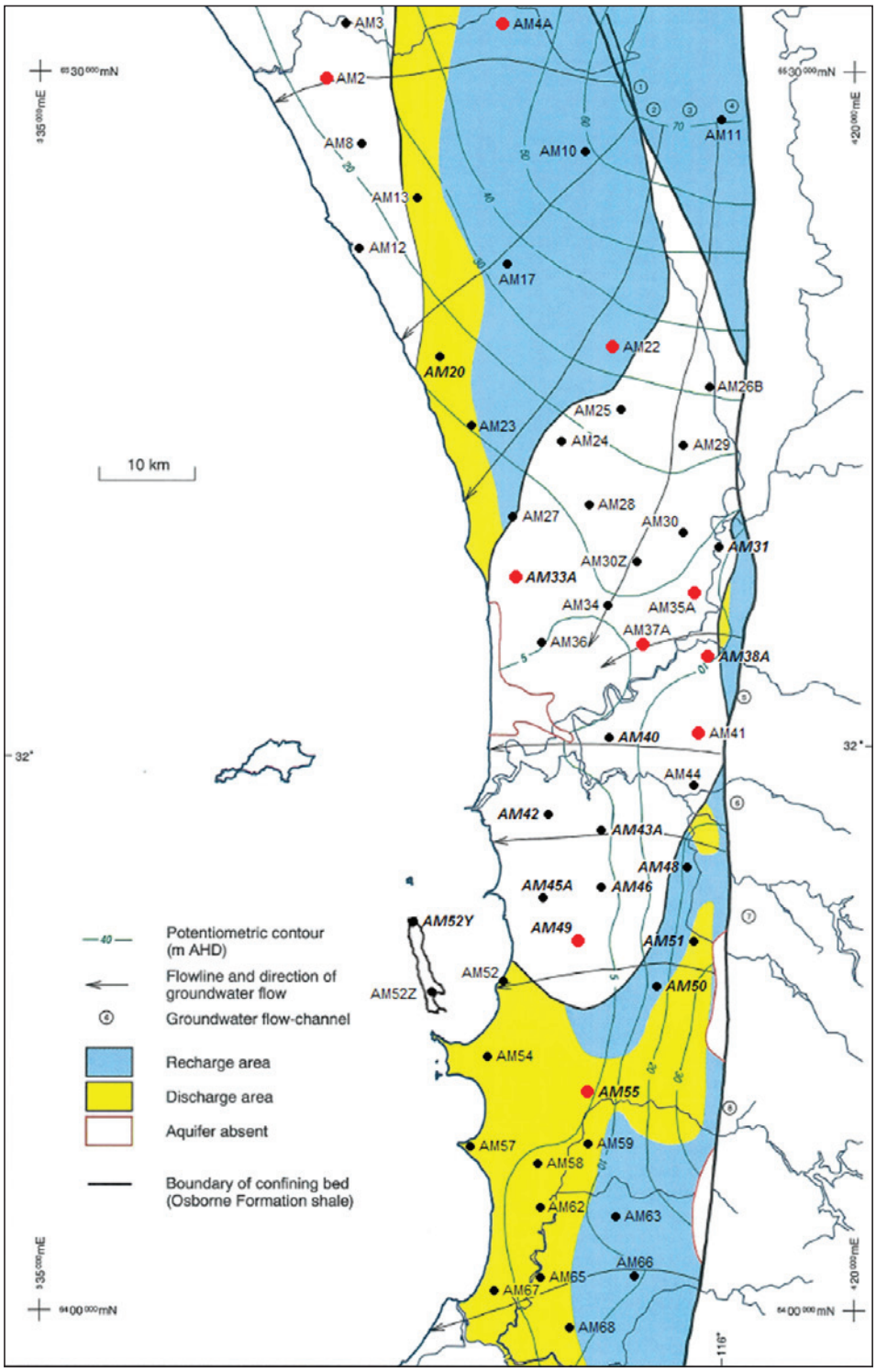

Figure 3.18: Wells with temperature logs in the Leederville Aquifer. Locations exhibiting evidence of advection are shown in red. Well names in bold and italics were logged by WAGCoE; well names in normal font were digitized from scans. Modified from Davidson [1995].

Horizontal temperature gradients

Another way to identify advective heat transport is through investigating the horizontal temperature gradients. When thermal conductivity λ is homogeneous everywhere in Equation 3.3-1, temperature profiles are linear and gradients are constant. If this assumption is relaxed to allow homogeneous thermal conductivity which can vary by formation, then vertical temperature profiles are still linear within each formation but horizontal gradients could vary because of refraction at formation boundaries [Haenel and Stegena, 1988]. The horizontal temperature gradient was calculated at each well within the Leederville Aquifer from measured data to investigate the pattern of temperature variability.

Reid et al. [2011a] interpolated all the logged and digitized temperature data located in Figure 3.15 into a three-dimensional rectangular voxel volume. Each voxel cell had a dimension of 1 km square horizontally and 10 m vertically. At each depth, these temperature values were numerically differentiated to produce the horizontal temperature gradients. A central difference algorithm utilized the values at the midpoint of the adjacent interpolated voxel cells:

$$\frac{\partial T}{\partial X} = \frac{T_{i+1} - T_{i-1}}{2(X_i - X_{i+1})} \qquad 3.3\text{-}4$$

where ∂T/∂X is the horizontal temperature gradient at location i (°C m^{-1}), $T_{i+1} - T_{i-1}$ is the temperature difference between locations i+1 and i–1 (°C), and $2(X_i - X_{i+1})$ is the distance between locations i+1 and i–1 (m). Temperature gradients were calculated both in the north-south and east-west directions at each well.

The magnitude of the horizontal temperature gradient was calculated from these two directional horizontal gradients. Figure 3.19 illustrates the interpolated horizontal temperature gradients at mid-depth in the Leederville Aquifer. To our knowledge, these magnitudes represent the first areally extensive picture of estimated horizontal thermal gradients. In other studies estimating groundwater flow from temperature measurements [Reiter, 2001, Verdoya et al., 2008], only individual wells were utilized and horizontal gradients could not be easily quantified.

Figure 3.19 indicates that the magnitude of the horizontal thermal gradient varies significantly within the Leederville Aquifer, with maximum values over an order of magnitude larger than typical variations of 5.0×10^{-4} °C m^{-1}. This variability could not be caused by variation in thermal conductivity alone, but instead is likely to be influenced by advective groundwater flow carrying heat. Most of the wells identified as being influenced by advection are located in regions with horizontal thermal gradients that are much larger than average.

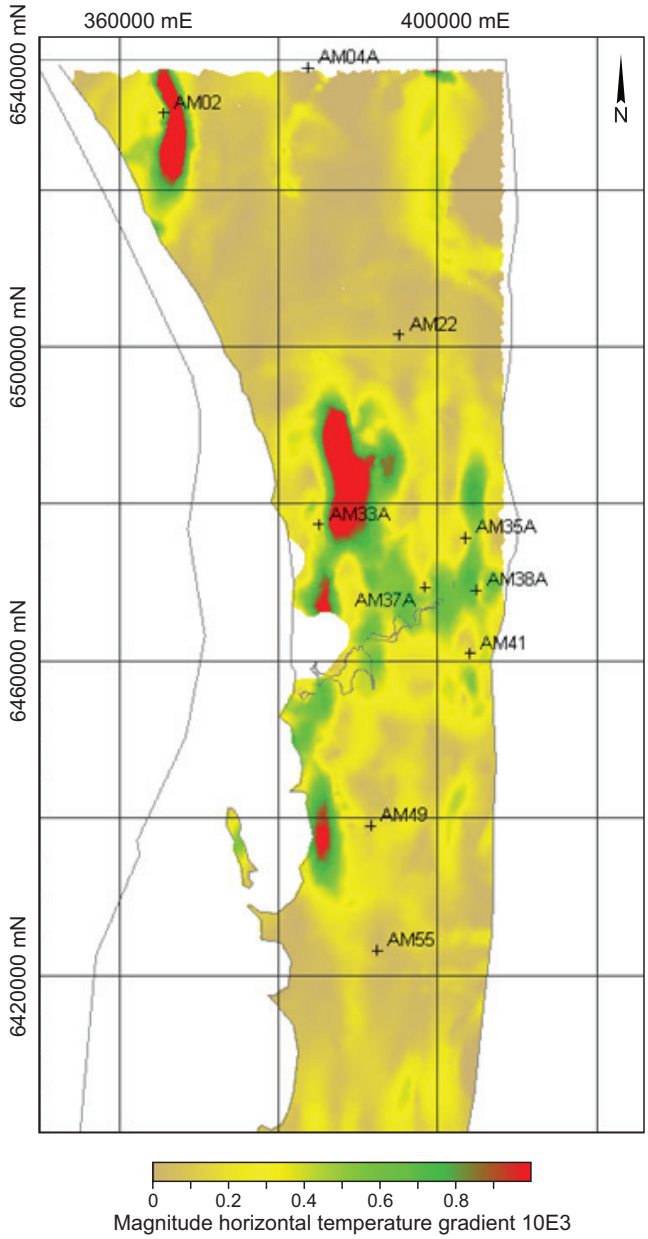

Figure 3.19: Interpolated horizontal thermal gradient magnitude (°C $m^{-1} \times 10^3$) at mid-depth in the Leederville Aquifer. Wells showing advective influence are overplotted.

3.3.4 Conclusions

This work has shown that advection can be a major source of subsurface heat movement and should be considered in any geothermal study in permeable systems. Evidence of advection may also be used to determine the geothermal potential of aquifer systems. If a formation is identified to have a constant inflow of warmer water, it is a prospective geothermal target. However, even assuming pure conduction, thermal gradients in the PMA suggest that relatively warm, shallow resources exist. Coupled analysis of thermal and hydrologic conditions implies that the aquifers in the PMA have potential for geothermal applications.

As advective influences on thermal profiles appear obvious in the Leederville Aquifer in the Perth Basin, some future work in quantifying this effect is recommended. First, the temperature deviations from conductive assumptions can be assessed using analytical solutions such as those compiled by Verdoya et al. [2008]. Magnitudes of groundwater velocity should be estimated where possible. Finally, the advective component of heat flow should be determined to compare with vertical conductive estimates. The current work has pointed out the importance of recognizing coupled heat and fluid transport and should be extended to allow more accurate geothermal exploration.

3.4 Potential for Convection in the Perth Basin

The economic viability of direct-use geothermal energy depends largely on the depth that must be drilled to reach the desired temperature. Thus, a primary goal of geothermal exploration is to identify areas where the geothermal gradient is anomalous: either anomalously high for energy usage or production or anomalously low, for heat rejection schemes. In sedimentary basins the geothermal gradient varies laterally and vertically due to several factors, including variations in thermal conductivity and radiogenic heat production between different rock units, varying depth to basement, and the competing effects of conductive, advective and convective heat transport.

Convection in particular has the potential to create localised regions of anomalous temperature at shallow depths, which may be viable targets for geothermal energy. Thus, determining whether convection is possible in the Perth Basin is important for predicting and understanding the likely distribution of geothermal resources in the basin. Theoretical analyses show that convection can only occur if a dimensionless parameter known as the Rayleigh number exceeds a critical value. The Rayleigh number is proportional to the permeability and thickness of the convecting layer; hence convection is most likely to occur in thick, highly permeable units such as aquifers.

The Yarragadee Aquifer is a likely candidate for convection in the Perth Basin. We assessed the potential for convection in the Yarragadee Aquifer in two ways: Firstly, by looking for evidence of convection in temperature and salinity data, and secondly, by using Rayleigh number analysis to determine the minimum permeability at which convection could occur in the Yarragadee Aquifer, and comparing this with permeability measurements on cores extract from lithological units of the Yarragadee Aquifer. Finally, we used numerical models to simulate convection in a simplified representation of the Yarragadee Aquifer, providing insight into the likely shape and spacing of convective upwellings, the degree of temperature enhancement that could be achieved by convection, and the fluid flow rates associated with convection.

The research presented here has been presented as a journal paper [Sheldon et al., 2012], a conference proceedings [Sheldon and Bloomfield, 2011], and an Honour's thesis [Glasson, 2011]. Additional journal publications on the salinity data are in preparation.

3.4.1 Convection theory

The theory of convection in porous media is covered in many texts. Much of the following information is taken from Nield and Bejan [1992] and Phillips [1991]. Convection is fluid flow driven by buoyancy arising from gradients in fluid density. In sedimentary basins these gradients arise from variations in temperature and groundwater salinity. Density often decreases with depth due to the increase in temperature, creating a buoyancy force that may give rise to convection. However, an increase in salinity with depth may counteract the effect of temperature on fluid density. Conversely, a decrease in salinity with depth enhances the density gradient and promotes convection. Convection involving transport of both heat and salt is described as thermohaline or double-diffusive convection.

Convection occurs if the buoyancy force that arises from a density gradient is sufficient to overcome the dissipative effects of viscous drag and diffusion of heat or salt. Whether this condition is satisfied can be determined, for simple systems at least, by evaluating a dimensionless parameter known as the Rayleigh number, and comparing it with the critical value that is required for convection. Convective flow is characterised by convection cells linking regions of fluid upwelling and fluid downwelling. Convective upwellings are associated with anomalously high temperatures at shallow depths (thermal highs), while downwellings are associated with anomalously low temperatures (thermal lows).

The Rayleigh numbers for thermal (RaT) and saline (RaS) convection in a horizontal layer of thickness H, with uniform properties and boundary conditions, are defined as follows (see Table 3.4 for nomenclature):

$$Ra_T = \frac{k\alpha\rho_0^2 c_f gH\Delta T}{\mu\lambda} \qquad 3.4\text{-}1$$

$$Ra_S = \frac{k\beta\rho_0 gH\Delta S}{\mu\phi D} \qquad 3.4\text{-}2$$

Symbol	Definition (units)
c_f, c_s	Specific heat capacity of pore fluid and solid (J kg^{-1} K^{-1})
D	Molecular diffusion coefficient of salt in pore fluid (m^2 s^{-1})
g	Gravity (m s^{-2})
H	Thickness of convecting layer (m)
k	Permeability (m^2)
α	Volumetric thermal expansion coefficient of pore fluid (1/°C)
β	Volumetric saline expansion coefficient of pore fluid (m^3 kg^{-1})
ΔS	Salinity difference across layer = S_{base} - S_{top} (kg m^{-3})
ΔT	Temperature difference across the layer = T_{base} - T_{top} (°C)
ϕ	Porosity
λ	Effective thermal conductivity of porous medium (W m^{-1} K^{-1})
λ_f, λ_s	Thermal conductivity of fluid and solid (W m^{-1} K^{-1})
μ	Fluid viscosity (Pa s)
ρ_f, ρ_s	Density of fluid and solid (kg m^{-3})
ρ_0	Reference fluid density (kg m^{-3})

Table 3.4: Nomenclature for convective theory.

Fluid density is assumed to vary linearly with temperature and salinity according to $\rho_f = \rho_0(1-\alpha\Delta T-\beta\Delta S)$. Note that α is positive and β is negative, hence Ra_T and Ra_S have opposite signs if both temperature and salinity increase with depth. The Rayleigh numbers are proportional to permeability and thickness of the layer; thus, convection is most likely to occur in thick, high permeability layers. If permeability is anisotropic, the smallest directional permeability (typically the vertical permeability in undeformed sedimentary rocks (Bear 1972)) is used to calculate Ra_T [Phillips, 1991].

$$Ra_T + Ra_S \geq Ra^* \qquad 3.4\text{-}3a$$

$$\Phi Ra_T + Ra_S \geq Ra^*(1+\Phi) \qquad 3.4\text{-}3b$$

Thermohaline convection is predicted to occur if one or both of the following conditions are satisfied: where Ra* is the critical Rayleigh number. Equation 3.4-3a is the condition for monotonic or stationary convection, and Equation 3.4-3b is the condition for oscillatory convection. In Equation 3.4-3b, ϕ is a ratio of the diffusivities of heat and salt, defined as:

$$\Phi = \frac{\lambda}{\Gamma\rho_0 c_f D} \qquad 3.4\text{-}4a$$

with

$$\Gamma = \frac{\phi\rho_0 c_f + (1-\phi)\rho_s c_s}{\rho_0 c_f} \qquad 3.4\text{-}4b$$

being the ratio of heat capacities of the fluid-saturated porous medium and the pore fluid.

By rearranging Equations 3.4-3a and 3.4-3b it can be shown that there is a value of ΔS above which convection is not possible regardless of the permeability:

$$\Delta S_{\max} = \max\left(-\frac{\phi\alpha\Delta T}{\Gamma\beta}, -\frac{\phi\alpha\Delta T}{\Gamma\beta\Phi}\right) \qquad 3.3\text{-}5$$

The value of the critical Rayleigh number, Ra*, depends on the boundary conditions of the convecting layer. The most appropriate values of Ra* for confined and unconfined aquifers are 12 and 17.65, respectively.

The reader should keep in mind that most theoretical analyses of convection are based on homogeneous and geometrically simple systems, whereas natural systems tend to be geometrically complex and heterogeneous. Thus, the application of convection theory to natural systems has some limitations. Permeability in particular is highly variable, often spanning several orders of magnitude within an aquifer. This issue is considered further below.

Another aspect to consider when assessing the potential for convection in a given aquifer is the competition between convection and advection. Advection is flow driven by forces other than

buoyancy, e.g. meteoric recharge. If the advective flow rate is similar to the convective flow rate, convection cells will migrate in the direction of the advective flow. At higher advective flow rates the convection cells will be completely eliminated [Raffensperger and Vlassopoulos, 1999]. The effects of advection are ignored in the following analysis for simplicity, but are considered further in the discussion section.

3.4.2 Hydrogeology of the Perth Basin

The following summary is derived from reports by Crostella and Backhouse [2000], Davidson [1995], Freeman and Donaldson [2006], Mory et al.[2005], Mory and Iasky [1997] and Playford et al. [1976]. The Perth Basin is a north-south elongate rift basin occupying the southwest of Western Australia. The onshore part of the basin encompasses the PMA and agricultural districts with smaller population centres to the north and south. It is bounded by the Darling Fault and Yilgarn Craton to the east, and the edge of the continental shelf to the west. The basin comprises a series of sub-basins, shelfs, troughs and ridges separated by normal and strike-slip faults, most of which strike approximately north-south or northwest-southeast. Basin fill is mainly Permian to Quaternary in age, comprising non-marine and shallow marine clastics and carbonates up to 15 km thick. Basin structure and stratigraphy are well-constrained by deep petroleum wells and seismic lines in the northern, central offshore and southern parts of the basin. This contrasts with the PMA, where water extraction and monitoring wells have been used to constrain the shallow stratigraphy but relatively little is known about the deeper structure.

The three major shallow aquifers of the Perth Basin are the Superficial, Leederville and Yarragadee Aquifers [Davidson, 1995]. The Superficial aquifer is thin (up to 70 m thick) and unconfined, and is dominated by advective flow driven by meteoric recharge with flow rates >1000 m yr^{-1} in some areas. The Leederville aquifer is partially confined, being hydraulically connected to the Superficial (above) and the Yarragadee (below). It is ~50-550 m thick, with estimated advective flow rates of 1-4 m yr^{-1}. The Yarragadee Aquifer is confined by the South Perth Shale, with connections to the Leederville Aquifer where the South Perth Shale is absent. The top of the aquifer is up to 1 km deep and it is > 2 km thick over much of the basin. Estimated flow rates in the top of the aquifer are ~0.9 m yr^{-1}. Flow rates in deep parts of the aquifer are unknown. Another aquifer, comprising the Lesueur Sandstone Formation, is probably too deep to be viable for geothermal energy in the PMA, but may be of interest in other parts of the basin where it reaches shallower depths [see Crostella and Backhouse, 2000].

This study focuses on the Yarragadee Aquifer, because it is the accessible aquifer with the greatest thickness and least influence from flow driven by recharge/discharge, and thus the most likely candidate for convection. It is also likely to be the most viable for geothermal energy, being deep enough to attain useful temperatures, but not so deep that drilling costs are prohibitive.

For the purpose of this study the Yarragadee Formation is used as a proxy for the Yarragadee Aquifer, although it is acknowledged that other formations (notably the Gage Sandstone, Cadda Formation and Cattamarra Coal Measures) contribute to the aquifer in some places [Davidson, 1995].

3.4.3 Evidence for convection: Temperature

This section considers whether temperature data from boreholes in the Perth Basin provide any evidence of convection. There are two types of data: BHTs from petroleum wells (obtained from well completion reports), and temperature logs from AM wells [Reid et al., 2011a].

The effect of convection in a confined aquifer is illustrated in Figure 3.20. Convection can be identified by the pattern of thermal highs and lows at a given depth (Fig. 3.20C) and by variations in the geothermal gradient, both laterally and with depth (Fig. 3.20B and D). Figure 3.21 shows the expected width of convection cells (i.e. the distance between convective thermal highs and thermal lows) as a function of aquifer thickness and permeability anisotropy (i.e. the ratio of horizontal to vertical permeability), based on an equation given by Phillips [1991]. We look for these patterns in temperature measurements from the Perth Basin.

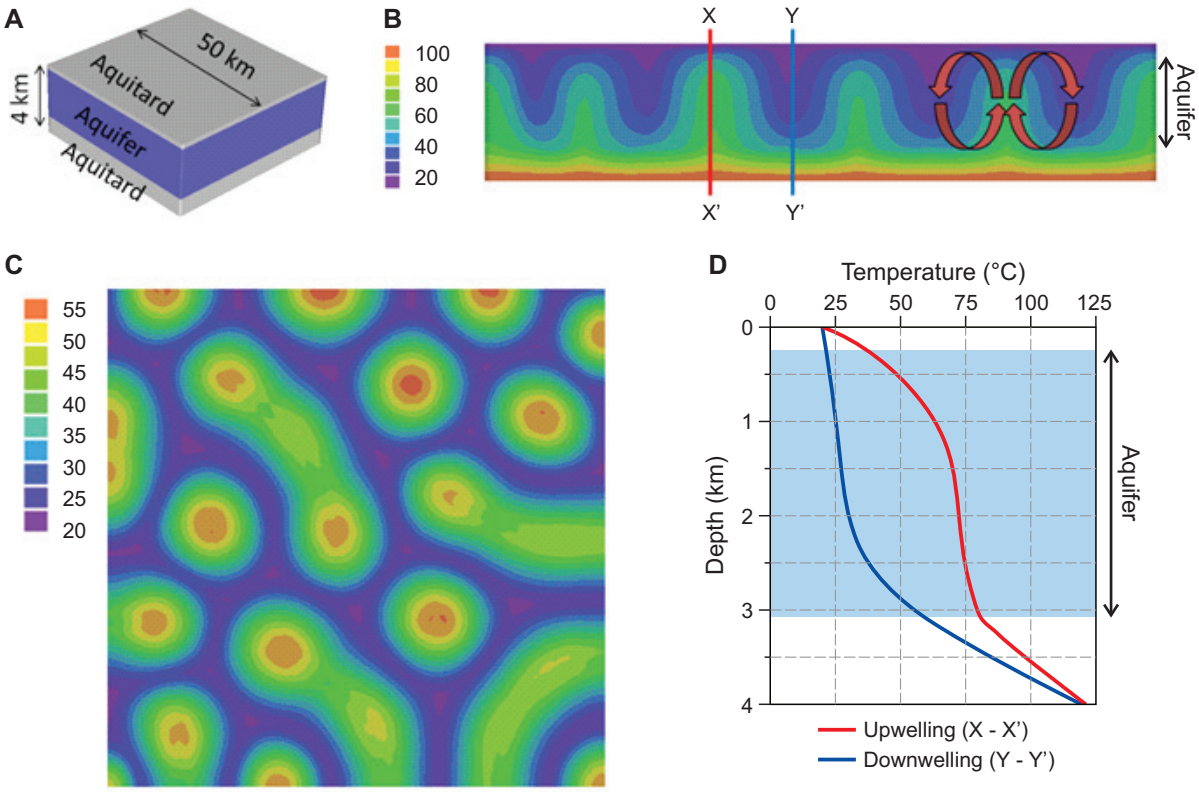

Figure 3.20: Temperature distribution due to convection in a horizontal confined aquifer. (A) Model geometry. Aquifer extends from 0.25 to 3 km depth (note vertical exaggeration). Geothermal gradient from top to bottom of model = 25 °C/km. (B) Temperature (°C) on a vertical section through model. (C) Temperature (°C) on a horizontal section through model near top of aquifer. (D) Vertical temperature profiles through an upwelling (X-X' in B) and a downwelling (Y-Y' in B). Note change in temperature gradient with depth.

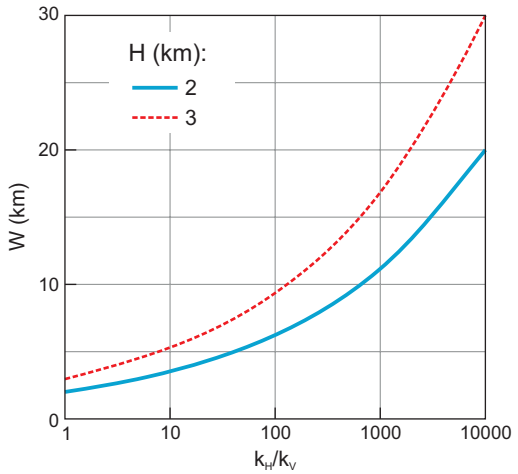

Figure 3.21: Width (W) of convection cells in a homogeneous horizontal aquifer as a function of aquifer thickness (H) and permeability anisotropy ratio (k_H/k_V).

Temperature gradients inferred from corrected BHTs in petroleum wells in the North Perth Basin were interpolated to produce the map shown in Figure 3.12. The map reveals patterns on various scales, including large-scale variations in geothermal gradient caused by variations in depth to basement, and smaller-scale variations with spacing of ~10-30 km between highs and lows. For example, there is a thermal low at Jurien Bay (temperature gradient ~25 °C/km) with thermal highs located approximately 20 km to the east (temperature gradient ~35 °C/km) and to the north (temperature gradient ~45 °C/km). While some of the patterns in Figure 3.12 may be artefacts related to the contouring algorithm, scarcity of data and errors in corrected BHTs, some of the variations are likely to be real. In particular, we have confidence in the patterning observed in the Dongara region due to the high density of petroleum wells there. Variation of temperature gradient in the Dongara region was highlighted previously by Horowitz et al. [2008], who also suggested it could be due to convection. The spacing of 10-30 km in that region is consistent with convection in a 3 km thick aquifer with permeability anisotropy ratio kH/kV >100 (Fig. 3.21).

BHTs provide a single measurement point (sometimes two or three points) for each well location, and the accuracy of BHTs is highly variable. A more detailed and accurate picture of the temperature variation with depth is provided by continuous down-hole temperature logs. Reid et al. [2011a] analysed temperature-depth profiles in 55 AM wells in the PMA. The temperature-depth profiles were used to calculate average temperature gradients in each formation. Figure 3.22 shows the temperature at -250 m AHD and -500 m AHD interpolated from the AM wells. Note the pattern of thermal highs and lows, with spacing on the order of 10-20 km, similar to the spacing observed in Figure 3.12. This pattern is influenced by data scarcity (limited by the spacing of boreholes for which continuous temperature logs were available) and the interpolation algorithm used to create the maps; the true spacing of thermal highs and lows may be smaller. Figure 3.23 shows the range of temperature gradients in the Gage Sandstone and the top part of the Yarragadee Formation, representing the top of the Yarragadee Aquifer. It can be shown that the range of temperature gradients in Figure 3.23 is consistent with the range that would be expected due to convection at moderate Rayleigh number in the Yarragadee Aquifer.

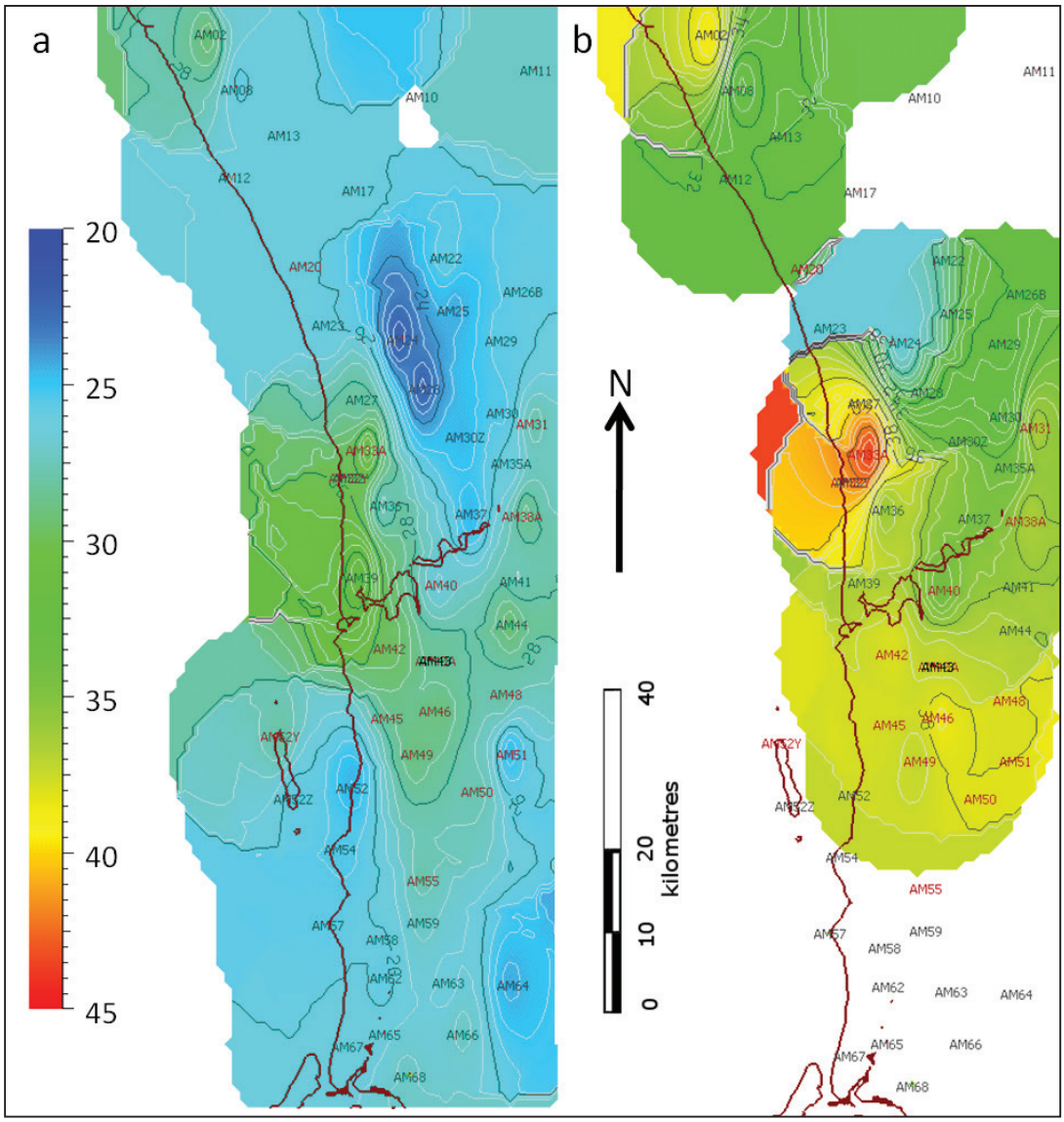

Figure 3.22: Temperatures (°C) in the PMA at (A) -250 m AHD and (B) -500 m AHD, interpolated from temperature logs in AM wells. Interpolation was performed using an inverse distance method. White areas indicate inadequate data to interpolate. After Reid et al. [2011a].

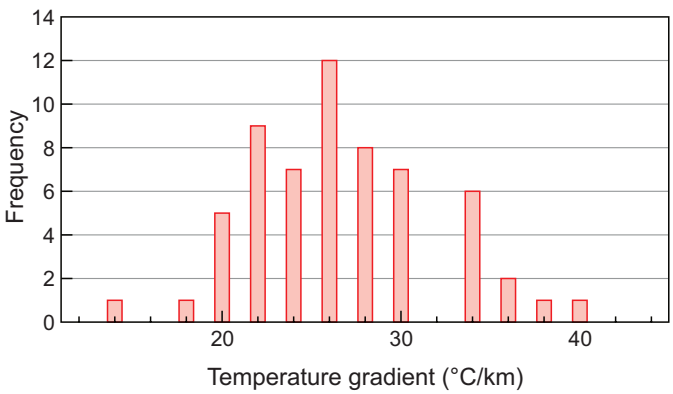

Figure 3.23: Histogram of temperature gradients in the upper part of the Yarragadee Aquifer (Gage and Yarragadee Formations) determined from temperature logs in AM wells. After Reid et al. [2011a].

The variations in temperature gradient described above could be explained at least in part by variations in thermal conductivity between and within geological units. To assess whether the observed patterns could be explained by a purely conductive model would require a 3D inversion approach which is beyond the scope of this investigation. It may be concluded that temperature measurements from AM and petroleum wells are consistent with convection in the Yarragadee Aquifer, but they do not prove that it is occurring.

3.4.4 Evidence for convection: Salinity

Salinity is observed to increase with depth in many sedimentary basins, or at least to display stratification into sub-horizontal layers [Bjorlykke et al., 1988, Kharaka and Thordsen, 1992]. This observation has been used to argue that large-scale convection is not occurring in such basins, because (1) the horizontal stratification would be disturbed by convection, and thus should not exist if convection is occurring, and (2) an increase in salinity with depth inhibits convection [Bjorlykke et al., 1988]. A brief assessment of what is known about salinity in the Yarragadee Aquifer is presented here and the implications for convection are considered.

Information about salinity in the Perth Basin comes from various sources, including measurements of salinity in groundwater samples from AM and water extraction wells; values reported in petroleum well completion reports; and values inferred from wireline logs in wells. Davidson [1995] presented a rough interpretation of salinity versus depth in a cross-section through the PMA, however his interpretation was based on very limited data below the top of the Yarragadee, especially onshore. To address the paucity of salinity data for the PMA, Glasson [2011] compiled published salinity values and calculated new values from wireline logs in petroleum wells for which suitable logs were available. Two methods were used: the resistivity method, which generates a continuous profile of salinity with depth, and the spontaneous potential method, which produces discrete values at points in the well where a transition from sandstone to shale can be identified on the wireline logs. Both methods have limitations and the calculated salinities should not be treated as accurate values. Nonetheless, the calculated salinities represent a substantial addition to the salinity database for the PMA. In particular, salinity-depth profiles obtained using the resistivity method reveal important information about variations in salinity with depth. Onshore wells generally showed an increase in salinity with depth, but this increase was not continuous; rather there were regions of fairly homogeneous salinity separated by regions of very heterogeneous (but generally increasing) salinity (Fig. 3.24A). Offshore wells showed a different trend: salinity generally decreased with depth and was more heterogeneous than in the onshore wells (Fig. 3.24B).

Convection tends to homogenise salinity [Trevisan and Bejan, 1987, Fournier, 1990], therefore the regions of relatively homogeneous salinity observed in the onshore wells could be taken as evidence for convection. Conversely, the regions of heterogeneous salinity in both onshore and offshore wells suggest that convection is not occurring in those regions. Decreasing salinity with depth, as observed in the offshore wells, would generally be expected to promote convection; however, the fact that the salinity gradient is preserved implies that large-scale convection is not occurring, presumably due to inadequate permeability.

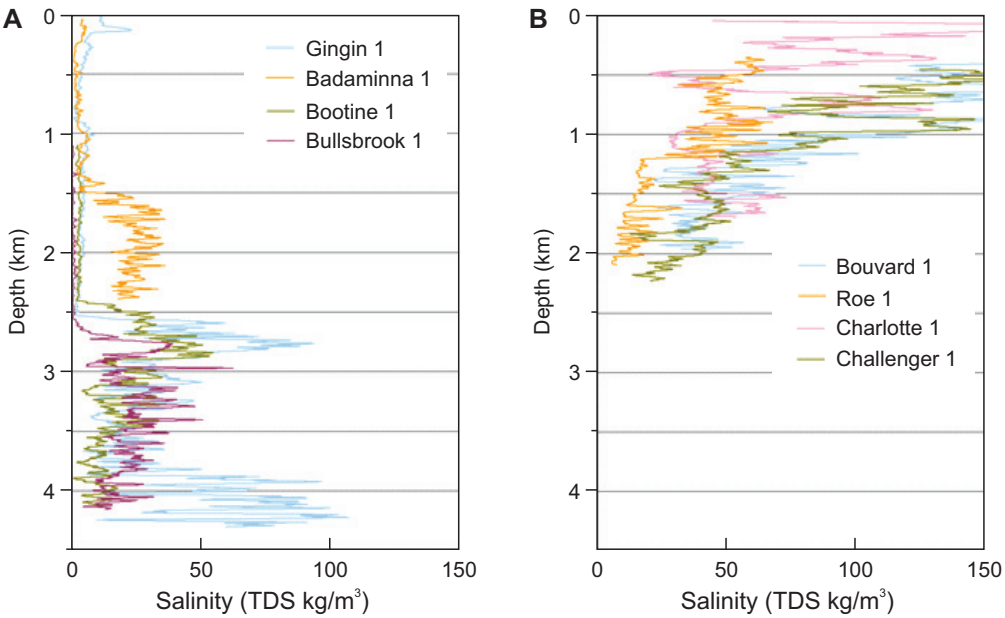

Figure 3.24: Salinity profiles derived from resistivity logs in (A) onshore and (B) offshore wells. Data compiled by Glasson [2011].

Table 3.5 summarises the depths of the homogeneous salinity regions in the onshore wells, and indicates the maximum accessible temperature in those regions (i.e. the temperature at the base of the potentially convecting layer, estimated from the geothermal gradient in that well derived from the BHT).

Well	Top of convecting layer (m below AHD)	Base of convecting layer (m below AHD)	Thermal gradient (°C/km)	Accessible temperature (°C)
Gingin1	189	2530	18.5	66.25
Bootine1	1100*	2400	25.4	80.96
Badaminna1	250	950	22.9	41.755
Bullsbrook1	1100*	2550	17.8	64.5
Cockburn1	300*	1100	20	42
Rockingham1	500	950	22.1	39.89
Pinjarra1	100*	300	20.9	26.27
Preston1	50*	150	17.8	22.67

Table 3.5: Potentially convecting layers in onshore petroleum wells. These layers correspond to the region of relatively uniform salinity in each well. An asterisk indicates that the top of the layer may be shallower than the stated value, however the resistivity log did not allow for estimation of salinity above this depth. The accessible temperature is the temperature at the base of the potentially convecting layer, estimated from the local thermal gradient. After Glasson [2011].

3.4.5 Rayleigh number analysis of the Yarragadee Aquifer

To calculate the Rayleigh number for the Yarragadee Aquifer it is necessary to determine appropriate values for the parameters that appear in the Rayleigh number equation. Of these parameters, permeability is by far the most variable and the least well-constrained. It can span several orders of

magnitude within a single geological formation. It also varies depending on the direction of measurement (i.e. it is anisotropic), tending to be larger horizontally (or parallel to bedding) than vertically. This variability is illustrated for the Yarragadee Aquifer in Figure 3.25.

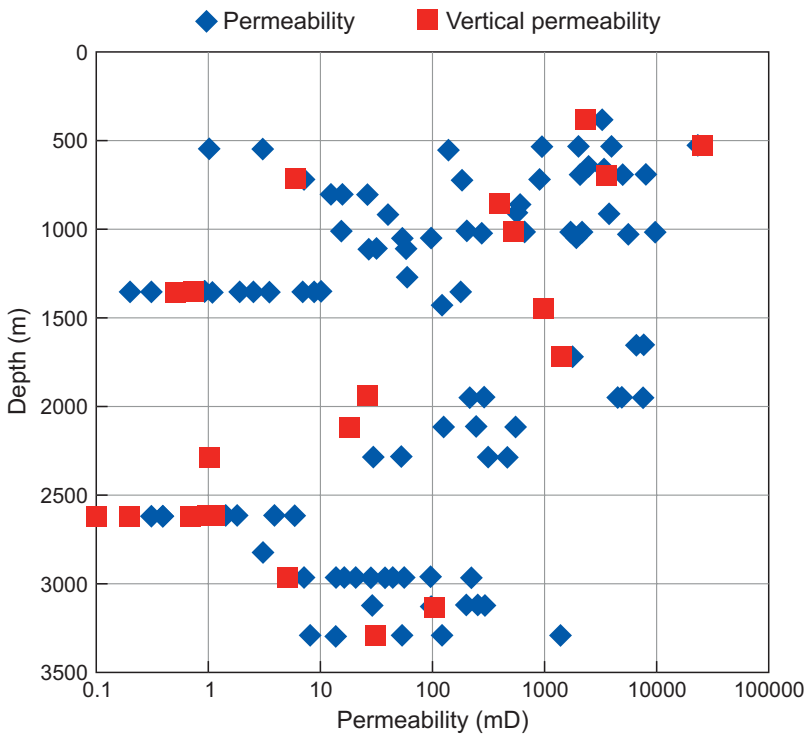

Figure 3.25: Permeabilities in the Yarragadee Aquifer measured in core samples from petroleum wells. Source: PressurePlot [CSIRO, 2011].

Thus it is not particularly meaningful to calculate the Rayleigh number of the Yarragadee Aquifer for a single value of permeability. Instead, we estimate the minimum permeability required for convection by rearranging Equations 3.4.3a and 3.4.3b, and using appropriate values for the other parameters that appear in the Rayleigh number. Calculations were performed for ranges of aquifer thickness, temperature gradient and salinity gradient representative of the Yarragadee Aquifer (assumed to correspond to the Yarragadee Formation in this study), and for thicknesses and temperature gradients representing five petroleum well locations. The results are shown in Figures 3.26 and 3.27.

For all wells the vertical permeability required for convection with $\Delta S = 0$ (Fig. 3.26) lies within the range of measured permeabilities (Fig. 3.25). An average vertical permeability of 10 mD (10-14 m^2) permits convection in a 2 km thick aquifer with a geothermal gradient of ~27 °C/km or above. If the average vertical permeability is only 1 mD, convection can occur only where the aquifer thickness is greater than 3.2 km for a geothermal gradient of 40 °C/km, or where the thickness exceeds 4 km for a geothermal gradient of 30 °C/km.

Figure 3.18 shows that a small salinity gradient is sufficient to inhibit convection for most reasonable values of aquifer thickness and geothermal gradient. None of the wells would be expected to display convection with $\Delta S = 20$ kg/m^3 (c.f. Figure 3.24 for typical salinity profiles). Given this upper limit on the salinity gradient, and the fact that salinity tends to be homogenised in any case by convection (see previous discussion on salinity), it would perhaps be more meaningful to calculate the permeability required for convection in the "potentially convecting layers" (i.e. layers of homogeneous salinity) identified in Table 3.5. This analysis has not yet been carried out.

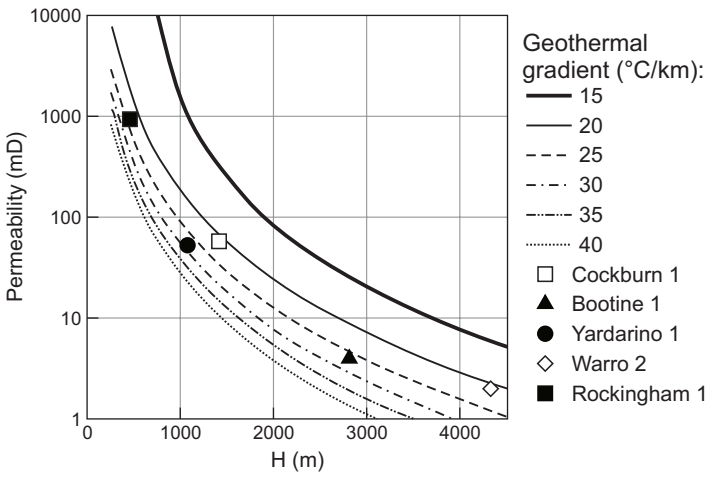

Figure 3.26: Vertical permeability required for convection as a function of aquifer thickness (H) and geothermal gradient, with ΔS = 0 kg/m³.

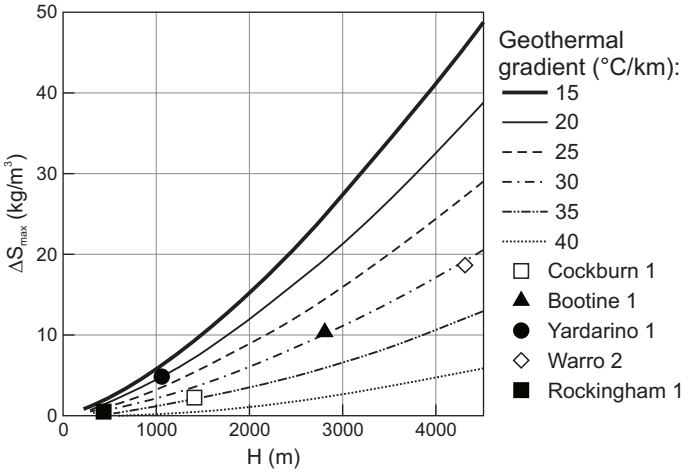

Figure 3.27: Maximum salinity difference (ΔS_{max}) at which convection can occur, as a function of aquifer thickness (H) and geothermal gradient.

3.4.6 Numerical models

Having established the range of conditions under which convection is theoretically possible according to Rayleigh number analysis, numerical simulations were used to explore further the characteristics of convection in the Yarragadee Aquifer. The simulations were run using FEFLOW, a finite element modelling package which solves the equations of groundwater flow, heat and mass transport in two or three dimensions [Diersch and Kolditz, 1998].

The numerical model comprised three horizontal layers, representing an aquifer of constant thickness bounded above and below by aquitards. The bottom of the model was located 1 km below the bottom of the aquifer, and the model area was 50 x 50 km. The position and thickness of the aquifer, the horizontal and vertical permeability of the aquifer, and the salinity gradient across the aquifer were varied. Full details can be found in Sheldon et al. [2012].

Figure 3.28 shows the results for one scenario. The convective upwellings range from circular to elongate in plan view. The convection cell width (i.e. half the distance between adjacent thermal highs) ranged from 3 to 12 km, depending on aquifer thickness and permeability. These distances are consistent with the following equation which expresses convection cell width as a function of aquifer thickness and permeability anisotropy [Phillips, 1991]:

$$W = H\left(k_H / k_V\right)^{0.25} \qquad 3.3\text{-}6$$

The maximum temperature attained in the convective upwellings depends on the temperature at the bottom of the aquifer, which in turn depends on the aquifer thickness and the geothermal gradient. Temperature enhancements of 10-40 °C relative to the conductive temperature profile were attained at 1 km depth. In the scenario shown below the maximum temperature at 1 km depth was 77 °C, and 65 °C at 500 m depth. The maximum fluid flux due to convection was up to 0.66 m yr^{-1}, which is of the same order of magnitude as an independent estimate of the advective fluid flux in the top of the Yarragadee Aquifer [Davidson, 1995]. The models confirmed that salinity is homogenised by convection, with the initial salinity gradient being modified to a uniform salinity through the aquifer, with steeper gradients in the aquitards above and below.

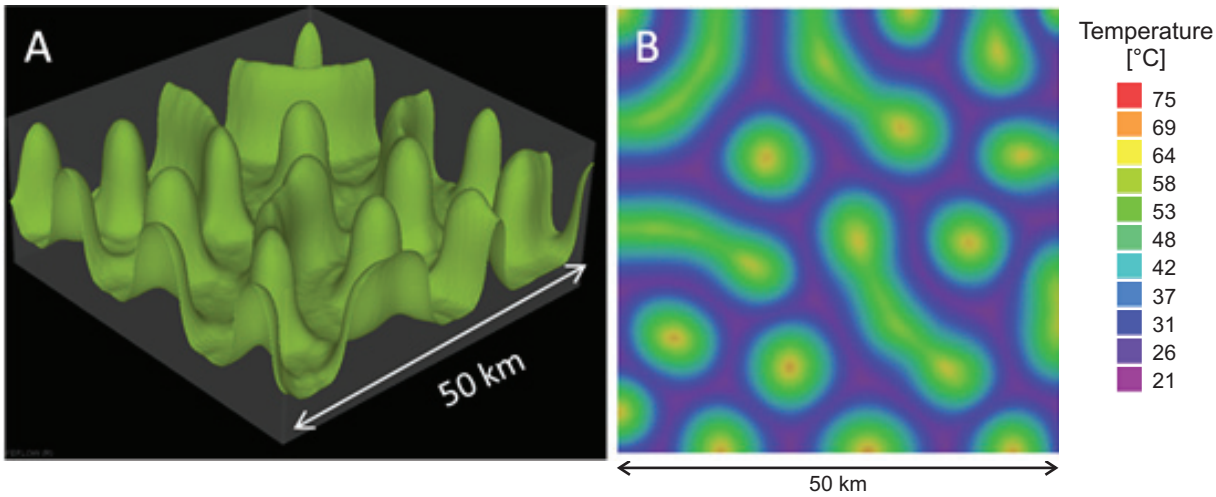

Figure 3.28: Temperature distribution due to convection in a horizontal confined aquifer (aquifer depth and thickness representing the Yarragadee Formation in the Bootine-1 well; horizontal permeability / vertical permeability = 10; horizontal permeability = 50 x permeability required for convection; ΔS = 10 kg m^{-3}). (A) 60 °C isosurface. Vertical exaggeration x10. (B) Temperature at 567 m depth (near top of aquifer).

3.4.7 Discussion

Rayleigh number analysis shows that convection may be possible in some parts of the Yarragadee Aquifer, depending on its thickness, permeability and geothermal gradient. Permeabilities required for convection fall within the range of measured values in the Yarragadee Aquifer. However, the usefulness of Rayleigh number calculations and convection simulations based on average permeability for predicting the occurrence of convection in heterogeneous systems has been questioned in the literature [Bjorlykke et al., 1988, Nield, 1994, Simmons et al., 2001, Simmons et al., 2010]. Assessing the potential for convection in realistic, heterogeneous permeability distributions is an important avenue for future research.

The numerical models predicted convection cell widths of ~10 km, which is at the lower end of the distances between thermal highs and lows (10-20 km) inferred from temperature measurements in the PMA. The discrepancy between modelled and measured (inferred) spacing could be explained

by the spacing of wells in the PMA, which limits the resolution at which thermal anomalies that can be identified. Furthermore, the shape and location of convection cells in the real aquifer would be controlled by geometric features such as faults and undulations in the top and bottom surfaces of the aquifer. The effect of true aquifer geometry on convection is explored further in Section 4.4 of this report.

The convective fluid flow rates predicted by the models are similar to estimated advective flow rates in the Yarragadee Aquifer [Davidson, 1995]. This means that convection cells are likely to migrate in the direction of advective flow [Raffensperger and Vlassopoulos, 1999]. This effect is explored in Section 4.4.

An important point highlighted by the numerical models is that convection cannot raise the temperature above that at the base of the aquifer in a purely conductive scenario. Therefore a useful rule-of-thumb for geothermal exploration would be to restrict the search to areas where the expected temperature at the base of the aquifer under non-convecting (i.e. conductive) conditions exceeds the target temperature. To apply this rule requires knowledge of the aquifer thickness and average geothermal gradient.

Calculating the maximum salinity gradient at which convection can theoretically occur is of limited use, because convection homogenises salinity within the convecting layer. Identification of homogeneous salinity layers in salinity-depth profiles obtained from resistivity logs is a useful tool for identifying possible locations of convection.

3.4.8 Conclusions

Temperature maps derived from subsurface temperature measurements in the Perth Basin reveal patterns that could be explained by convection. The spacing of thermal highs and the range of temperature gradients are consistent with theoretical models of convection. New salinity-depth profiles obtained from resistivity logs in petroleum wells reveal layers of relatively homogeneous salinity in onshore wells, which could also be indicative of convection. Conversely, regions of very heterogeneous salinity, or salinity increasing or decreasing with depth, imply that convection is not occurring.

Rayleigh number calculations and numerical models based on average properties suggest that convection may be possible within the Yarragadee Aquifer, depending on its thickness, geothermal gradient and permeability. Predicted convective fluid fluxes are similar to estimates of the advective flow rate in the Yarragadee Aquifer, therefore convection cells are likely to migrate in the direction of advective flow.

Temperature enhancements due to convection are predicted to be significant, with temperatures up to 85 °C occurring at 1 km depth, representing a 40 °C enhancement above the conductive temperature profile. Therefore, locating convective upwellings might be a good strategy for geothermal exploration, although the economic viability of exploiting an upwelling would depend on its size and many other factors. The temperature that can be attained in convective upwellings

is limited by the temperature at the bottom of the aquifer, and thus by its depth. Therefore, aquifer thickness is critical.

Defining the 3D permeability distribution in the Yarragadee Aquifer, and assessing the impact of this heterogeneous permeability distribution on convection, are priority areas for future research.

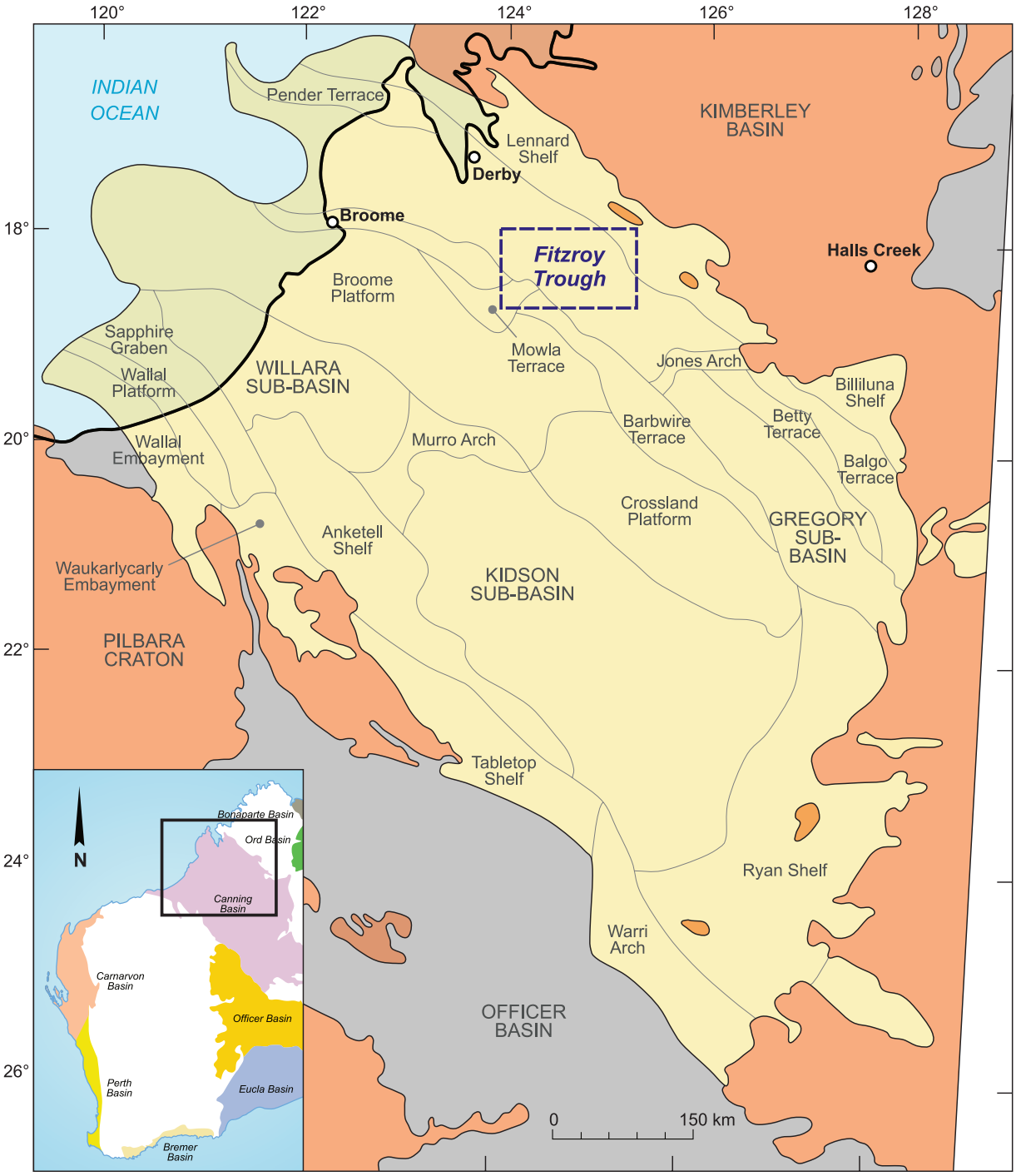

Figure 4.1: Map showing location of model area within Western Australia. The basin-scale model area is shown with a black rectangle in the Fitzroy Trough of the Canning Basin.

4. DETAILED HYDROTHERMAL MODELS

The previous section provided a broad overview of geothermal conditions in Western Australia. This section describes four detailed hydrothermal models created with much more specific focus on conditions in a particular geothermal regime. Section 4.1 describes a general workflow for deep geothermal exploration using numerical models, from the initial large-scale geological model to the fine-scale reservoir simulation. This workflow is demonstrated in a small area of the Canning Basin. A conductive thermal model of the entire Perth Basin is presented in Section 4.2, calibrated against BHT measurements from petroleum wells. Finally, Section 4.3 presents a detailed hydrothermal model of the PMA, focusing on the interplay between advective and convective heat transport, and the effects of varying permeability in faults and aquifers.

4.1 Use of Public Data: Canning Basin Workflow

Geothermal exploration requires significant amounts of data on subsurface conditions. Because very few data have been collected specifically for geothermal purposes, one of the aims of WAGCoE was to develop a catalogue of useful data obtained in other exploration fields [Corbel et al., 2010, Poulet et al., 2010a]. The most directly applicable data for exploration of HSAs are obtained from petroleum exploration. In Western Australia, the Department of Mines and Petroleum (DMP) maintains WAPIMS [Western Australian Department of Mines and Petroleum, 2012], an extensive database of petroleum exploration data undertaken by public and private industry. WAPIMS contains information on, amongst other items, drilled wells, petrophysical analysis of core samples, geophysical surveys, and production data.

The Canning Basin Workflow project aimed to complete an initial geothermal exploration study using publically available data. A low cost prefeasibility study should precede any larger investment in a deep assessment. The workflow outlined in this section is designed to quickly assess the potential of new HSA prospects, without having to collect new data but with awareness of associated uncertainties. This workflow is demonstrated on a case study in the Fitzroy Trough, Canning Basin, Western Australia (Fig. 1.1A).

The results from this section have previously been presented at conferences [Corbel and Poulet, 2010, Reid et al., 2010, Ricard et al., 2010, Corbel et al., 2011b], and a revised version of the combined work is being prepared for journal publication.

4.1.1 Introduction

We tested our workflow on a sub-basin of the Canning Basin, Western Australia (Figs. 1.1A and 4.1), using public data consisting of nine deep petroleum exploration wells, a geological map, a digital elevation model and some 2D seismic lines (Fig. 4.2a, upper left). The geologic model covered an area of 84 by 172 km^2 and extended to -3000 m AHD in depth.

The aim of this case study was to identify potential HSA targets using fluid and heat flow simulations at basin scale and then test the feasibility of these targets via smaller reservoir scale simulations. Because this study was a preliminary assessment with limited data, the modelling focused on simple

geometry and physical processes. The geologic modelling was performed with the modelling package SKUA®, the basin scale simulations using FEFLOW, and the reservoir scale simulations using TEMPEST-MORE.

4.1.2 Workflow and results

Structural modelling

The first step of the workflow is the structural modelling of the target basin. A basin scale geological model is developed using available data including interpreted seismic lines, well data or public reports. The quality of the model depends on the available data, and uncertainties must always be associated to the geological model. The aim of the three-dimensional geological model is to identify fault networks creating compartments in the geothermal reservoir but also to define the relationship between aquifers and aquitards, and their respective thicknesses.

Faults are critical in groundwater and geothermal exploration as they determine fluid flow behaviour. For the basin scale model we decided to keep only faults compartmentalizing the model or creating a major offset. We reviewed a seismic interpretation study of the area and kept ten major faults, two of them being sealed faults (Fig. 4.2, upper left). Because the basin scale simulator FEFLOW cannot easily handle dipping faults, we also decided to simplify the model and design all the faults as vertical.

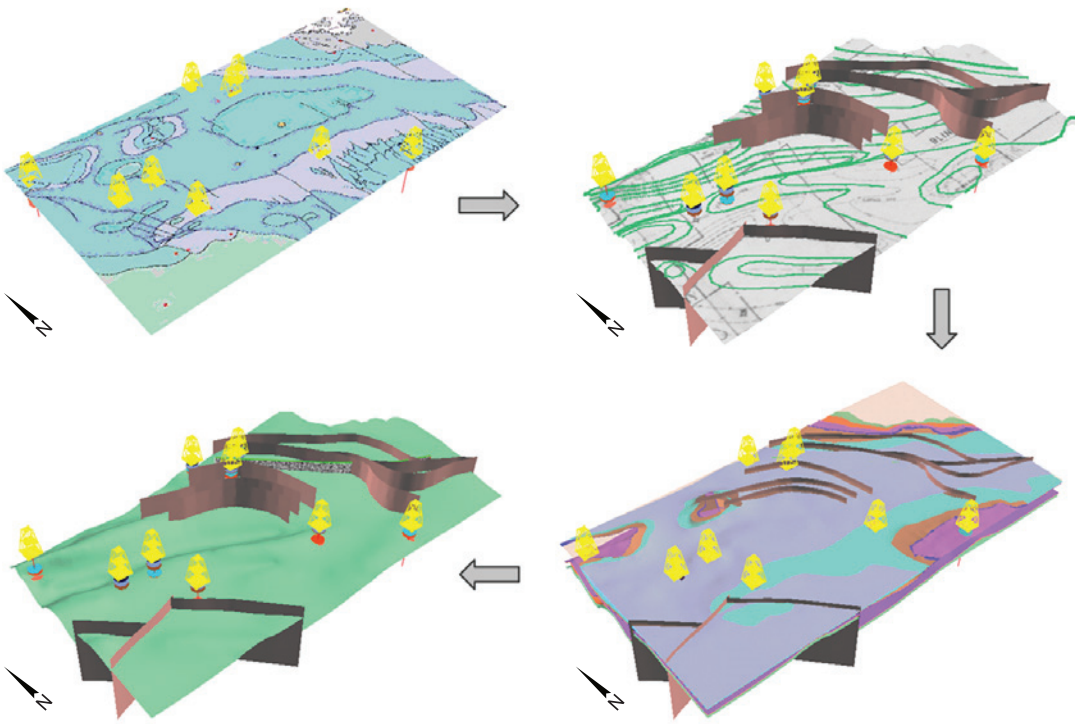

Figure 4.2: Three-dimensional geological modelling process of a geothermal prospect. First all data were imported into the modelling package SKUA® (upper left). Then the fault network was defined and a seismic interpretation study helped define the bottom of the deepest aquifer (upper right). After testing two different stratigraphic relationships for two formations we settled on the final model (lower right). At last we compared the final result with a few seismic lines and made sure that the main constraints on the aquifer were honoured (lower left).

For this study we targeted two main aquifers, the Grant and Poole aquifers. The Grant aquifer is contained within a formation overlying a major regional unconformity. As this unconformity lies at the lower depth limit for economic drilling for HSA, we decided to only model the formations above that unconformity. Modelling objectives limited our initial usage of seismic surveys to one seismic interpretation study that we used as secondary data. The unconformity was picked from the seismic study (Fig. 4.2, upper right) and forced to honour the well data when available. Then we defined a stratigraphic column for the area and modelled the above geological formations, testing a few different scenarios (Fig. 4.2, lower right).

As aquifer geometry has a huge impact on groundwater and HSA geothermal systems, we made sure that recharge and discharge areas were well represented and compartmentalization was well defined. To ensure the quality of the model we decided to cross-check the result with actual seismic lines that we did not use in the modelling process (Fig. 4.2, lower left). As we used quite sparse data, the misfit between the interpreted seismic lines and the three-dimensional model was quite variable. However, as formation thicknesses and orientation still made geologic sense, we decided that the model was acceptable for the purpose of basin scale modelling. For the purpose of reservoir simulations however, it would be ideal to add more details to get a more accurate model in the target subregion.

Basin scale hydrothermal modelling

Once the three-dimensional geological model was created, it was handed over as the basis for basin scale hydrothermal modelling. Rock, thermal and fluid properties as well as boundary conditions are defined using available data and understanding of the geothermal reservoir. The three-dimensional geological model is then populated with those properties and coupled heat and flow simulations are run to identify potential targets of smaller scale. The aim of basin scale hydrothermal modelling is to define temperature distributions, provide heat-in-place estimates, and identify prospective targets inside the geothermal reservoir.

For this preliminary model, steady-state heat and water flow conditions are assumed. In addition, rock properties are assumed to be constant by formation across the basin-scale model. Although these assumptions are certain to be untrue, limited data and restricted model development time make them sensible choices.

Sufficient public data exists for all major rock properties to be estimated. Some rock properties were estimated from the WAPIMS data. Compiled porosity, permeability, and density data from cored well cuttings analysis were available in spreadsheet form [Havord et al., 1997]. Average properties by formation were estimated from wells located in the Fitzroy Trough. Thermal conductivity and radiogenic heat production was assigned based on core measurements commissioned by the DMP [Driscoll et al., 2009]. Heat capacity was estimated from the density measurements [Waples and Waples, 2004a, Waples and Waples, 2004b]. In general, rock properties were assumed to be isotropic, except vertical permeability was decreased by a factor of ten from horizontal values, a commonly employed anisotropy assumption.

For a hydrothermal model, initial and boundary conditions include both heat and flow distributions. The mean annual surface temperature (MAST) was estimated from an Australia-wide study [Horowitz

and Regenauer-Lieb, 2009]; a constant value was assigned as a top temperature boundary condition. The temperature gradient was estimated from the MAST and three BHT estimates in petroleum wells provided by WAPIMS and summarised in two other geothermal reports [Chopra and Holgate, 2007, Driscoll et al., 2009] . A variable thermal gradient was extrapolated across the region from these three points and ranged from 30 to 36 °C km^{-1}. A basal heat boundary condition of 65 to 78 mW m^{-2} was assigned at 3000 m which reproduced the thermal gradients. Although some drill stem tests were available in WAPIMS, inconsistent reporting standards rendered this specific information unusable for the model. Instead for fluid initial distributions, a hydrostatic pressure distribution was assumed. Surficial areal recharge was assigned based on a small percentage of annual rainfall, due to the cyclonic rainfall pattern and high evaporative capacity in the region [Lindsay and Commander, 2006]. Salinity distributions were available [Ferguson et al., 1992], but were not utilised in this initial desktop study as they were reasonably constant with depth. Fixed head boundary conditions were applied on the western and eastern edges of the model domain to reproduce regional groundwater flow detailed in [Ghassemi et al., 1992].

The hydrothermal model was run to determine steady state conditions of temperature and hydraulic head (Fig. 4.3). These results were evaluated to identify geothermal prospects. Based on reservoir thickness, reservoir quality, and temperature distributions, two prospects were identified for further study (Fig. 4.4). Heat-in-place estimates [AGRCC, 2010] for these prospects were calculated from the model results.

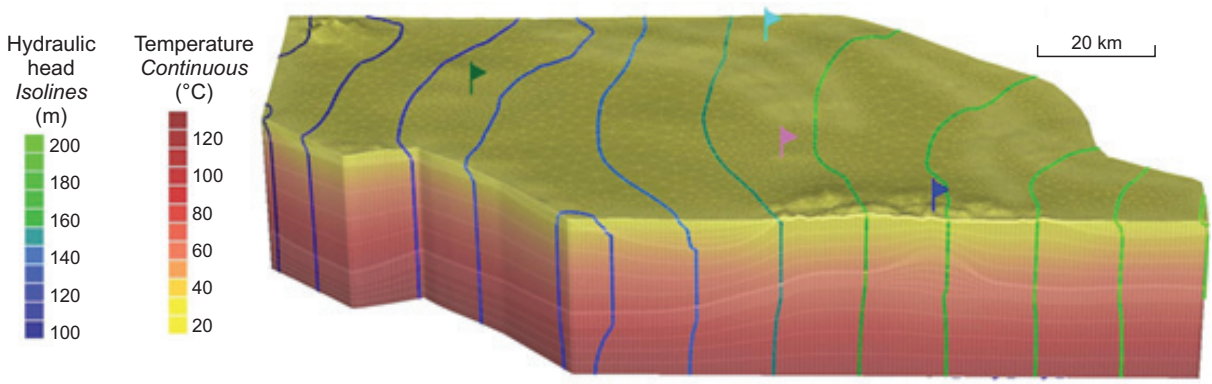

Figure 4.3: Hydrothermal model looking North, showing temperature (continuous contours, °C), hydraulic head (isolines, m) and locations of petroleum wells (flags). Vertical exaggeration x10.

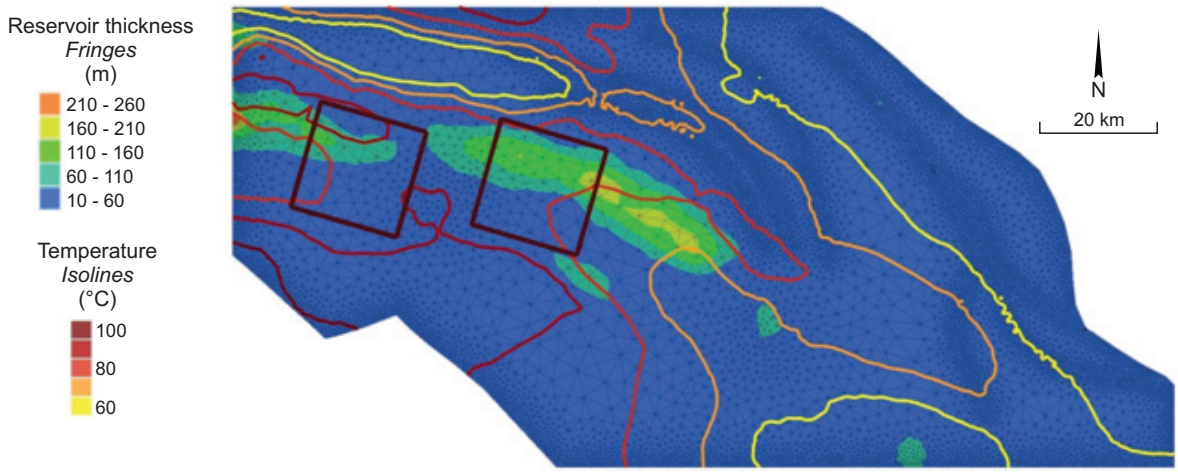

Figure 4.4: Identification of geothermal prospects (square maroon boxes) from Carolyn Formation thickness (filled contours) and modelled temperature (isolines).

Reservoir engineering

The geological model is then refined in the region of the new prospects to provide better resolution. Then reservoir modelling is performed as the last step of the exploration workflow. The reservoir modelling enables assessment of the sustainability of the geothermal targets in terms of well locations, flow rates and energy supply over a given period of time. The reservoir engineering workflow is further defined in Ricard et al. [2012].

Validation and uncertainty analysis

Once one likely geological scenario is chosen, it is important to always subject the final model to quality control using either new data or some data specially reserved for cross-validation. Because models are not reality, they will never perfectly fit new data added for cross-validation. However, surfaces should fit the data within an acceptable error depending on the data type and the uncertainties related to it. Figure 4.5 illustrates cross-checking of the geologic model using withheld data (a seismic line). For the geologic model, the major uncertainties are the fault locations and throws, which could be clarified by reprocessing existing seismic lines with additional emphasis on the first 2.5 seconds of data.

For the hydrothermal model, the major uncertainties are the constant thermal properties and the pressure distribution. The thermal properties used produce heat flow estimates commensurate with those independently modelled by Driscoll et al. [2009]. The hydrothermal model was also quality controlled by comparing the resulting pressure distribution to a measurement obtained from a drill stem test. Further improvements in the model could be obtained by the availability of independent temperature logs rather than point estimates for better calibration of thermal properties and boundary conditions, and additional hydraulic head measurements to better constrain head boundary conditions.

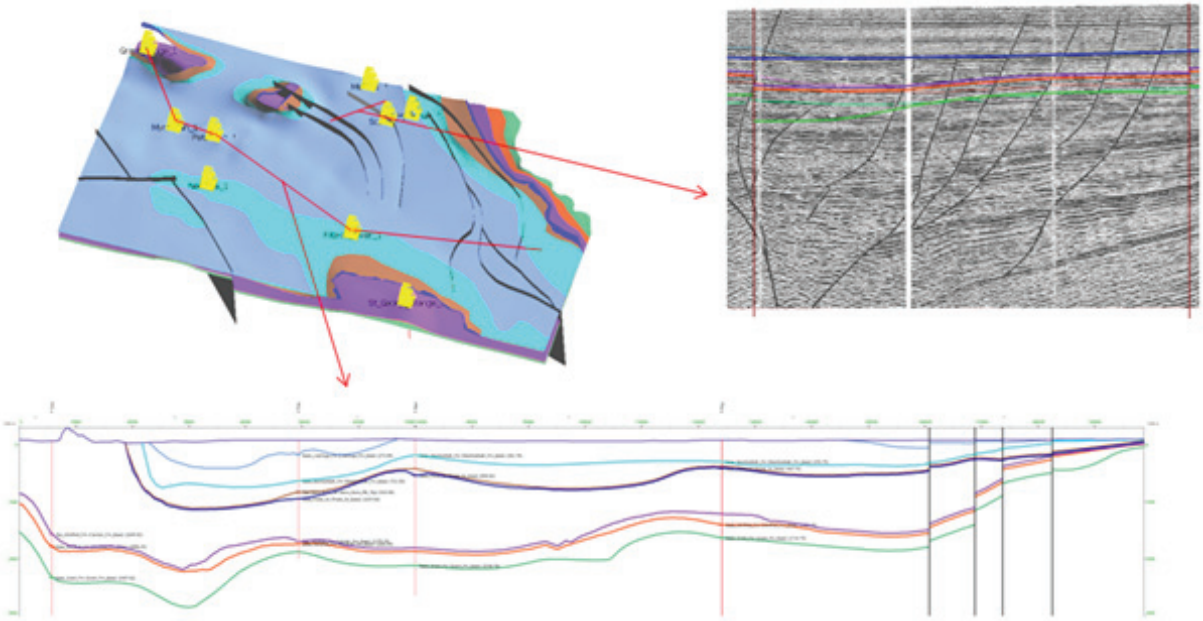

Figure 4.5: Quality control of structural model using withheld data. The seismic line cross-section shown on the right is overcoloured with horizon picks. These horizons are further displayed in a cross section shown at the bottom for more detailed operator review.

Further discussion of uncertainties in the geologic and basin-scale hydrothermal model can be found in Ricard et al. [2012]. In particular, uncertainties in reservoir geometry, hydraulic properties, and the temperature distribution provide the biggest risks for geothermal modelling.

4.1.3 Conclusions

The combined modelling workflow produced several essential elements for geothermal exploration. First, the structural model indicates the depths of aquifer contacts, the thickness of geothermal reservoirs, and compartmentalisation created by faults. Second, the large-scale hydrothermal model yields the temperature and pressure distribution in the reservoirs and provides low-enthalpy geothermal targets. Finally, the reservoir model provides good locations and design parameters for production and injection wells and assesses recoverable energy over time.

This modelling workflow provides a quick first assessment of the potential of an HSA geothermal reservoir, and defines preliminary targets for further investigation. The process identifies critical data needed for a better assessment and also determines the main physical aspects controlling the HSA reservoir behaviour.

4.2 Conductive Heat Transport Model of the Perth Basin

4.2.1 Introduction

The aim of this study is to obtain the temperature distribution of the entire Perth Basin from a high-resolution conductive heat transport simulation. As the model is restricted to conductive heat transport, local variations due to advective and convective heat transport are not considered. The model is intended to provide an overview of the large-scale temperature distribution to aid in large-scale geothermal resource estimations, and to provide a basis for subsequent smaller-scale hydrothermal simulations (see Section 4.3).

4.2.2 Methods

Geologic model

The geologic model covers the entire extent of the Perth Basin (Fig. 1.1B) except the northern offshore part (which is not of interest for geothermal exploration), from near 34.5 degrees south latitude to 28.5 degrees north latitude, and from around 113 to 116 degrees longitude. The size of the model area is 680 km (north-south) by 150 kilometres (east-west). A brief summary of the geologic model is provided here; further details and images are available in the companion report of Project 2 [Timms, 2012]. Input data consisted of previous interpretations of geologic structure, geophysical datasets of the entire basin, and petroleum well data.

The model comprises the Perth Basin sedimentary rocks, the upper and lower crust, and a section of the mantle below the Mohorovičić discontinuity (Moho). The basement geometry was taken from an interpretation by the Department of Mines and Petroleum, with modification to fit a simplified fault network. The Moho and the boundary between the upper and lower crust are derived from the model of Aitken [2010]. His model was constructed using a constrained gravity inversion technique, honouring specific seismic constraints and incorporating lateral density variations within the crustal layers. The upper crust is absent in some areas where the basin is very deep.

The geologic model was created with two geologic modelling packages: GoCad [Mallet, 1992, Caumon et al., 2009] and Geomodeller [Calcagno et al., 2008]. Due to the size of the domain and the large quantity of input data, the model was built in three sections: Southern, Central, and Northern Perth Basin. At the end of each domain, approximately one-quarter of the domain was extended to overlap the next domain's region. Because Geomodeller utilises an implicit geological modelling method, the generated geometry of the overlapping regions (central-north and central-south) was therefore slightly different in each of the three models.

The stratigraphic section of the sedimentary basin fill extends from Permian sediments at the base to Quaternary superficial sediments. Because formation interpretations differ across the latitude of the basin, each of the three sections contained a slightly different stratigraphic column. However, the formations have similar petrophysical rock properties.

The final model consists of top of formation surfaces, a fault network, and deep petroleum exploration wells and shallow groundwater wells which constraint the formation boundaries. Due

to the availability of more shallow well information in the area surrounding Perth, the Central Perth Basin model contains more detail and individual shallow formations. In total, fifteen geologic divisions were modelled.

Geothermal model

The geologic model is a continuous model in three dimensional space. For the numerical simulation of heat transport, a discrete version of the geologic model is required. The geologic model was divided into two primary models: a deep model from 120 kilometres in depth to sea level, and a shallow model from 16 km in depth to 500 metres above sea level. The deep model had four layers: sediments (with uniform average properties), upper crust, lower crust and mantle. This deep model was used to determine a thermal boundary condition at 16 km depth, which is just below the deepest part of the basin. The shallow model contained the sedimentary units from the geologic model and incorporated the detailed structure of the stratigraphic pile up to the ground surface. We used SHEMAT (Simulator for HEat and MAss Transfer) for the geothermal model [Clauser, 2003]. Because the geothermal model requires a rectangular prism domain, the shallow model was extended vertically from the ground surface to an elevation of 500 m AHD, with the intervening space filled either with ocean water or air.

The three domains (north, central and south) were simulated independently on rectilinear grids with perfectly overlapping points in the joining zones. Horizontal discretisation for both models was 500x500 m horizontally. Vertical resolution in the shallow model ranging from 25 m near the surface to 1 km at the base. Vertical resolution in the deep model ranged from 1 km near the surface to 5 km at depth. The total number of simulated cells was over 23 million for the deep model and nearly 50 million for the shallow model. Figure 4.6 shows the geologic structure discretised into the SHEMAT model. The coastline and major towns are shown on most 3D figures at zero elevation for reference.

The results of the three simulations were obtained as individual output files then combined in a single VTK file using a Python script. This script added a new variable to display the geology inconsistencies between overlapping model domains, allowing a qualitative inspection of the mismatch, as well as a quantitative error of the number of cells with conflicting geology information. The percentage of mismatched geologic cells was found to be less than 1.4% in the deep model and less than 6% over the joining areas. The shallow model contains more detailed structural information in the Central Perth Basin due to detailed mapping in this region. A smooth step interpolation was used to merge the values of all fields in the joining zones to ensure soft transitions. A visual inspection then confirmed the validity of the subdividing process with temperature profiles varying seamlessly across the three models.

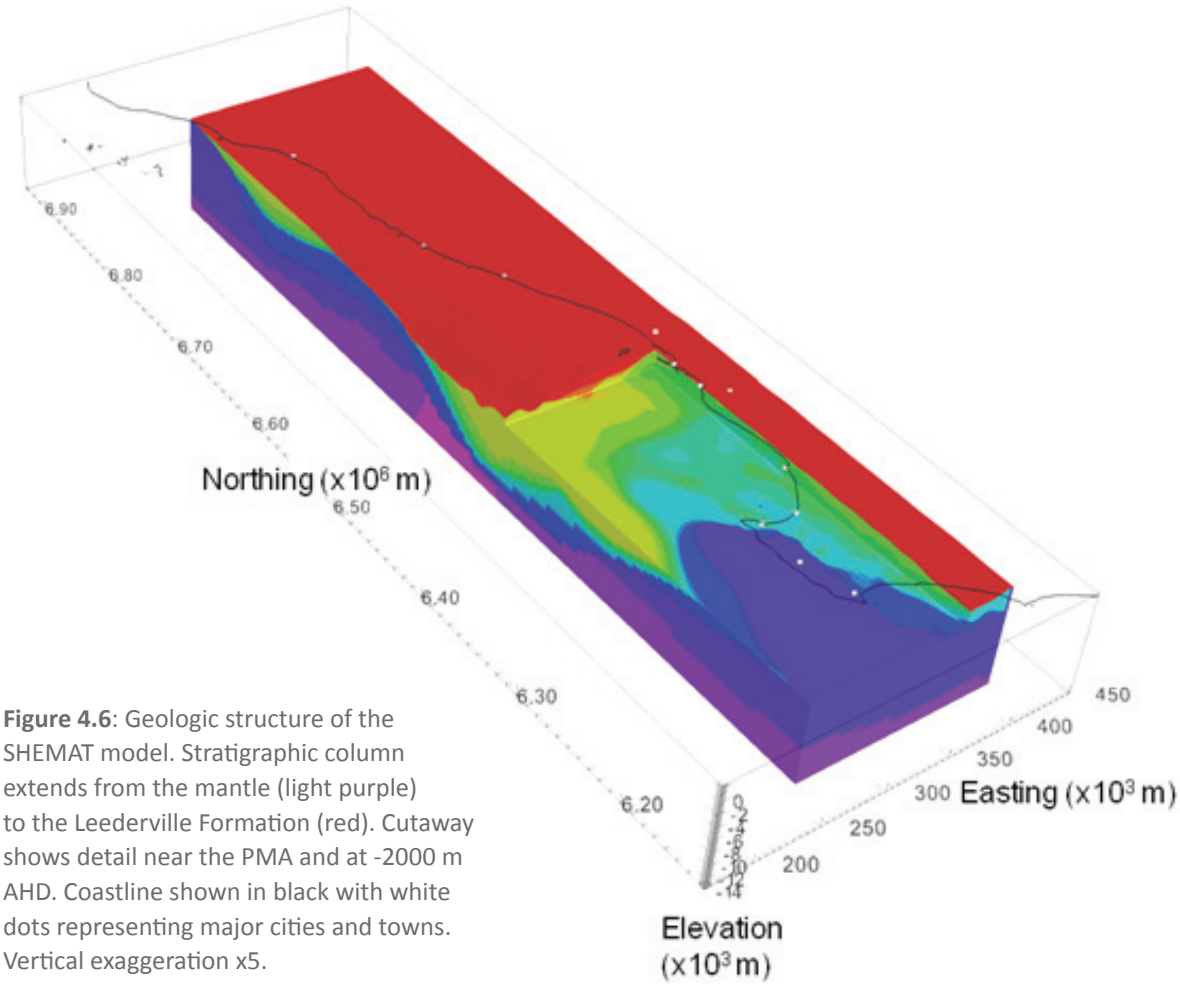

Figure 4.6: Geologic structure of the SHEMAT model. Stratigraphic column extends from the mantle (light purple) to the Leederville Formation (red). Cutaway shows detail near the PMA and at -2000 m AHD. Coastline shown in black with white dots representing major cities and towns. Vertical exaggeration x5.

Boundary conditions

The deep and shallow models were constrained to have continuous temperatures at the horizontal edges. The deep model was assigned a fixed temperature of 20 °C at the top surface. The shallow model had a more detailed temperature boundary condition. Onshore, the mean annual surface temperature (MAST) was applied at every location of the ground surface, interpolated from remote-sensing data [Horowitz and Regenauer-Lieb, 2009]. Offshore, variable temperature was applied at the sea surface based on a temperature survey of the Western Australian coast [Pearce et al., 1999]. The water temperature was constant east-west but varied linearly north-south. This temperature was fixed in the air and ocean water layers. In deep regions offshore, e.g. the Rottnest Trough, temperatures are likely to be lower than the surface water temperature. However, this boundary condition provides a reasonable first approximation to ocean conditions, which are generally shallower than 150 m in the model area.

For the basal boundary condition, a heat flux which varied from south (0.017 W m^{-2}) to north (0.030 W m^{-2}) was applied at the base of the deep model at 120 km. This value produced a heat flux at

the Mohorovičić discontinuity of approximately 0.02 W m^{-2} to 0.06 W m^{-2}, consistent with previous research [Sass and Lachenbruch, 1979, Goutorbe et al., 2008]. The heat flux of the deep model solution at 16 km below AHD provided the basal boundary condition for the shallow model. Figure 4.7 shows the surface temperature and derived basal heat flux distribution for the shallow model.

All simulation results represent a steady state condition.

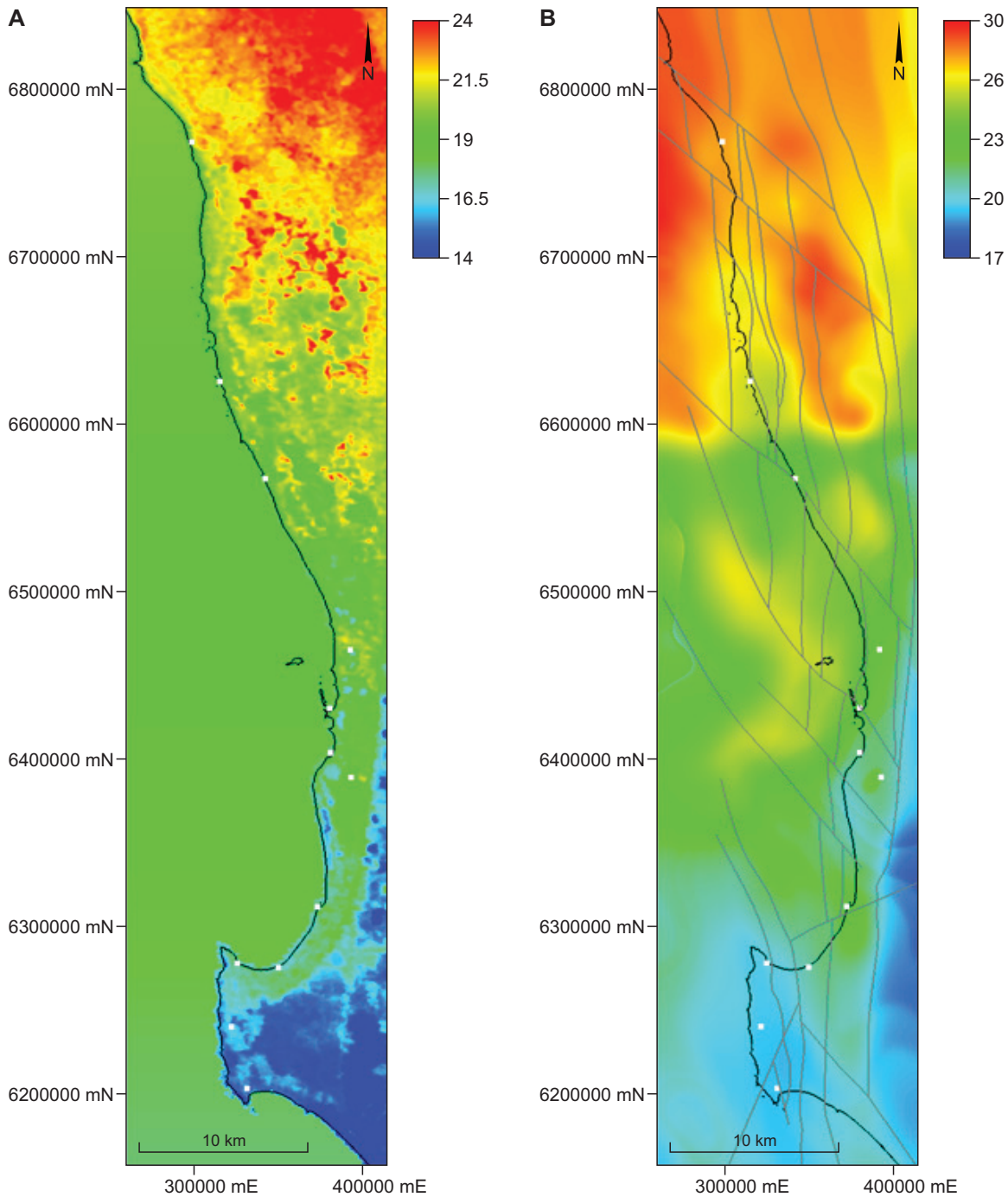

Figure 4.7: Boundary conditions for the shallow model.
(A) Surface temperature [°C]. (B) Heat flux at 16 km [mW m^{-2}].

Rock properties

Values for the material properties in each model unit are listed in Table 4.1. For steady-state heat conduction, only three rock properties are relevant: radiogenic heat production, thermal conductivity, and porosity. SHEMAT requires radiogenic heat production rates and thermal conductivity to be expressed as pure rock properties, which can be derived from bulk matrix values by correcting with porosity. The values were derived from specific studies within the Perth Basin [e.g. Hot Dry Rocks Pty Ltd, 2008, Reid et al., 2011a, CSIRO, 2011], more general Australian studies [e.g. Goutorbe et al., 2008], and worldwide ranges [e.g. Clauser, 2003, Waples and Waples, 2004a, Waples and Waples, 2004b]. Individual sources are noted below. Granitic rocks that outcrop to the east of the Perth Basin, i.e. beyond the Darling Fault, were assumed to be representative of upper crustal rocks underlying the basin. Table 4 1 notes formations that occur in only one of the sub-models of the geologic model.

Radiogenic heat production values for the sediments were derived from reports by HDRPL [2008] and the GSWA [2011a], combined with new values for shallow formations derived from gamma ray logs by Reid et al. [2011a]. Deep values for the crustal sections were suggested by Sass and Lachenbruch [1979]. Additional comments on the heat production rate in the upper crust rate are provided below in Section 4.2.4.

Thermal conductivities were initially derived from HDRPL [2008] and adjusted during calibration against measured temperatures. HDRPL reported values for water-saturated rock at 30 °C; these values were converted to thermal conductivities of the solid rock using the porosity and assuming thermal conductivity of the pore fluid to be 0.65 W m^{-1} K^{-1}. The resulting values are adjusted as a function of temperature by SHEMAT using the formulae proposed by Zoth and Hanel [1988]. Porosity varies considerably within each sedimentary unit; the values for sediments in Table 4.1 are representative values based on data in the Pressureplot database [CSIRO, 2011] and other published literature [Davidson, 1995, Crostella and Backhouse, 2000] where possible. Where porosity data were unavailable, representative values were chosen for other units. The upper and lower crust was assumed to have very low porosity. Note that the porosity values affect the relative contributions of rock and water to the thermal conductivity of the fluid-saturated rock.

Formation	Basinal differences	Porosity (-)	Radiogenic heat production (W m^{-3})	Thermal Conductivity(W m^{-1} K^{-1})
Mantle		0.01	0.0	4.0
Lower Crust		0.01	1.5 x 10-7	3.2
Upper Crust - Basement		0.01	2.4 x 10-6	2.7
Sue Group (Permian)		0.05	4.0 x 10-7	3.1
Kockatea Shale	Triassic CPB, NPB only	0.12	1.2 x 10-6	1.5
Woodada Formation	Triassic CPB, NPB only	0.11	5.0 x 10-7	4.3
Sabina Sandstone	Triassic SPB only	0.50	5.0 x 10-7	4.3
Lesueur Formation		0.09	5.0 x 10-7	3.8
Eneabba Formation		0.06	5.0 x 10-7	3.6
Cattamarra Coal Measures		0.10	4.5 x 10-7	4.1
Yarragadee Formation		0.20	5.0 x 10-7	4.3
Parmelia Formation		0.20	5.0 x 10-7	3.1
Gage Sandstone	CPB only	0.10	5.0 x 10-7	3.9
South Perth Shale	CPB only	0.10	8.0 x 10-7	1.5
Leederville Formation		0.30	6.0 x 10-7	3.4
Superficial Formation	CPB only	0.30	6.0 x 10-7	3.4

Table 4.1: Calibrated thermal properties for the steady-state conductive model.

Calibration

The simulated geothermal field was calibrated against temperature measurements. In the Perth Basin, 96 deep petroleum wells in the sedimentary units contain high quality BHT measurements which can be corrected for effects of measurement techniques. Within these 96 wells, 135 corrected BHTs were available, along with an associated standard deviation of temperature measurement. The report of Project 4 [Ricard et al., 2012] discusses how the data were selected for quality control, true formation temperatures (TFTs) determined, and error ranges derived. The spatial coverage of the measurements varies considerably. While 114 high-quality measurements are available in the North Perth Basin due to considerable exploration activity in the region, only 5 measurements are available in the South Perth Basin and 16 in the Central Perth Basin. No temperature measurements were available outside the Perth Basin sedimentary rocks, e.g. in the eastern Yilgarn Craton.

In the calibration procedure, rock properties and deep basal heat flux were altered to better match the measured temperatures. The simulated temperature was obtained at the measurement location through trilinear interpolation from the surrounding model node values. Simulated temperatures were considered “very good” if they fell within one standard deviation of the corrected BHT, and “good” if within two standard deviations. Two additional measures of goodness-of-fit were provided by the average temperature error in each model subdomain, and a squared residual weighted by the measurement error.

Initial sensitivity runs suggested that the most important parameters for calibration were the basal heat flux at 120 km and the radiogenic heat production value of the upper crust. The final calibrated parameters are shown in Table 4.1. Calibration efforts are continuing and are further described in Section 4.2.4.

4.2.3 Results

The resulting conductive heat transport model contains an enormous amount of information, comprising temperature estimates at nearly 50 million locations in the Perth Basin. The most detailed results are found in the upper 2.5 kilometres below AHD, where model spacing has vertical resolution of less than 50 metres. Resolution down to 4 km depth is less than 250 metres.

Temperature

The following figures are representative of the type of detail which can be obtained from the model. Figure 4.8 shows the isosurfaces of 100, 150, and 200 °C. The geologic layers below the basement structure are shown in grey, highlighting the area of the Perth Basin sediment fill. Note the generally elevated temperature in the North Perth Basin and the decrease in temperatures offshore from Perth, indicating the influence of cold waters in the Rottnest Trough. These three-dimensional surfaces show the scale of the simulation results across the entire basin. Because no snapshot of images can portray the entire picture, the entire temperature dataset is available for inspection from the WAGCoE geothermal catalogue [Corbel and Poulet, 2010].

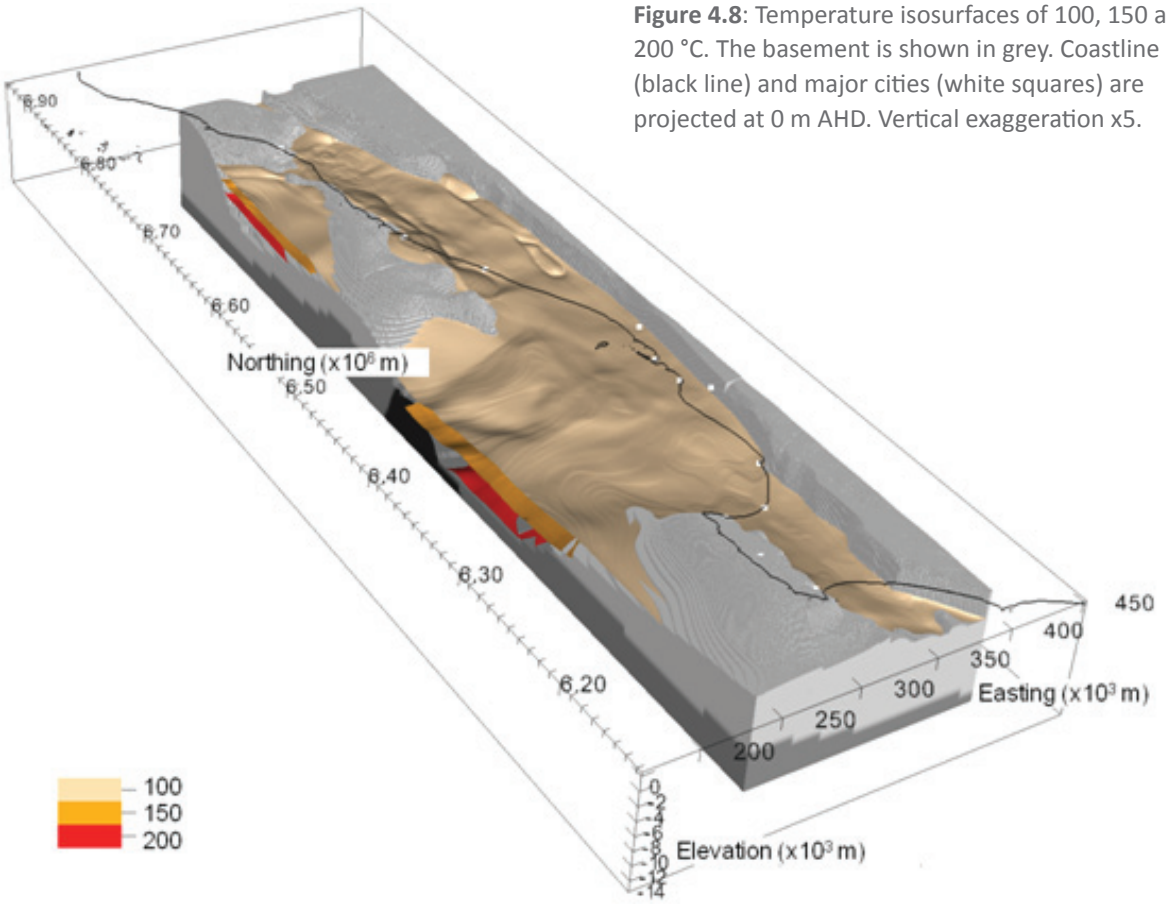

Figure 4.8: Temperature isosurfaces of 100, 150 and 200 °C. The basement is shown in grey. Coastline (black line) and major cities (white squares) are projected at 0 m AHD. Vertical exaggeration x5.

Figures 4.9 to 4.11 provide maps of the temperature at 1 km, 3 km, and 5 km depths below AHD, with colours showing temperature variability at a fixed depth. In all these figures, the coastline, major cities, and surface expressions of the fault network are shown for reference. As the faults are not vertical structures in the geologic model, they will be offset at depth from the indicated grey lines. At 1 kilometre below AHD, the conditions are strongly affected by the boundary condition of the cool ocean, and offshore temperatures are up to 20 degrees cooler than immediately onshore. Temperatures are higher east of the Urella and Darling Faults (the eastmost major fault shown in the figures), outside the Perth Basin. This temperature increase cannot be confirmed due to the lack of direct measurements. Within the sediments, higher temperatures generally exist in the north and are cooler by up to 15 degrees in the South Perth Basin. The highest temperatures are predicted near Cervantes (second city from the north) and just west of the major faults in the granitic Yilgarn craton. At 3 km in depth, the influence of the oceanic boundary condition is less pronounced and temperatures are more uniform east to west in the sediments. The high temperature area near the Beagle Ridge is due to relatively shallow basement structures overlain by insulating sediments. High temperatures are more pronounced in the Yilgarn Craton. Note the detail of temperature prediction near Dongara (furthest north city) and Cervantes (second city from the north). These high temperatures were not predicted in Figure 3.7, as the simplified model of Section 3.2 relied on interpolation and extrapolation of temperature gradients estimated from sparse measurements

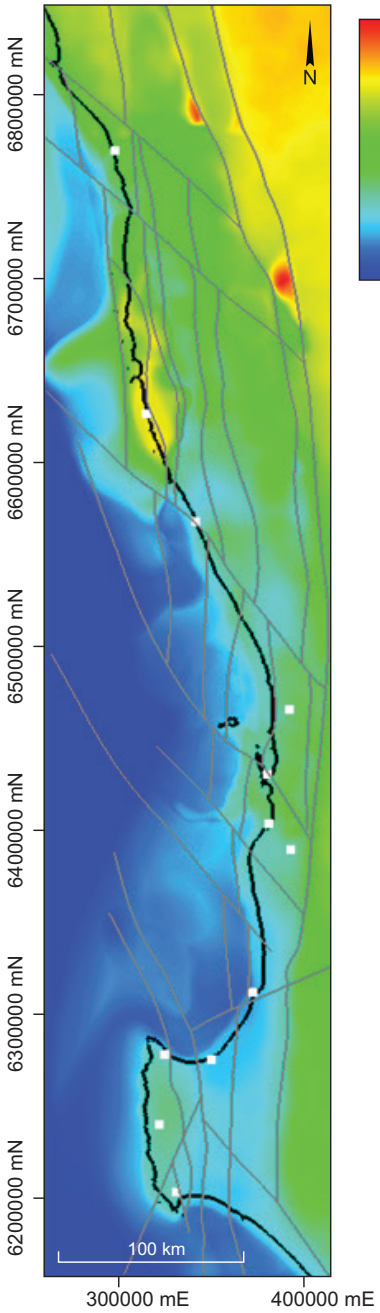

Figure 4.9: Temperature (°C) at -1 km AHD. Coastline (black line), major cities (white squares), and fault network (grey lines) are projected at 0 m AHD.

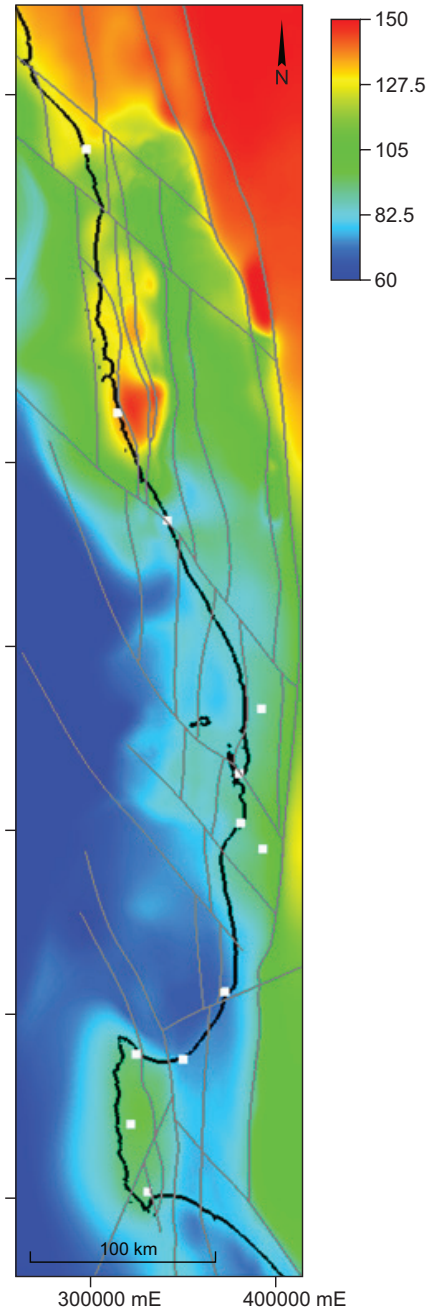

Figure 4.10: Temperature (°C) at -3 km AHD. Coastline (black line), major cities (white squares), and fault network (grey lines) are projected at 0 m AHD.

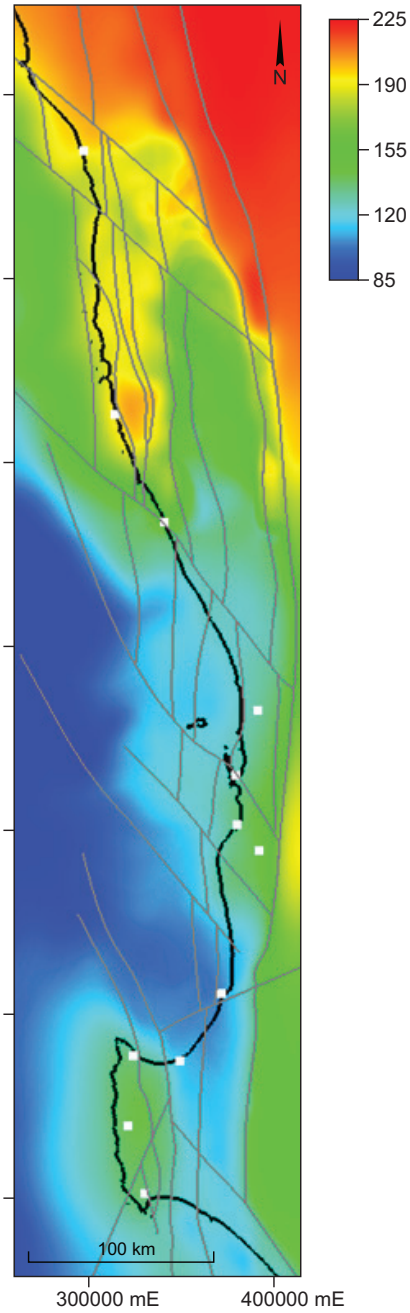

Figure 4.11: Temperature (°C) at -5 km AHD. Coastline (black line), major cities (white squares), and fault network (grey lines) are projected at 0 m AHD.

(BHTs), rather than prediction of temperatures from physical principles (i.e. conduction). At each of the depths, relatively increased temperatures are seen south of Perth, near Pinjarra. Here, the high thermal conductivity Yarragadee Formation is missing and heat is better retained. The central trough of the South Perth Basin, east of the Leeuwin Complex, contains the lowest onshore temperatures.

In addition to slices of data at depth, cross-sectional data can be overlain with the location of a given geologic unit, which is particularly helpful for geothermal schemes utilising the natural permeability of the major aquifer units. Figure 4.12 shows the temperature on constant latitude slices. The Yarragadee formation is shown in grey, indicating the strong North-South variability in depth and thickness of this major formation.

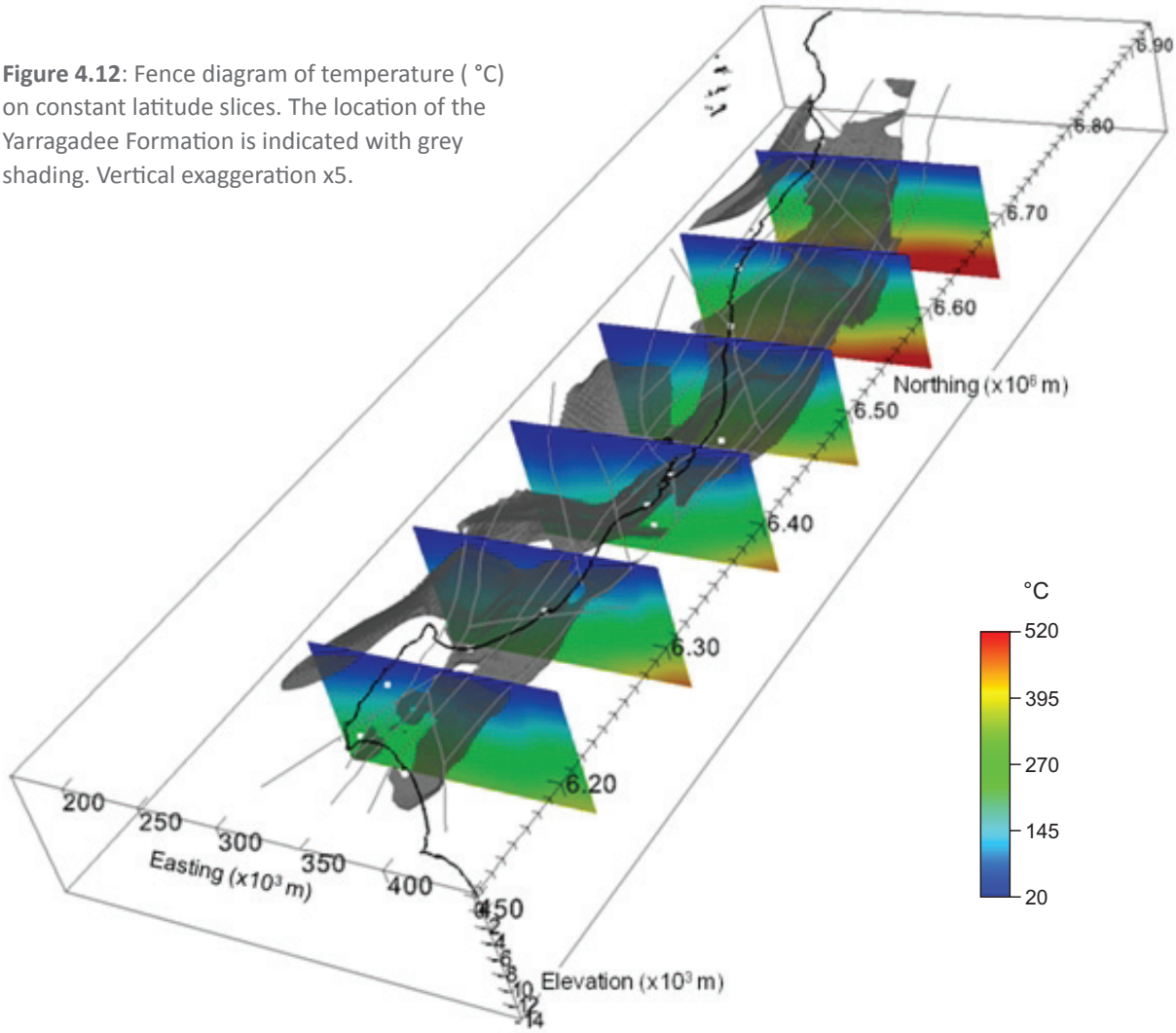

Figure 4.12: Fence diagram of temperature (°C) on constant latitude slices. The location of the Yarragadee Formation is indicated with grey shading. Vertical exaggeration x5.

In general, lower temperatures are seen in locations with thick sedimentary columns. Figure 4.13 shows another fence diagram, here with constant longitude slices. The basement structure is shown in grey. The highest temperatures occur in locations where basement rocks are close to the surface, due to the higher radiogenic heat production rate in the non-sedimentary rocks.

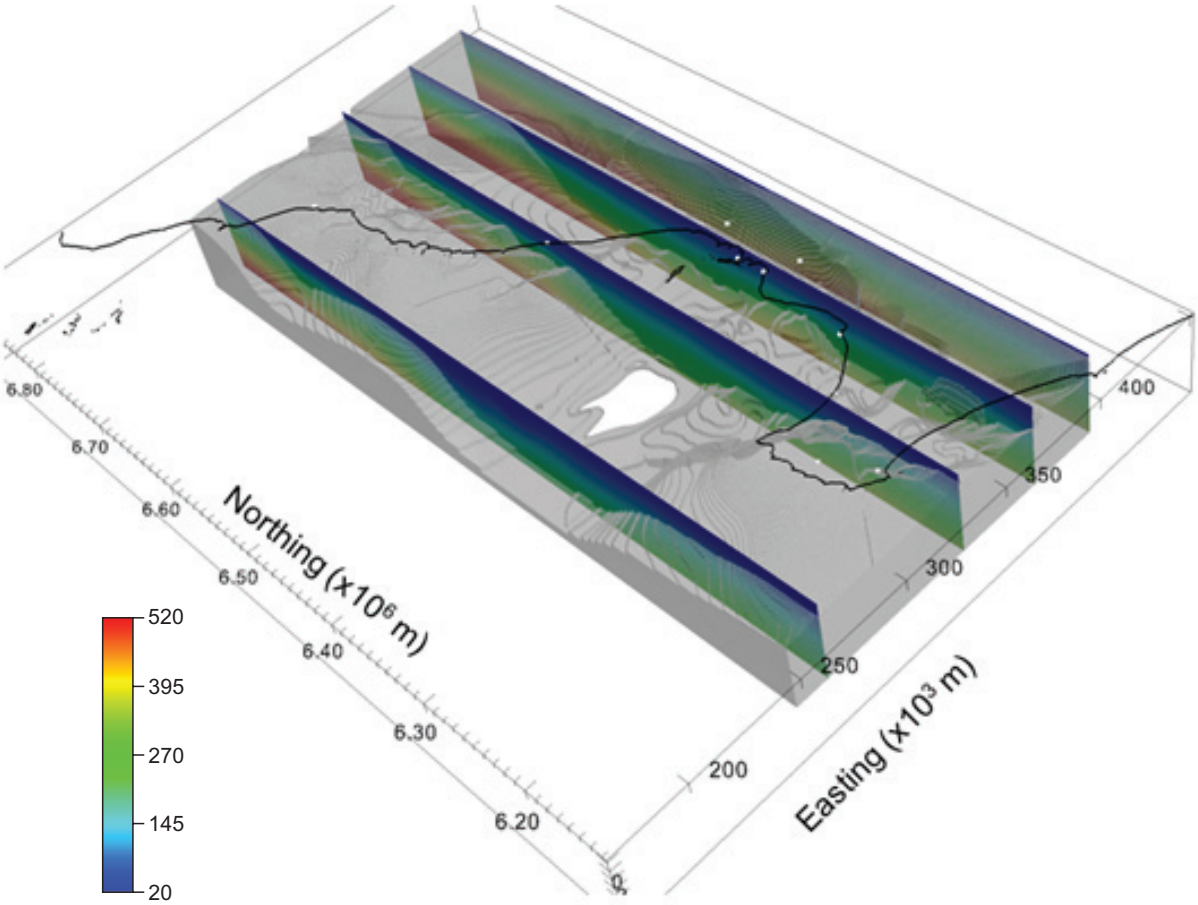

Figure 4.13: Fence diagram of temperature (°C) on constant longitude slices. In grey are shown the basement rocks. Cooler temperatures exist in areas with deep basement structure. Vertical exaggeration x5, East-West exaggeration x2.

Geothermal gradient

This large dataset of temperatures provided by the conductive model can also provide insight into the spatial distribution of geothermal gradients. Figure 4.14 through Figure 4.16 show geothermal gradients in map view at slices located 1, 3, and 5 km below AHD. Each figure shows the vertical geothermal gradient on the left and the positive magnitude of the horizontal gradient on the right in °C km^{-1}. The results are less smooth than the equivalent temperature slices shown above. In general, the highest geothermal gradients occur at fault boundaries, where temperatures can change considerably both vertically and horizontally.

The vertical temperature gradients generally increase with depth; the vertical gradients are higher at 5 km than at 3 km and at 1 km below AHD. This result is in contrast to a one-dimensional analysis of average vertical gradients calculated from petroleum wells presented in the companion report [Ricard et al., 2012]. The horizontal gradient is also generally larger at greater depths.

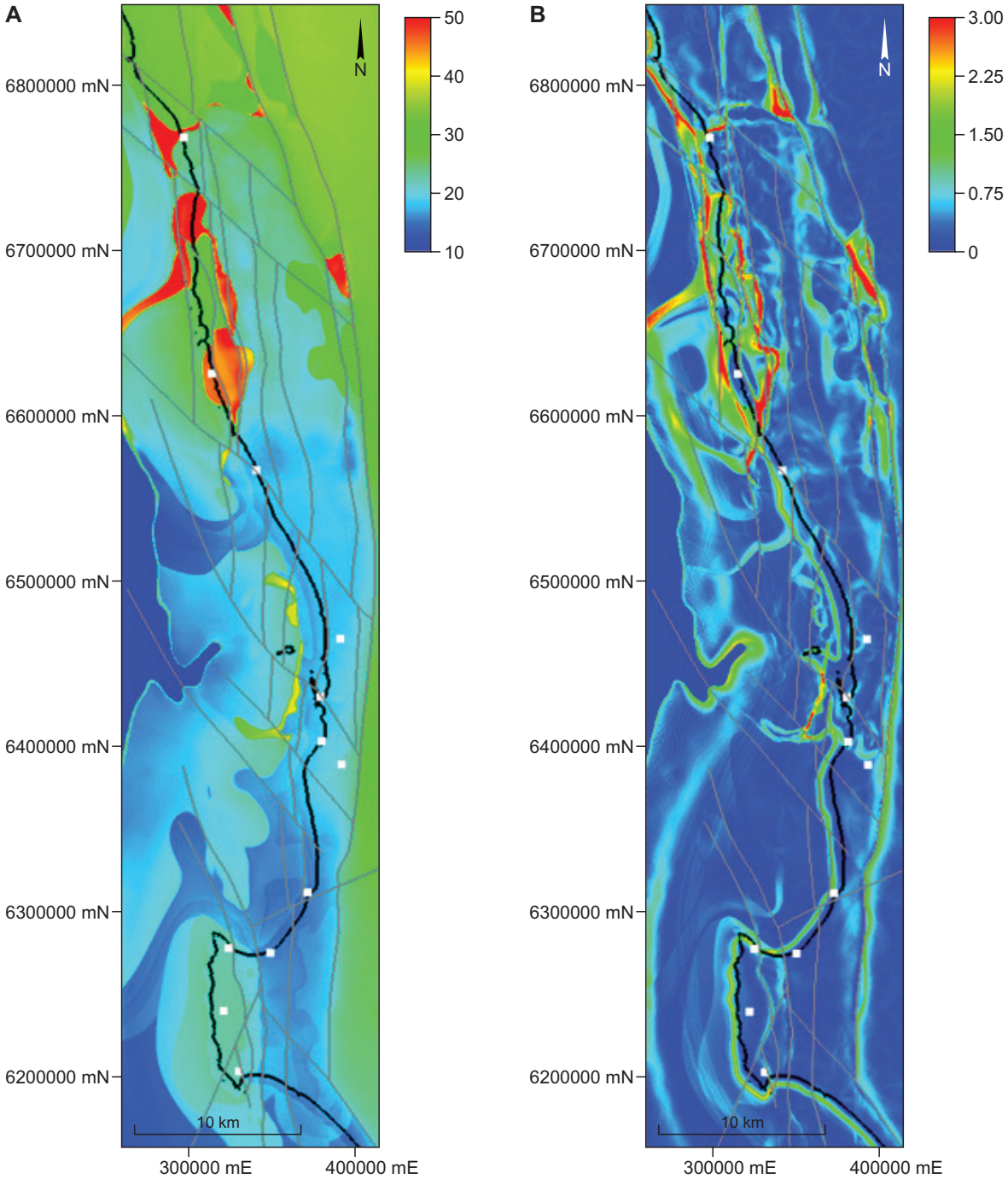

Figure 4.14: Geothermal gradients at -1 km AHD (°C km^{-1}). Vertical gradient (A) and horizontal gradient magnitude (B). Superimposed are coastline (black line), population centres (white squares) and expression of faults (gray lines) at 0 m AHD.

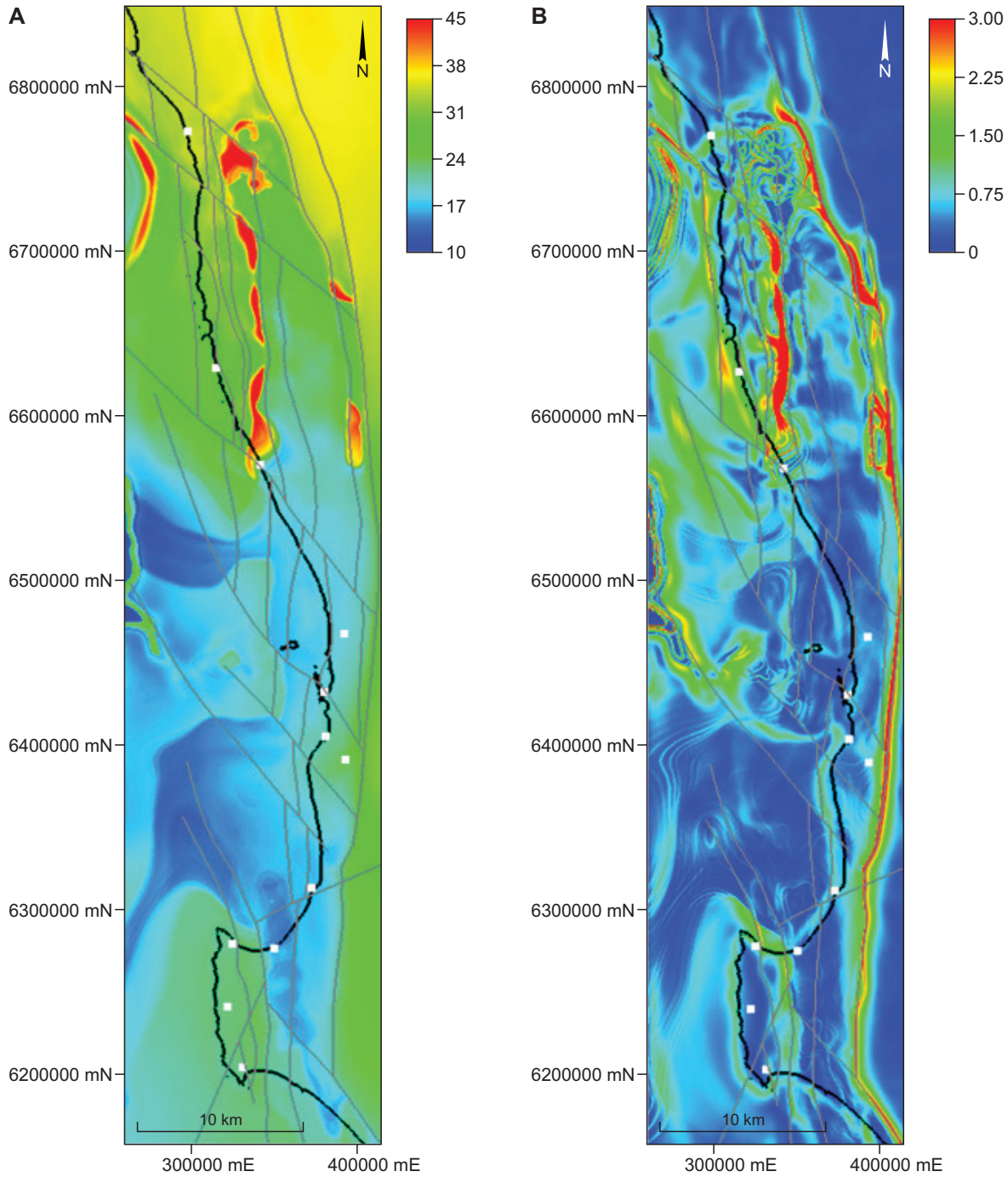

Figure 4.15: Geothermal gradients at -3 km AHD (°C km^{-1}). Vertical gradient (A) and horizontal gradient magnitude (B). Superimposed are coastline (black line), population centres (white squares) and expression of faults (gray lines) at 0 m AHD.

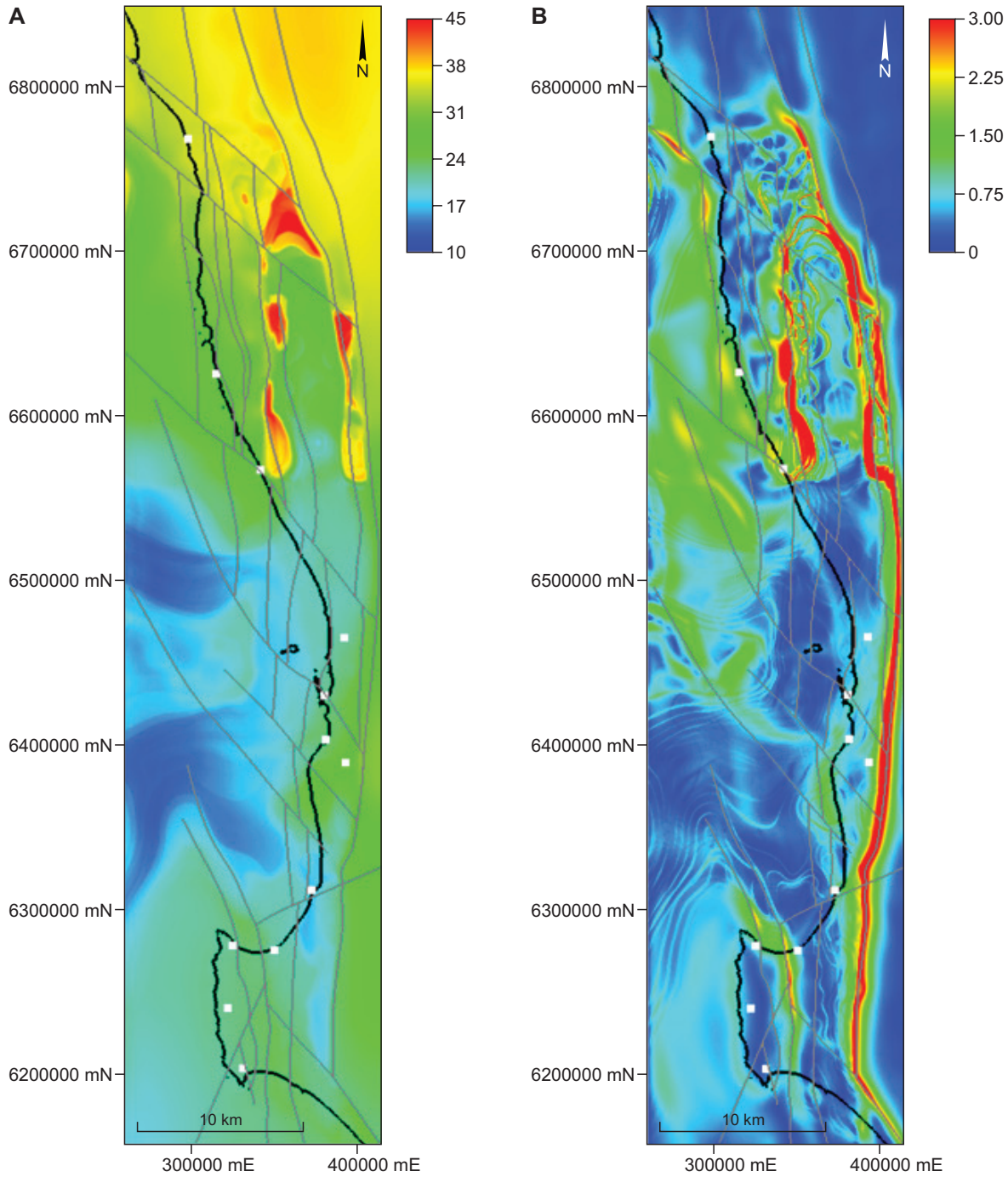

Figure 4.16: Geothermal gradients at -5 km AHD (°C km^{-1}). Vertical gradient (A) and horizontal gradient magnitude (B). Superimposed are coastline (black line), population centres (white squares) and expression of faults (gray lines) at 0 m AHD.

The horizontal temperature gradients are at least an order of magnitude smaller than the vertical geothermal gradients, indicating the overwhelming loss of heat through the Earth's surface. In most locations the horizontal gradient is negligible. At 1 km below AHD, the highest horizontal gradients occur at faults in the North Perth Basin. Deeper, the highest gradient occurs along the Darling Fault along the length of the Perth Basin, which reflects the steeply dipping nature of this major structural control. In some cases these high horizontal gradients may be exacerbated by rectangular geometry required by SHEMAT. Compare the horizontal gradient magnitudes from this large scale conductive model to the gradients shown in Figure 3.19, which has been derived from scattered temperature measurements in the shallow PMA. Again, the level of detail available from a physical model can provide more insight away from direct measurements.

That said, it is important not to draw too many conclusions from the spatial distribution of geothermal gradients calculated from a conductive model. In the absence of other non-conductive means of moving heat, a conductive model essentially maintains constant vertical heat flux (see Equation 3.3-1). The heat flux in the sedimentary pile is a product of the thermal conductivity and the geothermal gradient, with a small component added by radiogenic heat production. Hence the variability of geothermal gradient in a conductive model is primarily controlled by the variability of the thermal conductivity. Figure 4.17 demonstrates this point. Here, the isosurface of relatively high vertical geothermal gradient (-0.038 °C m^{-1}) is plotted in blue in the Perth Basin. This high value only occurs in the Central and North Perth Basin. Also plotted in Figure 4.17 is the location of the Kockatea Shale (North Perth Basin, pink) and the shallower South Perth Shale (green). Both shales are assigned low thermal conductivities in the model (see Table 4.1) based on the typically lower quartz content of shales than sandstones. The locations of high geothermal gradient and low thermal conductivity almost entirely overlap. Again, the most important parameter in geothermal prospectivity is the temperature rather than derived values such as geothermal gradient or heat flow.

Calibration quality

Calbiration of the model by comparison with temperature measurements is important for validation of the conductive model.

An example of the process of manual calibration can be seen in Figure 4.18. Here, the mismatch between measured and simulated temperatures is shown as points coloured by the magnitude of error. Blue points indicate that the model is under-predicting temperatures; red shows over-prediction. Shown in grey is the location of a particular geologic unit, in this case the Permian sediments of the Sue Group. Based on these types of mismatch representations, parameters are adjusted to closer match measurements while still honoring rock property measurements or previous research.

The comparison of simulation results to measured and corrected true formation temperatures (TFTs) is shown in Table 4.2 for the available 135 reliable temperature measurements in 96 wells. The table shows the location of the wells and an indication of the sub-model (South, Central, North) within the Perth Basin. The data include the measured BHT, the reliability of the measurement technique

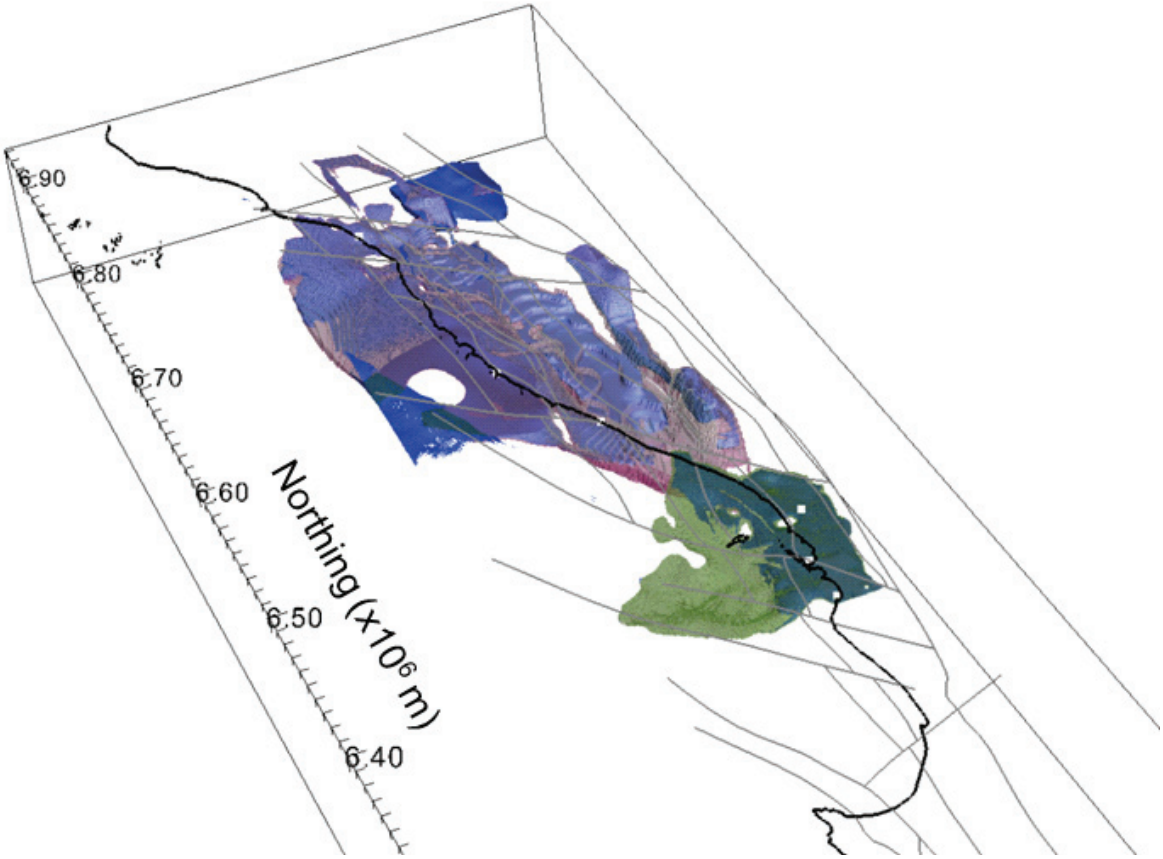

Figure 4.17: Isosurface (blue) of vertical geothermal gradient of 38 °C km^{-1}. Also shown are locations of shale formations: South Perth Shale (green) and Kockatea Shale (pink). Superimposed are coastline (black), population centres (white) and expression of faults at 0 m AHD (grey).

[Chopra and Holgate, 2007], the corrected TFT, the simulated temperature, the model residual, and the measurement standard deviation (see Ricard et al. [2012] for an explanation of the correction and error analysis techniques). The last column indicates whether the measurement residual was within one or two standard deviations of the corrected temperature.

Figure 4.19 shows the simulated temperature plotted agains the TFT, with point coloured by the residual or temperature mismatch. Also plotted is the one-to-one correspondence line. An ideal model would have residuals that are normally distributed, with zero mean (Fig. 4.20). In these figures we see that the average error is -5.3 °C, with a standard deviation of 12.8 °C. On average, the conductive model slightly underestimates temperature and does not reproduce all measurements within a 95% measurement error confidence. However, this residual analysis is valid only if the measured temperatures truly represent subsurface conditions created only by heat conduction. As discussed below (Section 4.2.4), this conduction model does not represent additional heat movement processes (i.e. advection or convection). A more reasonable measure of temperature mismatch at TFT is that 24% of measurements are reproduced within one standard deviation of the measurement error, and 45% are reproduced within two standard deviations (see Table 4.2).

Figure 4.18: Example of calibration. Temperature differences between corrected BHT measurements and simulation results are shown as squares coloured by the temperature mismatch (°C). Red dots indicate that the model is over-predicting; blue, under-predicting. The grey structure shows the location of the Permian Sue Formation. Coastline shown for reference.

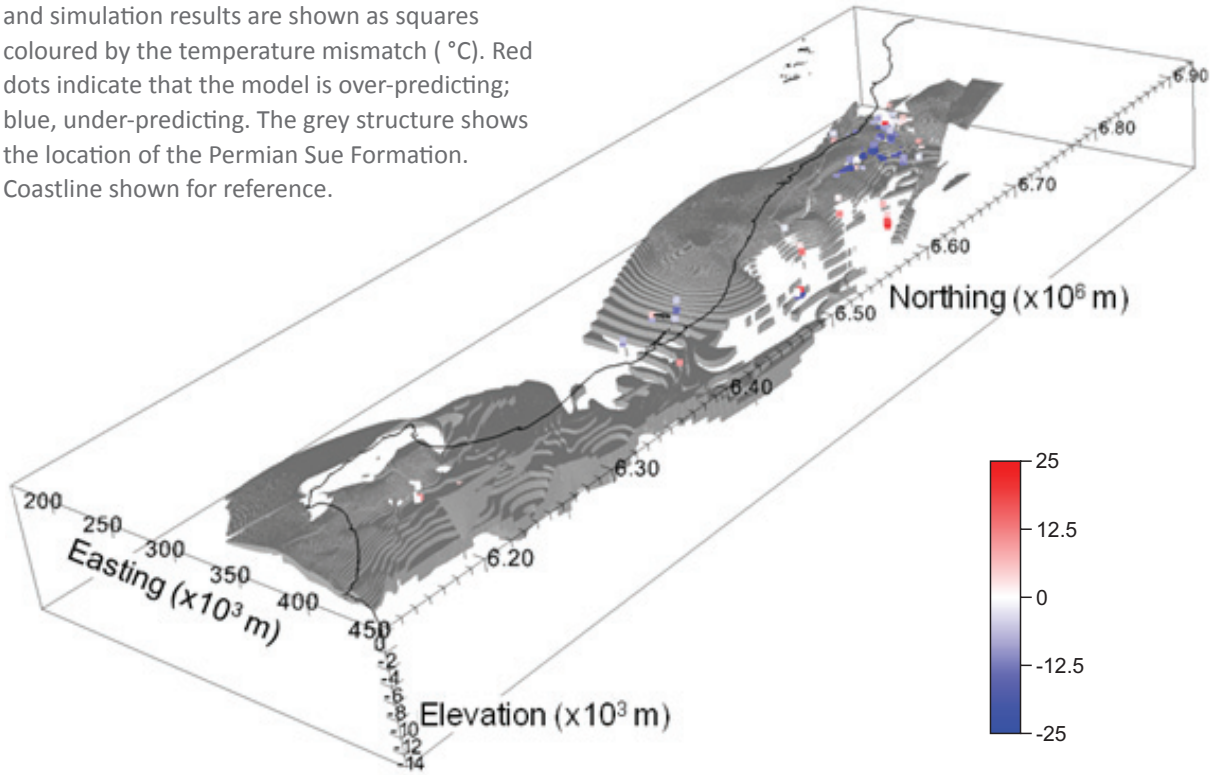

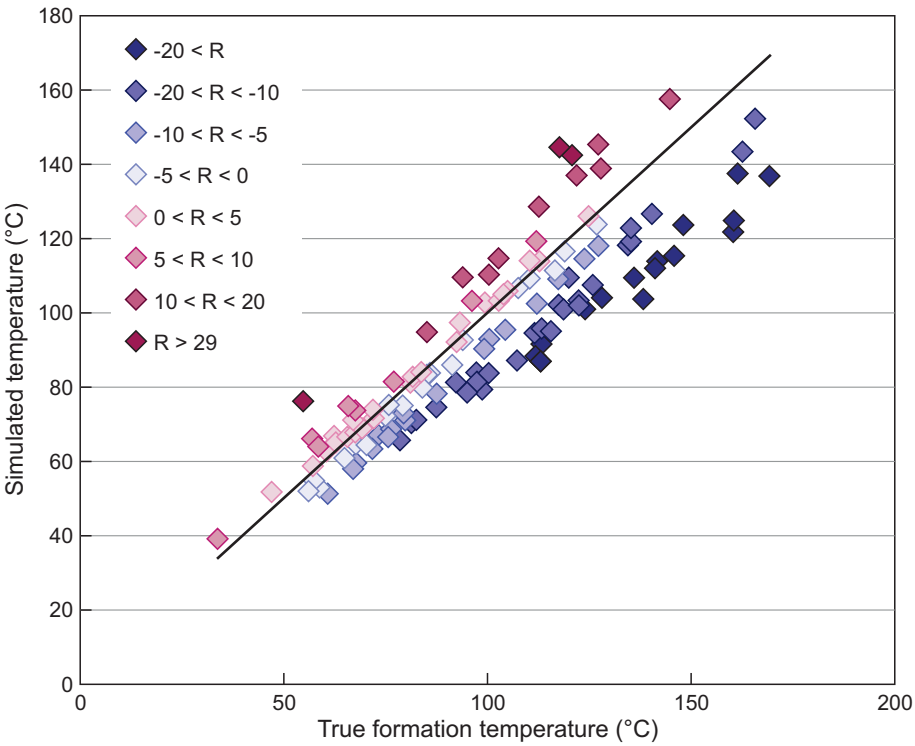

Figure 4.19: Difference between TFT and simulated temperature (°C) at well locations. R = simulated – TFT.

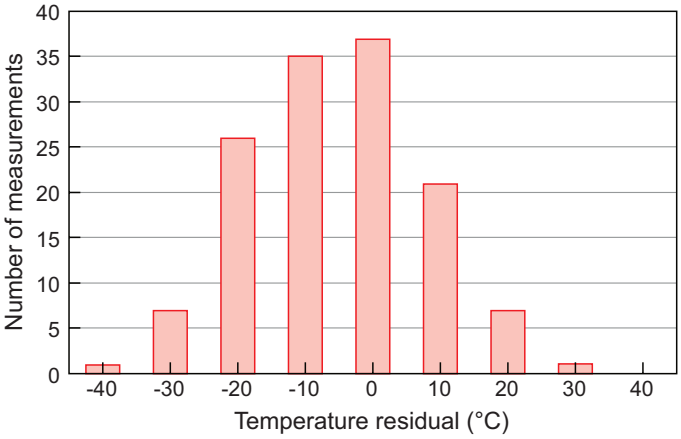

Figure 4.20: Histogram of temperature residuals (°C). Mean error across 135 measurements is -5.3 °C; standard deviation 12.8 °C.

4.2.4 Discussion

The temperature results presented provide a high-resolution and large-scale first order approximation of the geothermal conditions in the entire Perth Basin. The results should be interpreted with the understanding that small scale variability is impossible to model at the basin scale. Nonetheless, the model does provide a unified view of conductive heat processes in this large sedimentary basin.

The temperature model was calibrated with a few key constraining assumptions. First, we operate under the principle of parsimony, and minimise the number of variables to alter [Middlemis et al., 2001]. Therefore, unknown parameters such as basal heat flux and radiogenic heat production of deep formations are parameterised with the minimum number of parameters, such as a mean value or a linear fit. Although the stratigraphic column can vary considerably between the North and South Perth Basins [Crostella and Backhouse, 2000, Mory and Iasky, 1997], we have elected to use only 12 sedimentary units to characterise the gross behaviour of the stratigraphic distinctions.

Second, we assumed that rock properties are constant across the entire formation spatially. This simplification is clearly unrealistic, as previous measurements [Hot Dry Rocks Pty Ltd, 2008, Delle Piane and Israni, 2012] show variability within measurements taken in individual wells as well as from different latitudinal/longitudinal locations. Some justification for this approach can be found in recent studies highlighting the idea of “thermofacies” [Sass and Götz, 2012] which act as a reasonably unified formation in the thermal sense. In addition, the range of thermal conductivities of sedimentary rocks does not vary widely [Norden and Forster, 2006, Clauser, 2009] and any assumed values for particular facies types will be correct within an order of magnitude.

Another key assumption was that the adjoining Yilgarn craton was equivalent in thermal properties to the upper crust. New data on radiogenic heat production from the Leeuwin Complex [Hopkins, 2011] of near 4.0 µW m^{-3} are consistent with a previously published median value for granitoid rocks in and around the Perth Basin [Hot Dry Rocks Pty Ltd, 2008]. Our model calibrated to the Perth Basin utilises a much lower value of 2.40 µW m^{-3}. In addition, the basal heat flow across the entire basin was assumed to be the same under sedimentary basins and the adjacent craton. There is considerable evidence [Goutorbe et al., 2008, Bodorkos and Sandiford, 2006] that the heat flux under continental

margins such as the Perth Basin varies from the Precambrian shield. However, recent measurements of temperatures in the nearby Yilgarn craton were unavailable to use as calibration points for the model. Simulation results in the domain outside the sedimentary basin should therefore be considered preliminary, and future work should include a variation between sub-basin basement and cratonic rocks.

Most importantly, we assume that the corrected temperature measurements shown in Table 4 2 represent TFTs that are generated only by conductive processes within the Perth Basin. In reality, heat is moved within the sediments by advective [Reid et al., 2011a] and possibly convective [Sheldon et al., 2012] movement of groundwater. Throughout the extent of the Perth Basin, groundwater provides a significant water resource [e.g. Commander, 1974, Commander, 1978, Irwin, 2007] and the permeable aquifers are heavily used for water supply. In some aquifers, estimated flow rates can reach on the order of 1 m day^{-1} [Davidson, 1995]; these rates are sufficient to significantly transport large quantities of heat [e.g. Jessop and Majorowicz, 1994, Saar, 2011].

Evidence of non-conductive heat flow is easily seen in the temperature measurements utilised as calibration parameters in this report. For example, Gingin 1 is located in the Central Perth Basin and has two high quality (DST) temperature measurements at -3874 m AHD and -4453 m AHD. The respective temperature measurements are 93.3 and 160 °C. The geothermal gradient between these two measurements is 115 °C km^{-1}. If no measurement error is assumed, this gradient is wildly different than the more reasonable average geothermal gradient of 25 °C km^{-1} obtained from nearby Gingin 3. Indeed, the conductive results presented here cannot match these measured temperatures, and a residual error of 15.9 and -38.9 °C is found for the two depths. These two measurements alone heavily contribute to a high mismatch between the simulation results and the measurements in the Central Perth Basin. The high temperature variability at Gingin 1 could be caused by non-conductive effects in the formation or even in the exploration borehole [Powell et al., 1988]. Of course, despite extensive checking of the dataset, the measurements could simply represent human error when they were obtained or recorded.

In these results, we primarily present the simulated temperature and geothermal gradient. Little emphasis is placed on a quantitative estimate of heat flux. Heat flux is simply the geothermal gradient weighted by thermal conductivity, and cannot be measured independently of the two parameters. Because there are relatively few measurements of thermal conductivity in the Perth Basin, and we assume constant spatial values, the same relative information about heat flux can be obtained by investigating the spatial distribution of the temperature gradient. Indeed, locations of high heat flux do not directly give useful information about elevated temperature, which is the parameter of real concern in geothermal exploration. Previous studies of the North Perth Basin [Geological Survey of Western Australia, 2011a] have similarly pointed out that the high heat flux in the Yilgarn Craton is caused by the absence of insulating overlying sediments, and does not correspond to areas with prospective geothermal temperatures.

Research is continuing into calibrating the basin-scale model. The results shown here reflect manual adjustment of the rock properties and boundary conditions. Currently, parameter sensitivity software

Well name	Basin	Quality	Location Easting	Northing	Elevation	Temperature (°C) BHT measurement	True formation	Simulated	Residual	Standard deviation	Within SD?
Rutile 1	South	C or B	348170.7	6233724.2	-2511.0	68.8	71.6	71.0	-0.6	4.7	1
Whicher Range 2	South	A	350471.4	6254337.6	-3906.0	85.0	85.0	94.1	9.1	2.5	
Whicher Range 3	South	C or B	351479.6	6251004.9	-3750.5	88.6	92.1	91.2	-0.9	6.0	1
Whicher Range 3	South	A	351479.6	6251004.9	-4438.0	104.4	104.4	104.6	0.2	2.5	1
Wonnerup 1	South	A	358339.8	6277736.2	-4339.0	92.7	92.7	96.0	3.3	2.5	2
Araucaria 1	Central	C or B	345661.1	6434954.2	-1708.9	69.9	72.7	54.3	-18.4	4.8	
Araucaria 1	Central	C or B	345661.1	6434954.2	-2215.3	89.1	92.6	68.8	-23.8	6.1	
Bootine 1	Central	A	388223.4	6550244.5	-3752.5	107.2	107.2	106.4	-0.8	2.5	1
Bootine 1	Central	A	388223.4	6550244.5	-4084.0	112.2	112.2	113.1	0.9	2.5	1
Bootine 1	Central	C or B	388223.4	6550244.5	-4303.3	129.4	134.6	117.6	-17.0	8.8	2
Cataby 1	Central	A	340386.7	6603967.8	-1692.5	67.5	67.5	59.3	-8.2	2.5	
Gingin 1	Central	A	388203.4	6553951.9	-3873.7	93.3	93.3	109.1	15.8	2.5	
Gingin 1	Central	A	388203.4	6553951.9	-4452.5	160.0	160.0	121.1	-38.9	2.5	
Marri 1	Central	C or B	344360.1	6486680.1	-2585.8	93.6	97.3	71.4	-25.9	6.4	
Minder Reef 1	Central	C or B	343191.7	6489256.0	-1521.0	62.1	64.6	49.0	-15.6	4.2	
Mullaloo 1	Central	C or B	354623.4	6473354.2	-2015.5	76.1	79.1	62.9	-16.2	5.2	
Rockingham 1	Central	C	395555.5	6426582.9	-1561.9	54.5	56.6	64.6	8.0	3.7	
Tuart 1	Central	C or B	344915.1	6463910.6	-1065.6	45.2	47.0	39.9	-7.1	3.1	
Tuart 1	Centra	C or B	344915.1	6463910.6	-1589.9	68.8	71.5	51.0	-20.5	4.7	
Walyering 1	lCentral	A	353183.4	6601022.6	-3396.0	100.0	100.0	93.1	-6.9	2.5	
Walyering 3	Central	A	355978.0	6598966.5	-3939.0	102.2	102.2	103.3	1.1	2.5	1
Apium 1	North	C or B	312674.2	6755463.5	-2840.6	130.5	135.7	113.0	-22.7	8.9	
Arramall 1	North	C	315712.4	6725160.3	-2246.0	107.4	111.7	90.7	-21.0	7.3	
Arranoo 1	North	C	313103.5	6775121.0	-1734.5	77.6	80.7	83.9	3.2	5.3	1
Beekeeper 1	North	A	324589.9	6711673.2	-2846.0	116.1	116.1	114.0	-2.1	2.5	1
Beharra Springs 1	North	A	319747.8	6739152.5	-3416.0	135.0	135.0	127.2	-7.8	2.5	
Beharra Springs 2	North	B	320138.4	6737620.6	-3483.4	141.9	147.6	127.7	-19.9	7.0	
Beharra Springs 3	North	C	319702.2	6740115.1	-3503.0	135.0	140.4	130.9	-9.5	9.2	2
Bonniefield 1	North	C	297180.4	6771348.2	-1009.2	64.1	66.7	59.5	-7.2	4.4	2

Well name	Basin	Quality	Location Easting	Northing	Elevation	Temperature (°C) BHT measurement	True formation	Simulated	Residual	Standard deviation	Within SD?
Casuarinas 1	North	C or B	319994.2	6798873.0	-1095.3	58.8	61.1	67.6	6.5	4.0	
Cataby 1	North	A	340386.7	6603967.8	-1692.5	67.5	67.5	65.0	-2.5	2.5	2
Central Yardarino 1	North	C or B	310547.4	6768367.8	-2493.3	119.6	124.4	105.2	-19.2	8.1	2
Cliff Head 4	North	C or B	293153.8	6740700.2	-1582.4	76.6	79.7	66.8	-12.9	5.2	
Conder 1	North	C	297881.3	6785357.2	-250.0	32.3	33.6	40.1	6.5	2.2	
Coomallo 1	North	C	347732.8	6652728.1	-1218.8	54.8	57.0	59.2	2.2	3.7	
Coomallo 1	North	C	347732.8	6652728.1	-3496.8	95.9	99.7	111.4	11.7	6.5	1
Denison 1	North	B	301334.7	6765421.5	-2302.4	106.7	111.0	97.7	-13.3	5.2	2
Depot Hill 1	North	C	337141.2	6779731.1	-2467.8	122.5	127.4	109.4	-18.0	8.3	
Dongara 5	North	A	304077.9	6769589.4	-1546.0	54.4	54.4	78.6	24.2	2.5	
Dongara 21	North	C or B	306928.8	6764486.0	-1887.0	95.3	99.1	85.2	-13.9	6.5	
Dongara 24	North	A	307394.8	6764244.5	-1534.8	76.1	76.1	70.8	-5.3	2.5	
Dongara 25	North	A	308183.3	6763617.2	-1502.0	75.6	75.6	68.2	-7.4	2.5	
Dongara 26	North	C or B	302944.5	6763059.0	-1828.4	94.7	98.4	81.7	-16.7	6.4	
Dongara 27	North	C or B	307826.4	6768186.7	-1698.5	84.0	87.4	80.8	-6.6	5.7	2
Dongara 28	North	C or B	307128.5	6763381.7	-1848.2	88.1	91.7	83.9	-7.8-	6.0	2
East Lake Logue 1	North	A	321720.3	6698298.4	-2430.0	122.0	122.0	106.0	16.0	2.5	
Ejarno 1	North	A	313282.4	6755708.4	-2852.0	110.0	110.0	113.5	3.5	2.5	2
Erregulla 2	North	B	344610.6	6749508.0	-3262.9	114.3	118.9	120.7	1.8	5.6	1
Gairdner 1	North	C	321412.1	6671998.8	-2170.0	112.2	116.7	110.3	-6.4	7.6	1
Georgina 1	North	B	312740.3	6774597.2	-1828.5	79.9	83.1	87.0	3.9	3.9	2
Hakia 1	North	B	314922.6	6766589.3	-2739.0	118.0	119.9	113.7	-6.2	3.3	2
Horner West 1	North	B	309742.7	6775435.2	-1440.6	71.3	74.1	74.5	0.4	3.5	1
Hovea 1	North	C or B	309876.5	6755320.3	-2002.0	93.8	97.5	83.7	-13.8	6.4	
Hovea 2	North	C or B	310115.7	6755685.2	-2412.5	108.5	112.8	98.9	-13.9	7.4	2
Hovea 2	North	C or B	310115.7	6755685.2	-2680.5	123.2	128.1	107.2	-20.9	8.4	
Hunt Gully 1	North	B	320302.5	6779848.3	-1979.0	87.7	91.2	89.2	-2.0	4.3	1
Indoon 1	North	B	321603.4	6692812.7	-2255.0	112.7	117.2	104.0	-13.2	5.5	
Jay 1	North	C	310957.4	6781841.7	-1294.2	59.7	62.1	68.7	6.6	4.1	2

Well name	Basin	Quality	Location Easting	Northing	Elevation	Temperature (°C) BHT measurement	True formation	Simulated	Residual	Standard deviation	Within SD?
Leander Reef 1	North	C	280549.6	6741314.1	-1496.0	61.3	63.8	51.3	-12.5	4.2	
Leander Reef 1	North	B	280549.6	6741314.1	-1428.0	62.0	64.5	49.9	-14.6	3.0	
Leander Reef 1	North	B	280549.6	6741314.1	-2690.0	92.2	95.9	93.7	-2.2	4.5	1
Leander Reef 1	North	B	280549.6	6741314.1	-3233.5	129.7	134.9	110.3	-24.6	6.4	
Lockyer 1	North	A	331046.6	6770289.1	-3221.0	111.6	111.6	124.2	12.6	2.5	
Lockyer 1	North	C or B	331046.6	6770289.1	-3326.5	121.5	126.4	129.1	2.7	8.3	1
Mondarra 1	North	B	317219.1	6757262.4	-934.0	56.1	58.3	54.7	-3.6	2.8	2
Mondarra 1	North	B	317219.1	6757262.4	-2068.4	91.2	94.8	81.5	-13.3	4.5	
Mondarra 1	North	B	317219.1	6757262.4	-3065.1	122.2	127.1	122.0	-5.1	6.0	1
Mooratara 1	North	B	296854.8	6766623.7	-1500.0	76.2	79.2	74.8	-4.4	3.7	2
Mountain Bridge 1	North	C	317491.4	6724040.2	-3415.0	154.0	160.2	128.4	-31.8	10.5	
Mt Horner 3	North	A	313832.3	6776268.0	-1515.0	71.1	71.1	76.2	5.1	2.5	
Mt Horner 4	North	A	314319.9	6776209.5	-1326.0	78.3	78.3	68.0	-10.3	2.5	
Mt Horner 4	North	A	314319.9	6776209.5	-1746.0	77.2	77.2	83.4	6.2	2.5	
Mt Horner 4	North	A	314319.9	6776209.5	-1772.5	76.6	76.6	84.2	7.6	2.5	
Mt Horner 4A	North	C or B	314348.1	6776276.4	-1250.2	56.5	58.8	66.1	7.3	3.9	2
Mt Horner 5	North	C or B	314128.6	6776605.4	-1816.0	78.1	81.2	85.3	4.1	5.3	1
Mt Horner 5A	North	C or B	314206.8	6776584.5	-1278.3	66.7	69.4	67.1	-2.3	4.5	1
Mt Horner 6	North	C or B	314358.5	6775500.6	-1847.0	82.2	85.4	87.1	1.7	5.6	1
Mt Horner 7	North	A	314435.9	6776861.7	-1241.5	57.7	57.7	66.2	8.5	2.5	
Mt Horner 7	North	A	314435.9	6776861.7	-1407.0	68.8	68.8	70.9	2.1	2.5	1
Mt Horner 7	North	C or B	314435.9	6776861.7	-1842.2	81.5	84.8	86.0	1.2	5.5	1
Mt Horner 8	North	C or B	314488.1	6775846.4	-1303.0	60.1	62.5	67.2	4.7	4.1	2
Mt Horner 9	North	C or B	314613.3	6776458.1	-1233.0	57.7	60.0	65.6	5.6	3.9	2
Mt Horner 10	North	C	314947.2	6776004.7	-1440.7	64.0	66.6	73.5	6.9	4.3	2
Mt Horner 11	North	C or B	317183.3	6780430.9	-1368.5	64.0	66.6	70.4	3.8	4.3	1
Mungenooka 1	North	C or B	326639.4	6747368.3	-3842.5	156.1	162.3	149.0	-13.3	10.6	2
Murrumbah 1	North	C or B	322961.3	6773202.0	-2136.2	89.8	93.4	96.0	2.6	6.1	1
Narlingue 1	North	C	315456.7	6782850.8	-2127.3	108.4	112.7	95.2	-17.5	7.4	

Well name	Basin	Quality	Location Easting	Northing	Elevation	Temperature (°C) BHT measurement	True formation	Simulated	Residual	Standard deviation	Within SD?
North Erregulla 1	North	B	337476.4	6763786.6	-3448.0	119.7	124.5	131.2	6.7	5.9	2
North Yardanogo 1	North	A	316023.8	6738849.4	-1683.0	81.0	81.0	72.0	-9.0	2.5	
North Yardanogo 1	North	C	316023.8	6738849.4	-2379.8	108.3	112.6	89.4	-23.2	7.4	
Peron 1	North	B	322507.2	6685210.2	-1924.4	100.3	104.3	96.8	-7.5	4.9	2
Peron 1	North	B	322507.2	6685210.2	-2599.5	135.8	141.2	116.0	-25.2	6.7	
Point Louise 1	North	C	313952.9	6675337.8	-946.5	62.4	64.9	67.2	2.3	4.2	1
Redback 1	North	C or B	321765.9	6739887.1	-3800.8	155.0	161.2	142.2	-19.0	10.5	2
Robb 1	North	B	309926.8	6729990.4	-1963.3	96.3	100.1	86.1	-14.0	4.7	
South Yardanogo 1	North	C	316254.8	6735348.4	-2341.0	103.0	107.1	89.6	-17.5	7.0	
Tabletop 1	North	C	317183.3	6780430.9	-1785.0	80.6	83.8	83.2	-0.6	5.5	1
Twin Lions 1	North	C or B	294852.5	6749215.6	-1568.5	79.3	82.5	71.0	-11.5	5.4	
Vindara 1	North	C or B	299887.5	6735049.7	-1729.1	83.8	87.2	74.8	-12.4	5.7	
Walyering 1	North	A	353183.4	6601022.6	-3396.0	100.0	100.0	102.7	2.7	2.5	2
Walyering 3	North	A	355978.0	6598966.5	-3939.0	102.2	102.2	114.7	12.5	2.5	
Warradong 1	North	B	322526.9	6757361.5	-3714.7	162.5	169.0	142.	-26.9	8.0	
Warramia 1	North	B	377675.3	6660097.6	-1494.2	64.6	67.2	174.3	7.1	3.2	
Warro 1	North	C	378471.5	6662016.4	-1492.3	72.3	75.2	75.8	0.6	4.9	1
Warro 1	North	B	378471.5	6662016.4	-3172.4	105.7	109.9	116.0	6.1	5.2	2
Warro 1	North	B	378471.5	6662016.4	-3741.6	108.2	112.5	130.8	18.3	5.3	
Warro 1	North	B	378471.5	6662016.4	-4383.3	121.8	126.7	147.8	21.1	6.0	
Warro 1	North	A	378471.5	6662016.4	-4354.0	117.2	117.2	147.0	29.8	2.5	
Warro 2	North	C	378248.7	6662052.2	-1495.5	62.9	65.4	75.7	10.3	4.3	
Warro 2	North	C	378248.7	6662052.2	-4070.0	116.6	121.3	139.4	18.1	7.9	
Warro 2	North	A	378248.7	6662052.2	-4133.0	127.5	127.5	141.1	13.6	2.5	
Warro 2	North	B	378248.7	6662052.2	-4275.2	115.8	120.4	144.9	24.5	5.7	
Warro 2	North	B	378248.7	6662052.2	-4853.0	138.6	144.1	160.0	15.9	6.8	
Wattle Grove 1	North	B	296344.8	6774372.4	-809.2	54.5	56.7	55.7	-1.0	2.7	1
West Erregulla 1	North	C	336098.1	6743649.6	-3206.0	118.4	123.1	118.4	-4.7	8.1	1
West Erregulla 1	North	C	336098.1	6743649.6	-4064.0	158.8	165.2	158.3	-6.9	10.8	1

Well name	Basin	Quality	Location Easting	Northing	Elevation	Temperature (°C) BHT measurement	True formation	Simulated	Residual	Standard deviation	Within SD?
West White Point 1	North	A	309828.0	6752210.6	-2241.2	98.9	98.9	93.2	-5.7	2.5	
Woodada 01	North	B	320284.0	6702528.5	-2343.0	119.3	124.1	103.9	-20.2	5.8	
Woodada 01	North	A	320284.0	6702528.5	-2357.3	117.0	117.0	104.3	-12.7	2.5	
Woodada 01	North	B	320284.0	6702528.5	-2373.0	117.6	122.3	104.8	-17.5	5.8	
Woodada 01	North	C	320284.0	6702528.5	-2538.8	120.6	125.4	109.7	-15.7	8.2	2
Woodada 02	North	B	321528.1	6702626.4	-2453.2	132.8	138.1	105.9	-32.2	6.5	
Woodada 03	North	A	321813.0	6707122.5	-2477.0	98.9	98.9	105.3	6.4	2.5	
Woodada 03	North	B	321813.0	6707122.5	-2520.3	99.3	103.3	106.6	3.3	4.9	1
Woodada 04	North	B	320688.2	6698182.9	-2269.3	113.7	118.2	101.5	-16.7	5.6	
Woodada 05	North	C	320291.4	6705086.5	-1001.5	57.8	60.1	51.8	-8.3	3.9	
Woodada 05	North	C	320291.4	6705086.5	-2310.5	113.5	118.0	103.0	-15.0	7.7	2
Woodada 05	North	B	320291.4	6705086.5	-2806.8	139.8	145.4	117.7	-27.7	6.8	
Woodada 06	North	B	320434.9	6700750.3	-2139.5	110.7	115.1	97.5	-17.6	5.4	
Woodada 06	North	B	320434.9	6700750.3	-2707.0	135.3	140.7	114.4	-26.3	6.6	
Woodada 08	North	C or B	320993.3	6695083.0	-2270.2	119.0	123.8	103.2	-20.6	8.1	
Woodda 09	North	A	322452.7	6692796.2	-2350.0	103.3	103.3	106.6	3.3	2.5	2
Woodada 10	North	C or B	319356.8	6700196.4	-2338.2	107.5	111.8	104.6	-7.2	7.3	1
Wye 1	North	C	304525.8	6777849.9	-700.8	53.5	55.6	53.1	-2.5	3.6	1
Yardarino 5	North	C or B	311475.8	6766113.6	-2548.1	117.6	122.3	104.8	-17.5	8.0	

Table 4.2: Temperature measurements and simulated values at 96 wells in the Perth Basin.

is being used to determine an optimal set of boundary conditions and rock properties that reflect previously measured values. Initial results have already shown that the basal heat flux at the base of the deep model and radiogenic heat production in the upper crust are the parameters which change simulation results most significantly when altered.

4.2.5 Conclusions

This simulation presents the first geothermal model of the entire Perth Basin in Western Australia. With nearly 50 million cells, the geology and temperature are resolved to 0.5 km horizontally and between 25 m and 1 km vertically. The detailed model extends to a depth of 16 km, and is informed by a deeper model extending below the Mohorovičić discontinuity. The model is calibrated against measured temperatures reflecting the TFT and achieves an average accuracy of -5 °C in matching the 135 measurements. Temperature is the primary geothermal resource, and the analysis of geothermal gradient and heat flow is shown to have less relevance.

The model provides an enormous resource for investigating the effects of conductive heat flow within the Perth Basin, but cannot account for possibly non-advective heat movement such as that caused by moving groundwater. For further analysis of detailed regions, the simulated model is provided online via the WAGCoE geothermal data catalogue.

4.3 Hydrothermal Model of the Perth Metropolitan Area

4.3.1 Introduction

The conductive model described in the previous section provides insight into the large-scale temperature distribution in the Perth Basin. It does not, however, account for the effects of advective and convective heat transport on the temperature distribution in the basin, and this may account for some of the discrepancies between the conductive model and temperature measurements. The potential for convective flow in the Perth Basin was highlighted in Section 3.4 of this report, which indicated that the temperature distribution could be strongly influenced by convection in areas where the Yarragadee Aquifer is thick and has high average permeability. Evidence for advective heat transport was discussed in Section 3.3. Clearly these mechanisms of heat transport play an important role and are likely to influence the distribution of temperature in the Perth Basin. However, modelling coupled heat transport and fluid flow in the entire Perth Basin (i.e. on the same scale as the conductive model) is beyond the limit of current computational capacity. Therefore we modelled heat transport and fluid flow in a small part of the basin, the PMA, utilising the new detailed geological model of the PMA developed in Project 2 (see companion report by Timms (Ed.) [2012]) to constrain the geometry of the aquifers, aquitards and faults. The location of the model is shown in Fig. 1.1B.

4.3.2 Model geometry, properties and boundary conditions

The hydrothermal model extends from the ground surface to 4.5 km below sea level, encompassing the Superficial, Leederville and Yarragadee Aquifers and ending in the top of the Cattamarra Coal Measures (Fig. 4.21). The Eastern boundary of the model represents the Darling Fault and the

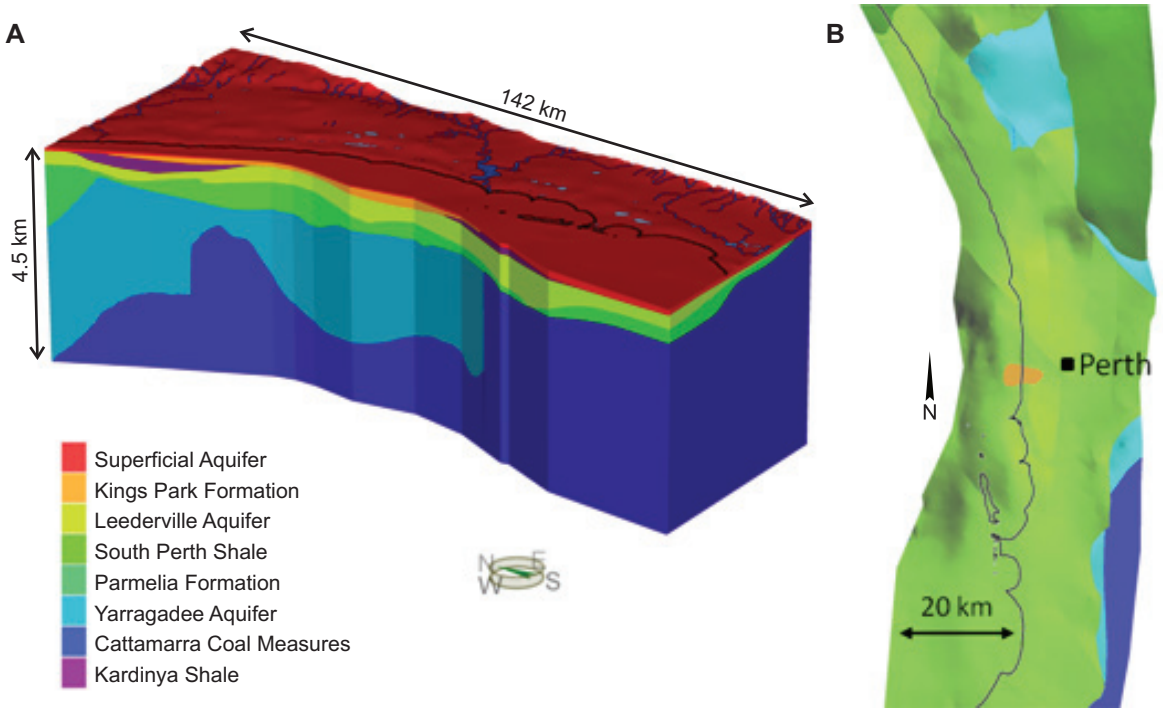

Figure 4.21: Geometry of PMA hydrothermal model. (A) 3D view. The model is 142 km long (North-South) and the base is 4.5 km below AHD. Note vertical exaggeration (x10). (B) Plan view of model with Leederville and Superficial Aquifers removed, demonstrating connectivity between Leederville and Yarragadee Aquifers. The aquifers are connected where the Yarragadee Aquifer is visible. Coastline shown for reference.

Western boundary represents the Badaminna Fault System (offshore). The geological units of the PMA model [Timms, 2012] were grouped into aquifers and aquitards. Faults were represented either as offsets in the geological layers, or as vertical low-permeability layers linking the offsets. Faults in sedimentary basins can have either higher or lower permeability than their host rocks; the assumption of low permeability in this case is supported by work conducted by WAGCoE, which showed that a fault in the North Perth Basin has lower permeability than the surrounding rocks [Olierook, 2011].

Simulations were performed using FEFLOW, a finite element modelling package which solves the equations of groundwater flow, heat and mass transport in two or three dimensions [Diersch and Kolditz, 1998]. The model domain comprises porous rocks saturated with saline pore fluid. Heat and salt are transported by advection (i.e. with the moving pore fluid) and diffusion. Fluid flow is driven by gradients in hydraulic head, which arise from variations in height of the water table, and from density gradients due to variations in temperature and salinity. Convection can occur if the buoyancy forces arising from density gradients are sufficient to overcome diffusion and viscous resistance to flow; such conditions may arise in thick, highly permeable aquifers such as the Yarragadee Aquifer.

Tables 4.3 and 4.4 list the property values used in the hydrothermal models. Fluid density was modelled using an equation of state for pure water (Magri, 2009) adjusted for salinity using the saline expansion coefficient (Table 4.3). Fluid viscosity was varied with temperature and salinity according to FEFLOW's built-in viscosity function. Permeability is the least well-constrained of all the rock properties, with measurements typically spanning several orders of magnitude even within a geological unit. The permeabilities shown in Table 4.4 are representative values for each unit based on the PRAMS calibration report (Department of Water, 2008) and permeability measurements in the PressurePlot database (www.pressureplot.com). Simulations were run with three different values of permeability in the Yarragadee aquifer (Table 4.4) to assess the impact of permeability on convection. These values fall within the range of permeabilities in the Yarragadee Formation estimated from wireline logs in the Cockburn-1 well [Timms, 2012]. Permeability was assumed to be anisotropic [Bear, 1972], with vertical permeability 10 times smaller than horizontal permeability throughout the model.

Property	Value (units)	References
Longitudinal dispersivity	5 m	Arya et al., 1988
Transverse dispersivity	0.5 m	Arya et al., 1988
Specific storage	10^{-6} m^{-1}	Turcotte and Schubert, 1982, Strategen, 2004
Specific heat capacity (rock)	850 J kg^{-1} K^{-1}	Vosteen and Schellschmidt, 2003, Waples and Waples, 2004a
Specific heat capacity (fluid)	4150 J kg^{-1} K^{-1}	Wagner et al., 2000
Thermal conductivity (fluid)	0.65 Wm^{-1} K^{-1}	Wagner et al., 2000
Saline expansion coefficient	-7.5×10^{-4} m^3 kg^{-1}	IOC et al., 2010
Diffusion coefficient of salt	4.5×10^{-9} m^2 s^{-1}	Li and Gregory, 1974, Poisson and Papaud, 1983

Table 4.3: Properties treated as constants in the hydrothermal models.

	Porosity	Horizontal hydraulic conductivity (m day^{-1})	Horizontal permeability (mD)	Thermal Conductivity (W m^{-1} K^{-1})	Radiogenic heat production (μW m^{-3})
Superficial Aquifer	0.3	10	11800	1.6	0.2
Kings Park Formation	0.1	0.1	118	1.4	0.3
Kardinya Shale	0.1	0.0001	0.118	1.4	0.6
Leederville Aquifer	0.3	1	1180	3.4	0.6
South Perth Shale	0.1	0.0001	0.118	1.8	0.8
Parmelia Formation	0.2	0.0001	0.118	3.1	0.5
Yarragadee Aquifer	0.2	0.01, 0.1, 1.0	11.8, 118, 1180	4.3	0.5
Cattamarra Coal Measures	0.1	0.0001	0.118	4.1	0.5
References:	*1*	*1, 2*		*3*	*4, 5*

Table 4.4: Properties of geological units in the hydrothermal models. Conversion from hydraulic conductivity to permeability assumes fluid viscosity = 0.001 Pa s, fluid density = 1000 kg m^{-3}. References: (1) CSIRO PressurePlot database (www.pressureplot.com); (2) PRAMS calibration report [Department of Water, 2008]; (3) Hot Dry Rocks Pty Ltd [2008]; (4) Reid et al. [2011]; (5) GSWA [2011a]

The top of the model was the topography (onshore) and sea level (offshore). The water table elevation [Department of Water, 2008] was used as the hydraulic head boundary condition except in the Gingin area, where a constant pressure boundary condition of -300 kPa was used due to insufficient detail in the water table data. Temperature was fixed at 20 °C on the top boundary and

110 °C on the bottom boundary, representing a geothermal gradient of ~20 °C/km (exact value depending on topography), which is a conservative value for the PMA [Crostella and Backhouse, 2000]. Salinity was fixed on the top boundary at 35 000 kg m^{-3} offshore (i.e. the salinity of seawater) and 0 kg m^{-3} onshore, and 15 kg m^{-3} on the bottom boundary. The sides of the model were impermeable and non-conductive to heat or salt.

4.3.3 Mesh generation and modelling workflow

The standard approach to mesh construction in FEFLOW assumes that the geological units can be represented as a series of vertically stacked layers, each layer being continuous across the model domain. A 2D mesh (usually triangular) is generated on the top surface and propagated vertically down through the layers. The mesh can be refined around features of interest e.g. wells, with the refinements being duplicated in all layers. This approach is easy to use and works well if the thickness of the layers does not vary greatly, but it breaks down if: (i) the contacts between layers are steep; or (ii) some layers are very thin or absent in parts of the model. In such cases some of the mesh elements will have extreme aspect ratios which are likely to lead to numerical instabilities and/or inaccuracies in the numerical solution, especially when modelling dynamic convecting systems. These problems can be avoided by using a regular voxel mesh, i.e. a mesh composed of orthogonal hexahedral elements. Such meshes can be generated in other software and imported into FEFLOW. The main disadvantage of using such a mesh is that sloping surfaces have a stepped form. However, this disadvantage is outweighed by the improved numerical performance on such a mesh. A further disadvantage is that very fine resolution may be required to resolve thin layers and small geometric features, thus resulting in a very large mesh which may exceed the computational capacity of FEFLOW and/or the hardware on which it is run.

To mitigate these problems in the PMA hydrothermal model, simulations were performed in 2 stages. In Stage 1, a conventional FEFLOW mesh was created from the PMA model, using the surfaces from SKUA [Timms, 2012]. The model was run in steady-state mode to obtain an approximate solution for temperature, hydraulic head and salinity in the PMA. In Stage 2, a regular voxel mesh was generated from the PMA model in SKUA, excluding everything above the top of the Leederville Aquifer. Excluding the units above the Leederville Aquifer avoided the need to resolve very thin geological layers, which would have required a very fine voxel mesh. The voxel mesh was converted to a FEFLOW FEM file using a custom-written Python script. This FEM file was read into FEFLOW, and the temperature, hydraulic head and salinity obtained in Stage 1 were applied as boundary conditions at the top of the Leederville Aquifer. The voxel mesh filled a rectangular box, therefore it had some “null” elements that were outside the actual model domain, at the top and sides of the box. Null elements at the sides of the box were deleted after reading the mesh into FEFLOW. Null elements at the top could not be deleted because FEFLOW requires all model layers to exist everywhere in the model; these null elements were effectively ignored in the simulation by assigning the top boundary condition to nodes within the model (i.e. the top of the Leederville Aquifer) and assigning low permeability to the null elements.

To check for mesh dependence the model was run on 3 different mesh resolutions: coarse, medium and fine (Table 4.5). The finest mesh was limited by memory requirements in FEFLOW and the available computational resources. Similar results were obtained on all three meshes, therefore the fine mesh was considered to provide sufficient resolution to capture the behaviour of the system. All results shown below are on the fine mesh.

Grid type	Resolution	Nodes	Layers	Cell size x,y,z (m)
Triangular FEFLOW mesh	Coarse	360824	45	irregular
Voxel (hexahedra)	Coarse	384103	100	1248 x 1440 x 47
Voxel (hexahedra)	Medium	421680	139	1578 x 1447 x 33
Voxel (hexahedra)	Fine	656040	139	1234 x 1131 x 33

Table 4.5: Mesh types and resolutions for the hydrothermal model.

Simulations were run in transient mode for a period of 109 days (2.7 million years), which was sufficient time to overcome initial transient behaviour and to establish a dynamic steady state. The geometry and properties of the model were assumed to remain constant during the simulation period. The initial transient behaviour (prior to attainment of dynamic steady state) was influenced by the initial conditions of the model and should not be interpreted as having any geological meaning. The time taken to overcome the initial transient behaviour and establish a dynamic steady state (~1 million years) may be a natural timescale of the system that has some geological significance, although it might also be influenced by the initial conditions and numerical modelling algorithms. It is instructive to consider this timescale, and the overall duration of the simulations, in the context of the geological history of the Perth Basin. The basin has behaved as a passive margin since the late Cretaceous therefore its structure and stratigraphy would have remained largely unchanged since then except the Superficial Aquifer, which is mainly Quaternary in age. The geometry, properties and boundary conditions (water table, surface temperature) of the Superficial Aquifer would undoubtedly have changed over the the past few million years, and this has not been taken into account in the simulations. However, the assumption of constant geometry and properties for the deeper units is not unreasonable.

4.3.4 Results

The simulation results show that the temperature distribution in the PMA is likely to be strongly influenced by both advection (driven by meteoric recharge) and convection, with the exact behaviour depending on the permeability of the Yarragadee Aquifer and that of the faults.

Model results are shown below on a horizontal plane that cuts through the middle of the Yarragadee aquifer. The exact depth of this plane (1171 m) has no particular significance. The temperature distribution is also illustrated by isosurfaces.

Effect of permeability in the Yarragadee

The effect of varying permeability (hydraulic conductivity) in the Yarragadee Aquifer is illustrated in Figures 4.22, 4.23 and 4.24, which show temperature and fluid flux at the end of the simulation

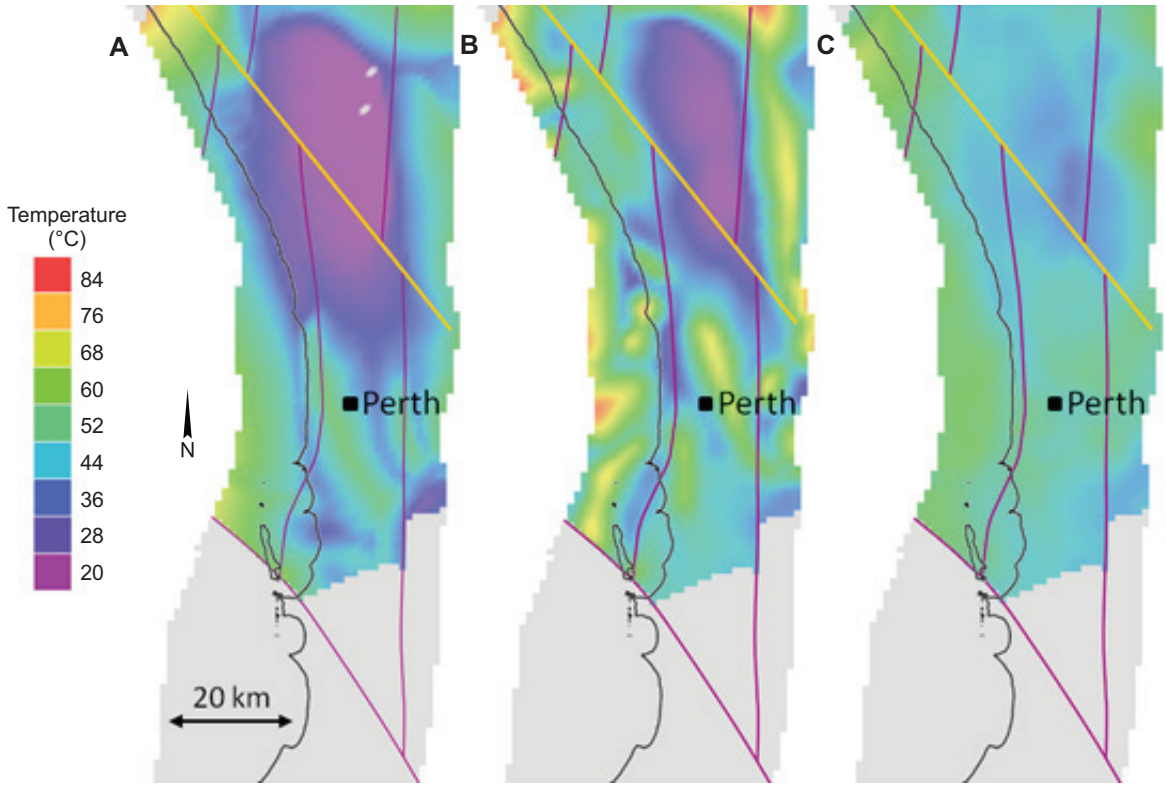

Figure 4.22: Temperature in the Yarragadee Aquifer at 1171 m depth at end of simulation. Faults modelled as offsets. Horizontal hydraulic conductivity in the Yarragadee Aquifer: (A) 1 m day^{-1}; (B) 0.1 m day^{-1}; (C) 0.01 m day^{-1}. Grey shaded area is outside the Yarragadee Aquifer. Purple and yellow lines indicate faults.

with the three different values of permeability in the Yarragadee Aquifer (Table 4-4). In the highest permeability scenario, the system is dominated by recharge from the Leederville into the Yarragadee Aquifer in the North, and in a small area in the South, creating very low temperatures there. In the intermediate permeability scenario, low temperatures due to recharge in the North are restricted to a smaller area, and convection occurs in the central part of the model below Perth. Convection is indicated by the pattern of thermal highs and lows (Fig. 4.22B) and by the alternating directions of fluid flow vectors (Fig. 4.23B). In the lowest permeability scenario, temperatures are quite uniform; there is no convection and very little advection (compare fluid flux magnitudes between the scenarios in Figure 4.23).

The competition between advection (driven by recharge) and convection causes the convection cells to migrate from North to South in the intermediate permeability scenario. This is demonstrated by fluctuations in temperature at individual points in the model (Fig. 4.25). The period of these fluctuations is ~330 000 years and their magnitude is up to 25 °C. The high permeability scenario displays small temperature fluctuations with a much shorter period; these may represent unstable or oscillatory convection behaviour, which is expected to occur at high permeabilities [Nield, 1994]. In the low permeability scenario the temperature is steady.

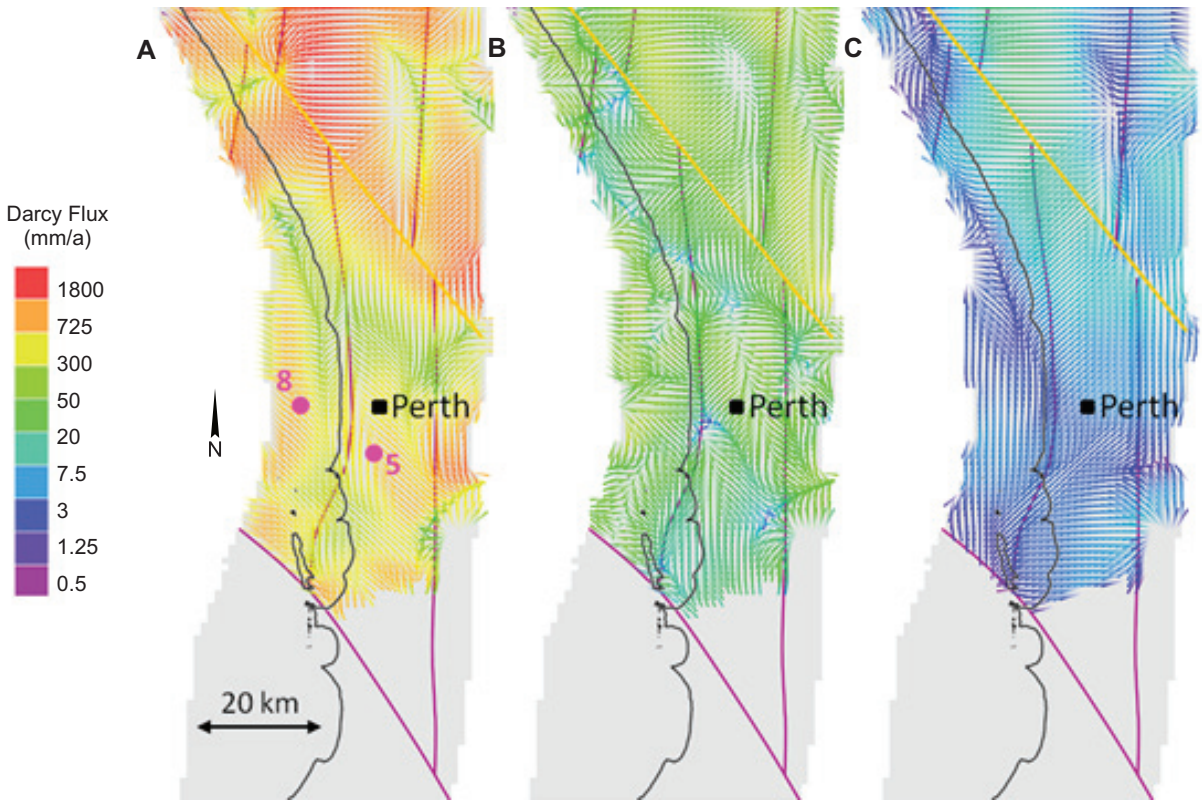

Figure 4.23: Darcy fluid flux in the Yarragadee Aquifer at 1171 m depth at end of simulation. Faults modelled as offsets. Horizontal hydraulic conductivity in the Yarragadee Aquifer: (A) 1 m day^{-1}; (B) 0.1 m day^{-1}; (C) 0.01 m day^{-1}. Grey shaded area is outside the Yarragadee Aquifer. Locations for Figure 4.25 are shown in pink. Purple and yellow lines indicate faults.

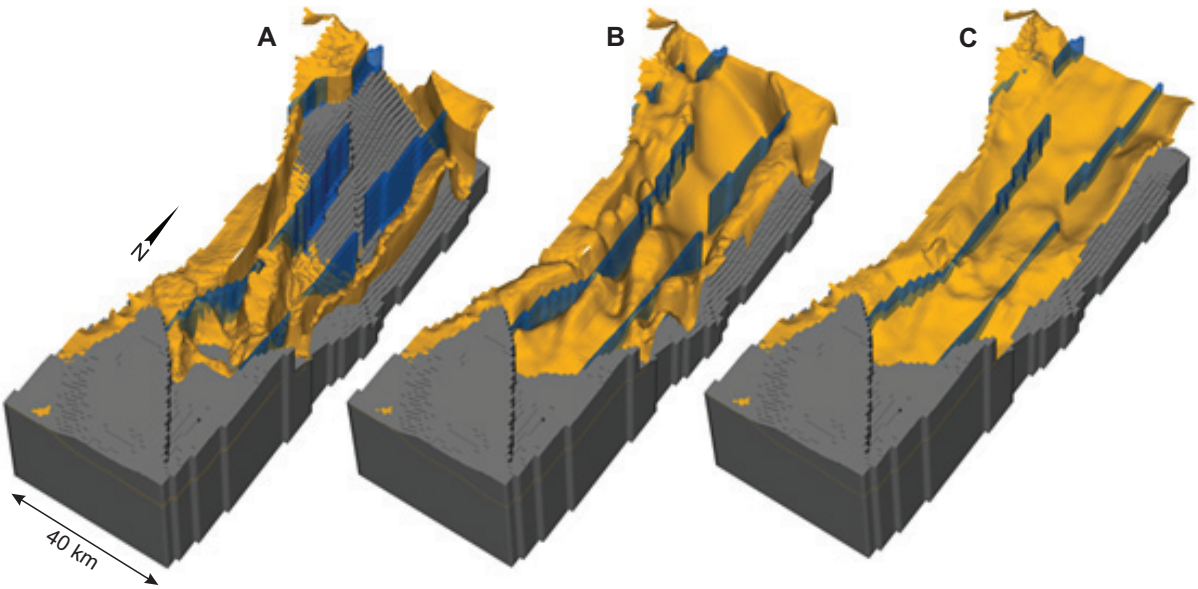

Figure 4.24: Isosurface of 45 °C temperature at end of simulation. Faults modelled as offsets (shown as shaded blue areas). Horizontal hydraulic conductivity in Yarragadee Aquifer: (A) 1 m day^{-1}; (B) 0.1 m day^{-1}; (C) 0.01 m day^{-1}. Vertical exaggeration x10.

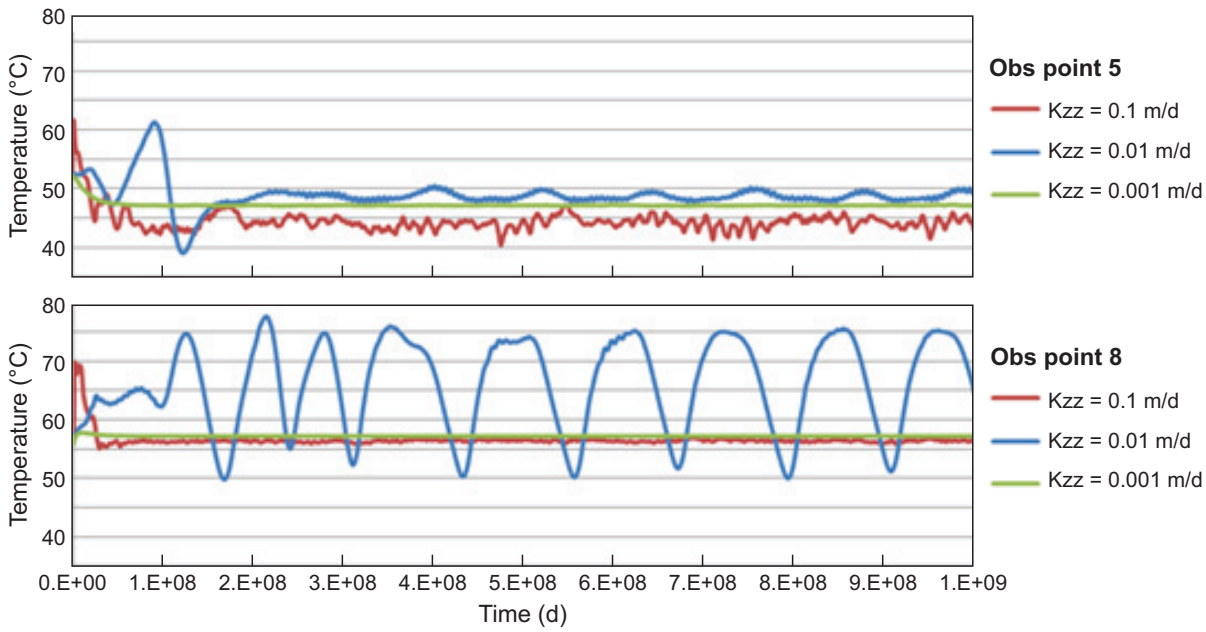

Figure 4.25: Temperature histories at two points in the model for three hydraulic conductivity values in the Yarragadee Aquifer (legend indicates vertical hydraulic conductivities). Locations 5 and 8 are shown in Figure 4.23.

Effect of faults

To assess the influence of faults on the hydrothermal system, three different fault scenarios were investigated: faults as offsets (same permeability as surrounding rocks), faults with permeability 10 times smaller than the surrounding rocks, and faults with very low permeability (effectively impermeable). The intermediate permeability value was used in the Yarragadee Aquifer. The results are shown in Figures 4.26 to 4.29.

The general pattern of low temperature due to recharge in the north and convection in the central part of the model remains the same in all fault scenarios. The offset and low-permeability fault scenarios display very similar behaviour, but the impermeable fault scenario is quite different. In the impermeable fault scenario the convection cells are bounded by the faults, with thermal highs and lows aligned adjacent to the faults (Figs. 4.26C, 4.27C and 4.28). There is also a different pattern of convection in the northeast corner of the model in this scenario, and the shape of the cold area created by recharge in the north differs from that in the other scenarios. The effect of impermeable faults is further emphasised by comparing fluid streamlines in the three fault scenarios (Fig. 4.29). Streamlines cross the faults in the offset and low permeability faults scenarios, but are channelled between the faults in the impermeable fault scenario. Note also the sharp change in hydraulic head across the North-South trending faults in the impermeable fault scenario, which is not seen in the other fault scenarios (Fig. 4.29).

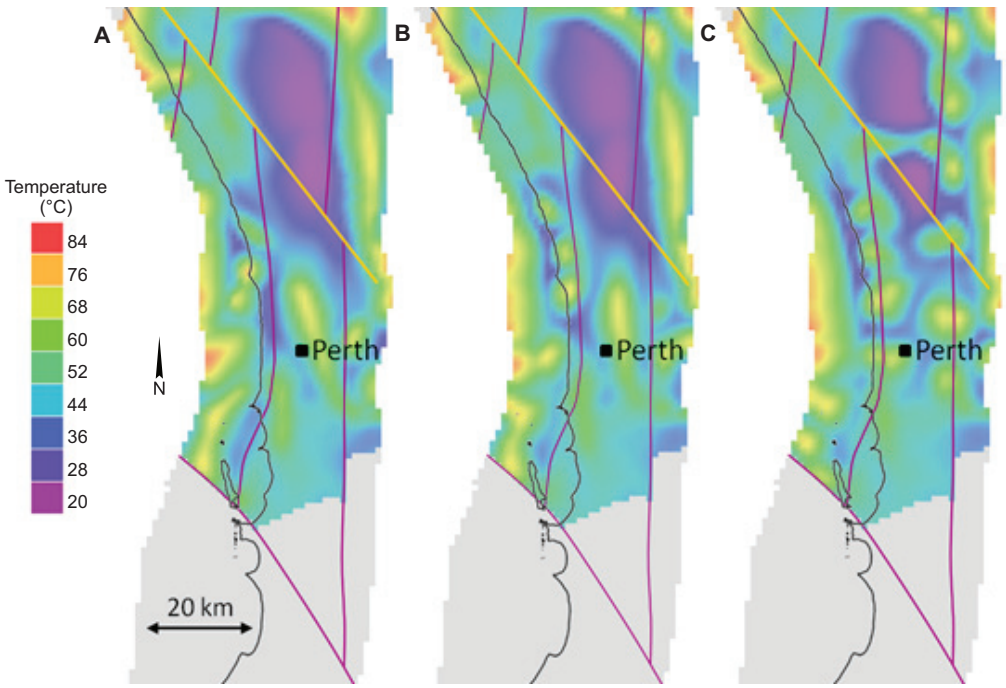

Figure 4.26: Temperature in the Yarragadee Aquifer at 1171 m depth at end of simulation. Horizontal hydraulic conductivity in the Yarragadee Aquifer = 0.1 m day^{-1}. (A) Faults as offsets. (B) Low permeability faults. (C) Impermeable faults. Grey shaded area is outside the Yarragadee Aquifer. Purple and yellow lines indicate faults; the yellow fault was always modelled as an offset.

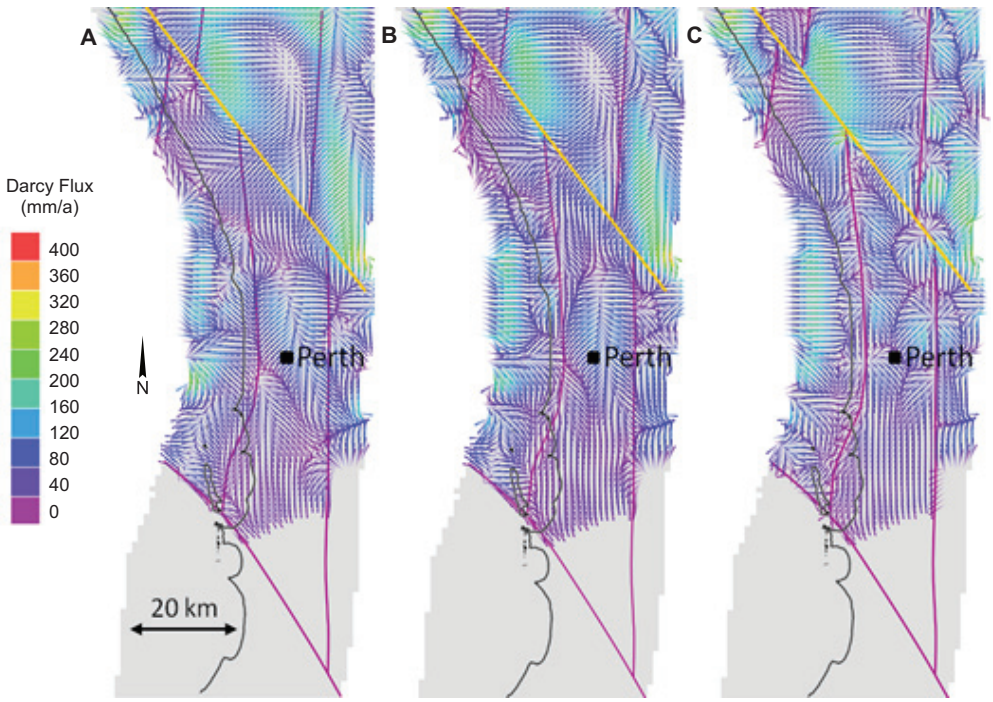

Figure 4.27: Darcy fluid flux in the Yarragadee Aquifer at 1171 m depth at end of simulation. Horizontal hydraulic conductivity in the Yarragadee Aquifer = 0.1 m day^{-1}. (A) Faults as offsets. (B) Low permeability faults. (C) Impermeable faults. Grey shaded area is outside the Yarragadee Aquifer. Purple and yellow lines indicate faults; the yellow fault was always modelled as an offset.

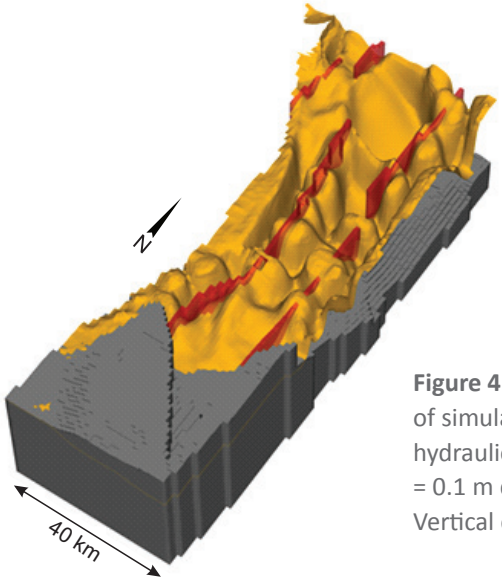

Figure 4.28: Isosurface of 45 °C temperature at end of simulation, impermeable fault scenario. Horizontal hydraulic conductivity in the Yarragadee Aquifer = 0.1 m day^{-1}. Faults shown as red shaded areas. Vertical exaggeration x10.

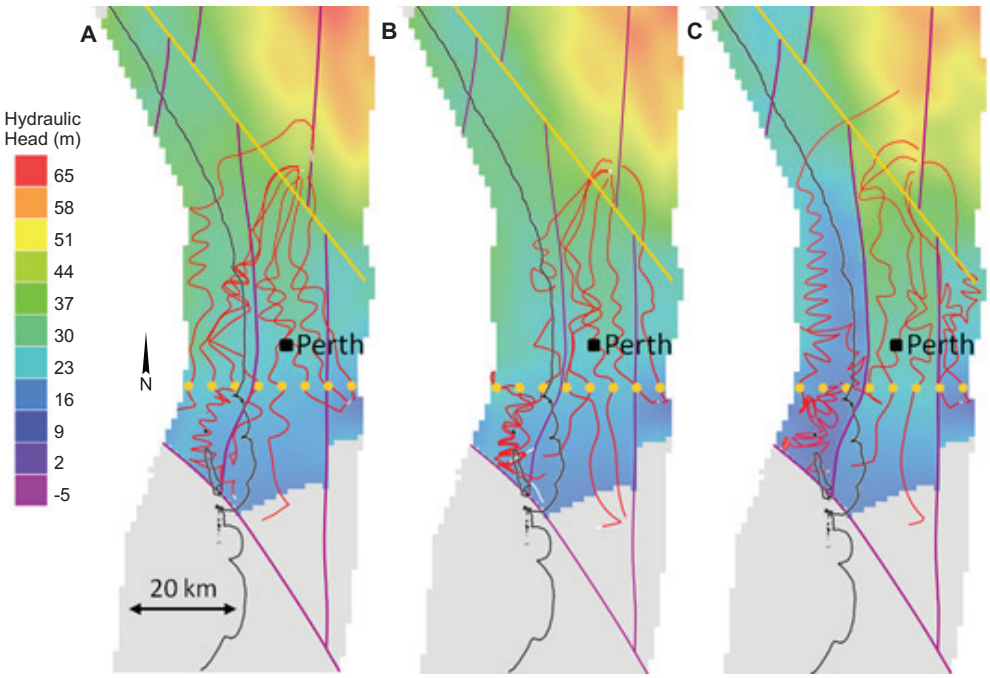

Figure 4.29: Fluid streamlines superimposed on hydraulic head [m] in the Yarragadee Aquifer at 1171 m depth at end of simulation. Streamlines calculated forwards and backwards from an East-West line of points (yellow dots) across the middle of the Yarragadee Aquifer. Horizontal hydraulic conductivity in the Yarragadee Aquifer = 0.1 m day^{-1}. (A) Faults as offsets. (B) Low permeability faults. (C) Impermeable faults. Grey shaded area is outside the Yarragadee Aquifer. Purple and yellow lines indicate faults; the yellow fault was always modelled as an offset.

4.3.5 Discussion

The hydrothermal model of the PMA shows that the behaviour of the system is critically dependent on permeability in the Yarragadee Aquifer. Importantly, significant convection occurs only at the intermediate permeability value of the three values that were tested. It does not occur at lower permeability, because the Rayleigh number is sub-critical (see Section 3.4 for discussion of Rayleigh number in the Yarragadee Aquifer), and it does not occur at high permeability because the system is dominated by advection driven by recharge from the Leederville Aquifer. Thus, constraining the true permeability of the Yarragadee Aquifer is critical to understanding the hydrothermal regime. The intermediate permeability is arguably the most representative value based on the permeability-depth profile obtained from wireline logs [Timms, 2012]. However, it is questionable whether using a constant, average permeability is reasonable in a system where permeability varies considerably both laterally and horizontally. Simulating heat transport and fluid flow in more realistic permeability distributions is an important avenue for future work.

If convection does occur, the simulations predict that it will be focused in the central part of the model, i.e. directly beneath Perth and offshore to the West. Temperatures of ~75 °C are attained in the convective upwellings at 1.1 km depth, representing a much more viable geothermal resource than the non-convecting scenarios. Predicting the locations of these thermal highs at the present day is difficult because they move with time. However, the rate of migration is very slow relative to human timescales (period ~330 000 years), therefore if a convective upwelling can be found it is unlikely to move significantly within the timeframe of a geothermal utilisation project.

It is clear from these simulation results that purely conductive models cannot be used to make accurate predictions about subsurface temperature in the PMA, or indeed anywhere with high-permeability aquifers that can support significant advection or convection. This is an important conclusion for research into HSA geothermal systems.

The effect of faults on the hydrothermal system depends on their permeability relative to the host rocks. Making the permeability of the faults one order of magnitude smaller than their host rocks had relatively little effect on the results, but assigning a very low permeability to the faults (making them effectively impermeable) influenced the behaviour significantly, effectively pinning the location of convection cells. The concept of convection cells bounded by impermeable faults has been suggested previously for the Taupo geothermal system in New Zealand [Rowland and Sibson, 2004].

The effect of impermeable faults on hydraulic head (Fig. 4.29C) is interesting because this could explain the mismatch between the PRAMS groundwater model and hydraulic head measurements. The PRAMS model has been calibrated to match hydraulic head measurements in most wells in the PMA, however some wells could not be matched [Department of Water, 2008]. This could be due to previously unrecognised faults, which are not included in the PRAMS model, acting as barriers to fluid flow and thus influencing the hydraulic head on either side. The hydrothermal model presented here does not simulate the shallow parts of the PMA (i.e. those parts covered by PRAMS) in detail and thus cannot be directly calibrated against shallow groundwater wells. However, the results do show that hydraulic head can be significantly different either side of an impermeable fault (Fig. 4.29C). A

map of the mismatch between measured hydraulic head and the hydraulic head predicted by PRAMS [Department of Water, 2008] shows a change from positive to negative mismatch across the two North-South trending faults of our model, suggesting that there may be a steep gradient in head across those faults as predicted by our simulations. Therefore the inclusion of these faults in PRAMS may potentially help to reduce the mismatch between PRAMS and well measurements.

The voxel mesh used in the hydrothermal models is not ideally suited to representing narrow features such as faults. The width of the faults in the models was imposed by the horizontal mesh resolution (1.1-1.5 km). This is probably one to two orders of magnitude wider than the true width of fault zones in the PMA [e.g. Mooney et al., 2007]. The width of faults in the model is unlikely to influence their hydraulic effect (i.e. acting as barriers to flow), but it does influence their thermal effect. For example, if a convective upwelling occurs immediately adjacent to a fault, its effect on temperature on the other side of the fault is influenced by the fault width, because the width influences the time for heat to be transferred across the fault by conduction. Whether this effect is important on the timescale of the models is unclear and requires further assessment.

4.3.6 Conclusions

Heat transport and fluid flow were simulated in the PMA, using a new geological model created by WAGCoE to constrain the geometry of aquifers, aquitards and faults. The simulations show that convection and advection may have a strong influence on the distribution of heat in the subsurface, therefore these processes must be considered when making predictions about geothermal resources. It was shown that convection could be occurring beneath Perth and directly offshore, depending on the effective large-scale permeability in the Yarragadee Aquifer, and that faults can affect the heat flow behaviour significantly if they have very low permeability. Convection creates local thermal highs that may be useful as geothermal resources. These convective upwellings are stationary on a human timescale, but their location is difficult to predict because they move over geological time. Future work should focus on constraining the 3D permeability distribution in the Yarragadee Aquifer, and exploring the effect of this heterogeneous permeability on convection.

5. COMPUTATIONAL METHODS FOR INVESTIGATING HYDROTHERMAL RESOURCES

The previous results represent the state-of-the-art in applications of hydrothermal modelling in Western Australia. They stem from a close collaboration between geologists, engineers, and computer scientists. In this section, we present some of the tools behind these results and indicate how research into this area allows deeper understanding of the physical processes affecting geothermal.

In Section 5.1, the numerical model *escriptRT* is introduced. This reactive transport model is significantly based on thermodynamical principles, which allows a more precise coordination between the subsurface fluid and rock phases. The equilibrium states of the fluid and the rock properties are defined with multiple equations of states and derived from databases of fundamental mineral properties. The flexible nature of the coding in Python, and the open-source nature, allows the easy addition of new computational and analysis tools. Analytical and computational benchmarks for *escriptRT* are presented here for the first time.

Section 5.2 presents an extension of *escriptRT* to include not only thermal-hydrologic- and chemical-coupling, but also mechanical deformation. This combined "THMC" formulation is extremely useful for analysing fundamental problems in geothermics, such as the deformation of rocks caused by hydro-fracturing in enhanced geothermal systems.

Finally, Section 5.3 presents a novel methodology for examining measures of uncertainty in both geological models and in the resulting hydrothermal models. The methods are enabled by the use of flexible workflow approach for automatically generating models. The integration of these techniques can lead to much better consideration of risk in geothermal exploration.

5.1 Thermodynamic Reactive Transport Simulations: *escriptRT*

This section was published as [Poulet et al., 2011a] and presents *escriptRT*, a new Reactive Transport simulation code for fully saturated porous media which is based on a finite element method (FEM) combined with three other components: (i) a Gibbs free energy minimisation solver for equilibrium modelling of fluid–rock interactions, (ii) an equation of state for pure water to calculate fluid properties and (iii) a thermodynamically consistent material database to determine rock material properties.

5.1.1 Introduction

Transport of heat and chemical species in porous media is a critical component in understanding many geological processes such as convection, precipitation and dissolution of minerals, which can be applied to geothermal systems or the formation of ore deposits. There already exist some good descriptions and robust codes to address this class of problems [e.g. Pruess et al., 1999, Bartels et al., 2003, Diersch, 2005, Geiger et al., 2006, Ingebritsen et al., 2006]. It is usually no trivial task, however, for researchers to modify or extend these codes as those developments require a full set of different skills, from a deep geo-scientific knowledge to a high proficiency in software development

and numerical analysis. The task can be even more daunting as the code gets more sophisticated and the changes required need to be compliant with all underlying software and hardware architecture choices. Object Oriented Programming is fortunately increasingly used and facilitates the researcher's work but none of the mentioned codes satisfy for example the full separation of concerns (SoC) paradigm [Hürsch and Lopes, 1995] in order to let the expert user focus on geosciences only.

The escript module [Gross et al., 2008] provides a generic environment for modellers to develop simulations solving partial differential equations (PDE) using the Python programming language. Its numerical solver can run in parallel and also offers the ability to work on unstructured 2D and 3D meshes, which enables one to model complex and geologically realistic structures for example. This modelling library is separated by design from the underlying solver and provides with its modelframe approach an ideal modularity which is key to *escriptRT*'s architecture. The development of *escriptRT* was indeed motivated by the need of a powerful but also user-friendly, flexible, and extensible platform.

The purpose of this code is to allow geologists with different levels of numerical skills to focus on the definition of their problem at a geoscientific level, with the possibility to interact with the code at different levels but with no attendant obligation to become experts in applied mathematics and numerical programming.

This section is articulated in three parts and presents (i) the classical system of equations describing all geological processes considered, (ii) all solvers within our code dealing with those equations, and (iii) some benchmarks to validate the code.

5.1.2 Reactive transport formulation

The *escriptRT* code models the transport of heat and solutes in porous media, as well as the chemical reactions between the fluid and the host rock. The physical formulation of the problem is based on the assumption that we are dealing with a porous medium fully saturated with a single phase fluid, for which Darcy's law applies [Bear, 1979]. We assume that the fluid and hosting rock are always in thermodynamic and chemical equilibrium. Following the finite element methodology we consider a representative volume element Ω of rock and decompose it as a sum of its solid and porous components.

In this sub-section we are presenting the formulation of *escriptRT*, which solves sequentially a set of decoupled governing equations. We describe consecutively all process models involved, which employ direct couplings and indirect feedbacks [Poulet et al., 2010b]. We define a direct coupling to be the proper handling of the dynamical updates of all variables involved in the solved system of equations. We refer by indirect feedback to the sequential update of selected variables in some of the equations, while their time evolution is neglected in others.

Pressure equation

All processes simulated by *escriptRT* are based on a description of fluid flow in saturated porous media. The pore pressure equation follows from the fluid mass conservation and can be written as

$$\beta_r \phi \rho_f \frac{dp}{dt} - \underline{\nabla}.\left(\rho_f \frac{k}{\mu_f} \underline{\nabla} p\right) = -\nabla.\left(\rho_f^2 \frac{k}{\mu_f} \underline{g}\right) + \alpha_f \phi \rho_f \frac{dT}{dt} - \gamma_f \phi \rho_f \frac{dX}{dt} \qquad 5.1\text{-}1$$

where α_f is the thermal expansivity, β_f the compressibility, γ_f the chemical expansivity, φ the porosity, ρ_f the fluid density, p the pore pressure, T the temperature, t the time, k the thermal conductivity, μ_f the fluid density, and g the gravity vector. See Poulet et al. [2011a] for details of the derivations.

Temperature equation

We assume thermal equilibrium between the solid and liquid components of the medium. We neglect the effects of mechanical deformation (which will be considered later in Section 5.2) and the related thermal expansion of the solid part of the system. In respect to the liquid component we also neglect any heating due to viscous dissipation. The temperature is then transported via the standard advection diffusion equation [Nield and Bejan, 2006]:

$$\overline{\rho\, C_p} \frac{\partial T}{\partial t} + \left(\rho C_p\right)_f \underline{u}.\underline{\nabla} T - \underline{\nabla}.\left(\bar{D} \underline{\nabla} T\right) = Q \qquad 5.1\text{-}2$$

where u is the relative velocity of the fluid with respect to the solid, Q is a radiogenic heat source, $\overline{\rho\, C_p} = \phi(\rho C_p)_f + (1-\phi)(\rho C_p)_s$ and $\bar{D} = \phi D_f + (1-\phi) D_s$ is the averaged rock diffusion coefficient.

Transport of chemical elements

In the mass transport model we regard the fluid as being composed of a set of chemical species in the aqueous phase. Those species are transported with the fluid and we consider them to be in chemical equilibrium with the solid minerals of the surrounding rock matrix at the end of every discrete time step. These assumptions allow the transport problem to be solved for a limited set of reaction invariants instead of the full set of chemical species. This approach is similar to the concepts of “tenads” introduced by Rubin [1983], as well as the tableaux defined by Morel [1983]. We use as dependent variables the masses of chemical elements constituting the chemical species, as well as the total electrical charge of the species. The achieved reductions of the size of the system and the computations in total are considerable. For example, a typical simulation would involve tens of chemical elements but hundreds of chemical species, and therefore the codes transporting chemical species would solve much larger systems of PDEs.

Another advantage of using the masses of chemical element as dependent variables is the improved numerical stability of the system of transport equations. Indeed, when the full list of chemical species is treated as dependent variables, intensive precipitation/dissolution of minerals can cause appearances and disappearances of some species according to local conditions, resulting in pulses of zero/non-zero masses. This can cause numerical difficulties to the solver and requires special attention [Guimarães et al., 2007]. This issue is generally not present when transporting chemical elements.

The advection-diffusion of chemical elements considered as

$$\phi \frac{\partial C_i}{\partial t} + \phi \underline{u}.\underline{\nabla} C_i - \vec{\nabla}.\left(\phi \underline{\underline{D}}.\underline{\nabla} C_i\right) = 0 \qquad 5.1\text{-}3$$

where C_i is the molarity of the ith chemical element in liquid phase in the system. The dispersion tensor D) accounts for molecular diffusion, longitudinal and transverse dispersions, but not for tortuosity which we neglect. We also assume that all chemical elements in liquid phase disperse in the same way.

After this transport step, chemical equilibrium is computed from the current composition, temperature and pore pressure using a Gibbs free energy minimisation solver presented in the next subsection.

5.1.3 Reactive transport solvers

This subsection presents the various solvers used to solve the constitutive equations presented in Section 5.1.2 .

The Finley solver

All PDEs are solved using the escript modelling library and its Finley solver [Davies et al., 2004], which solves a PDE given in weak form. For the case of a scalar unknown solution u the weak form is

$$\int_\Omega \left(\mathrm{Mv}\frac{\partial \mathrm{u}}{\partial \mathrm{t}} + \underline{\nabla}\mathrm{v}.\underline{\underline{\mathrm{A}}}.\underline{\nabla}\mathrm{u} + \underline{\nabla}\mathrm{v}.\underline{\mathrm{B}}\mathrm{u} + \mathrm{v}\underline{\mathrm{C}}.\underline{\nabla}\mathrm{u} + \mathrm{vDu}\right)\mathrm{d}\Omega = \int_\Omega \left(\underline{\nabla}.\underline{\mathrm{X}} + \mathrm{vY}\right)\mathrm{d}\Omega \qquad 5.1\text{-}4$$

which needs to be fulfilled for all so-called test functions v. To simplify the presentation, boundary conditions are ignored. It is assumed that this equation is solved for a sufficiently small time interval such that it can be assumed that the PDE coefficients M, A), B, C, D, X and Y are constant in time and are independent from the unknown solution u. In order to support the usage of compute clusters and multi-core architectures, Finley is parallelised for both shared and distributed memory using element and node colouring on shared memory via OpenMP and domain decomposition on distributed memory via the Message Passing Interface (MPI) library.

The GibbsLib solver for chemical equilibrium

Chemical equilibrium of the mass composition is solved using a Gibbs free energy minimization technique at prescribed temperature and pressure. It includes the masses of the chemical elements and water (so called bulk composition), which were computed during the transport step (see Section 5.1.2). The chemical species existing at equilibrium are found using the WinGibbs solver [Shvarov, 1978] (via WinGibbs.dll), which is the solver used within the HCh geochemical modelling package [Shvarov and Bastrakov, 1999].

The equation of state (EOS) solver for fluid properties

EscriptRT currently handles a single phase flow, and as a starting point of its fluid EOS we selected three different models for pure water: the IAPWS-95 [Wagner and Prüß, 2002], IAPWS-97 [Wagner

et al., 2000] and revised HKF model [Helgeson et al., 1981, Shock et al., 1992, Tanger and Helgeson, 1988]. The HKF model EOS provides thermodynamic consistency with WinGibbs. The fluid EOS module of *escriptRT* is critical to the modelling accuracy obtained. For example fluid density is the main driver for convection [Nield and Bejan, 2006]. The water density EOS covers a wide range from 0 to 1,000 °C and 0 to 5,000 bar. Other water properties are defined on narrower ranges, but nevertheless are sufficient to define the general conditions of many geological scenarios with a single liquid phase.

The PREMDB database for rock properties

Solid material properties are calculated in a similar way to fluid properties and are considered as dependent on temperature and pressure. We are using PreMDB [Siret et al., 2008] for that purpose, which is a thermodynamically consistent material database based on thermodynamic potential functions to calculate all reversible material properties. Our code allows the solid density ρ_s, specific heat $C_{(p,s)}$ and thermal conductivity k_s to be interpolated from tabulated values for temperature and pressure. PreMDB also employs various published empirical relationships, which are especially useful to compute thermal conductivity.

5.1.4 Computer platforms compatibility

The solvers presented in this section are available on all computer platforms, except for the chemical solver which only runs on Windows. As a result, *escriptRT* can be used on all machines we have available within WAGCoE, including the large clusters provided by CSIRO and iVEC. The escript library has been developed with parallelism in mind and scalability tests were performed and presented for example by the developers team in [Gross et al., 2010]. Those tests show that escript scales reasonably well up to 1 000 processors, and more tests are currently being run on larger clusters to test the limits further. Those tests also include some analysis specific to the hardware used to perform the simulations. Figure 5.1 shows an example of a scalability benchmark run on a cluster at the University of Queensland in 2010 to identify the impact of the number of processes per node up to 128 cores.

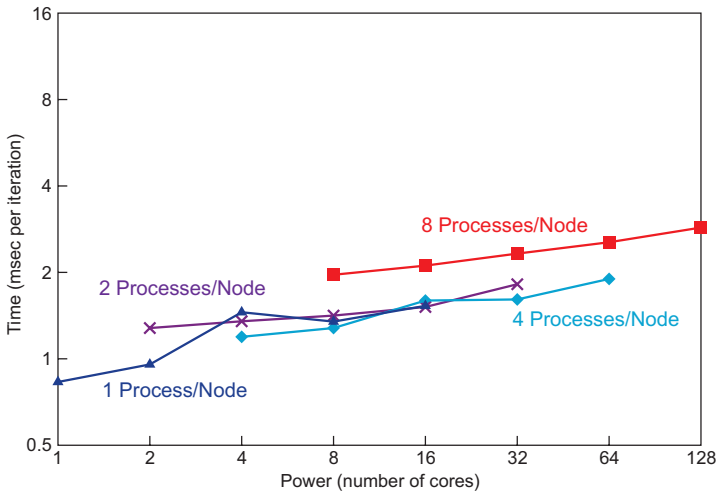

Figure 5.1: Scalability test of escript library. Elapsed Time per Iteration Step with different numbers of MPI ranks on Rackable C1001-TY3 cluster with about 15000 unknowns per rank. Figure from Gross et al. [2010].

While the usage of the chemical solver is limiting the code to run on Windows platforms, the inherent nature of individual chemical updates at mesh nodes makes it an ideal candidate for parallelisation.

An *escriptRT* simulation including chemical reactions run in parallel on the CSIRO/iVEC Windows Cluster was presented in Poulet et al. [2011a].

5.1.5 Benchmarks

This section presents several benchmarks to validate the heat and mass transport algorithms of the *escriptRT* code. The benchmark problems are of 3 types:

- Problems for which an analytical solution exists, such that the accuracy of the numerical solution can be assessed by comparison with the analytical solution;
- Problems for which there is no analytical solution, which can be validated by comparison with other numerical codes;
- A geologically realistic problem to demonstrate the ability of the code to simulate large 3D scenarios relevant to geothermal exploration.

The benchmarks are as follows:

1. 1D conductive heat transport with source term, steady state solution
2. 1D diffusive tracer transport, steady state solution
3. 1D advective-conductive heat transport, steady state solution
4. 1D advective-diffusive tracer transport, steady state solution
5. 1D advective-conductive heat transport, transient
6. 1D advective-diffusive tracer transport, transient
7. Onset of free thermal convection (2D)
8. Elder problem (2D)
9. Convection with anisotropic permeability (2D)
10. 3D Convection with layered permeability

Benchmarks 1 to 6 are of Type 1 and concern one-dimensional transport of heat or mass (e.g. salt) through a porous medium. The equations describing advective-diffusive transport of heat and mass

$$\frac{\partial X}{\partial t} = -\mathbf{v} \cdot \nabla X + \nabla \cdot (D \nabla X) + A \qquad 5.1\text{-}5$$

are specific cases of the general advection-diffusion equation for a conserved quantity, X:

where v is the transport velocity, D the diffusion coefficient and A the source term. These terms are

$$\mathbf{v}_{heat} = \rho_f c_f \mathbf{u} / (\rho c)_m, \quad D_{heat} = \lambda / (\rho c)_m, \; A_{heat} = Q \qquad 5.1\text{-}6a$$

$$\mathbf{v}_{tracer} = \mathbf{u} / \phi, \quad D_{tracer} = D_f, \; A_{tracer} = 0 \qquad 5.1\text{-}6b$$

defined as follows for heat (X = T) and mass (X = C) transport:

See Table 5.1 for nomenclature. Analytical solutions exist for the one-dimensional form of Equation 5.1-5 under steady state (dX/dt = 0) and transient conditions (dX/dt ≠ 0); these are compared with the corresponding numerical solutions in Benchmarks 1 to 6 below.

The remaining benchmarks verify that the code can simulate density-driven flow (convection), which is important for investigating geothermal systems.

Symbol	Definition (units)	Symbol	Definition (units)
A	Rate of production of X (X s^{-1})	T	Temperature (°C)
c_f, c_s	Specific heat capacity of fluid and solid (J kg^{-1} K^{-1})	T_0, T_H	Temperature at *z* = 0 and *z* = H (°C)
C	Concentration of tracer in pore fluid (kg m^{-3})	u	Darcy fluid flux (m^3 m^{-2} s^{-1})
C_0, C_H	Concentration at *z* = 0 and *z* = H	v	Magnitude of v (m s^{-1})
D	Diffusion coefficient of X (m^2 s^{-1})	v	Transport velocity of X (m s^{-1})
D_f	Molecular diffusion coefficient of tracer in pore fluid (m^2/s)	x, y, z	Cartesian coordinate axes (z positive upwards) (m)
E	Global error	X	A conserved quantity
g	Gravity (m/s^2)	α	Courant overstep
h	Size of finite elements in flow direction (m)	α_z	Wavenumber of free thermal convection
H	Height of model (m)	β	Volumetric thermal expansion coefficient of pore fluid (1/°C)
k	Permeability (m^2)	$\Delta\tau$	Timestep (s)
L	Length of model (m)	ϕ	Porosity
P	Fluid pressure (Pa)	γ	Density factor (dense fluid tracer)
Pe, Pe_{local}	Global and local Peclet numbers (Pe_{local} = Pe h/H)	λ	Effective thermal conductivity of porous medium (W m^{-1} K^{-1})
q	Conductive heat flux at z = 0 (W m^{-2})	λ_ϕ, λ_σ	Thermal conductivity of fluid and solid (W m^{-1} K^{-1})
Q	Rate of heat production (W m^{-3})	μ	Fluid viscosity (Pa s)
Ra, Ra_c	Rayleigh number, minimum critical Rayleigh number	ρ_ϕ,ρ_σ	Density of fluid and solid (kg m^{-3})
t	Time (s)	ρ_0	Reference fluid density at T = T0 (kg m^{-3})
t'	Dimensionless time		

Table 5.1: Nomenclature for escriptRT benchmarks.

Benchmark 1: 1D conductive heat transport with source term, steady state solution

This test concerns the steady-state distribution of temperature in a vertical column of height H, with u = 0 (i.e. diffusive heat transport only) and uniform heat production Q, subject to fixed temperature TH at the top of the column (z = H), and either fixed temperature T_0 or fixed heat flux q at the base of the column (z = 0). The steady-state solutions for these boundary conditions are as follows [Turcotte and Schubert, 1982]:

$$T = T_H + \frac{Q}{2\lambda}\left(H^2 - z^2\right) - \frac{q}{\lambda}\left(H - z\right) \qquad 5.1\text{-}7a$$

$$T = T_H + \frac{Q}{2\lambda}\left(Hz - z^2\right) + \left(T_0 - T_H\right)\left(1 - \frac{z}{H}\right) \qquad 5.1\text{-}7a$$

The numerical solution was compared with the corresponding analytical solution for a range of values of Q, λ, H, q and T_0. Tests were run on a variety of meshes, comprising rectangular or triangular elements (2D), and hexahedral or tetrahedral elements (3D). The numerical model was initialised with uniform temperature TH and was run for sufficient time to reach steady-state.

All combinations of meshes and parameter values reproduced the analytical solution with a very high degree of accuracy. This is illustrated in Figure 5.2, which shows that the analytical and numerical solutions are indistinguishable in two scenarios on an unstructured triangle mesh.

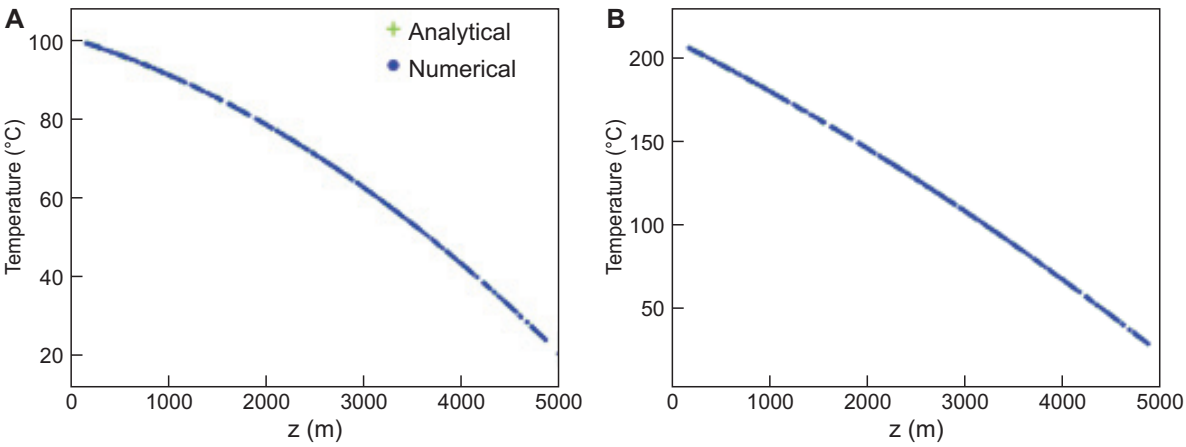

Figure 5.2: Steady-state analytical and numerical solutions for 1D conductive heat transport on an unstructured triangle mesh. H = 5000 m, Q = 10-5 W m^{-3}, λ = 3 W m^{-1} K^{-1}. (A) Fixed temperature at base (T_0 = 100 °C). (B) Fixed heat flux at base (q = 0.09 W m^{-2}).

Benchmark 2: 1D diffusive tracer transport, steady state solution

The steady-state analytical solution for diffusive tracer transport in a vertical column of height H, with fixed tracer concentration C_0 at z = 0 and C_H at z = H, is simply a linear variation in C with depth:

$$C = C_H + (C_0 - C_H)\left(1 - \frac{z}{H}\right) \qquad 5.1\text{-}8$$

The numerical solution was compared with the analytical solution for a range of values of D_f, H, and C_0, on the same meshes as were used for Benchmark 1.

All combinations of meshes and parameter values reproduced the analytical solution with a very high degree of accuracy. This is illustrated in Figure 5.3, which shows that the analytical and numerical solutions are indistinguishable on an unstructured triangle mesh.

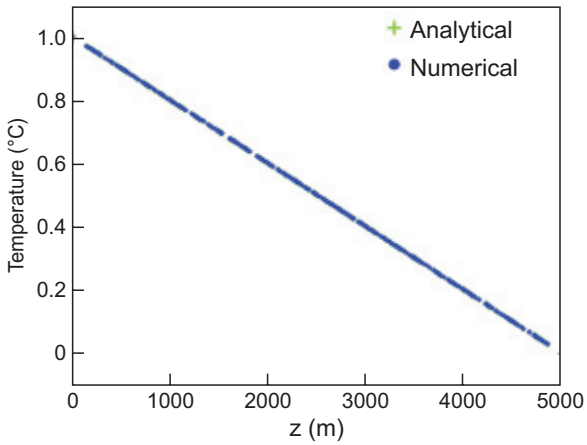

Figure 5.3: Steady-state analytical and numerical solutions for 1D diffusive tracer transport on an unstructured triangle mesh. H = 5000 m, D_f = 10^{-8} m^2 s^{-1}, C_0 = 1 kg m^{-3}.

Benchmark 3: 1D advective-conductive heat transport, steady state solution

The steady-state solution for temperature in a vertical column subject to uniform upward throughflow (u_z = constant; u_x = u_y = 0) and no heat production (Q = 0), with fixed temperature T_H and fixed fluid pressure P_H at the top boundary (z = H) and fixed temperature T_0 at the base (z = 0), is:

$$T = T_H + (T_0 - T_H)\frac{1 - e^{Pe(z/H - 1)}}{1 - e^{-Pe}} \qquad 5.1\text{-}9a$$

where

$$Pe = \frac{\rho_f c_f u_z H}{\lambda} \qquad 5.1\text{-}9b$$

For the case of fixed conductive heat flux (q) on the lower boundary, the solution is:

$$T = T_H - \frac{qH}{Pe\lambda}\left(e^{Pe} - e^{Pe(z/H)}\right) \qquad 5.1\text{-}9c$$

[Zhao et al., 1999]. The dimensionless parameter Pe is the global Peclet number, which indicates the relative importance of advection and conduction over distance H. We also define the local Peclet number, $Pe_{local} = Pe\Delta z/H$, which indicates the relative importance of advection and conduction over the length of a single finite element in the direction of flow (Δz).

The numerical solutions for the fixed temperature and fixed heat flux boundary conditions were compared with the corresponding analytical solutions. Models were initialised with uniform temperature T_H and were run for sufficient time to reach steady state. Different values of Pe were obtained by varying uz while keeping ρ_f, c_f and λ constant. The local Peclet number was varied for a given Pe by varying the mesh density (20 or 200 elements in the flow direction).

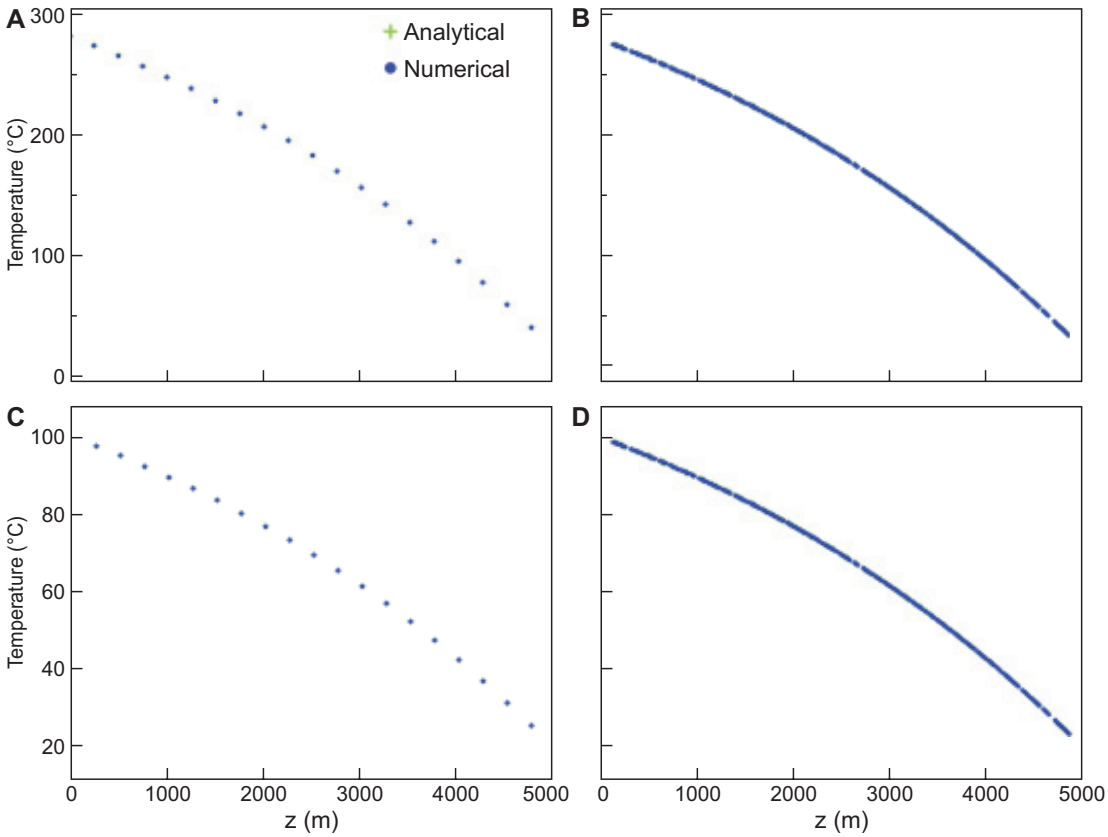

Figure 5.4: Numerical and analytical solutions for steady-state advective-conductive heat transport with Pe = 1, H = 5000 m, λ = 3 W m^{-1} K^{-1}. (A) Structured triangle mesh, fixed heat flux at base (q = 0.09 W m^{-2}). (B) (A) Unstructured triangle mesh, fixed heat flux at base (q = 0.09 W m^{-2}). (C) Structured triangle mesh, fixed temperature at base (T_0 = 100 °C). (D) Unstructured triangle mesh, fixed temperature at base (T_0 = 100 °C).

The analytical solution was reproduced with a very high degree of accuracy in scenarios with Pe = 1 (Fig. 5.4). Accuracy decreased with increasing Pe; this is illustrated in Figure 5.5, which shows the numerical and analytical solutions on coarse (top) and fine (bottom) meshes with the global Peclet number increasing from left to right. High Pe scenarios are characterized by a sharp drop in temperature near the top boundary, which cannot be resolved on the coarse mesh (Δz = 250; Fig. 5.5C) but is reproduced with reasonable accuracy on the fine mesh (Δz = 25 m; Fig. 5.5F).

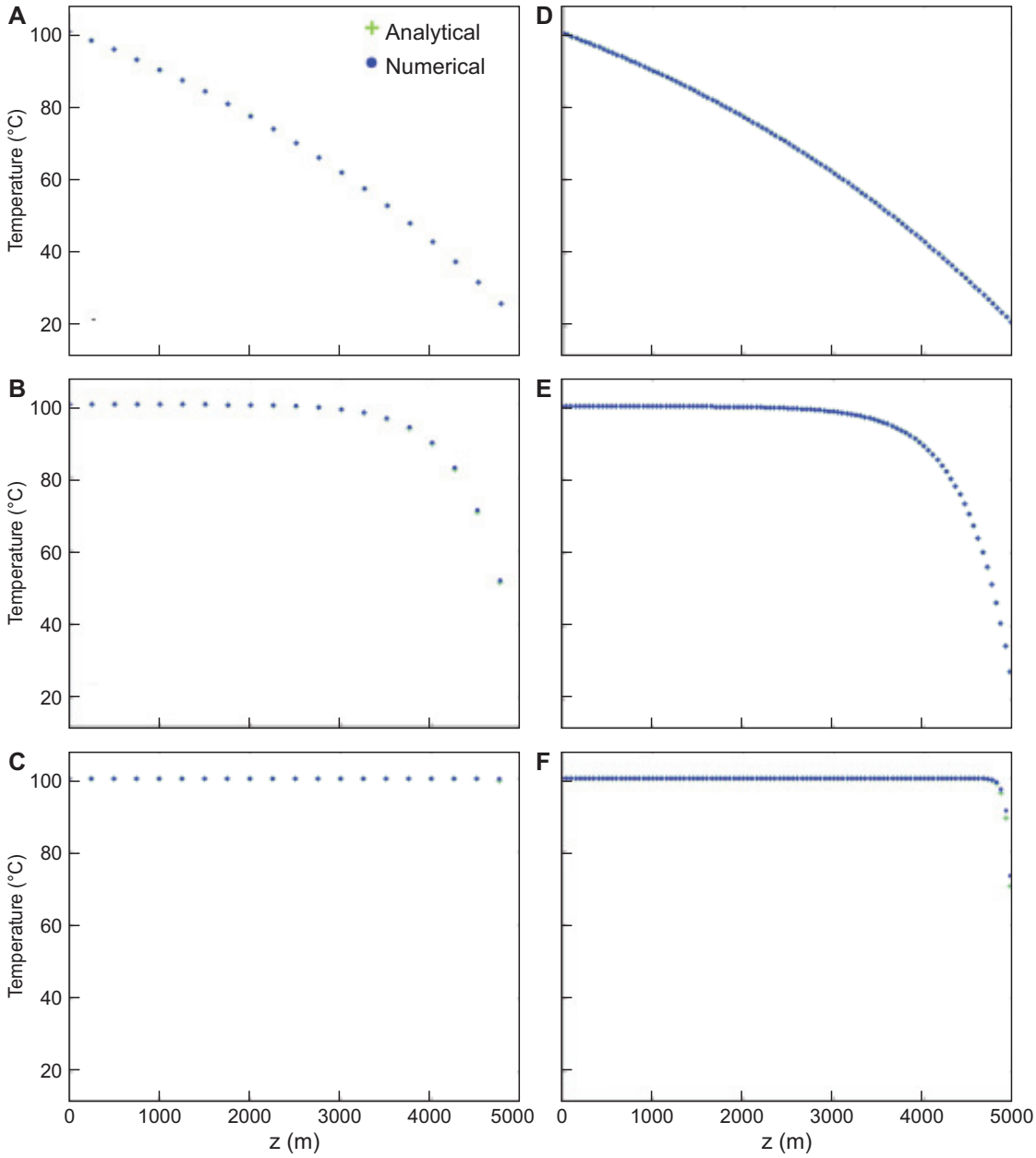

Figure 5.5: Effect of mesh resolution (Δz) and Pe on accuracy of the numerical solution for steady-state advective-conductive heat transport. H = 5000 m, λ = 3 W m^{-1} K^{-1}, T_0 = 100°C, structured rectangle mesh. (A) Pe = 1, Δz = 250 m. (B) Pe = 10, Δz = 250 m. (C) Pe = 100, Δz = 250 m. (D) Pe = 1, Δz = 25 m. (E) Pe = 10, Δz = 25 m. (F) Pe = 100, Δz = 25 m.

Numerical solutions to strongly advective problems (i.e. problems with high Pe) commonly display spatial instability in the vicinity of temperature (or concentration) fronts, which manifests as spatial oscillations in the temperature field either side of the front. This problem was not encountered with *escriptRT*.

Benchmark 4: 1D advective-diffusive tracer transport, steady state solution

The steady-state solution for tracer concentration in a vertical column subject to uniform upward throughflow (u_z = constant; $u_x = u_y = 0$), with fixed concentration C_H and fixed fluid pressure P_H at the top boundary (z = H) and fixed concentration C_0 at the base (z = 0), is:

$$C = C_H + (C_0 - C_H)\frac{1 - e^{Pe(z/H-1)}}{1 - e^{-Pe}} \qquad \text{5.1-10a}$$

where

$$Pe = \frac{u_z H}{\phi D_f} \qquad \text{5.1-10b}$$

and $Pe_{local} = Pe\Delta z/H$ as before. The numerical solution was compared with the analytical solution for a range of values of Pe, H and C_0. Different values of Pe were obtained by varying u_z while keeping H, ϕ and D_f constant. Models were initialised with uniform tracer concentration $C = C_H$ and were run for sufficient time to reach steady state.

The results were very similar to those for the equivalent heat transport problem (Benchmark 3; see Figures 5.4 and 5.5 above), displaying the same dependence on mesh resolution and Pe.

Benchmark 5: 1D advective-conductive heat transport, transient

The analytical solution for temperature in a vertical column subject to uniform upward throughflow (u_z = constant; $u_x = u_y = 0$) and no heat production (Q = 0), with the initial temperature equal to zero throughout the column, fixed temperature T_0 at the base (z = 0) and T = 0 at z = ∞ is:

$$T = \frac{T_0}{2}\left[\operatorname{erfc}\left(\frac{z - vt}{\sqrt{4Dt}}\right) + \exp\left(\frac{vz}{D}\right)\operatorname{erfc}\left(\frac{z + vt}{\sqrt{4Dt}}\right)\right] \qquad \text{5.1-10b}$$

where erfc is the complementary error function [Ogata and Banks, 1961]. This equation describes the propagation of a temperature front through the column. The boundary condition at z = ∞ is approximated in *escriptRT* by fixing T = 0 at z = H, such that the analytical solution is valid until the temperature begins to change at the top of the column (z = H).

The accuracy of transient solutions is expected to be influenced by the size of the timestep, with larger timesteps resulting in reduced accuracy, e.g. smearing of sharp fronts in the transported quantity. We parameterise the timestep in terms of the Courant overstep, α, such that $\Delta t = \alpha h/v$ where h is the size of the mesh elements in the flow direction and v is the magnitude of the transport velocity.

Comparisons of the numerical and analytical solutions were performed with varying u_z (expressed in terms of the global and local Peclet number), mesh density (20 or 200 rectangular elements in the flow direction), dimensionless time ($t' = tv/H$) and Courant overstep (α).

Figure 5.6 shows the effect of varying the timestep length. As expected, accuracy decreases with increasing Courant overstep, especially in the vicinity of the sharp temperature front. However the overall character of the sharp front is maintained.

Figure 5.7 shows the transient solution propagating through time. Accuracy is maintained as the sharp temperature front is transported.

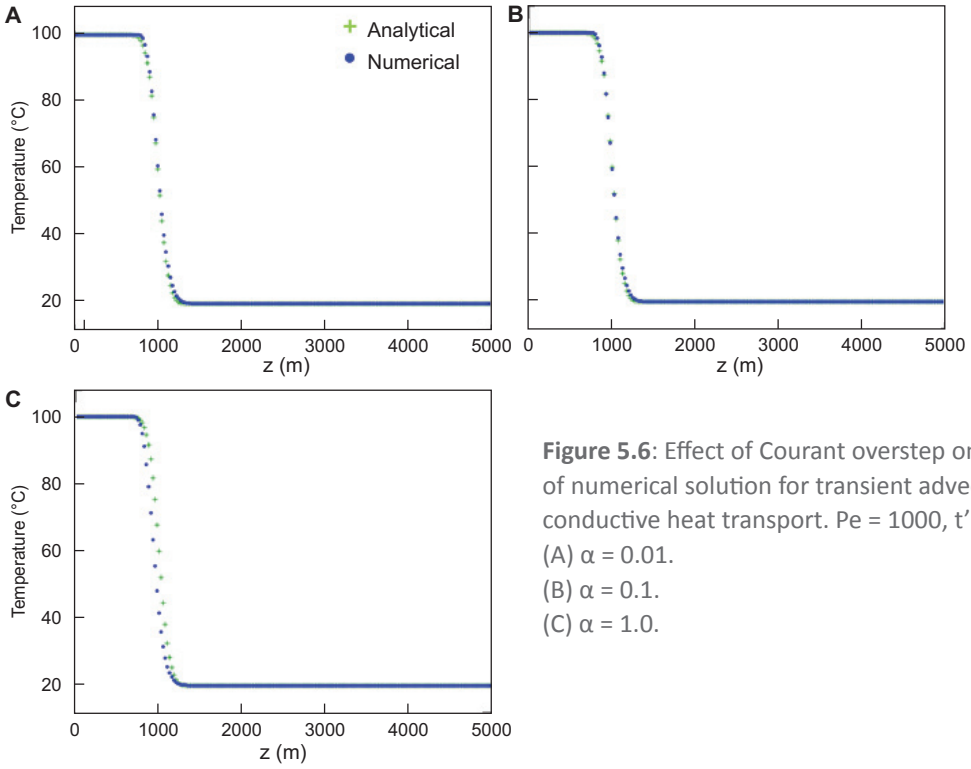

Figure 5.6: Effect of Courant overstep on accuracy of numerical solution for transient advective-conductive heat transport. Pe = 1000, t' = 2.
(A) α = 0.01.
(B) α = 0.1.
(C) α = 1.0.

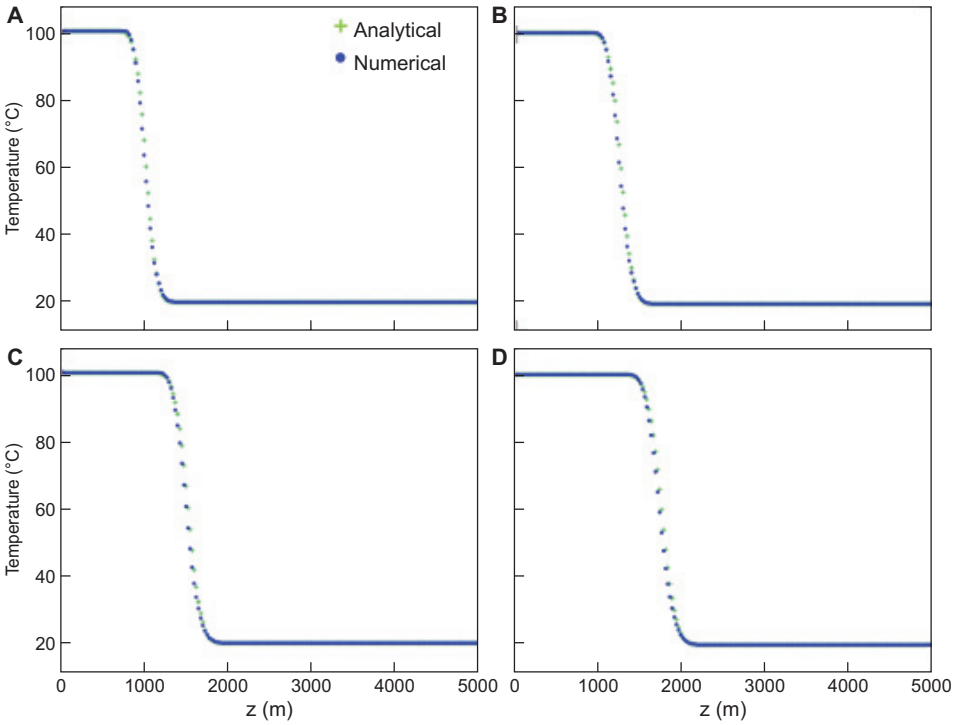

Figure 5.7: Transient solution propagating through time
(Pe = 1000, α = 0.1).
(A) t' = 2.0.
(B) t' = 2.5.
(C) t' = 3.0.
(D) t' = 3.5.

As with the steady-state solutions, accuracy decreases with increasing Pe (Fig. 5.8). However, the overall character of the solution is maintained even in high Pe scenarios.

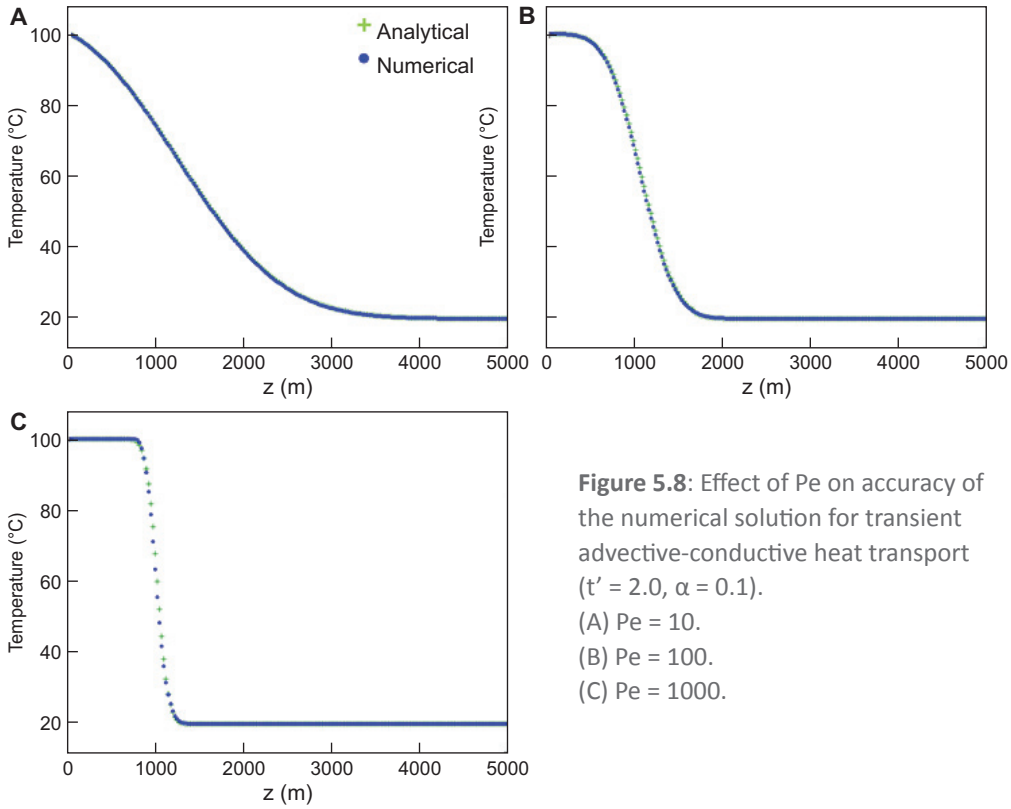

Figure 5.8: Effect of Pe on accuracy of the numerical solution for transient advective-conductive heat transport (t' = 2.0, α = 0.1).
(A) Pe = 10.
(B) Pe = 100.
(C) Pe = 1000.

Figure 5.9 illustrates the effect of mesh resolution. The numerical solution displays smoothing of the temperature front (numerical dispersion) on the coarse mesh (Fig. 5.9A; Pe_{local} = 50), which is not apparent on the fine mesh (Fig. 5.9B; Pe_{local} = 5).

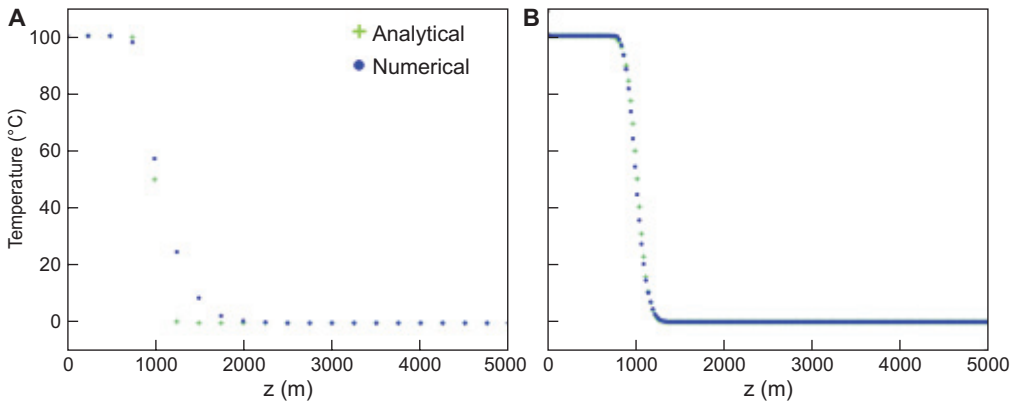

Figure 5.9: Effect of mesh resolution on accuracy of the numerical solution for transient advective-conductive heat transport (Pe = 1000, t' = 2.0, α = 0.1).
(A) Coarse mesh (Δz = 250 m). (B) Fine mesh (Δz = 25 m).

These results show that *escriptRT* can reproduce the transient solution for 1D advective-conductive heat transport with an acceptable level of accuracy, depending on Pelocal (which in turn depends on the mesh resolution, transport velocity and thermal conductivity) and Courant overstep. Accuracy always improves with decreasing Pe_{local} and decreasing α. The solution is spatially and temporally stable regardless of Pe and α.

Benchmark 6: 1D advective-diffusive tracer transport, transient

The transient analytical solution for 1D advective-diffusive tracer transport with upward through-flow is:

$$C = \frac{C_0}{2}\left[\operatorname{erfc}\left(\frac{z - vt}{\sqrt{4Dt}}\right) + \exp\left(\frac{vz}{D}\right)\operatorname{erfc}\left(\frac{z + vt}{\sqrt{4Dt}}\right)\right] \qquad 5.1\text{-}12$$

This equation describes the propagation of a tracer concentration front through the column. Tests corresponding to those carried out for transient advective-conductive heat transport (see Benchmark 5, above) were performed to check the ability of RT to reproduce the transient analytical solution for advective-diffusive tracer transport. The results were very similar to those for Benchmark 5.

Benchmark 7: Onset of free thermal convection (2D)

Free thermal convection is an important mechanism of heat transport in some geothermal systems, therefore it is important to verify that *escriptRT* can predict correctly the onset of free convection at the appropriate conditions.

The theory of free convection in porous media is covered in several texts [e.g. Nield and Bejan, 1992]. We consider the case of free thermal convection in a horizontal layer of length L and height H, with fixed temperature T_H at the upper boundary and T_0 at the lower boundary. The Boussinesq approximation is applied; that is, fluid density is treated as a constant except in the buoyancy term, where it depends linearly on temperature. Free thermal convection should occur spontaneously in this horizontal layer if the Rayleigh number, Ra, is greater than or equal to a critical value (Ra_c). The Rayleigh number is defined as:

$$Ra = \frac{k\rho_0^2 c_f \beta g H \Delta T}{\lambda \mu} \qquad 5.1\text{-}13$$

where $\Delta T = T_0 - T_H$ (°C) is the temperature difference across height H, and all other terms are defined in Table 5.1.

For the case considered here (i.e. top and bottom boundaries of the layer are impermeable and have fixed temperatures), $Ra_c = 4\pi^2$ if L/H is an even integer. For moderate values of Ra/Ra_c, convection takes the form of stable convective rolls with wavelength 2H. A transition to unstable or oscillatory convection occurs at a second critical value, Ra_{c2}, which lies between 240 and 300 [Nield and Bejan, 1992].

Tests were run on 2D meshes with triangular or rectangular elements, with L/H = 2 or 10. The temperature was initialised with a uniform vertical gradient between T_0 and T_H, then a perturbation was applied in one corner. The ratio Ra/Ra_c was varied to confirm that the code could predict the onset of free convection at Ra/Ra_c close to 1, and to verify the number and form of convection cells for scenarios with $Ra/Ra_c > 1$.

Each test was run until it had reached a steady state, or to a maximum of 100 million years. The attainment of steady state was assessed by monitoring the Nusselt number (Nu), which represents the ratio of convective to conductive heat transport. Nu = 1 implies conduction, Nu > 1 implies that convection is taking place. All scenarios started with Nu > 1 due to the initial temperature perturbation. The subsequent evolution of Nu indicated whether convection was taking place.

The results are illustrated in Figures 5.10 to 5.13 and Table 5.2. The results confirm that:

- *escriptRT* predicts the onset of convection at Ra/Ra_c very close to 1 (Table 5.2; convection occurs at $Ra/Ra_c \leq 1.03$ in all cases).
- *escriptRT* produces the correct number and shape of convection cells, i.e. wavelength = 2H (Table 5.2, Fig. 5.12).
- *escriptRT* produces oscillatory convection at $Ra/Ra_c = 10$ (Table 5.2, Figs. 5.10, 5.11 and 5.13).
- The Nusselt number is exactly 1.0 for $Ra/Ra_c < 1$, settles to a steady value > 1 for moderate values of Ra/Ra_c, and oscillates within a steady range for $Ra/Ra_c = 10$ (Figs. 5.10 and 5.11).

Scenarios with $Ra/Ra_c = 1.01$ took a very long time to establish convection and reach a steady-state. It is possible that the scenarios which failed to convect with $Ra/Ra_c = 1.01$ and 1.02 (see Table 5.2) might establish convection if they were run for longer.

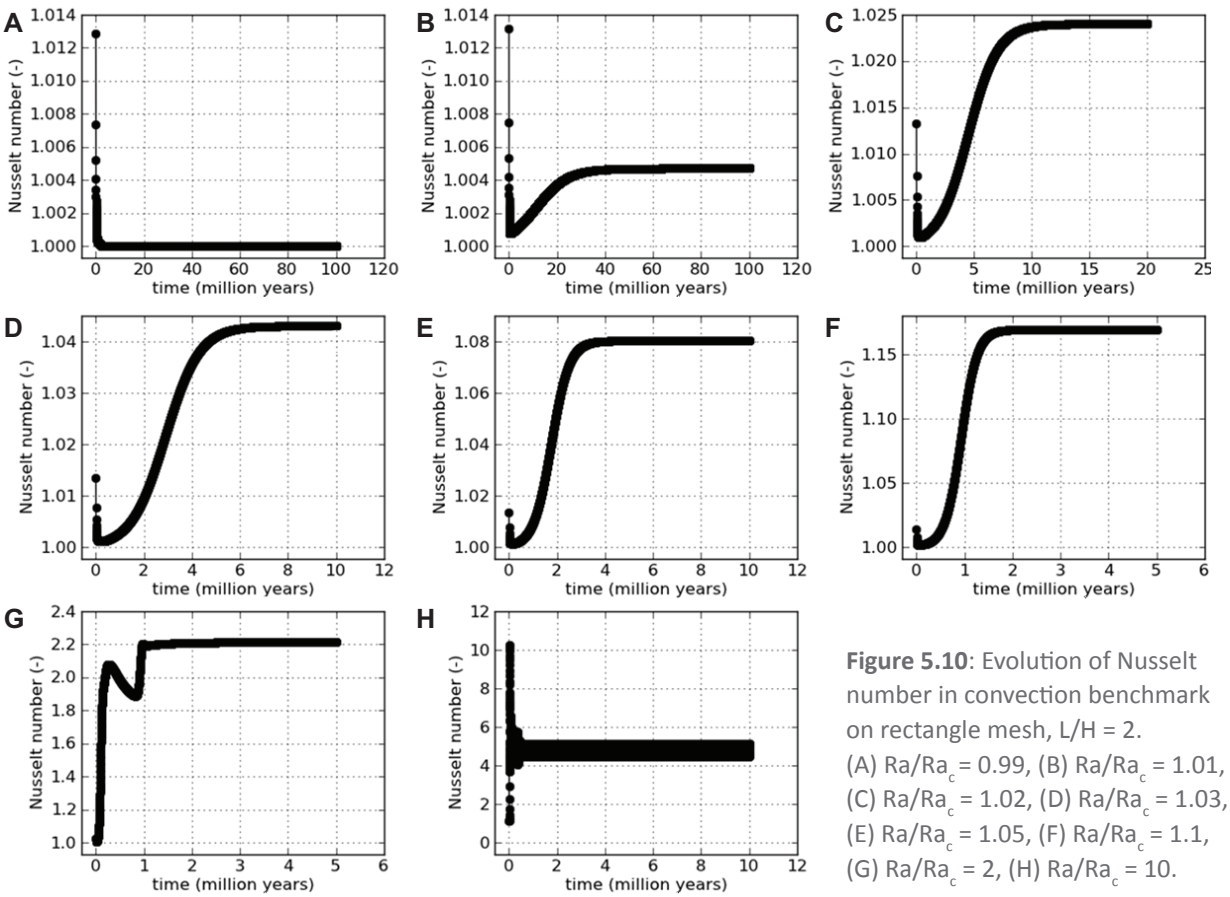

Figure 5.10: Evolution of Nusselt number in convection benchmark on rectangle mesh, L/H = 2. (A) $Ra/Ra_c = 0.99$, (B) $Ra/Ra_c = 1.01$, (C) $Ra/Ra_c = 1.02$, (D) $Ra/Ra_c = 1.03$, (E) $Ra/Ra_c = 1.05$, (F) $Ra/Ra_c = 1.1$, (G) $Ra/Ra_c = 2$, (H) $Ra/Ra_c = 10$.

Table 5.2: Number of convection cells created on rectangular and triangular meshes.

Ra/Ra_c	Rectangle L/H = 2	Rectangle L/H = 10	Structured triangle L/H = 2	Unstructured triangle L/H = 2
0.95	0	0	0	0
0.97	0	0	0	0
0.98	0	0	0	0
0.99	0	0	0	0
1.01	2	0	0	2
1.02	2	5	0	2
1.03	2	5	2	2
1.05	2	5	2	2
1.10	2	5	2	2
2.00	2	5	2	2
10.0	Oscillating	Oscillating	Oscillating	2 with small oscillations

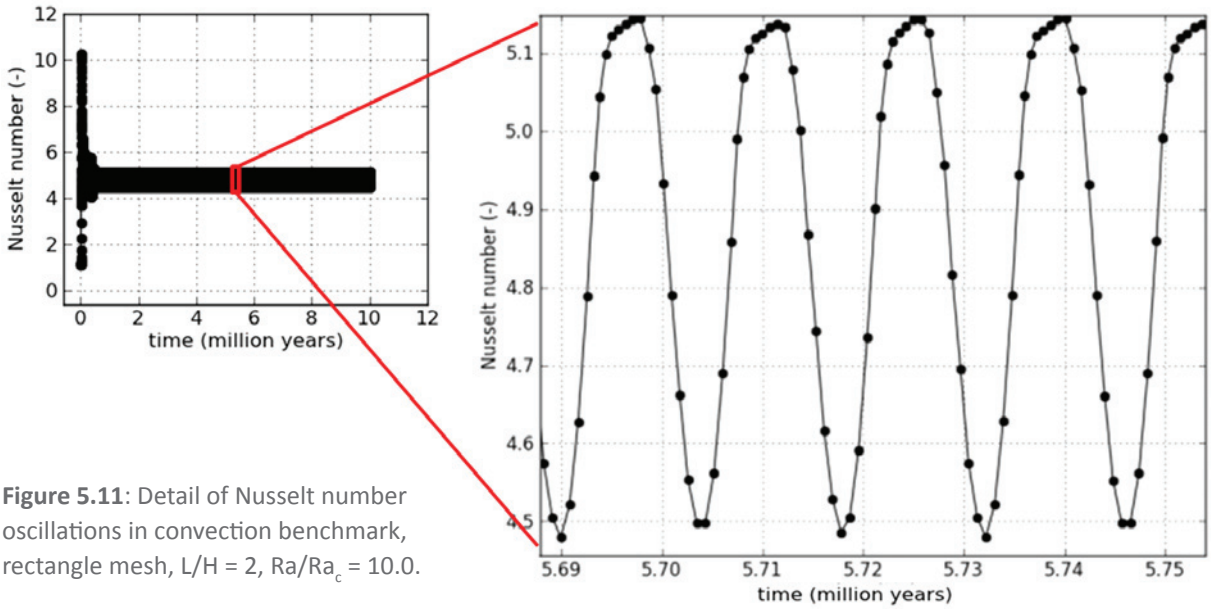

Figure 5.11: Detail of Nusselt number oscillations in convection benchmark, rectangle mesh, L/H = 2, Ra/Ra_c = 10.0.

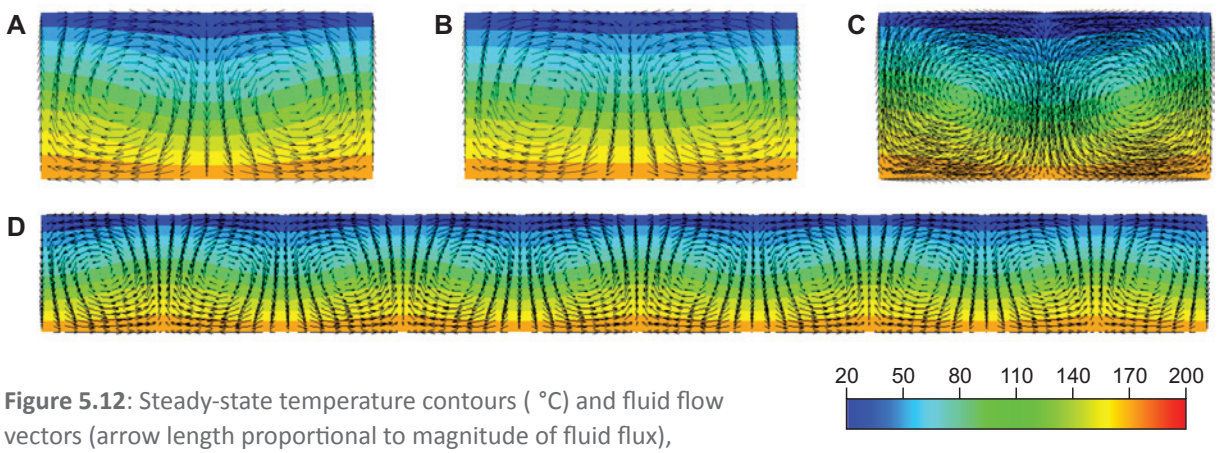

Figure 5.12: Steady-state temperature contours (°C) and fluid flow vectors (arrow length proportional to magnitude of fluid flux), Ra/Ra_c = 1.03, H = 5 km.
(A) Rectangle mesh, L/H = 2, maximum fluid flux 2.7 x 10^{-10} m s^{-1}.
(B) Structured triangle mesh, L/H = 2, maximum fluid flux 1.3 x 10^{-10} m s^{-1}.
(C) Unstructured triangle mesh, L/H = 2, maximum fluid flux 3.1 x 10^{-10} m s^{-1}.
(D) Rectangle mesh, L/H = 10, maximum fluid flux 2.3 x 10^{-10} m s^{-1}.

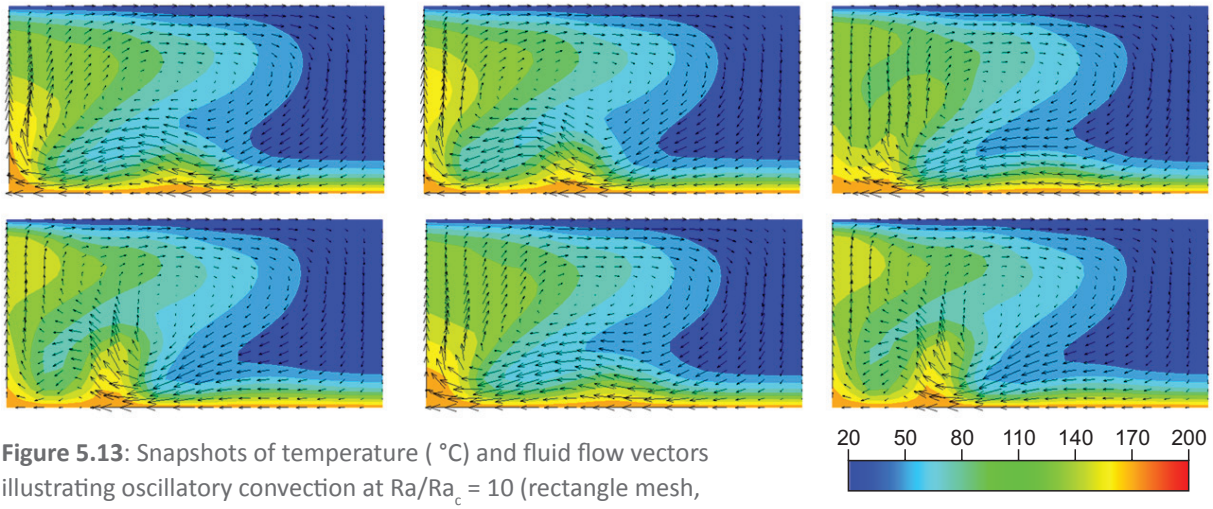

Figure 5.13: Snapshots of temperature (°C) and fluid flow vectors illustrating oscillatory convection at Ra/Ra_c = 10 (rectangle mesh, L/H = 2, H = 5 km). The shape and position of the convection cells oscillates through time.

Benchmark 8: Elder problem (2D)

The Elder problem [Elder, 1967] is a Type 2 benchmark that is widely used to validate density-driven flow simulators, however its usefulness as a benchmark has been questioned because it has no analytical solution and the results are highly mesh-dependent [Diersch and Kolditz, 2002]. We include the Elder problem as a benchmark to show that *escriptRT* can produce results for this problem that are similar to the results for other numerical codes.

In the Elder problem, a saline fluid that is 20% denser than pure water sinks downwards from a source region occupying part of the top boundary of a vertical rectangular domain. The domain is 600 m wide by 150 m tall, and the saline fluid is introduced by fixing the salinity over a 300 m distance along the middle of the top boundary. Temperature is assumed to be constant and to have no effect on fluid density. All boundaries are impermeable, except at the top corners where the fluid pressure is fixed. The Elder problem was reproduced in *escriptRT* with the following properties and boundary conditions:

Initial conditions: C = 0 kg m-3, ρ_f = 1000 kg m^{-3}

Boundary conditions: C = 1 kg m^{-3}, ρ_f = 1200 kg m^{-3} (150 < x < 450 m, z = 150 m); C = 0 (z = 0 m); P = 0 Pa (x = 0 and x = 600 m, z = 150 m).

Properties: μ = 0.001 Pa s; γ = 200; D_f = 3.565 x 10-6 m^2 s^{-1}; Ø = 0.1; k = 4.845 x 10^{-13} m^2.

The parameter γ defines the dependence of fluid density (ρ_f) on salinity (C):

$$\rho_f = \rho_0 + C\gamma \qquad 5.1\text{-}14$$

Models were run on coarse, medium and fine meshes of 3 types:

- Rectangular elements: 900, 3813 and 15687 elements
- Asymmetric triangular elements: 1800, 7626 and 31374 elements
- Symmetric triangular elements: 2128, 8091 and 32571 elements

Each model was run with timesteps of 1.0, 0.1 and 0.01 years for a total duration of 20 years. Figure 5.14 shows the concentration contours after 20 years.

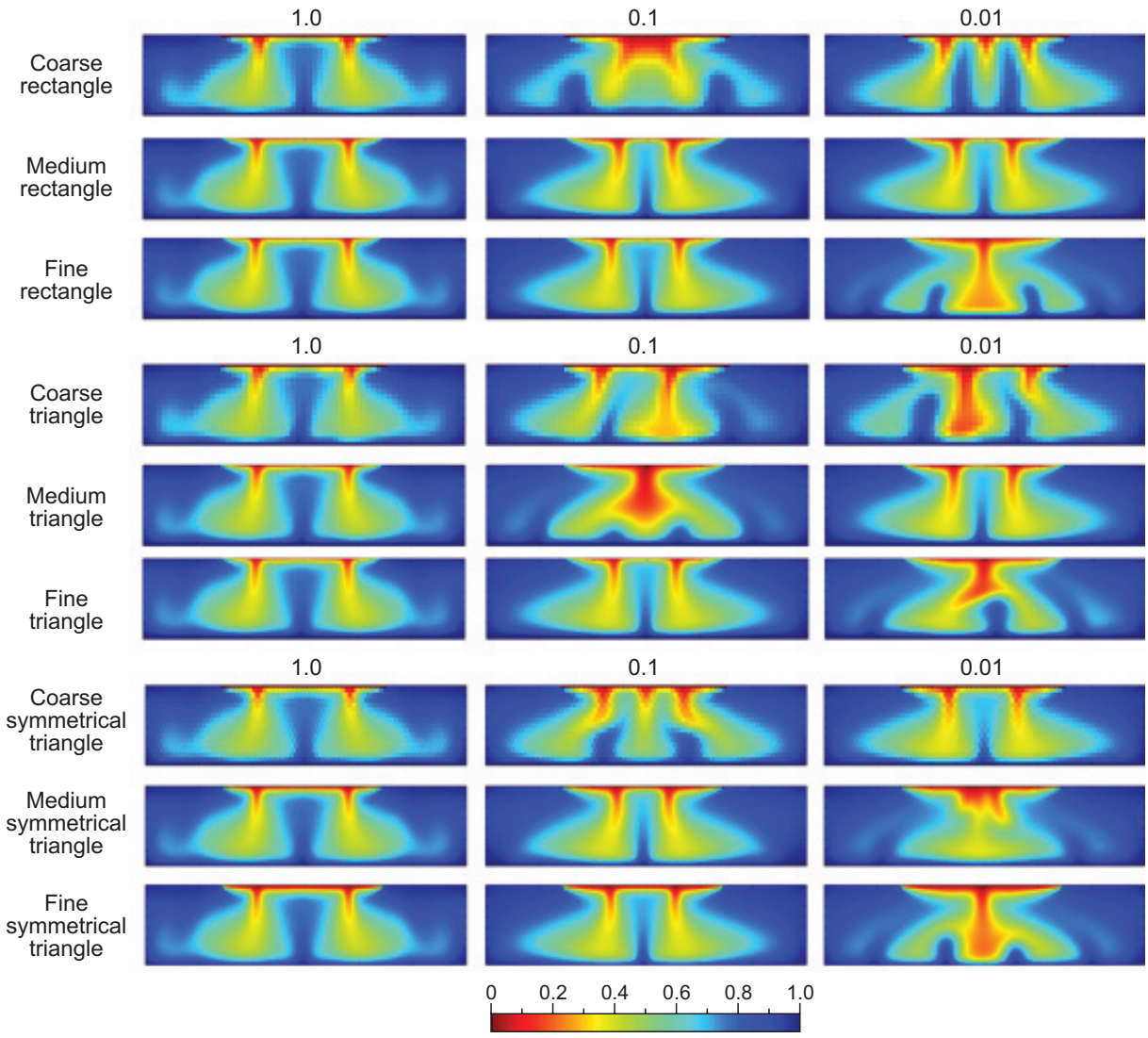

Figure 5.14: Salt concentration (kg m^{-3}) after 20 years in the Elder problem using 3 different mesh types (rectangle, structured triangle and symmetrical structured triangle) with coarse, medium and fine resolution. Timestep = 1 year (left), 0.1 years (middle) and 0.01 years (right). Model size = 600 x 150 m.

The results show that:

- The solution to the Elder problem is mesh-dependent, depending on both the shape of the elements and the mesh resolution.
- The solution is always symmetrical about the centre line on rectangle meshes.
- Asymmetric solutions occur on triangle meshes in some cases, especially with the smallest timestep (0.01 years; right hand column in Fig. 5.14).

In most cases the solution comprises two down-welling lobes of high concentration either side of a central upwelling. Some combinations of mesh and timestep produce 1 or 3 downwelling lobes. All of these forms have been produced previously by other codes [Diersch and Kolditz, 2002].

It might seem counter-intuitive that the solution becomes less symmetrical with decreasing timestep. One generally expects numerical solutions to become *more accurate* with decreasing timestep. In fact this is exactly what is displayed in Figure 5.14: tiny errors introduced by the mesh discretisation are propagated more accurately through time with a smaller timestep, thus producing an asymmetric solution. Larger timesteps tend to smooth out small fluctuations ("numerical diffusion"), regardless of whether these fluctuations are real or are errors introduced by the mesh. Thus, the solution remains symmetrical with a larger timestep, because the mesh artifacts are smoothed out.

We conclude that *escriptRT* produces solutions to the Elder problem that are similar to those produced by other codes, and agree with Diersch and Kolditz [2002] that the solution is highly mesh-dependent.

Benchmark 9: Convection with anisotropic permeability (2D)

Permeability is likely to be strongly anisotropic in sedimentary basins [Bear, 1972], therefore it is important that *escriptRT* can simulate fluid flow with anisotropic permeability.

Implementation of anisotropic permeability in *escriptRT* is at an early development stage. We present a preliminary result showing that *escriptRT* produces the expected behaviour in a convecting system with anisotropic permeability.

The test concerns 2D convection in a square box with impermeable boundaries all round, except the top boundary at which the fluid pressure is fixed. The ratio of horizontal to vertical permeability is 2. Figure 5.15 shows the fluid flow streamlines. The pattern is very similar to that shown in Figure 6.12 of Nield and Bejan [1992]. Therefore we conclude that *escriptRT* is behaving as expected with anisotropic permeability, at least in this preliminary semi-quantitative comparison.

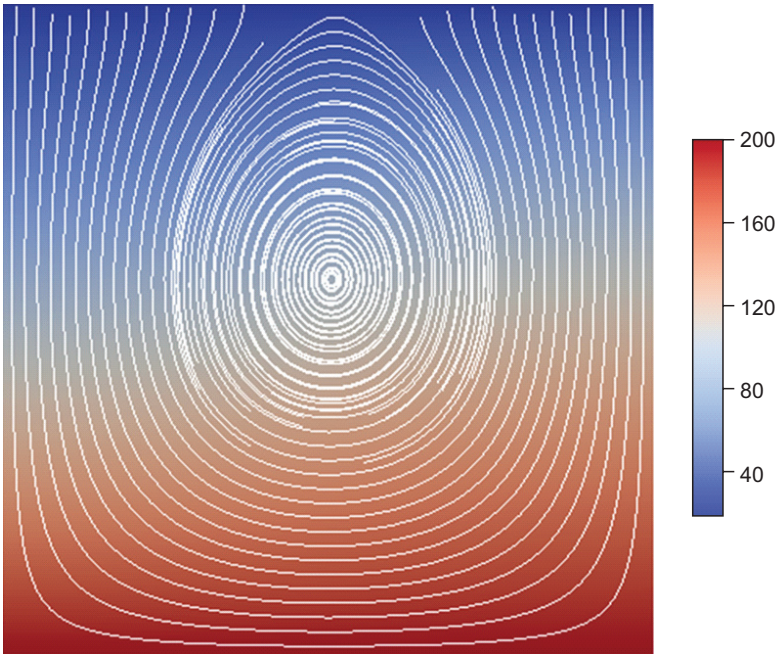

Figure 5.15: Fluid flow streamlines and temperature contours (°C) due to convection in a square box with anisotropic permeability.

Benchmark 10: 3D Convection with layered permeability

This is a Type 3 benchmark, representing a scenario of interest to WAGCoE. The benchmark problem concerns convection in a 3D box comprising horizontal layers of varying thickness and permeability. The properties and thicknesses of these layers are intended to be a loose representation of the stratigraphy in the Perth Basin (Table 5.3). Fluid properties, initial and boundary conditions are listed below. The mesh comprises 545000 hexahedral elements, and thus is large enough to benefit from running the simulation in parallel. The test was run on 12 CPUs on iVEC's EPIC supercomputer.

Layer name	Thickness (m)	Density (kg m^{-3})	Porosity	Permeability (10^{-15} m^2)	Specific heat capacity (J kg^{-1} K^{-1})	Thermal conductivity (W m^{-1} K^{-1})
Superficial Aquifer	200	2000	0.2	500	790	1.5
Leederville Aquifer	160	2000	0.2	500	790	3.0
South Perth Shale	160	2370	0.05	0.01	820	2.0
Yarragadee Aquifer	1000	2180	0.2	1000	790	3.0
Cattamarra Coal Measures	2320	2385	0.05	0.01	820	2.0
Lesueur Sandstone	2700	2620	0.2	100	790	3.0
Sue Group	2680	2400	0.05	0.01	820	2.0
Basement	800	2650	0.05	0.01	720	2.9

Table 5.3: Layer thicknesses and properties for layered convection benchmark.

Thermal boundary conditions:

Top: T = 20 °C

Bottom: T = 20 + 0.03H °C, where H is the total height of the model.

Sides: No heat flux

Fluid flow boundary conditions:

Top: P = atmospheric pressure

Bottom and sides: No flow normal to boundaries

Initial conditions: Conductive steady state, hydrostatic fluid pressure. A small temperature perturbation (0.002 °C) was applied at the centre of the model to initiate convection.

Fluid properties:

Viscosity: 1.002 x 10^{-3} Pa s

Specific heat capacity: 4185 J kg^{-1} K^{-1}

Thermal conductivity: 0.5858 W m^{-1} K^{-1}

Density: $\rho = \rho_0(1-\beta(T-T_0))$ with β = 2 x 10^{-4} 1/K, ρ_0 = 1000 kg m^{-3} and T_0 = 20 °C.

The results of the simulation after 410 000 years are shown below (Fig. 5.16). The model took 16 hours of simulation time to reach this point. Convection occurs in the Yarragadee Aquifer and the Lesueur Sandstone, with the wavelength of the convection cells being smaller in the Yarragadee due to its smaller thickness. Figure 5.16 B demonstrates that the fluid flow vectors are calculated correctly

where there is a large permeability contrast between layers; specifically, the vectors are exactly parallel to the boundary between the high permeability layer (the Yarragadee) and the bounding low permeability layers. This behaviour was not modelled correctly in previous versions of the code.

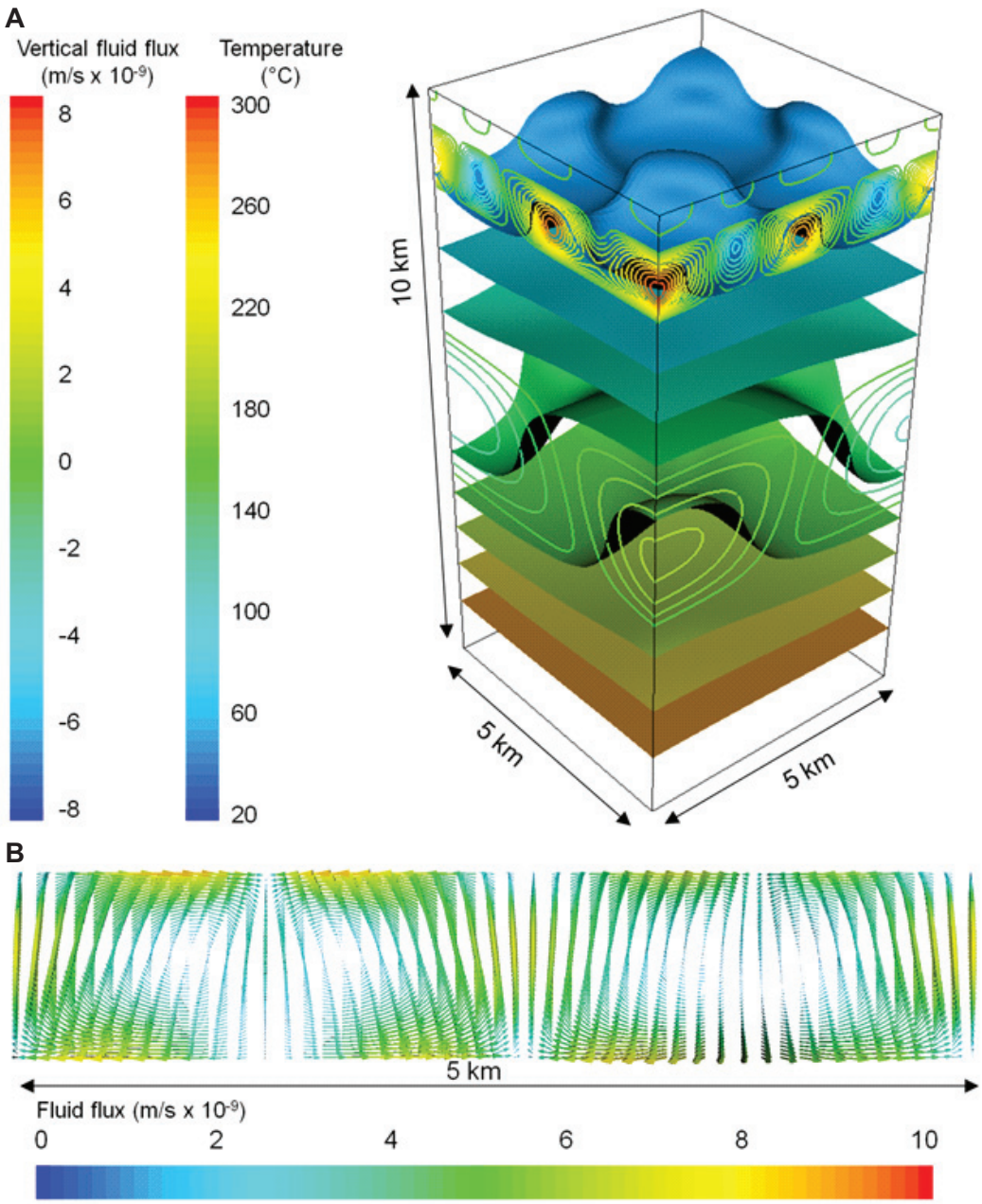

Figure 5.16: Results of Benchmark 10: 3D convection with layered permeability.
(A) Temperature isosurfaces and contours of the vertical component of fluid flux.
(B) Fluid flux vectors on a vertical section through the Yarragadee Aquifer.

Benchmarks summary

The results of the benchmark tests show that:

- *escriptRT* simulates diffusive transport with an extremely high level of accuracy;
- *escriptRT* can model advective-diffusive transport problems with a high level of accuracy, depending on Peclet number, mesh resolution and timestep. Sharp fronts in concentration or temperature (characteristic of high Pe scenarios) are smoothed out unless the timestep is sufficiently small (Courant overstep <= 0.1) and the mesh is sufficiently fine;
- The *escriptRT* solutions to advective–diffusive transport problems are temporally and spatially stable;
- escripRT predicts the onset of free thermal convection in a horizontal layer at or very close to the critical Rayleigh number;
- *escriptRT* predicts the correct number and form of convection cells in a horizontal layer for Ra_c < Ra < Ra_c2;
- *escriptRT* predicts oscillatory convection in a horizontal layer for Ra > Rac_2;
- Preliminary results indicate the correct behavior in convecting scenarios with anisotropic permeability;
- *escriptRT* produces solutions to the Elder problem that are similar to those produced by other codes, depending on timestep, mesh type and mesh resolution;
- *escriptRT* can simulate convection in a large 3D model with large permeability contrasts between layers.

5.1.6 Conclusions

The motivation behind the development of *escriptRT* was to provide a powerful but also user-friendly, flexible, and extensible platform. This allows numerical modelling geologists to focus on the definition of their geophysical/geochemical problem at hand at the constitutive level without necessarily having to become experts at the same time in applied mathematics and programming. The software architecture of *escriptRT* presents some advantages in terms of flexibility (capacity to be adapted or modified), extensibility (simplicity to add new features) and re-usability (possibility to easily use some components or to couple with other codes), all derived from the usage of carefully chosen components. A modular object-oriented architecture was implemented using escript. Python was mainly used as a high-level glue language to connect components while the numerics were efficiently implemented using lower-level languages. In this section we also presented some benchmarks to validate the fluid flow and transport algorithms of the code, including a 3D example to demonstrate the ability of the code to simulate convection on a large mesh with large contrasts in permeability between layers. The benchmarks show that *escriptRT* is suitable for simulating geothermal systems, including large 3D models which can be run on multiple processors in parallel.

5.2 Thermal-Hydrological-Mechanical-Chemical (THMC) coupling of geological processes

This section was published as Poulet et al. [2011b] and presents a method to couple the thermal (T), hydraulic (H) and fluid-rock chemical (C) interaction capabilities of *escriptRT* (see Section 5.1) with a rate-dependent mechanical (M) formulation of the finite element method including continuum damage mechanics for geomaterials implemented using Abaqus/StandardTM.

5.2.1 Introduction

The natural complexity of geological systems has motivated researchers to consider the processes of thermal transfer (T), hydraulic flow in porous media (H), mechanical deformation (M) and fluid-rock chemical interactions (C) in a coupled manner. These processes when considered individually rarely explain observed geological features. Different combinations of those THMC processes have previously been studied and are based on theoretical frameworks like the one developed by Coussy [2004]. Most THMC applications; however, occur in engineering domains such as nuclear waste disposal, gas and oil recovery, hot-dry-rock geothermal systems, or contaminant transport [Lanru and Xiating, 2003], and it is still rare to see THMC analyses of larger scale geological systems such as those involved in ore body formation [Lanru and Xiating, 2003, Tsang et al., 2004, Shao and Burlion, 2008]. This observation can be explained by two main reasons. The first one is that coupled numerical simulation of all processes still represents a significant computational challenge and cannot currently be solved within weeks, the typical time-scale of a mineral exploration programs [Potma et al., 2008]. The second reason, which follows, is that geoscientists understand the importance of conceptualising their problems [Andersson and Hudson, 2004] and are often able to identify a subset of relevant processes which represent the first-order controls in their studies. These reduced-dimensionality models often disregard the complex feedback interactions between processes, which might not always be negligible.

There are many different potential feedbacks between all processes [e.g. Lanru and Xiating, 2003] and the complexity of this set of checks and balances justifies coupled THMC simulations for various geological scenarios. Numerical simulations are specifically adapted to understand and isolate particular feedbacks as they allow scenarios to be investigated methodically under changing conditions, including the sets of processes considered. They often provide an indispensable tool to analyse the relative importance of various feedback mechanisms and the competition of rates of processes. Coupling mechanisms are critical factors for the localisation of geological structures such as folds or shear zones, which are often vital to the formation of ore bodies. Shear heating in thermo-mechanical simulations, for example, has helped to understand shear zone formations at the kilometre scale [Regenauer-Lieb and Yuen, 2004]. Additional coupling mechanisms can inhibit or accentuate those behaviours, and damage mechanics is now a recognised means to enhance localisation [Regenauer-Lieb, 1998, Bercovici and Ricard, 2003, Karrech et al., 2011].

In this section we present a new THMC code designed to increase our understanding of hydrothermal and geothermal geological systems. This coupled code is based on escriptRT [Poulet, 2011] for the thermal, hydraulic and chemical processes, as well as an Abaqus [ABAQUS/Standard, 2008] user material implementation [Karrech et al., 2011] for the mechanical deformation, including continuum

damage mechanics. The section is composed of two parts. We first introduce the constitutive models for the THMC processes, including the important feedbacks considered (Section 5.2.2). These include a link between the damage parameter and the evolution of porosity, affecting in turn the rock permeability. Section 5.2.3 then illustrates the importance of considering all THMC processes for mineral exploration by simulating a generic unconformity-related albitisation scenario.

5.2.2 Constitutive model

The constitutive model presented in this paper applies to a fully saturated porous medium, where a fluid phase interacts with the host rock mechanically, energetically and chemically. This model integrates several processes which are coupled sequentially. We consider a Representative Volume Element (RVE) Ω of a material specimen containing a solid skeleton and a fluid saturating the porous space, and undergoing non-uniform inelastic deformation from an arbitrary fixed reference configuration.

Continuum damage mechanics

The mechanical model we use for the skeleton is based on a damaged visco-plasticity model for frictional geomaterials under the assumption of small deformation, as introduced by Karrech et al. [2011] and derived from the Continuum Damage Mechanics (CDM) approach established by Kachanov [1958] and used extensively by Lemaître and Chaboche [2001]. This model is described using a classical Helmholtz free energy $\psi(\epsilon_{i,j}, \alpha_{i,j}, T, D)$ where ϵ represents the total strain tensor, α the inelastic strain tensor, T the temperature and D a scalar damage parameter. We also postulate a custom dissipation function (see Karrech et al. [2011] for details) to account for shear dissipation, volumetric change, rate sensitivity and damage.

Porosity

We consider the evolution of the rock porosity Ø from its initial value $Ø_0$ due to mechanical and chemical processes [Kuhl et al., 2004, Fusseis et al., 2009]

$$\phi - \phi_0 = \phi_m^e + \phi_m^p + \phi_c \qquad 5.2\text{-}1$$

where $Ø_m^e$ and $Ø_m^p$ represent the elastic and plastic partitions of the porosity variation due to mechanical deformation [Armero, 1999], and $Ø_c$ represents the porosity evolution due to mineral dissolution and precipitation.

We base the calculation of $Ø_m^p$, the porosity update due to continuum damage, on an elementary interpretation of damage as spherical void growth in rocks. The scalar damage parameter D for a given RVE can be interpreted as the proportion of void surface intersecting the RVE boundary surface over the whole surface [Cocks and Ashby, 1980]. If we consider a RVE of characteristic length R containing voids of radius r we obtain the relationship $D \propto (r/R)^2$. The porosity Ø is itself defined as the volume ratio of the void compared to the whole RVE, hence $\phi \propto (r/R)^3$. We can then deduce that $\phi \propto D^{3/2}$. Considering a maximum porosity value of $Ø_{max}$ for a totally damaged element we then postulate the following damage-porosity evolution:

$$\phi_m^p = (\phi_{max} - \phi_0)D^{3/2} \qquad 5.2\text{-}2$$

Effective stress

All pores are assumed to be fully saturated with an interstitial ideal fluid which exerts a static pressure p on solid grains. Following Biot's approach [Biot, 1941] this pressure term is accounted for to calculate the effective or equivalent stress as

$$\sigma_{eq}^{ij} = \sigma^{ij} + bp\delta^{ij} \qquad 5.2\text{-}3$$

b is the Biot coefficient defined in Coussy [2004] as b=1-K/k_s, where K and k_s are respectively the bulk moduli of the empty porous solid and of the solid matrix forming the solid part of the porous solid. The elastic part of the evolution of porosity can be expressed [Coussy, 2004] as

$$d\phi_m^e = bd\epsilon - \alpha_\phi dT + dp/N \qquad 5.2\text{-}4$$

where ϵ represents the volumetric strain, α_ϕ is the thermal expansion coefficient of the porosity, and N is the Biot modulus defined as $1/N = (b - \phi_0)/k_s$.

Fluid transport

Fluid transport through the porous medium is described using the classical Darcy law under the assumption of quasi-static fluid flow and neglecting the tortuosity effect. After derivations (see Poulet et al., [2011a]) we obtain the pore pressure equation as

$$\beta_r \phi \rho_f \frac{dp}{dt} - \nabla \cdot \left(\rho_f \frac{k}{\mu_f} \nabla p\right) = -\nabla \cdot \left(\rho_f^2 \frac{k}{\mu_f} \nabla p\right) - \phi \rho_f \nabla \cdot \underline{v_s} + \alpha_r \phi \rho_f \frac{dT}{dt} - \gamma_f \phi \rho_f \frac{dX}{dt} - b\rho_f \frac{d\epsilon}{dt} \qquad 5.2\text{-}5$$

where we use the same notations as in Section 5.1.2. The fluid properties (density, viscosity, specific heat, compressibility and thermal expansivity) are calculated from one of the three equations of state (EOS) for pure water available in the *escriptRT* code [Poulet et al., 2011a]. This choice allows us to account for the important variation of fluid properties (especially density) in a realistic way for low concentrations of chemical species, and with a first order approximation for salinity.

Heat transport

We assume the solid and liquid components of the medium to be in thermal equilibrium. Heat is then transported via the standard advection diffusion equation [Nield and Bejan, 2006] with an additional shear heating source term with the same notations as in Section 5.1.2. $\dot{\varepsilon}_{diss}$ is the dissipative strain rate from creep and plastic deformations, and χ is the nondimensional Taylor-Quinney heat conversion efficiency coefficient. In this study we fix the χ constant in time with a value of 0.9 in agreement with most material values [Chrysochoos and Belmahjoub, 1992].

$$\overline{\rho\, C_p} \frac{\partial T}{\partial t} + \left(\rho C_p\right)_f \underline{q}.\underline{\nabla}\mathrm{T} - \underline{\nabla}.\left(\overline{D}\underline{\nabla}\mathrm{T}\right) = Q + \chi \sigma^{eq} \dot{\epsilon}^{diss} \qquad 5.2\text{-}6$$

Chemistry

The mass transport for chemical species and the fluid-rock chemical reactions are treated as described in Section 5.1.2.

Permeability evolution

Permeability is one of the most critical parameters in the calculation of transport equations and there exist many empirical relationships linking it to porosity under different assumptions [e.g. Kühn, 2009]. We selected the Blake-Kozeny equation presented in McCune et al. [1979]:

$$k = k_0 \left(\frac{\phi}{\phi_0}\right)\left(\frac{1-\phi_0}{1-\phi}\right)^2 \qquad 5.2\text{-}7$$

and validated its usage in combination with the damage-porosity relationship introduced above by comparing the porosity evolution as a function of the damage parameter with a matching law presented in Pijaudier-Cabot et al. [2009]. This law was developed to model the interaction between material damage and transport properties of concrete. However it was derived from two asymptotic cases where theoretical modelling exists, for low and high values of damage, and can therefore be applied to a wider range of geomaterials. Figure 5.17 shows good agreement between this matching law and two results obtained with different values of the maximum porosity ϕ_{max} . ϕ_{max}=1 represents the case where the fully damaged rock (D=1) is completely dissolved. It reproduces very well the asymptotic behaviour of the Poiseuille flow for large values of damage, where permeability is controlled by a power function of the crack opening. This model however leads to excessive values of permeability in that case (D→1) as it can also exaggerate the value of porosity for a fully damaged rock. We chose the value ϕ_{max}=0.9 to overcome this problem as shown on Figure 5.17. The results obtained still match closely the reference law visually, including for large values of damage. There is a loss of the asymptotic behaviour for D→1 which is non critical as we are following the common practice of artificially capping the value of damage to a maximum of 0.9.

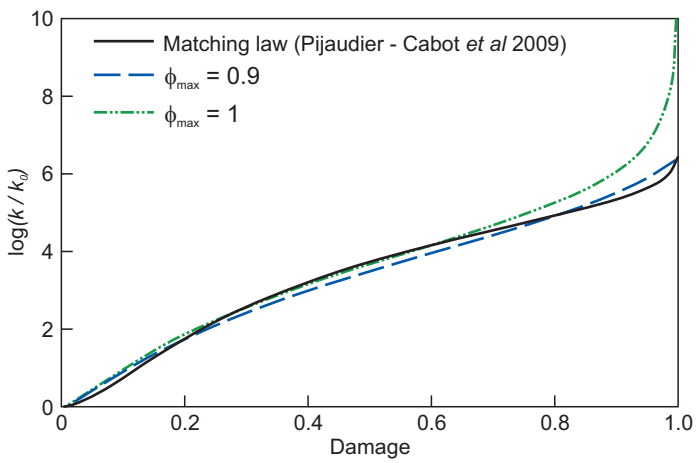

Figure 5.17: Comparison of permeability evolution as functions of damage. Our results fit the matching law from Pijaudier-Cabot et al. [2009].

5.2.3 Application to albitisation

This subsection presents an application to albitisation to illustrate the formulation presented and the corresponding code implemented by coupling Abaqus™ and *escriptRT*. This example is generic enough to highlight the interest of this code for multiple applications, including geothermal studies, and this particular geochemical scenario was only selected for its simplicity.

Problem description

Albitisation is a common alteration process in which albite forms by the replacement of primary feldspars, both K-feldspar and plagioclase.

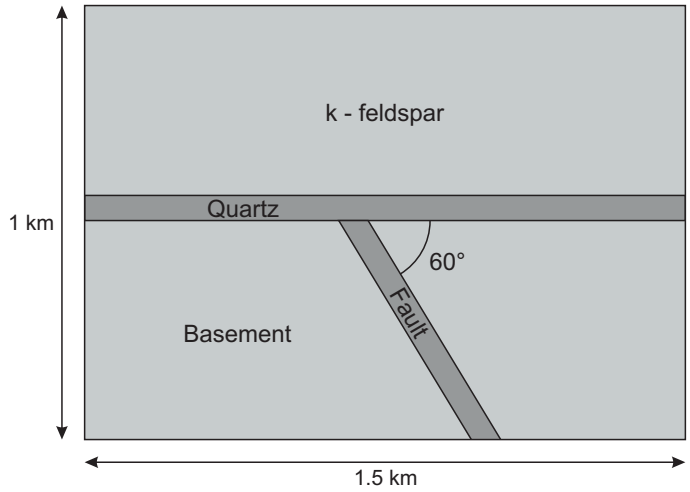

Figure 5.18: Initial model geometry and composition

The initial model is a 1.5 x 1 km two-dimensional cross section as shown on Figure 5.18. A 500 m thick basal unit comprising albite and quartz in equilibrium with an NaCl brine is overlain by a unit comprising K-feldspar and quartz in equilibrium with a KCl brine. The two units are separated by a 50 m thick impermeable quartz layer which ruptures during fault development allowing fluid migration between the two units and subsequent albitisation of the K-feldspar layer as fluids move up the fault zone. An initial fault zone, 50 m thick with a dip of 60°, is placed in the basement to localise a new shear zone within the upper layers of the model and which deforms the quartz layer.

$$KAlSi_3O_8 + Na^+ \leftrightarrow NaAlSi_3O_8 + K^+ \qquad 5.2\text{-}8$$

Mechanical, thermal and fluid properties used in the model are presented in Table 5.4. Boundary conditions are applied on the top surface of the model to simulate its burial 5 km below ground, with a temperature of 150 °C, a pore pressure of 49 Mpa, an effective rock pressure of 76 Mpa with a Biot coefficient of 0.85, and a fixed chemical composition. A hydrostatic initial pore pressure gradient and an initial geothermal gradient of 30 °C/km are applied through the section and the system is equilibrated for those conditions. The model is then considered to be under compression with horizontal velocity boundary conditions of 4 mm yr^{-1} applied on the right hand side, no horizontal displacement on the left boundary, and no horizontal fluid or heat fluxes on both sides. Free slip, fixed temperature and a fixed chemical composition (after initial equilibrium) are applied on the bottom boundary. Changes in porosity as a result of geochemical reactions were excluded for this study, whose purpose is to demonstrate the first order importance of porosity and permeability enhancements through damage. Full albitisation can induce a molar volume decrease of approximately 8%. Since this simulation only calculates the onset of albitisation, we are neglecting the chemical induced changes in porosity which we expect to be small compared to those induced by damage. This assumption will be tested when the results are presented.

The model was first initialised without any compression to obtain an equilibrium solution for the temperature (T) and pore pressure (P) fields, with fluid properties dependent on T and P. The simulation was then run for more than 30 000 years under compression.

	Upper layer	Quartz layer	Basement	Fault
Mineralogy (volume percentages)	K-feldspar (60%) Quartz (40%)	Quartz (100%)	Albite (60%) Quartz (40%)	Albite (60%) Quartz (40%)
Fluid composition (molarity)	KCl (0.1)	NaCl (0.1)	NaCl (2.0)	NaCl (2.0)
Density (kg m^{-3})	2400	2400	2600	2600
Young's modulus (Gpa)	32	32	72	48
Poisson ratio (-)	0.29	0.29	0.20	0.20
Cohesion (Mpa)	20	20	30	30
Friction angle (°)	30	30	30	30
Thermal expansion ($x10^{-5}K^{-1}$)	2.4	2.4	2.4	2.4
Porosity (%)	15	5	5	10
Log permeability (m^2)	16	18	18	17
Specific heat ($J.kg^{-1}.K^{-1}$)	850	850	850	850
Thermal conductivity ($W.m^{-1}.K^{-1}$)	3.1	3.1	3.1	3.1

Table 5.4: Initial material properties and mineralogy.

Results

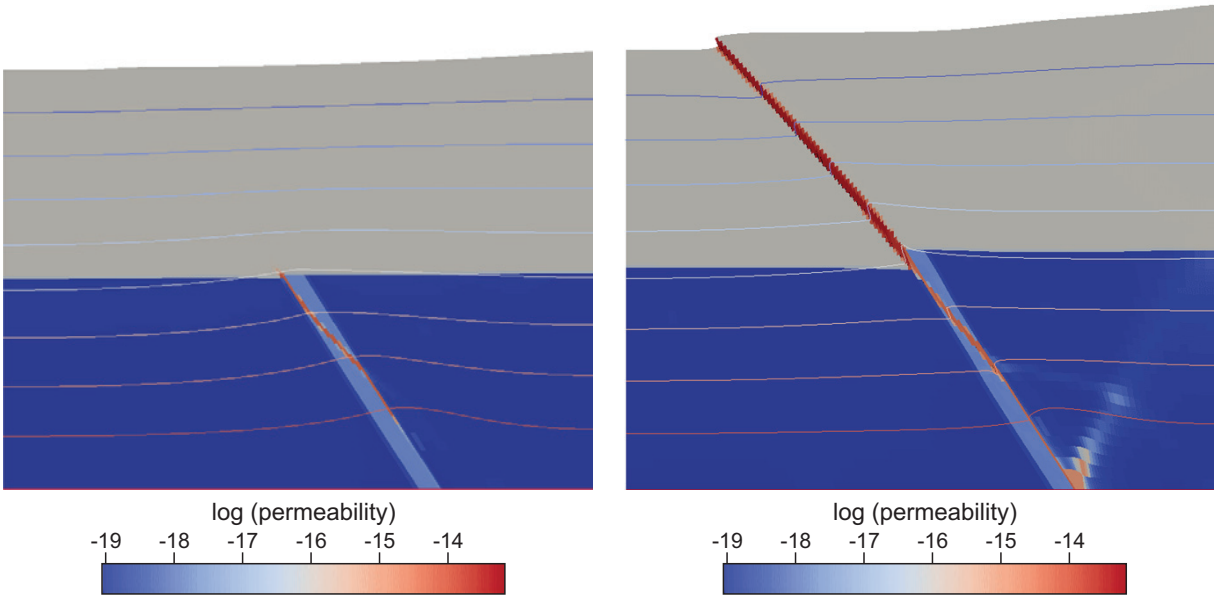

Figure 5.19: Log permeability after 15 000 years (left) and 30 000 years (right). Temperature contours are overlaid from 150°C at the top surface to 180°C at the bottom, with 10°C intervals.

Plastic strain initiates at the intersection of the pre-existing fault and the unconformity. This reactivates the original fault and then propagates upwards into the upper layer. Damage follows the plastic strain evolution, and in turn porosity and permeability (Fig. 5.19). The opening of this fluid pathway allows hotter fluid from the basement to propagate upwards through the unconformity and reach the upper rocks, where albitisation occurs (Fig. 5.20). Figure 5.20 shows the permeability evolution at a point in the opening shear zone above the unconformity, showing sudden jump in time over more than three orders of magnitude over a short period of time (~1000 years). This simulation highlights the time evolution of this dynamic system, where albitisation only starts 5000 years after the fault was created over the unconformity.

At the end of the simulation we observe a maximum of 12% albite formed (as a percentage of total feldspar content), which would represent less than 1% porosity decrease based on a 8% molar volume decrease for full albitisation. This result shows that chemical porosity evolution, in this particular example, is indeed negligible compared to the change of porosity attributed to damage. This validates the initial assumption not to consider chemically induced porosity changes in this application.

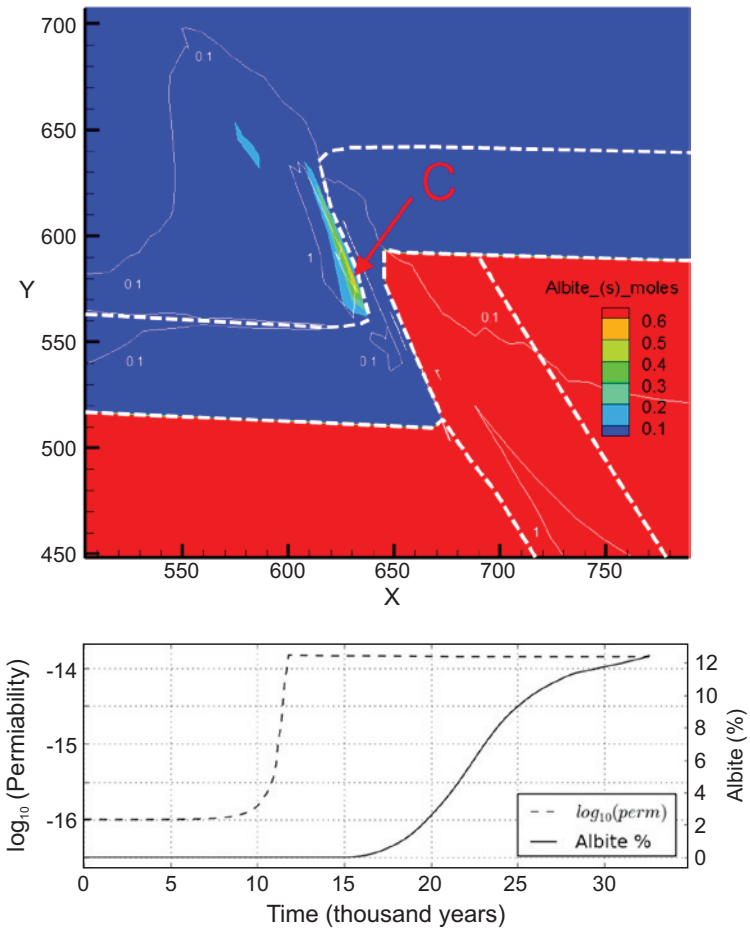

Figure 5.20: Distribution of albite mineralisation around fault zone after 32,600 years. Top: K-feldspar is replaced by albite just above the fault zone. Bottom: Evolution of permeability and volume % albite as a proportion of total feldspar content at point C.

5.2.4 Conclusions

The mechanical model used in this study includes a continuum damage mechanics formulation which is linked to permeability through the evolution of porosity. This significant feedback allows fluid pathways to be dynamically generated from the localisation of shear zones in particular. The importance of this phenomenon is illustrated by a numerical study of a generic albitisation scenario involving a pre-existing fault and an unconformity. While a full geochemical study of this example is beyond the scope of this section, a significant conclusion from this study is that the coupling of THMC processes and the evolution of permeability mechanism can allow us to examine the progression of geochemical reactions in comparison with the rates of other processes from the fluid motion within the host rock. They can be used as well to predict the distribution of alteration assemblages which in term can provide vectors to mineralisation. This information could also be used to recognise prospective geophysical responses in mineral exploration [Chopping and Cleverley, 2008]. The features and results of the simulation presented may be applicable to a wide range of hydrothermal ore deposits as they show that: (i) the inclusion of damage in the code produces narrow discrete shear zone which match more closely those observed in nature, (ii) damage mechanics reproduces the logarithmic pattern of rock pulverisation which can be observed in nature on the sides of shear

zones, (iii) permeability creation as a function of damage greatly enhances flow rates and focusing, and (iv) elevated flow rates can affect geochemical reactions by increasing the supply of reactants as well as changing the temperature through heat advection. In this example the effects of damage on permeability are shown to be significantly greater than those caused by poro-elasticity. While we did not specifically address chemical/dissolution induced porosity changes, we also interpret the effects of damage to be significantly greater in this particular example where the changes in mineralogy resulted in a minor change in molar volume. Simulating scenarios where the fracturing of an impermeable seal promotes fluid flow from deep reservoirs into overlying sequences can be used to examine processes in many mineral systems including unconformity-related uranium systems as well as Archean gold systems.

5.3 Incorporation of Uncertainty in the Simulation Workflow

The geothermal exploration results presented previously represent a close collaboration within a team of geoscientists and numerical modellers. The skills and insights provided by different team members allows these complicated models to be seamlessly integrated from geologic, hydrologic, and geothermal perspectives. WAGCoE has aimed to produce a workflow which can be utilised by other research groups and exploration companies across Australia and the world. One such workflow was developed by Florian Wellmann in his Ph.D. research. The work presented below was originally published in two conference proceedings [Wellmann et al., 2011c, Wellmann and Regenauer-Lieb, 2012], a journal paper [Wellmann and Regenauer-Lieb, 2011], and his Ph.D. thesis [Wellmann, 2011]. This work focuses not only on the mechanics of moving from raw data to simulation results, but how this integrated workflow can be used to answer fundamental questions about the uncertainty of model results.

5.3.1 Introduction

Structural geological models are commonly used to determine the property distribution for flow simulations. Geological models always contain uncertainties, so an important question is: If the geological model is uncertain, how uncertain are the simulated flow fields?

Many standard methods exist to evaluate uncertainties of specific observables in reservoir simulations, for example temperatures at an observation point or oil production in a well [e.g. Finsterle, 2004, Suzuki et al., 2008, Bundschuh and Arriaga, 2010]. However, uncertainties at observation points are not necessarily suitable to analyse the uncertainty within the whole system. We test here the hypothesis that system measures based on the concept of entropy can be applied to analyse and compare system-wide uncertainties in geological models and in simulated hydrothermal flow fields. These measures can then be applied to evaluate the correlation of uncertainties in both systems.

We will first outline the concepts of information entropy, used here to quantify uncertainties in a set of structural geological models, and thermal entropy production, applied to evaluate the thermodynamic state of a simulated flow field. We will then outline a specifically developed workflow

that enables the automatic simulation of a set of hydrothermal flow fields from stochastically generated realizations of structural geological models. Applying this workflow, we will then use both system-based measures to evaluate uncertainties in a concrete example of a geothermal resource-scale study in the North Perth Basin, Western Australia.

5.3.2 System-based measures of uncertainty

Information entropy

We apply information entropy as a quantitative measure for the quality of a structural geological model, as introduced in Wellmann et al. [2011b]. Information entropy is based on the Shannon Entropy model [Shannon and Weaver, 1948], originally defined to evaluate the amount of missing information in a transmitted message. We apply the concept in the context of structural geological models to describe the information entropy for a point in time and space:

$$H(x,t) = \sum_{m=1}^{M} p_m(x,t) \log p_m(x,t) \qquad 5.3\text{-}1$$

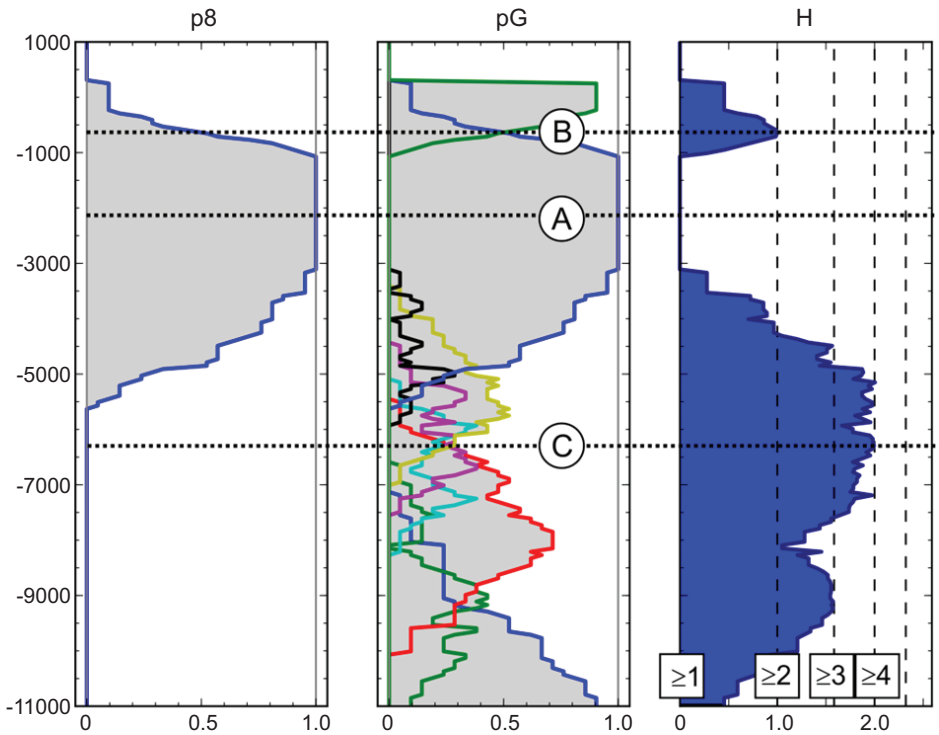

Figure 5.21: Example of the application of information entropy to evaluate uncertainties in a hypothetical drill hole (ordinate axis is elevation in metres). Left: probability of encountering one specific geological unit. Middle: probability for all geological units in the model (each colour represents a different geological unit). Right: information entropy combining the probability of all units into one meaningful measure. H = 0 implies there is only 1 possible unit (probability = 1; label A). For every value H > 0, at least two units can occur e.g. if two units are equally probable, H = 1 (label B); if 4 units are equally probable, H = 2 (label C) [Wellmann, 2012].

The quantitative interpretation of the measure is straightforward and can be illustrated with a simple example of the probability of encountering several geological units in a borehole (Fig. 5.21). The data in this figure are derived from stochastic realizations of a structural geological model where the exact position of a structural boundary at depth is uncertain. The left graph in Figure 5.21 shows the probability of encountering one specific geological unit at a potential drilling site at depth. At around sea level near the top of the figure, the probability of encountering this formation is low, according to the stochastically generated set of structural models. Below -1000 m, the unit is present in all realizations and the probability of finding it is 1. Below -3000 m, the probability decreases and below -6000 m, the unit was not observed in any realizations and the probability is accordingly 0 again.

The probability representation for the occurrence of one unit is a practical way to visualize uncertainties for a single unit; however, it quickly becomes confusing when more than one unit are analysed (middle graph in Fig. 5.21).

Calculating the information entropy from all combined probabilities provides a clear picture of uncertainties in the model (right graph in Fig. 5.21). Where one unit has a probability of 1, H is zero: there is no uncertainty (horizontal label “A”). For every value of H > 0, at least two units can occur. If two values are exactly equally probable, then H = 1 (label “B”), and accordingly for higher values: at label “C”, 4 units are equally probable.

The extension of the concept, illustrated on a vertical transect above, into a spatial context is straightforward [Goodchild et al., 1994]. As an example, we consider a geological map, consisting of three geological units, where the exact position of the boundary between the three units is uncertain (Fig. 5.22a). The uncertainty about the position of the boundaries can be transferred into probability maps for each of the units (Fig. 5.22b). Here we show discrete maps with probability values assigned to grid cells for each of the geological units. Equation 5.3-1 can then be used to calculate the information entropy of each of these cells. The map of cell entropies (Fig. 5.22c) provides a clear representation of the spatial uncertainties, similar to the borehole example of Figure 5.21. Cells where one unit has a probability of 1 (e.g. at label “A”) have a cell information entropy of zero because no uncertainty exists at this point. Cells where more than one unit are probable have a higher information entropy (label “B” and “C”) and the highest entropy exists where all three units are almost equally probable (label “D”), reflecting the highest uncertainty at this point.

The previous examples highlight how information entropy can be used to visualize uncertainties in a meaningful way. However, in order to quantify the overall uncertainties in the whole model space, an additional measure is required.

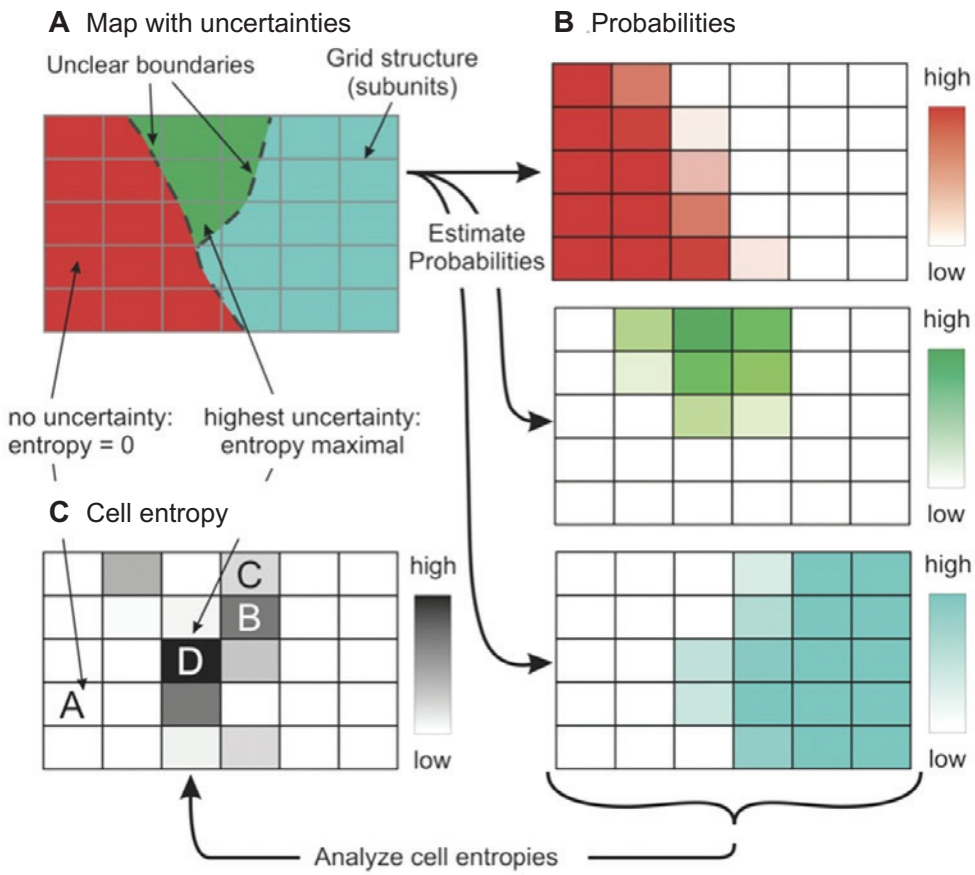

Figure 5.22: Information entropy in a spatial context: (a) map of three geological units with uncertain boundaries; (b) discreet probability maps for each of the units; (c) information entropy for each cell, derived from the cell probabilities: the entropy is zero when one unit has a probability of 1 at this cell (e.g. label "A"); the value increases when more than one unit is probable and highest when all units are almost equally probable (label "D"). Figure from Wellmann [2011a].

As an extension of the concept of information entropy at a point, the total information entropy for the whole model space can be defined as a sum:

$$\begin{aligned} H_T(t) &= -\frac{1}{N}\sum_{x=1}^{N} H(x,t) \\ &= -\frac{1}{N}\sum_{x=1}^{N}\sum_{m=1}^{M} p_m(x,t)\log p_m(x,t) \end{aligned} \qquad 5.3\text{-}2$$

In accordance with the cell entropy, the total information entropy provides a single measure of uncertainties in the entire model: if the geological units are exactly known everywhere, the entropy is zero. For an increasing number of uncertain cells, the total information entropy of the model increases, capturing the increase in uncertainty.

Thermal entropy production

Thermodynamic measures can be applied to describe the state and to predict the response of a system, without having to know all detailed processes within the system. The thermodynamic measure of entropy production is related to dissipative heat processes within a system. The entropy of a diabatic system changes if heat is supplied or removed from the system. The entropy production, the change of entropy, is defined as the ratio between the change in heat Q and the temperature T [e.g. Callen, 1985]:

$$\dot{S} \equiv \frac{\delta Q}{T} \qquad 5.3\text{-}3$$

Entropy is produced due to reversible and irreversible processes. If we only consider the entropy production due to thermal dissipation in a slow moving fluid in a permeable matrix, the entropy production is reduced to the heat that is supplied normal to the boundary A by the heat flux qh at a temperature T [Ozawa et al., 2003]:

$$\dot{S} = \oint_A \frac{1}{T} q_h \cdot n \, \mathrm{d}A \qquad 5.3\text{-}4$$

In a conductive system in steady state, all heat fluxes are balanced and no thermal entropy is produced. The situation is different in an advective system. Here, advective heat transport leads locally to an increase in entropy production.

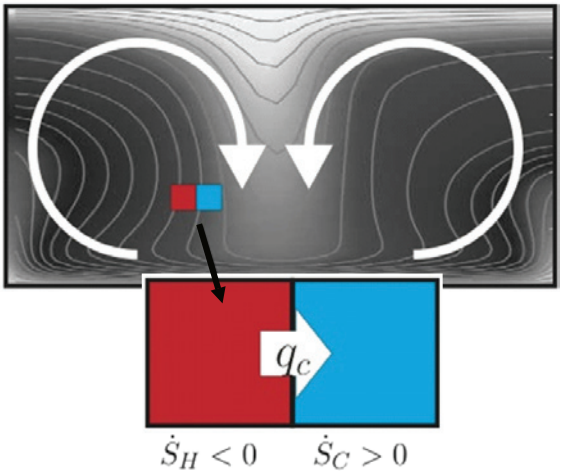

Figure 5.23: Entropy production in a convective system: the advective transport of relatively cold fluid parcels downwards induces locally a conductive heat transport, resulting in a non-zero entropy production.

A simple convection system is presented in Figure 5.23. The black and white background image shows a typical convection temperature profile where darker colours correspond here to hotter temperatures. The white arrows indicate dominating fluid flow, disturbing the temperature field. In the central part of this model, colder fluids are transported downwards by this fluid flow (downwelling zone). These colder fluid parcels induce locally a conductive temperature flux from the adjacent warmer areas (subfigure in Fig. 5.23) and this flux results in a non-zero entropy production of the system, even if it is in steady state. The analogue behaviour exists in the upwelling zone.

Entropy production can therefore be related to the heat transport mechanisms within a system: if a system is in steady state, the entropy production is zero if heat transport is purely conductive. As soon as convection sets in, the entropy production is greater than zero and increasing for more vigorous convective systems. In fact, the entropy production is directly related to the Nusselt number, a measure of the heat transfer [Regenauer-Lieb et al., 2010].

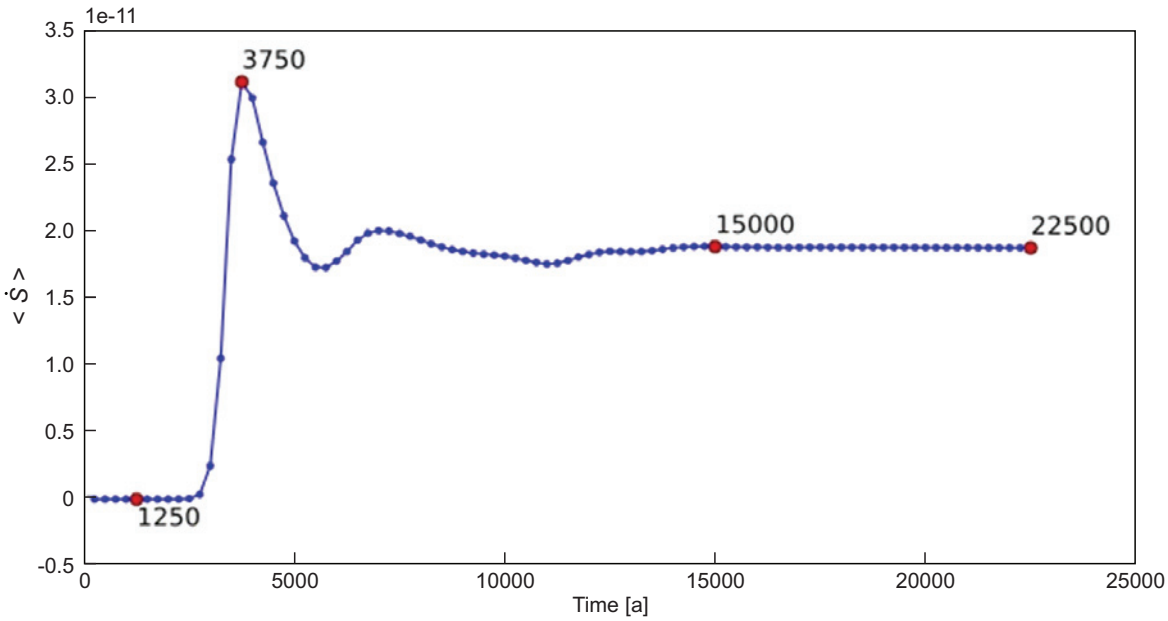

Figure 5.24: Average specific entropy production during the onset of convection in a simple system; From an initial conductive steady state, the system goes through a phase of high entropy production until it reaches a convective equilibrium state with a finite non-zero entropy production.

In order to obtain a measure of the state of the entire system, we apply the average specific entropy production, calculated as the average value of the specific entropy productions in subsystems, scaled by the mass:

$$\langle \dot{s} \rangle = \frac{1}{V} \int_V \frac{\dot{S}}{m} \, \mathrm{d}V \qquad 5.3\text{-}5$$

This measure provides an insight into the state of the entire system and classifies it with a single number. As an example, in Figure 5.24, the development of entropy production over time is presented for the onset of convection in a simple homogeneous system. Plotted here is the average entropy production of the entire system. Until convection sets in, the entropy production is zero. It then increases to a maximum value (at 3750 years), but then decreases again to a finite non-zero value when the convective system reaches a steady state.

This example indicates that thermal entropy production can be used to classify the hydrothermal state of the system with one meaningful value. We will use this value below to evaluate how a system reacts to changes in the constraining parameters.

5.3.3 Structural uncertainty workflow

Our aim is to evaluate the influence of uncertainties in structural geological models on simulated flow predictions for reasonably complex and realistic geological scenarios. We developed a method that enables stochastic geological model generation and the direct simulation of hydrothermal flow fields for all realizations of the geological model. Here, we are outlining the standard steps that are usually

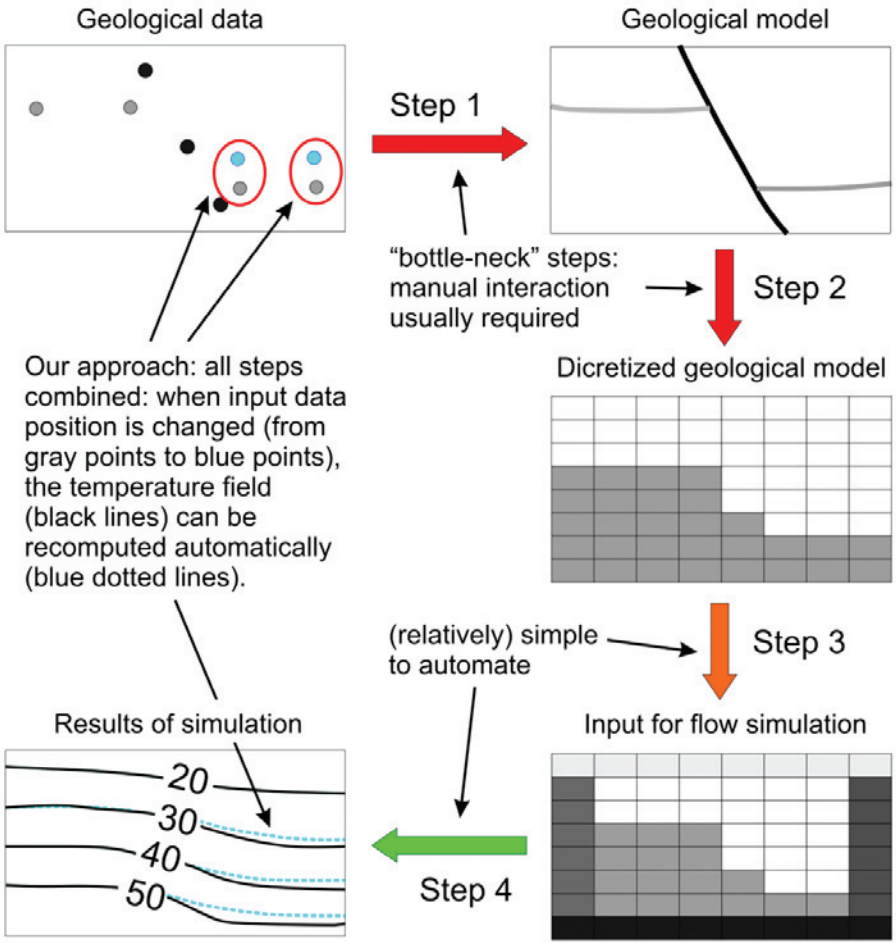

Figure 5.25: Typical modelling steps from original geological data to simulated fluid and heat flow fields and the typical ''bottle-neck'' steps: the geological modelling and mesh generation are difficult to automate (red arrows). We are addressing these steps with our approach to enable an automatic update of the simulated flow fields when geological input points are changed (blue points and dotted lines)

performed for a hydrothermal simulation on the scale where the structural setting (and not, for example, the sedimentary system) is the main control on relevant properties (porosity, permeability, etc.). The main steps are also visualized in Figure 5.25.

Geological modelling

The first step is usually to create a structural representation of the subsurface, a geological model, as a starting point for the simulation (Fig. 5.25, Step 1). This can range from very simple plate models to highly complex interpolations of a variety of input data in full 3-D. Many different (mostly commercial) tools exist to create subsurface models [e.g. Mallet, 1992, Turner, 2006, Calcagno et al., 2008] mainly differing in the way they interpolate between data points (e.g. surface or volume methods) and the flexibility of input data types they can deal with (seismics, well-logs, structural measurements, etc.). All these approaches have different advantages and disadvantages but finally the aim to create a representation of the subsurface structure. One important difference is the automation. With explicit modelling methods, many manual steps are required to create a valid three-dimensional geological model based on a changed set of input data [Caumon et al., 2009], especially in complex geological settings with fault networks or overturned folds. Implicit methods [e.g. Calcagno et al., 2008] enable an automatic model reconstruction for cases where the input data set is moderately changed (but might have other disadvantages).

Processing of the subsurface model to a simulation grid

The structural model has to be discretised into a format that is recognized by the simulation code. Typical examples are rectilinear meshes for finite difference (FD) simulation codes or tetrahedral meshes for finite element (FE) codes, but many other mesh types are possible. Depending on the complexity of the structural model, and the required mesh discretisation, this step can be very tedious and time-consuming (Fig. 5.25, Step 2).

Set-up of the input file for the simulation

After the subsurface model is discretised into a mesh format, relevant flow properties have to be assigned to each cell (or to connections between cells). The properties depend on the type of simulation. For example, for coupled fluid and heat flow simulations permeability, porosity, compressibility, thermal conductivity, density and heat production rate have to be defined. Additionally, boundary conditions and simulation parameters have to be assigned, according to the type of the studied simulation problem (Fig. 5.25 Step 3).

Process simulation

Once the mesh structure is defined and all relevant parameters are assigned to the cells, the simulation can be initiated. A wide variety of different software codes exists, depending on the studied flow problem. An important point for the purpose of this paper is that many flow simulators can easily be automated: when the input file is changed, the flow field can be re-computed (Fig. 5.25, Step 4).

Considering the whole standard workflow, from the raw geological information to simulated flow field, specifically the first steps, i.e. the geological modelling and the discretisation of the model into a useful mesh format, usually require at least some manual interaction. The objective of this work is to bridge this gap - and to enable an automatic update of the simulation results when the raw geological information is changed (as shown in Fig. 5.25).

Combination and automation of all steps

In our developed workflow we integrate established simulation and modelling software, and a variety of own programs, into a single framework in the scripting language Python. We did not write own simulation software as such, but extended the functionality of existing codes, to allow a combination and integration that has not been possible before.

Geological modelling

The first step is the construction of the geological model on basis of the discretised observations. We apply here an implicit geological modelling method based on a potential-field approach [Lajaunie et al., 1997]. The method is implemented in the geological modelling software GeoModeller (www.geomodeller.com). With this method, it is possible to recompute the geological model automatically, once all other model settings and parameters are defined (see Calcagno et al. [2008] for a detailed description of the modelling method). We wrote a set of Python modules to access the raw data and relevant methods of the geological modelling capabilities.

The discretised geological observations are stored in an XML-file, together with further geological constraints, like the stratigraphic relationships between geological units (onlap, erosive, sub-parallel) and the influence of faults. We defined a Python object definition to parse the XML-file and facilitate data access with Python functions. We also defined several other functions to perform some simple tasks associated with the geological data and the geological model. Object definition and functions are combined in a Python module.

The functionality of the modelling software itself is available externally via an API. For the purpose of the approach presented here, the methods to perform the model interpolation and to access the simulation results are important. We integrated the relevant parts of the API, available to date only as a Windows Dynamically Linked Library (DLL), into a Python module.

Mesh generation

The geological model itself is a continuous function in 3-D space. As flow simulations require a discretised version of the model, with a clear definition of cells and assigned properties, the geological model has to be processed into a mesh structure (commonly referred to as ''meshing''). We implemented a mapping approach for 3-D rectilinear meshes into our workflow. Once the mesh structure is defined, a geological identifier is assigned to each cell, according to the distribution of the subsurface geology (i.e. the geology is mapped on the grid structure). To date, we limited our approach to the relatively simple rectilinear mesh structures, but more complex mesh structures (including extruded triangular and FE-type meshes) should be possible as well.

Property assignment

Relevant properties for the specific type of flow simulation are then assigned to each cell, according to the geological identifier. Simple statistical simulations or parameter functions can easily be implemented in this step. It is, for example, possible to assign parameters randomly, according to a parameter distribution, or to change parameters as a function of depth below surface.

Simulation

The possibility to automate the set-up of the input file for the numerical simulation clearly depends on the hydrothermal simulation code used. We have implemented modules for the control of two commonly used fluid and heat flow simulation codes: TOUGH2 [Pruess et al., 1999] and SHEMAT [Clauser, 2003]. Both of these codes are controlled with ASCII input files, without the requirement of a graphical user interface. We have developed Python modules that enable the direct construction of these input files, including all simulation settings and several postprocessing options. Details of these Python modules are presented in Wellmann et al. [2011a].

Combination of previous steps

The workflow itself and most of our own programs are written in the open-source scripting language Python (www.python.org). Python is widely used in scientific computations [e.g. Langtangen, 2006], because it is a flexible, object-oriented language and a wide variety of extension modules are available for numerical methods, data analysis and visualization. It is possible to use parallel scripting functionalities and Python interpreters are available for almost every operating system.

The single elements of our workflow are integrated in separate modules and can be combined as required. It is also possible to run the single steps interactively from the Python command line. Furthermore, additional scientific and numeric Python modules can be integrated, for example to define an optimal rectilinear mesh structure or for an automated postprocessing and plotting of the simulation results. The direct integration of all our modules ensures flexibility in the simulation process.

If all modules are integrated into one controlling script (where all parameters and settings are defined), the whole process from discretised geological data to the results of the simulation can be completely automated.

Combining this workflow with a stochastic geological modelling method [Wellmann et al., 2010], we obtain a method to generate multiple geological model realizations and the subsequent flow simulations for these models automatically.

5.3.4 Case study: North Perth Basin, Western Australia

Using the workflow described above, we present an application of both measures, information entropy and thermal entropy production, for a complex case study to investigate the influence of geological data quality on the uncertainty of geological model and flow predictions. Our case study is a geothermal resource area in the North Perth Basin, Western Australia (Fig. 5.26, left). The geological setting is a half-graben structure with a deep sedimentary basin (> 10 km in depth). As seismic resolution is poor in the region and few wells penetrate deep into the basin, two main structural uncertainties exist in this region [Mory and Iasky, 1997]:

- The exact position of the geological surfaces at depth is not well known;
- Additional faults might exist in the basin.

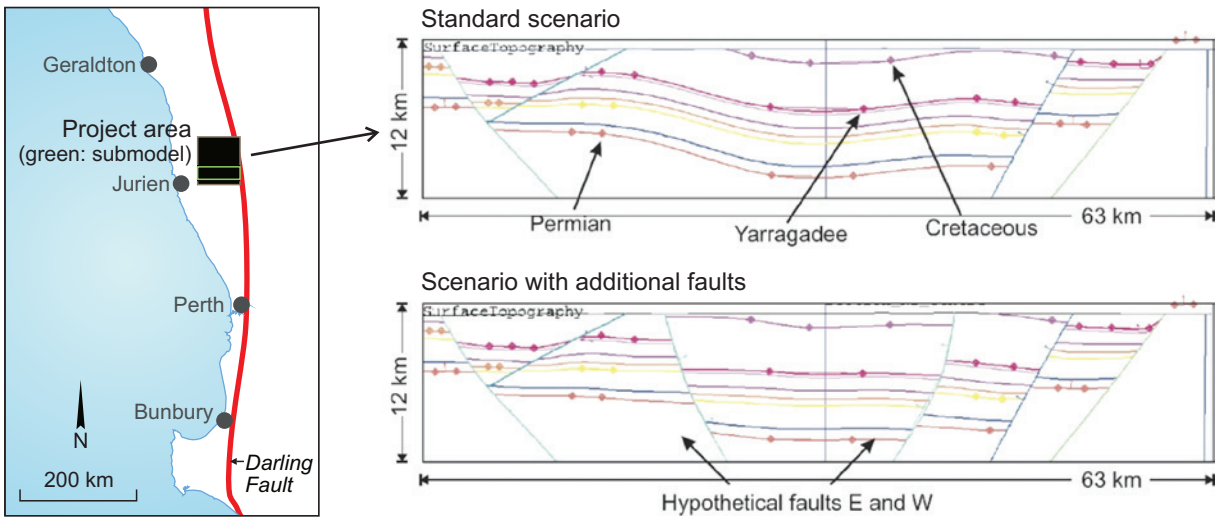

Figure 5.26: Left figure: Location of the model area in the North Perth Basin; the simulated hydrothermal model is a full three-dimensional submodel (green) of a regional scale geological model; Right: vertical section through the model showing geological structures and control points for the standard scenario and a scenario with additional faults in the basin.

Based on these two main types of uncertainty, we evaluate two uncertainty scenarios: in the first case (Fig. 5.26, standard scenario), only the position of geological surfaces at depth is considered uncertain. In the second case (Fig. 5.26, fault scenario), additional normal faults are introduced, in accordance with the general tectonic setting.

The aim of the study is to evaluate for these scenarios how decreasing accuracy in the initial geological data affects the simulated hydrothermal flow fields. A Gaussian error was assumed for all data points in Figure 5.26. Standard deviations are increasing with depth, from 50 m to 1000 m for the high accuracy data case, to 150 m to 2000 m for the low accuracy data case (see Table 5.5).

For each of these scenarios, 20 realizations of the structural geological model were created, and the coupled hydrothermal flow field was simulated for each of these structural realizations with the workflow presented above. The geological model is discretised into a regular grid with 250 x 25 x 200 cells. The model has a size of 63 km x 15 km x 12 km. Flow boundary conditions are no-flow at all boundaries. Thermal boundary conditions are basal heat flux, fixed annual mean temperature at the top and no flow at lateral boundaries. For more details about the hydrothermal simulation itself, see Wellmann et al. [2011c].

For each of these scenarios, the information entropy of the structural geological model and thermal entropy productions of each of the realizations for a simulation time of 100 000 years are calculated.

The cell information entropy for the low data accuracy case of both scenarios is presented in Figure 5.27. The increase of uncertainties in the structural model with depth is clearly visible, as well as the influence of the additional faults.

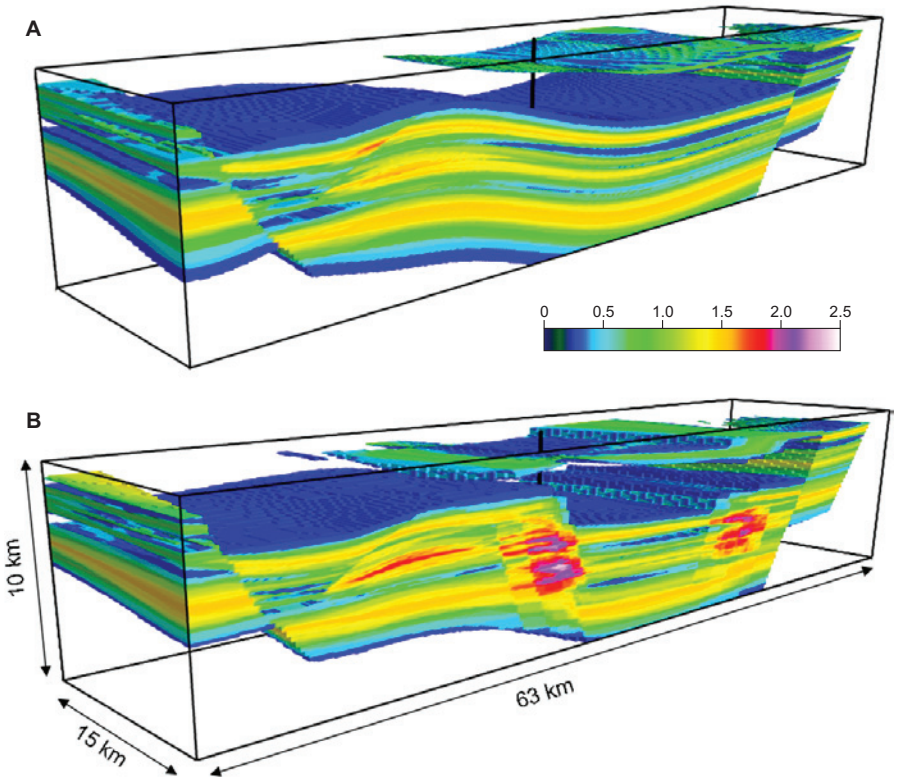

Figure 5.27: Visualisation of cell information entropies for the case of low data accuracy in (A) the standard scenario and (B) the scenario with additional faults, filtered for values of H>0.

Scenario	Shallow	Deep	Additional faults
1A	50	300	n/a
1B	100	600	n/a
1C	150	900	n/a
2A	50	300	1000
2B	100	600	1500
2C	150	900	2000

Table 5.5: Standard deviations [metres] assigned to the geological surface contact points for the scenarios with (1 A-C) and without (2 A-C) faults (see Fig. 5.26). The subscenarios A-C simulate the effect of decreasing geological data quality.

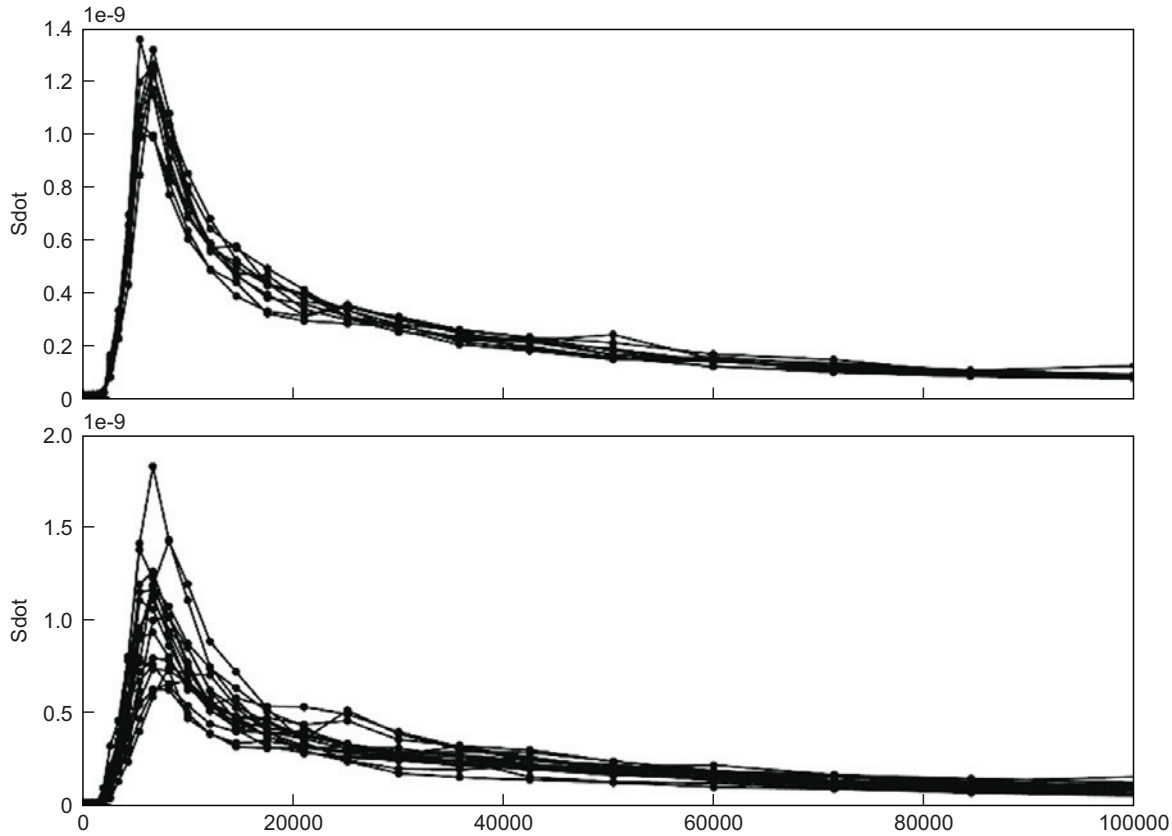

Figure 5.28: Average specific thermal entropy production during the equilibration phase of hydrothermal simulations for scenarios 2A (high data quality; top) and 2C (low data quality; bottom).

Figure 5.28 shows the development of the average specific thermal entropy production over a simulation time of 100 000 years. Presented here are the results for the scenario with additional faults: the high data accuracy (Scenario 2A) and the low data accuracy (Scenario 2C) cases. Initially, all models are in a conductive steady state and entropy production is accordingly zero. Then, convection sets in and the entropy production increases to a maximal value. After approximately 60 000 years, the hydrothermal systems appear to reach a finite entropy production states. It is clearly visible that the average specific entropy production values show a higher variability for the cases of low data accuracy. This behaviour is specifically obvious in the initial phase where convection sets in (around 10 000 years).

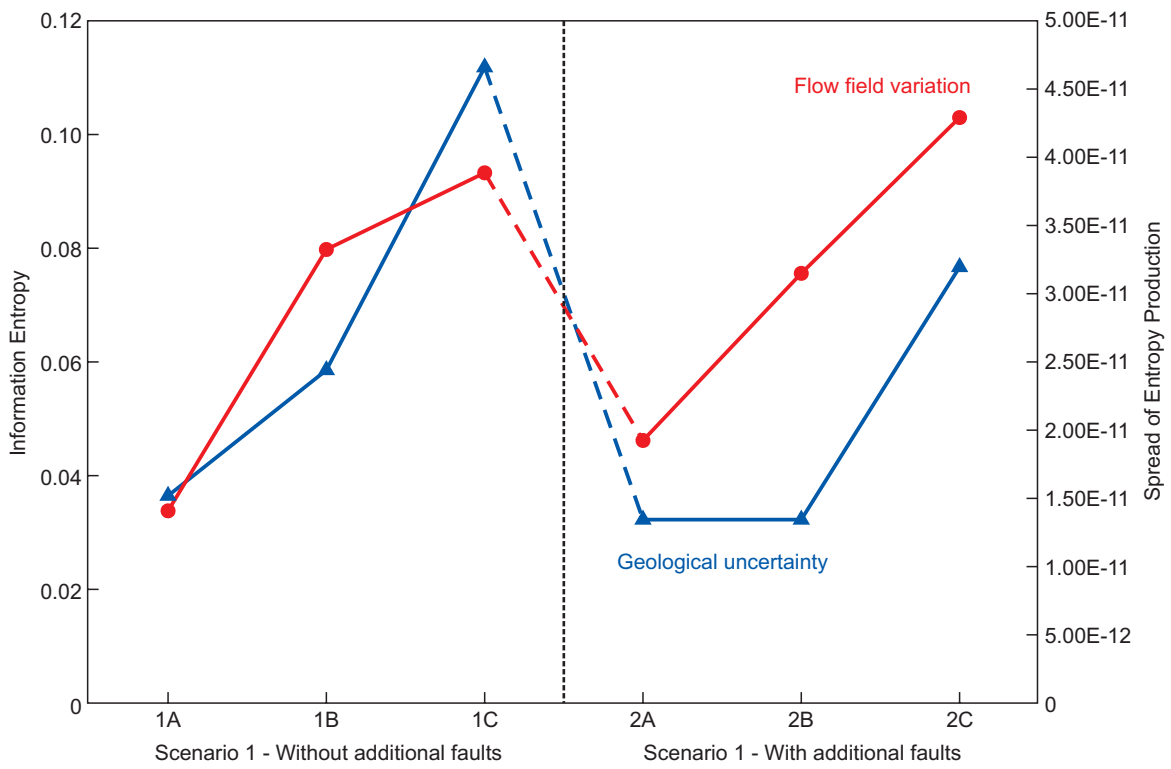

Figure 5.29: Comparison of geological uncertainty, evaluated with total information entropy, and flow field variation, determined from the spread of average specific entropy production for the different geological scenarios and decreasing data quality.

We now apply the total information entropy (Equation 5.3-2) and the spread (25th to 75th percentile) of the average specific entropy production (Equation 5.3-5) of the final simulation time step as measures of the system uncertainties. Results are presented in Figure 5.29. A comparison suggests that the overall uncertainties for both scenarios are similar, and that uncertainties increase with reduced data quality. It is interesting to note that, from scenario 2A to 2B, the uncertainty in the geological model increases, whereas the flow field variation does not significantly increase. A possible interpretation is that the additional faults in the basin have a stabilizing effect on the flow fields [e.g. Garibaldi et al., 2010].

5.3.5 Conclusions

The application of information entropy and thermal entropy production as system-based measures shows that they can be used as meaningful measures to interpret and compare uncertainties in subsurface geology and simulated flow fields. With both concepts, it is possible to derive a scalar value that is related to the state of uncertainty within each system. The total information entropy of a geological model represents the average uncertainty for the occurrence of a geological unit at each point in the model. The average specific thermal entropy production is directly related to the dominating heat transfer mechanisms in the hydrothermal model.

We applied the measures here in a case study to compare the influence of geological data accuracy on geological model uncertainty and flow field variability. The results show that both the geological model and the simulated subsurface flow fields are affected by a varying quality of geological input data. In fact, in this case uncertainties in the geological model and in the simulated flow fields respond in a similar way to decreasing accuracy of the geological input data. However, the difference in the flow field variation response for the two different geological scenarios indicates that geological structures have an important controlling effect on the flow behaviour.

The ability to describe the state of uncertainty in a system with a meaningful scalar value provides a way forward for physically based data compression as geological modelling and geothermal simulations are becoming more data-intensive. In future work, we will explore the possibility to integrate these values in stochastic inversion methods.

The comparison of geological uncertainties and flow field variation as a function of geological data quality has only been possible with the development of a dedicated workflow combining geological modelling and geothermal flow simulations. Even though sophisticated methods already exist that combine geological models with flow simulations [Suzuki et al., 2008], the methods presented here are, to the best of our knowledge, the first approach to integrate the accuracy of the geological input data itself. This is an important step forward as it enables the consideration of the quality of the initial geological data, even for complex fully three-dimensional geological settings.

It is worth noting that the system-based measures are applicable in a much broader context. We applied them here in the context of stochastic structural geological modelling and data intensive simulations. However, they could similarly be used to only compare results of two specific scenarios, or to analyse probability fields derived with different methods, for example geostatistical simulations. We envisage a wide range of possible applications of the measures in the context of geological models and hydrothermal simulations.

6. DISCUSSION

6.1 Synthesis of research results

The results presented in this report provide a comprehensive snapshot of geothermal numerical modelling and data analysis applied to Western Australia.

The prospectivity studies demonstrate the importance of good data, even if obtained from non-geothermal sources. The WAGCoE data catalogue is a crucial tool for amalgamating data useful to geothermal studies. For HSA projects, reservoir quality including thickness and permeability is a crucial determinant to the success of a geothermal scheme.

The studies of advection and convection in the Perth Basin point out that non-conductive process can be a major component of subsurface heat movement and should be considered in any geothermal study of porous systems. The inclusion of these processes into hydrothermal modelling greatly increases the numerical complexity and, more importantly, the data required for model input and calibration. Temperature enhancements due to moving fluids can be significant, and can provide a good target for further geothermal exploration. Knowledge of the hydraulic properties of the aquifers is essential, and highlights the need for additional information to define three-dimensional permeability and thermal property distributions in the major formations.

Specific detailed geothermal models of the Perth Basin provide great detail about the subsurface temperature conditions, and for hydrothermal models, the influence of fluid flow on the heat resource. Fluid and heat flow are strongly controlled by the underlying geologic structure. The detailed models identify critical data needed to complete the model and determine the main physical aspects controlling the geothermal reservoir behaviour. Calibration against field measurements can provide an important check for input data parameters; temperature measurement is relatively inexpensive and should be considered in any field investigation. However, existing data can often provide sufficient detail for preliminary desktop studies, without the need for additional financial expenditure. From a capability development point of view, the demands of comprehensive hydrothermal modelling studies point out the importance of developing an integrated modelling team and a seamless workflow to go from geologic data to final reservoir longevity results.

The theoretical and numerical tools developed by the WAGCoE team are important components to future geothermal numerical modelling. *escriptRT* provides a powerful but also user-friendly, flexible, and extensible platform which can easily be used by numerical modelling geologists. The coupling of thermal, hydrogeologic, mechanical, and chemical processes within the code allows consideration of additional physical phenomena in the conceptual model, and the ability to test and determine the most important processes in geothermal system behaviour. Likewise, the uncertainty workflow provides a comparison of geological uncertainties and flow field variation as a function of geological data quality. This tool provides an urgently needed way to quantify risk in the geothermal exploration process.

The hydrothermal modelling team of WAGCoE has provided important perspectives on geothermal exploration in Western Australia, going beyond the typical modelling workflow to predict temperature regimes, test hypotheses about non-conductive heat transport, estimate parameters, and quantify uncertainty.

6.2 Future directions

WAGCoE has provided a comprehensive sweep of geothermal modelling applied to Western Australia. However, our work does have some important limitations which should be addressed in future studies.

First, the conductive model presented in Section 4.2 can be used as a first-order approximation to steady state conditions for future simulations of hydrothermal processes in the Perth Basin by providing boundary conditions. Ongoing work into calibration of this model will provide information about the sensitivity of the results to parameter values and help direct future programs to more extensively measure uncertain controls in the geothermal models. The large-scale conductive model provides important data for a comprehensive resource analysis of the entire Perth Basin.

With this basis, the new tool of *escriptRT* should be used to provide coupled modelling of thermal and hydrogeological processes on realistic grids throughout the Perth Basin. The flexibility of *escriptRT* will allow more detailed representations of geologic formations than is possible in the codes that were used for the numerical models described in this report (Feflow and Shemat), from deep and poorly sampled formations to shallow well-understood aquifers. A multiphysics approach should be undertaken to determine where fluid flow is important and requires detailed simulation, and similarly determine where meaningful averages can substitute for computationally expensive models.

Second, the specific hydrothermal models presented here do not account for intra-formation heterogeneity of rock properties, due to insufficient data on parameter variability. Research in multiple fields [e.g. Simmons et al., 2010, Kuznetsov et al., 2010, Watanabe et al., 2010] shows that heterogeneity can strongly influence heat flow. One future aim is to better establish the three-dimensional permeability distribution in the Perth Basin using forward stratigraphic modelling [Corbel et al., 2012] integrated with additional laboratory measurements and well-log interpretations. There is some theoretical evidence to suggest that variability will decrease the likelihood of density-induced convection. Stochastic realisation techniques [Wellmann, 2011] will allow quantification of the uncertainty associated with the modelling process and upscaling point measurements. Similar work on the variability of thermal conductivity using density as an analogue can lead to additional insights into the conductive transport of heat.

Finally, a more structured approach to investigating the uncertainties in geothermal simulation could be undertaken with the new numerical tools and theoretical framework. Uncertainties in the structural model, such as the location of faults or deep formation boundaries or the influence of fault permeabilities, should be propagated through into hydrothermal models. By running multiple model realisations on supercomputers, geothermal exploration risk can be better defined to help the geothermal industry.

REFERENCES

ABAQUS/Standard (2008). User's Manual Version 6.7. Hibbit, Karlsson and Sorenson Inc., Pawtucket.

Agemar, T., Alten, J., Kühne, K., Maul, A., Pester, S., Wirth, W., and Schulz, R. (2007). Development of a Geothermal Information System for Germany. In Proceedings European Geothermal Congress, 2007.

AGRCC (2010). The geothermal reporting code, second edition (2010). Technical report, The Australian Geothermal Energy Group (AGEG) and the Australian Geothermal Energy Association (AGEA). Australian Code for Reporting of Exploration Results, Geothermal Resources and Geothermal Reserves.

Aitken, A. (2010). Moho geometry gravity inversion experiment (MoGGIE): A refined model of the Australian Moho, and its tectonic and isostatic implications. Earth and Planetary Science Letters, 297(1-2):71–83.

Anderson, M. (2005). Heat as a ground water tracer. Ground Water, 43(6):951–968.

Andersson, J. and Hudson, J. (2004). T-H-M-C modelling of rock mass behaviour - 1 : the purposes, the procedures and the products. In Stephanson, O., editor, Coupled Thermo-Hydro-Mechanical-Chemical Processes in Geo-Systems - Fundamentals, Modelling, Experiments and Applications, volume 2 of Elsevier Geo-Engineering Book Series, 433–438. Elsevier.

Armero, F. (1999). Formulation and finite element implementation of a multiplicative model of coupled poro-plasticity at finite strains under fully saturated conditions. Computer Methods in Applied Mechanics and Engineering, 171(3-4):205 – 241.

Arya, A., Hewett, T., Larson, R., and Lake, L. (1988). Dispersion and reservoir heterogeneity. SPE Reservoir Engineering, 3(1):139–148.

Bachler, D., Kohl, T., and Rybach, L. (2003). Impact of graben-parallel faults on hydrothermal convection–Rhine Graben case study. Physics and Chemistry of the Earth, Parts A/B/C, 28(9-11):431–441.

Bartels, J., Kühn, M., and Clauser, C. (2003). Numerical simulation of reactive flow using SHEMAT. In Clauser, C. (Ed.) Numerical simulation of reactive flow in hot aquifers, 5–74. Springer.

Bear, J. (1972). Dynamics of fluids in porous media. Elsevier, New York.

Bear, J. (1979). Hydraulics of Groundwater. McGraw-Hill series in water resources and environmental engineering. London: McGraw-Hill.

Beardsmore, G. and Cull, J. (2001). Crustal heat flow: a guide to measurement and modelling. Cambridge University Press.

Bercovici, D. and Ricard, Y. (2003). Energetics of a two-phase model of lithospheric damage, shear localization and plate-boundary formation. Geophysical Journal International, 152(3):581–596.

Bestow, T. (1982). The potential for geothermal energy development in Western Australia. Technical Report 1982/6, Geological Survey of Western Australia.

Biot, M. A. (1941). General theory of three-dimensional consolidation. Journal of Applied Physics, 12(2):155–164.

Bjorlykke, K., Mo, A., and Palm, E. (1988). Modelling of thermal convection in sedimentary basins and its relevance to diagenetic reactions. Marine and Petroleum Geology, 5(11):338–351.

Blöcher, M., Zimmermann, G., Moeck, I., Brandt, W., Hassanzadegan, A., and Magri, F. (2010). 3D numerical modeling of hydrothermal processes during the lifetime of a deep geothermal reservoir. Geofluids, 10(3):406–421.

Bloomfield, G. (2010). Hydrogeologic study of geothermal logging in the Perth Metropolitan Area, Western Australia. Honours thesis, School of Earth and Environmental Science, University of Western Australia.

Bodorkos, S. and Sandiford, M. (2006). Thermal and mechanical controls on the evolution of Archean crustal deformation: examples from Western Australia. In Benn, K., Mareschal, J.-C. and Condie, K. (Eds.), Archean geodynamics and environments, 131–147. American Geophysical Union.

Bundschuh, J. and Arriaga, M. (2010). Introduction to the Numerical Modeling of Groundwater and Geothermal Systems: Fundamentals of Mass, Energy, and Solute Transport in Poroelastic Rocks, volume 2. Leiden, The Netherlands: CRC Press.

Calcagno, P., Chilès, J., Courrioux, G., and Guillen, A. (2008). Geological modelling from field data and geological knowledge: Part I. Modelling method coupling 3D potential-field interpolation and geological rules. Physics of the Earth and Planetary Interiors, 171(1-4):147–157.

Callen, H. (1985). Thermodynamics and an Introduction to Thermostatistics, volume 1. Wiley-VCH, 2nd edition.

Caumon, G., Collon-Drouaillet, P., Le Carlier de Veslud, C., Viseur, S., and Sausse, J. (2009). Surface-based 3D modeling of geological structures. Mathematical Geosciences, 41(8):927–945.

Chopping, R. and Cleverley, J. (2008). Flowpaths and drivers: Creating forward geophysical models from reactive transport simulations. In Korsch, R.J. and Barnicoat, A.C. (Eds.), New Perspectives: The foundations and future of Australian exploration, Geoscience Australia Record 2008/09, 23–28.

Chopra, P. (2005). Hot artesian water powers an outback town in Australia. Geo-Heat Center Quarterly Bulletin, 26(2):25–26.

Chopra, P. and Holgate, F. (2007). Geothermal energy potential in selected areas of Western Australia. unpublished, Earthinsite.com. Prepared for the Geological Survey of Western Australia, Statutory petroleum exploration report G31888 A1.

Chrysochoos, A. and Belmahjoub, F. (1992). Thermographic analysis of thermomechanical couplings. Archives of Mechanics, 44(1):55–68.

Clauser, C. (2003). Numerical simulation of reactive flow in hot aquifers: SHEMAT and processing SHEMAT. Springer Verlag.

Clauser, C. (2009). Heat transport processes in the Earth's crust. Surveys in geophysics, 30(3):163–191.

Clauser, C., Griesshaber, E., and Neugebauer, H. (2002). Decoupled thermal and mantle helium anomalies: Implications for the transport regime in continental rift zones. Journal of geophysical research, 107(B11):2269.

Clauser, C. and Villinger, H. (1990). Analysis of conductive and convective heat transfer in a sedimentary basin, demonstrated for the Rheingraben. Geophysical Journal International, 100(3):393–414.

Cocks, A. and Ashby, M. (1980). Intergranular fracture during power-law creep under multiaxial stresses. Metal Science, 14(8-9):395–402(8).

Commander, D. (1974). Hydrogeology of the Mandurah-Pinjarra area. In Western Australia Geologic Survey Annual Report, volume 1973, 20–25.

Commander, D. (1978). Geology and hydrogeology of the Eneabba borehole line. Geological Survey of Western Australia Report 1978/7.

Corbel, S., Colgan, E., Reid, L., and Wellmann, J. (2010). Building 3D geological models for groundwater and geothermal exploration. In Groundwater 2010, Canberra, Australia. International Association of Hydrogeology.

Corbel, S., Griffiths, C., Dyt, C., and Ricard, L. (2012). Hot sedimentary aquifer characterizatoin using stratigraphic forward modelling, Perth Basin, Australia. In Proceedings, Thirty-Seventh Workshop on Geothermal Reservoir Engineering, Stanford, California. Stanford University.

Corbel, S. and Poulet, T. (2010). WAGCoE data catalogue for geothermal exploration. In Proceedings - 2010 6th IEEE International Conference on e-Science, eScience 2010, 89–94.

Corbel, S., Reid, L., and Ricard, L. (2011). Prefeasibility geothermal exploration workflow applied to the Fitzroy Trough, Western Australia. In Middleton, M. F. and Gessner, K. (Eds.), Western Australian Geothermal Energy Symposium, volume 1, 25, Perth, Australia.

Coussy, O. (2004). Poromechanics. Wiley.

Crostella, A. (1995). An evaluation of the hydrocarbon potential of the onshore northern Perth Basin, Western Australia. Geological Survey of Western Australia Report 43.

Crostella, A. and Backhouse, J. (2000). Geology and petroleum exploration of the central and southern Perth Basin, Western Australia. Geological Survey of Western Australia Report 57.

CSIRO (2011). Pressureplot. http://www.pressureplot.com/.

Davidson, W. (1995). Hydrogeology and groundwater resources of the Perth Region, Western Australia. Geological Survey of Western Australia Bulletin 142.

Davidson, W. and Yu, X. (2008). Perth regional aquifer modelling system (PRAMS) model development: Hydrogeology and groundwater modelling. Hydrogeological Record Series HG 20, Western Australian Department of Water, Perth.

Davies, M., Gross, L., and Mühlhaus, H.-B. (2004). Scripting high performance earth systems simulations on the SGI Altix 3700. In Werner, B. (Ed.), Proceedings of the 7th International Conference on High Performance Computing and Grid in the Asia Pacific Region, 244 –251. IEEE Computer Society.

de Marsily, G. (1986). Quantitative Hydrogeology. Academic Press.

Delle Piane, C., Esteban, L., Timms, N. and Israni, S. (2012). Physical properties of Cretaceous and Jurassic units of the Perth Basin, Western Australia: implications for geothermal exploration. Geophysical Journal International, in preparation.

Department of Water (2008). Perth regional aquifer modelling system (PRAMS) model development: Calibration of the Coupled Perth Regional Aquifer Model PRAMS 3.0. Hydrogeological record series HG28, Western Australian Department of Water.

Dezayes, C., Genter, A., Thinon, I., Courrioux, G., and Tourlière, B. (2008). Geothermal potential assessment of clastic triassic reservoirs (Upper Rhine Graben, France). In 32nd Workshop on Geothermal Reservoir Engineering, 28–30.

Diersch, H.-J. (2005). FEFLOW finite element subsurface flow and transport simulation system, reference manual. WASY, Institute for Water Resources Planning and Systems Research, Berlin.

Diersch, H. J. G. and Kolditz, O. (1998). Coupled groundwater flow and transport: 2. Thermohaline and 3D convection systems. Advances in Water Resources, 21(5):401–425.

Diersch, H. J. G. and Kolditz, O. (2002). Variable-density flow and transport in porous media: Approaches and challenges. Advances in Water Resources, 25(8-12):899–944.

Driscoll, J., Mortimer, L., Waining, B., Cordon, E., and Beardsmore, G. (2009). Geothermal energy potential in selected areas of Western Australia (Canning Basin). Technical Report DOIR0681008, Department of Mines and Petroleum, Western Australia, Hot Dry Rocks Pty Ltd.

Drury, M., Jessop, A., and Lewis, T. (1984). The detection of groundwater flow by precise temperature measurements in boreholes. Geothermics, 13(3):163–174.

Elder, J. W. (1967). Transient convection in a porous medium. Journal of Fluid Mechanics, 27:609–and.

Ferguson, J., Etminan, H., and Ghassemi, F. (1992). Salinity of deep formation water in the Canning Basin, Western Australia. BMR Journal of Australian Geology and Geophysics BJAGDT,, 13(2):93–105.

Finsterle, S. (2004). Multiphase inverse modeling: Review and iTOUGH2 applications. Vadose Zone Journal, 3(3):747.

Fournier, R. O. (1990). Double-diffusive convection in geothermal systems: the Salton Sea, California, geothermal system as a likely candidate. Geothermics, 19(6):481–496.

Freeman, M. and Donaldson, M. (2006). Geology of the southern Perth Basin and Margaret River wine district, southwestern Western Australia – a field guide. Western Australian Geological Survey Record 2006/20.

Fusseis, F., Regenauer-Lieb, K., Liu, J., Hough, R. M., and De Carlo, F. (2009). Creep cavitation can establish a dynamic granular fluid pump in ductile shear zones. Nature, 459(7249):974–977.

Garibaldi, C., Guillou-Frottier, L., Lardeaux, J., Bonte, D., Lopez, S., Bouchot, V., and Ledru, P. (2010). Thermal anomalies and geological structures in the Provence basin: Implications for hydrothermal circulations at depth. Bulletin de la Societe Geologique de France, 181(4):363.

Geiger, S., Driesner, T., Heinrich, C., and Matthäi, S. (2006). Multiphase thermohaline convection in the earth's crust: II. Benchmarking and application of a finite element – finite volume solution technique with a NaCl–H2O Equation of State. Transport in Porous Media, 63(3):435–461.

Geological Survey of Western Australia (2011a). 3D geological model building, and 3D temperature and heat flow calculation for the northern Perth Basin. Western Australian Geological Survey Record 2011/6.

Geological Survey of Western Australia (2011b). Summary of petroleum prospectivity, Western Australia 2011. Technical report, Geological Survey of Western Australia.

Geoscience Australia (2011). OZCHEM national whole rock geochemistry database. Accessed 9 February 2012.

Ghassemi, F., Etminan, H., and Ferguson, J. (1992). A reconnaissance investigation of the major Paleozoic aquifers in the Canning Basin, Western Australia, in relation to Zn-Pb mineralisation. BMR Journal of Australian Geology and Geophysics,, 13(2):37–57.

Ghori, K., Mory, A., and Iasky, R. (2005). Modeling petroleum generation in the Paleozoic of the Carnarvon Basin, Western Australia: Implications for prospectivity. AAPG bulletin, 89(1):27.

Gibson, H., Seikel, R., FitzGerald, D., Middleton, M., and Ghori, A. (2011). 3D geology, temperature, heat flow and thermal gradient modeling of the north Perth Basin, Western Australia. In Society of Exploration Geophysicsists Meeting, 1227–1231, San Antonio, TX.

Glasson, S. (2011). Investigation of salinity within the Yarragadee Aquifer in the Perth area. Honour's thesis, School of Engineering, University of Western Australia.

Goodchild, M., Chih-Chang, L., and Leung, Y. (1994). Visualizing fuzzy maps. In Visualization in geographical information systems, 158–167. London: John Wiley and Sons.

Goutorbe, B., Lucazeau, F., and Bonneville, A. (2008). Surface heat flow and the mantle contribution on the margins of Australia. Geochemistry Geophysics Geosystems, 9(5):Q05011.

Gross, L., Fenwick, J., Gao, L., and Green, D. (2010). A comparison of clusters with Intel "Nehalem" and "Harpertown" processors using an FEM benchmark. In 4th eResearch Australasia Conference, Gold Coast, Australia. 8-12 Nov 2010.

Gross, L., Mühlhaus, H., Thorne, E., and Steube, K. (2008). A new design of scientific software using Python and XML. Pure and Applied Geophysics, 165(3):653–670.

Guimarães, L. D., Gens, A., and Olivella, S. (2007). Coupled thermo-hydro-mechanical and chemical analysis of expansive clay subjected to heating and hydration. Transport in Porous Media, 66:341–372.

Haenel, R. and Stegena, L. (1988). Fundamentals of geothermics. In Haenel, R., Rybach, L. and Stegena, L. (Eds.) Handbook of terrestrial heat-flow density determination: with guidelines and recommendations of the International Heat Flow Commission, 9–58. Springer.

Havord, P., Apak, S., and Carlsen, G. (1997). Permo-Carboniferous petroleum reservoir data, selected wells, Canning Basin, Western Australia. Technical Report Record 1996/11, Geological Survey of Western Australia, Department of Minerals and Energy, Perth. Edition 1.

He, S. and Middleton, M. (2002). Heat flow and thermal maturity modelling in the Northern Carnarvon Basin, North West Shelf, Australia. Marine and petroleum geology, 19(9):1073–1088.

Helgeson, H. C., Kirkham, D. H., and Flowers, G. C. (1981). Theoretical prediction of the thermodynamic behavior of aqueous electrolytes by high pressures and temperatures; IV, Calculation of activity coefficients, osmotic coefficients, and apparent molal and standard and relative partial molal properties to 600 °C and 5kb. American Journal of Science, 281(10):1249–1516.

Hopkins, J. (2011). Relationships in the Leeuwin Complex mineralogy, lithology and heat production, Western Australia. Honours thesis, Curtin University.

Horne, R. (1997). Modern well test analysis: A computer-aided approach. Petroway, Palo Alto, CA.

Horowitz, F., K, R.-L., and et al, W. J. (2008). Evidence for hydrothermal convection in the Perth Basin, Australia. In Gurgenci, H. and Budd, A., editors, Proceedings of the Sir Mark Oliphant International Frontiers of Science and Technology Australian Geothermal Energy Conference.

Horowitz, F. and Regenauer-Lieb, K. (2009). Mean annual surface temperature (MAST) and other thermal estimates for Australia and New Zealand from 6 years of remote sensing observations. In Proceedings, NZ Geothermal Workshop.

Hot Dry Rocks Pty Ltd (2008). Geothermal energy potential in selected areas of Western Australia (Perth Basin). Technical report, Department of Industry and Resources, Western Australia.

Hot Dry Rocks Pty Ltd (2009). Geothermal energy potential in selected areas of Western Australia (Canning Basin). Technical report, Department of Industry and Resources, Western Australia.

Hot Dry Rocks Pty Ltd (2010a). Geothermal energy potential in selected areas of Western Australia (Bonaparte Basin). Technical report, Department of Industry and Resources, Western Australia.

Hot Dry Rocks Pty Ltd (2010b). Geothermal energy potential in selected areas of Western Australia (Carnarvon Basin). Technical report, Department of Industry and Resources, Western Australia.

Hot Dry Rocks Pty Ltd (2010c). Geothermal energy potential in selected areas of Western Australia (Officer Basin). Technical report, Department of Industry and Resources, Western Australia.

Hürsch, W. L. and Lopes, C. V. (1995). Separation of concerns. Technical report, College of Computer Science, Northeastern University.

Hurter, S. and Schellschmidt, R. (2003). Atlas of geothermal resources in Europe. Geothermics, 32(4-6):779–787.

Hyndman, R., Lambert, I., Heier, K., Jaeger, J., and Ringwood, A. (1968). Heat flow and surface radioactivity measurements in the Precambrian shield of Western Australia. Physics of the Earth and Planetary Interiors, 1(2):129–135.

Ingebritsen, S. E., Sanford, W. E., and Neuzil, C. (2006). Groundwater in Geologic Processes. Cambridge University Press, 2nd edition.

IOC, SCOR, and IAPSO (2010). The international thermodynamic equation of seawater – 2010: Calculation and use of thermodynamic properties. Technical report, UNESCO.

Irwin, R. (2007). Hydrogeology of the Dongara borehole line. Hydrogeological Record Series HG 4, Department of Water.

Jessop, A. and Majorowicz, J. (1994). Fluid flow and heat transfer in sedimentary basins. Geological Society, London, Special Publications, 78(1):43–54.

Kachanov, L. M. (1958). Time of the rupture process under creep conditions. Izvestiya Akademii Nauk SSSR, Otdelenie Teckhnicheskikh Nauk, 8:26–31.

Karrech, A., Regenauer-Lieb, K., and Poulet, T. (2011). Continuum damage mechanics for the lithosphere. Journal of Geophysical Research, 116:B04205, 14 pp.

Kharaka, Y. and Thordsen, J. (1992). Stable isotope geochemistry and origin of waters in sedimentary basins. In Clauer, N. and Chaudhuri S. (Eds.), Isotopic signatures and sedimentary records, 411–466. Springer.

Kuhl, D., Bangert, F., and Meschke, G. (2004). Coupled chemo-mechanical deterioration of cementitious materials. Part I: Modeling. International Journal of Solids and Structures, 41(1):15 – 40.

Kühn, M. (2009). Modelling feedback of chemical reactions on flow fields in hydrothermal systems. Surveys in Geophysics, 30:233–251. 10.1007/s10712-009-9055-5.

Kuznetsov, A., Nield, D., and Simmons, C. T. (2010). The effect of strong heterogeneity on the onset of convection in a porous medium: Periodic and localized variation. Transport in Porous Media, 81:123–139.

Lajaunie, C., Courrioux, G., and Manuel, L. (1997). Foliation fields and 3D cartography in geology: principles of a method based on potential interpolation. Mathematical Geology, 29(4):571–584.

Langtangen, H. (2006). Python scripting for computational science, volume 3. Springer Verlag.

Lanru, J. and Xiating, F. (2003). Numerical modeling for coupled Thermo-Hydro-Mechanical and Chemical processes (THMC) of geological media——international and Chinese experiences. Chinese Journal of Rock Mechanics and Engineering, 22:1704–1715.

Larking, A. and Meyer, G. (2010). Geothermal energy in the Perth Basin, Australia – Comparisons with the Rhine Graben. In Australian Geothermal Energy Conference, Adelaide, South Australia.

Lemaître, J. and Chaboche, J.-L. (2001). Mécanique des matériaux solides. Dunod, Paris.

Li, Y.-H. and Gregory, S. (1974). Diffusion of ions in sea water and in deep-sea sediments. Geochimica et cosmochimica acta, 38(5):703–714.

Lindsay, R. and Commander, D. (2006). Hydrogeological assessment of the Fitzroy Alluvium. Hydrogeological Record Series HG 16, Department of Water, Western Australia.

Mallet, J. (1992). Discrete smooth interpolation in geometric modelling. Computer-aided design, 24(4):178–191.

Matthews, C. (2009). Geothermal energy prospectivity of the Torrens Hinge Zone: evidence from new heat flow data. Exploration Geophysics, 40(3):288–300.

Matthews, C. and Beardsmore, G. (2008). New heat flow data from south-eastern South Australia. Exploration Geophysics, 38(4):260–269.

McCune, C. C., Fogler, H. S., and Kline, W. E. (1979). An experimental technique for obtaining permeability-porosity relationships in acidized porous media. Industrial and Engineering Chemistry Fundamentals, 18(2):188–191.

Middlemis, H., Merrick, N., Ross, J., and Rozlapa, K. (2001). Groundwater modelling guidelines for Australia–An overview. In Proceedings, MODSIM 2001 International Congress on Modelling and Simulation, Canberra.

Mooney, W., Beroza, G., and Kind, R. (2007). Fault zones from top to bottom: A geophysical perspective. In Handy, M., Hirth, G., and Hovius, N., editors, Tectonic Faults: Agents of change on a dynamic Earth, 9–46. MIT Press, Cambridge, USA.

Morel, F. (1983). Principles of aquatic chemistry. J. Wiley, New York.

Mory, A. and Iasky, R. (1997). Stratigraphy and structure of the onshore northern Perth Basin, Western Australia. Western Australia Geological Survey Report 46.

Mory, A., Haig, D.W., McLoughlin, S. and Hocking, R.M. (2005). Geology of the Northern Perth Basin Western Australia: A field guide. Western Australia Geological Survey Record 2005/9.

Muffler, P. and Cataldi, R. (1978). Methods for regional assessment of geothermal resources. Geothermics, 7(2-4):53–89.

Nextgen Networks (2011). Regional Backbone Blackspots Program – Geraldton. URL. Accessed 2 February 2011.

Nield, D. and Bejan, A. (1992). Convection in porous media. Springer-Verlag, New York.

Nield, D. A. (1994). Estimation of an effective Rayleigh number for convection in a vertically inhomogeneous porous-medium or clear fluid. International Journal of Heat and Fluid Flow, 15(4):337–340.

Nield, D. A. and Bejan, A. (2006). Convection in porous media. Springer-Verlag, New York.

Norden, B. and Forster, A. (2006). Thermal conductivity and radiogenic heat production of sedimentary and magmatic rocks in the Northeast German Basin. AAPG bulletin, 90(6):939.

Ogata, A. and Banks, R. (1961). A solution of the differential equation of longitudinal dispersion in porous media, United States Geological Survey Professional Paper 411-A.

Olierook, H. (2011). Fault-related strain accommodation and diagenesis in the Northern Perth Basin: Implications for fluid pathways. Honours thesis, Curtin University.

Ondreka, J., Rusgen, M., Stober, I., and Czurda, K. (2007). GIS-supported mapping of shallow geothermal potential of representative areas in south-western Germany – Possibilities and limitations. Renewable Energy, 32(13):2186–2200.

Oschmann, V. (2010). Going renewable: Germany's energy future. Presentation at CSIRO, Kensington, Western Australia on 19 May 2010.

Ozawa, H., Ohmura, A., Lorenz, R., and Pujol, T. (2003). The second law of thermodynamics and the global climate system: a review of the maximum entropy production principle. Rev. Geophys, 41(4):1018.

Pearce, A., Rossbach, M., Tait, M., and Brown, R. (1999). Sea temperature variability off Western Australia 1990 to 1994. Fisheries Research Report 111, Fisheries Western Australia, Perth, Western Australia.

Pester, S., Agemar, T., Alten, J., Kuder, J., Kuehne, K., Maul, A., and Schulz, R. (2010). GeotIS–the Geothermal Information System for Germany.

Phillips, O. (1991). Flow and reactions in permeable rocks. Cambridge University Press, Cambridge, UK.

Pijaudier-Cabot, G., Dufour, F., and Choinska, M. (2009). Permeability due to the increase of damage in concrete: From diffuse to localized damage distributions. Journal of Engineering Mechanics, 135(9):1022–1028.

Playford, P., Cockbain, A., and Low, G. (1976). Geology of the Perth Basin, Western Australia. Geological Survey of Western Australia Bulletin 124.

Poisson, A. and Papaud, A. (1983). Diffusion coefficients of major ions in seawater. Marine Chemistry, 13(4):265–280.

Potma, W., Roberts, P. A., Schaubs, P. M., Sheldon, H. A., Zhang, Y., Hobbs, B. E., and Ord, A. (2008). Predictive targeting in Australian orogenic-gold systems at the deposit to district scale using numerical modelling. Australian Journal of Earth Sciences, 55(1):101–122.

Poulet, T. (2011). Reactive Transport in damageable geomaterials - Thermal-Hydrological-Mechanical-Chemical coupling of geological processes. PhD thesis, University of Western Australia.

Poulet, T. and Corbel, S. (2012). WAGCoE data catalogue. Final report of Project 1, Perth Basin assessment program. CSIRO Report EP118209, Western Australian Geothermal Centre of Excellence.

Poulet, T., Corbel, S., and Stegherr, M. (2010a). A geothermal web catalog service for the Perth Basin. In Australian Geothermal Energy Conference, Adelaide.

Poulet, T., Gross, L., Georgiev, D., and Cleverley, J. (2011a). *escriptRT*: reactive transport simulation in Python using escript. Computers and Geosciences, in press.

Poulet, T., Regenauer-Lieb, K., and Karrech, A. (2010b). A unified multi-scale thermodynamical framework for coupling geomechanical and chemical simulations. Tectonophysics, 483(1-2):178 – 189.

Poulet, T., Regenauer-Lieb, K., Karrech, A., Fisher, L., and Schaubs, P. (2011b). Thermal-hydraulic-mechanical-chemical coupling using *escriptRT* and Abaqus. Tectonophysics, 526-529(1-2):124–132.

Powell, W., Chapman, D., Balling, N., and Beck, A. (1988). Continental Heat-flow density. In Haenel, R., Rybach, L. and Stegena, L. (Eds.), Handbook of terrestrial heat-flow density determination: with guidelines and recommendations of the International Heat Flow Commission, 167. Springer.

Pribnow, D. and Schellschmidt, R. (2000). Thermal tracking of upper crustal fluid flow in the Rhine Graben. Geophysical Research Letters, 27(13):1957–1960.

Pruess, K., Oldenburg, C., and Moridis, G. (1999). TOUGH2 user's guide, version 2.0. Lawrence Berkeley National Laboratory.

Quaschning, V. and Jourdan, H. (2010). Renewable Energy and Climate Change. Wiley Online Library.

Raffensperger, J. P. and Vlassopoulos, D. (1999). The potential for free and mixed convection in sedimentary basins. Hydrogeology Journal, 7(6):505–520.

Rath, V., Wolf, A., and Bücker, H. (2006). Joint three-dimensional inversion of coupled groundwater flow and heat transfer based on automatic differentiation: sensitivity calculation, verification, and synthetic examples. Geophysical Journal International, 167(1):453–466.

Regenauer-Lieb, K. (1998). Dilatant plasticity applied to Alpine collision: ductile void growth in the intraplate area beneath the Eifel volcanic field. Journal of Geodynamics, 27(1):1 – 21.

Regenauer-Lieb, K., Chua, H., Wang, X., Horowitz, F., Wellmann, F., Fusseis, F., Poulet, T., Sheldon, H., Trefry, M., Wilkes, P., Hoskin, T., Seibert, S., Cawood, P., Reddy, S., Wilson, M., Evans, N., Timms, N., Clarke, C., Batt, G., Gaede, O., McInnes, B., Webb, S., Cleverley, J., Aspandiar, M., Danisik, M., Dyskin, A., Pasternak, E., Karrech, A., Healy, D., Prentice, N., Shannahan, T., Thorn, C., Harvey, S., and M., M. (2009). The Western Australian Geothermal Centre of Excellence. In Australian Geothermal Energy Conference, Brisbane, Australia.

Regenauer-Lieb, K., Karrech, A., Chua, H., Horowitz, F., and Yuen, D. (2010). Time-dependent, irreversible entropy production and geodynamics. Philosophical Transactions of the Royal Society A, 368(1910):285.

Regenauer-Lieb, K. and Yuen, D. (2004). Positive feedback of interacting ductile faults from coupling of equation of state, rheology and thermal-mechanics. Physics of The Earth and Planetary Interiors, 142(1-2):113 – 135.

Reid, L., Bloomfield, G., Botman, C., Ricard, L., and Wilkes, P. (2011a). Temperature regime in the Perth Metropolitan Area: Results of temperature and gamma logging and analysis, June/July 2010. Technical report, Western Australian Geothermal Centre of Excellence.

Reid, L., Bloomfield, G., Botman, C., Ricard, L., and Wilkes, P. (2012). Shallow geothermal regime in the Perth metropolitan area. Australian Journal of Earth Science, in press.

Reid, L., Bloomfield, G., Ricard, L., Wilkes, P., and Botman, C. (2011b). Geothermal logging in Perth, Western Australia. In Australian Geothermal Energy Conference 2011, Melbourne, Australia.

Reid, L., Corbel, S., Ricard, L., Trefry, M., and Wellmann, J. (2010). Modelling hot sedimentary geothermal aquifers: A groundwater perspective. In National Groundwater Conference 2010. International Association of Hydrogeologists.

Reiter, M. (2001). Using precision temperature logs to estimate horizontal and vertical groundwater flow components. Water Resources Research, 37(3):663–674.

Ricard, L., Corbel, S., Reid, L., and Trefry, M. (2010). Assessing sustainability of geothermal resources for Hot Sedimentary Aquifer systems. In National Groundwater Conference 2010. International Association of Hydrogeologists.

Ricard, L., J-B., C., and G., P. (2011). Temperature interpretation and modelling for geothermal applications: GeoTemp. In Middleton, M. F. and Gessner, K. (Eds.), Western Australian Geothermal Energy Symposium, Perth, Australia.

Ricard, L., Reid, L., and Trefry, M. (2012). Reservoir productivity and sustainability of low-temperature geothermal resources. Final report of Project 4, Perth Basin assessment program. Technical report, Western Australian Geothermal Centre of Excellence.

Rowland, J. V. and Sibson, R. H. (2004). Structural controls on hydrothermal flow in a segmented rift system, Taupo volcanic zone, New Zealand. Geofluids, 4(4):259–283.

Rubin, J. (1983). Transport of reacting solutes in porous media: Relation between mathematical nature of problem formulation and chemical nature of reactions. Water Resources Research, 19(5):1231–1252.

Runci, P. (2005). Renewable energy policy in Germany: An overview and assessment. Technical report, Joint Global Change Research Institute, College Park, MD. Available online at http://www.globalchange.umd.edu/energytrends/germany/.

Saar, M. (2011). Review: Geothermal heat as a tracer of large-scale groundwater flow and as a means to determine permeability fields. Hydrogeology Journal, 1–22.

Sass, I. and Götz, A. (2012). Geothermal reservoir characterization: a thermofacies concept. Terra Nova, 1–6.

Sass, J. and Lachenbruch, A. (1979). Thermal regime of the Australian continental crust. In McElhinny, M.W. (Ed.), The Earth: Its origin, structure and evolution, 301–351. Academic Press, London.

Shannon, C. and Weaver, W. (1948). The mathematical theory of communication. Bell System Technical Journal, 27:379–423.

Shao, J.-F. and Burlion, N. (2008). Thermo-hydromechanical and chemical coupling in geomaterials and applications. In Proceedings of the 3rd International Symposium GeoProc'2008, Polytech-Lille, France. Wiley.

Sheldon, H. and Bloomfield, G. (2011). Salinity in the Yarragadee aquifer: Implications for convection and geothermal energy in the Perth Basin. In Middleton, M. F. and Gessner, K. (Eds.), Western Australian Geothermal Energy Symposium, Perth, Australia.

Sheldon, H.A., Florio, B., Trefry, M., Reid, L.B., Ricard, L.P., and Ghori, K.A.R. (2012). The potential for convection and implications for geothermal energy in the Perth Basin, Western Australia. Hydrogeology Journal, DOI 10.1007/s10040-012-0886-7.

Shock, E., Oelkers, E., Johnson, J., Sverjensky, D., and Helgeson, H. (1992). Calculation of the thermodynamic properties of aqueous species at high pressures and temperatures. Effective electrostatic radii, dissociation constants and standard partial molal properties to 1000 °C and 5kbar. Journal of the Chemical Society, Faraday Transactions, 88(6):803-826.

Shvarov, Y. V. (1978). Minimization of the thermodynamic potential of an open chemical system. Geochemistry International, 15 (6):200–203.

Shvarov, Y. V. and Bastrakov, E. N. (1999). Hch: a software package for geochemical equilibrium modelling. User Guide. Geoscience Australia Record1999/25, Australian Geological Survey Organisation, Canberra. 61 p.

Simmons, C. T., Fenstemaker, T. R., and Sharp, J. M. (2001). Variable-density groundwater flow and solute transport in heterogeneous porous media: Approaches, resolutions and future challenges. Journal of Contaminant Hydrology, 52(1-4):245–275.

Simmons, C. T., Kuznetsov, A. V., and Nield, D. A. (2010). Effect of strong heterogeneity on the onset of convection in a porous medium: Importance of spatial dimensionality and geologic controls. Water Resources Research, 46:W09539.

Siret, D., Poulet, T., Regenauer-Lieb, K., and Connolly, J. (2008). PreMDB, a thermodynamically consistent material database as a key to geodynamic modelling. Acta Geotechnica, 4(2):107-115.

Strategen (2004). South West Yarragadee - Blackwood groundwater area. Water study report. Water and Rivers Commission of Western Australia.

Suzuki, S., Caumon, G., and Caers, J. (2008). Dynamic data integration for structural modeling: model screening approach using a distance-based model parameterization. Computational Geosciences, 12(1):105–119.

Swift, M. (1991). Heat flow modelling: a generalized two-dimensional diffusive and convective numerical model for the Exmouth Plateau, offshore Northwest Australia. Tectonophysics, 194(4): 409–426.

Swift, M., Boyd, R., O'Brien, D., and Lorenzo, J. (1992). Heat flow and thermal history of the Exmouth Plateau. In von Rad, U. and Haq, B.U. (Eds.) Proceedings of the Ocean Drilling Program, Scientific Results, 363–375.

Tanger, J. C. and Helgeson, H. C. (1988). Calculation of the thermodynamic and transport properties of aqueous species at high pressures and temperatures; revised equations of state for the standard partial molal properties of ions and electrolytes. American Journal of Science, 288:19–98.

Thomas, B. (1984). Hydrocarbons, source rocks, and maturity trends in the Northern Perth Basin, Australia. Petroleum geochemistry and basin evaluation: AAPG Memoir, 35:391–403.

Timms, N. (Ed.) (2012). Project 2 final report: A new geological understanding of the Perth Basin, Western Australia. Western Australian Geothermal Centre of Excellence.

Trevisan, O. V. and Bejan, A. (1987). Mass and heat transfer by high rayleigh number convection in a porous medium heated from below. International Journal of Heat and Mass Transfer, 30(11):2341–2356.

Tsang, C.-F., Stephansson, O., Kautsky, F., and Jing, L. (2004). Coupled THM processes in geological systems and the decovalex project. In Stephanson, O. (Ed.), Coupled Thermo-Hydro-Mechanical-Chemical Processes in Geo-Systems - Fundamentals, Modelling, Experiments and Applications, 3 – 16. Elsevier.

Turcotte, D. and Schubert, G. (1982). Geodynamics: Applications of continuum physics to geological problems. Wiley, New York.

Turner, A. (2006). Challenges and trends for geological modelling and visualisation. Bulletin of Engineering Geology and the Environment, 65(2):109–127.

Verdoya, M., Pasquale, V., and Chiozzi, P. (2008). Inferring hydro-geothermal parameters from advectively perturbed thermal logs. International Journal of Earth Sciences, 97(2):333–344.

Vosteen, H. and Schellschmidt, R. (2003). Influence of temperature on thermal conductivity, thermal capacity and thermal diffusivity for different types of rock. Physics and Chemistry of the Earth, Parts A/B/C, 28(9-11):499–509.

Wagner, W., Cooper, J., Dittmann, A., Kijima, J., Kretzschmar, H., Kruse, A., Mareš, R., Oguchi, K., Sato, H., Stöcker, I., et al. (2000). The IAPWS industrial formulation 1997 for the thermodynamic properties of water and steam. Journal of Engineering for Gas Turbines and Power, 122:150.

Wagner, W. and Prüß, A. (2002). The IAPWS Formulation 1995 for the thermodynamic properties of ordinary water substance for general and scientific use. Journal of Physical and Chemical Reference Data, 31(2):387–535.

Waples, D. and Waples, J. (2004a). A review and evaluation of specific heat capacities of rocks, minerals, and subsurface fluids. Part 1: Minerals and nonporous rocks. Natural resources research, 13(2):97–122.

Waples, D. and Waples, J. (2004b). A review and evaluation of specific heat capacities of rocks, minerals, and subsurface fluids. Part 2: Fluids and porous rocks. Natural resources research, 13(2):123–130.

Watanabe, N., Wang, W., McDermott, C., Taniguchi, T., and Kolditz, O. (2010). Uncertainty analysis of thermo-hydro-mechanical coupled processes in heterogeneous porous media. Computational Mechanics, 45(4):263–280.

Wellmann, J. F., Horowitz, F. G., and Regenauer-Lieb, K. (2010). Influence of geological structures on fluid and heat flow fields. In Proceedings, Thirty-Fifth Workshop on Geothermal Reservoir Engineering, Stanford, California. Stanford University.

Wellmann, J. F. (2011). Uncertainties have a meaning: Quantitative interpretation of the relationship between subsurface flow and geological data quality. PhD thesis, University of Western Australia.

Wellmann, J. F., Croucher, A., and Regenauer-Lieb, K. (2011a). Python scripting libraries for subsurface fluid and heat flow simulations with TOUGH2 and Shemat. Computers and Geosciences, in press.

Wellmann, J. F., Horowitz, F. G., and Regenauer-Lieb, K. (2009). Concept of an integrated workflow for geothermal exploration in Hot Sedimentary Aquifers. In Proceedings, Australian Geothermal Energy Conference, Brisbane.

Wellmann, J. F. and Regenauer-Lieb, K. (2012). Effect of geological data quality on uncertainties in geological models and subsurface flow fields. In Proceedings, Thirty-Seventh Workshop on Geothermal Reservoir Engineering, Stanford, California. Stanford University.

Wellmann, J. F., Reid, L. B., Horowitz, F. G., and Regenauer-Lieb, K. (2011b). Geothermal resource assessment: Combining uncertainty evaluation and geothermal simulation. In Enhanced Geothermal Systems, AAPG/SEG/SPE Hedberg Research Conference, California, USA.

Wellmann, J. F., and Regenauer-Lieb, K. (2012). Uncertainties have a meaning: Information entropy as a quality measure for 3-D geological models. Tectonophysics, 526-529, 207–216.

Wellmann, J. F., Reid, L. B., and Regenauer-Lieb, K. (2011c). From outcrop to flow fields: combining geological modeling and coupled THMC simulations. In Liu, J. (Ed.), GeoPROC 2011: Cross Boundaries Through THMC Integration, 6-9 July.

Western Australian Department of Mines and Petroleum (2012). Petroleum and Geothermal Information WAPIMS. Accessed 5 January 2012.

Zhao, C. B., Hobbs, B. E., and Muhlhaus, H. B. (1999). Theoretical and numerical analyses of convective instability in porous media with upward throughflow. International Journal for Numerical and Analytical Methods in Geomechanics, 23(7):629–646.

Zoth, G. and Haenel, R. (1988). Appendix. In Haenel, R., Rybach, L., and Stegena, L. (Eds.), Handbook of terrestrial heat-flow density determination: with guidelines and recommendations of the International Heat Flow Commission, 449–466. Springer.

Zschocke, A., Rath, V., Grissemann, C., and Clauser, C. (2005). Estimating Darcy flow velocities from correlated anomalies in temperature logs. Journal of Geophysics and Engineering, 2:332.

APPENDIX A. LISTING OF STUDENTS

Full name	Level	Start	End	Institution	Academic supervisor	WAGCOE supervisor	Topic
Thomas Poulet	PhD	Oct-07	Jul-11	UWA	Klaus Regenauer-Lieb	Regenauer-Lieb	Reactive Transport in damageable geomaterials - Thermal-Hydrological-Mechanical-Chemical coupling of geological processes
Florian Wellmann	PhD	Jan-08	Aug-11	UWA	Klaus Regenauer-Lieb	Regenauer-Lieb/Reid	Uncertainties have a meaning: Quantitative interpretation of the relationship between subsurface flow and geological data quality
Len Baddock	PhD	Aug-09	Ongoing	UWA	Karl-Heinz Wyrwoll, Phil Commander, Craig Simmons	Regenauer-Lieb	Heat transport by groundwater within the Yarragadee Formation, northern Perth Basin: lithological, structural and diagenetic influences
Brendan Florio	PhD	2010	Ongoing	UWA	Thomas Stemler	Horowitz/Trefry	Convection dynamics in porous media
Libby Colgan	Msc	Feb-10	Jun-11	Curtin	Michael Kuhn	Reid	Geospatial data analysis of geothermal data
Tom Beckerling	Hons	Aug-11	Jun-12	UWA	Thomas Stemler	Sheldon	Convection dynamics - numerical modelling
Allison Hortle	PhD	Nov-10	Ongoing	UWA	Klaus Regenauer-Lieb	Regenauer-Lieb/Trefry	Co_2 storage in saline hydrodynamic aquifers: Interaction with and monitoring of groundwater systems
Sarah Glasson	Hons	2011	Nov-11	UWA	Carolyn Oldham	Sheldon/Reid	Salinity in the Yarragadee aquifer
JJ Leong	Hons	Feb-10	Nov-11	Curtin	Brett Harris	Reid	Time lapse temperature and induction logging for numerical modelling
William Tran	Hons	Feb-10	Nov-10	Curtin	Brett Harris	Reid/Wilkes	Pre-feasibility study of geothermal energy within the Perth metropolitan region
Nathan White	Hons	Feb-10	Nov-10	UWA	Thomas Stemler	Trefry	Hydrothermal convection in the Perth Basin: geothermal energy extraction
Gemma Bloomfield	Hons	Jun-10	Nov-10	UWA	Klaus Gessner	Reid	Hydrogeologic Study of Geothermal Logging in the Perth Metropolitan Area
Susan Lissiman	Hons	Jun-11	Nov-11	UWA	Carolyn Oldham	Reid	Heat dumping to shallow aquifers in the Perth Metropolitan Area
Oliver Schilling	Msc	Oct-11	Feb-11	ETH-Zurich	Wolfgang Kinzelbach	Sheldon/Reid	Convection in the Perth Basin: Impact of aquifer geometry and regional groundwater flow
Dylan Irvine	PhD	Dec-11	Ongoing	Flinders Adelaide	Craig Simmons	Sheldon	Impact of heterogeneous permeability on convection

APPENDIX B. CONFERENCE AND WORKSHOP CONTRIBUTIONS

Appendix B.1 Conference Presentations and Attendance

The research presented in this report has been presented in local and international conferences. In addition to publicising work performed by WAGCoE or affiliated students, conference participation provides an important forum for attendees to be exposed to related research and develop professional networks in the geothermal field. Notable conferences attended include:

Australian Geothermal Energy Conference, 2009. Brisbane, Australia

10th Australasian Environmental Isotope Conference and 3rd Australasian Hydrogeology Research, 2009. Perth, Australia

Australian Geothermal Energy Conference, 2010. Adelaide, Australia

European Geosciences Union General Assembly, 2010. Vienna, Austria

Geo-computing, 2010. Brisbane, Australia

Geomod, 2010. Lisbon, Portugal

GeoNZ, 2010. Auckland, New Zealand

National Groundwater Conference, 2010. Canberra, Australia

American Geophysical Union Conference, 2010 and 2011. San Francisco, California USA

Australian Geothermal Energy Conference, 2011. Melbourne, Australia

Enhanced Geothermal Systems, 2011. Napa, California, USA

GeoProc2011: Cross Boundaries through THMC Integration, 2011. Perth, Australia

Mathematical Geosciences at the Crossroads of Theory and Practice, 2011. Salzburg, Austria

Western Australian Geothermal Energy Symposium, 2011. Perth. This conference was organised in large part by members of WAGCoE.

Stanford Geothermal Reservoir Engineering Workshop, 2011 and 2012. Palo Alto, California, USA

Presentations given at these conferences are listed in Appendix C.

Appendix B.2 Short Courses

WAGCoE coordinated four educational short courses containing topics on hydrothermal modelling in Hot Sedimentary Aquifers. The audience for these outreach initiatives ranged from university Honours students, to secondary school teachers, to practicing engineers in related fields, to geothermal-industry focused presentations.

Appendix B.2.1 Direct Use Applications for Hot Sedimentary Aquifers

This one day short course preceded the Australian Geothermal Energy Conference (AGEC), located in Adelaide S.A. in November 2010. AGEC is the premier geothermal conference in Australia and has presentations focusing on scientific research and industrial developments. The short course was organized by WAGCoE and had fourteen paid participants from industry, academia, and local and state governments. Presenters were from WAGCoE and the University of Melbourne. The curriculum covered

Hot sedimentary aquifers

Geologic Factors and Hydrothermal Modelling

Geothermal Heat Pumps

Air Conditioning and Deslination

Participants received course material handouts incorporating the presentations. Participation during the course was vigorous and positive feedback was received afterwards.

Appendix B.2.2 Geothermal Energy Systems

This one day short course was sponsored by the Australian Institute of Refrigeration, Airconditioning and Heating (AIRAH) and held in Perth in February 2011. The focus was on utilising geothermal heat for the built environment. The nearly 40 participants were primarily professionals located in the construction and design fields. Presenters were from WAGCoE and local geothermal and energy companies. Topics covered included

Commercial perspectives

Historical use of geothermal in Perth

Introduction to geothermal principals

Commercial energy networks

Geothermal air conditioning

Design of sustainable, zero-emission geothermal cities

Appendix B.2.3 Geothermal Energy Resources

This week-long Honours course was taught at the University of Western Australia (UWA) in April 2011 as EART4423. The unit was open to UWA and Curtin University geoscience students enrolled in BSc Honours and four-year degrees and provided course credit towards degree requirements. Three students completed the entire course although up to ten students attended some lectures. In addition, postgraduate students, staff, and visitors also attended some modules. The unit was structured to include topics of

Direct Heat Use in Perth

Tectonic Perspective on Geothermal Systems

Thermal Geologic Properties and Concepts

Basic Hydrogeologic Concepts

Engineering Perspectives on Direct Use Geothermal

Geothermal Geophysics

Geothermal Reservoir Engineering

Geothermal Chemistry

The unit was finalised with a written examination and students received course materials.

Appendix B.2.4 SPICE

The SPICE program is a secondary science teachers' enrichment series created by the University of Western Australia with support from the Western Australian Department of education. SPICE develops teaching and learning resources for classrooms, provides professional development for teachers, and facilitates interaction with scientists. Members of WAGCoE were heavily involved in the development of a curriculum resource on Geothermal Energy. The learning module focuses on the physical concepts of specific and latent heat and illustrates the principals with applications to geothermal energy. Specific resources range from an overview video engaging students in the possibilities for the use of geothermal energy, interactive design of a geothermal heating system for a swimming pool, comparison of sustainable energy requirements, and analysis of case studies. The curriculum and resources are available for free for any Western Australian secondary teachers. More information can be found at http://www.spice.wa.edu.au/home

In addition to the development of the learning resources, members of WAGCoE have acted as scientific experts for secondary school teachers during their professional development courses. They have presented topics to teachers on tectonic regimes leading to geothermal systems, hydrothermal modelling, and geothermal cities.

APPENDIX C. SCIENTIFIC PUBLICATIONS

Publications with WAGCoE authors related to geothermal characterisation and hydrothermal modelling are listed in this section, even if they have been included in the References section above. Some of these publications may also appear in reports relating to other projects with WAGCoE's Program 1. Note that WAGCoE authors may have generated publications on additional topics which are not included in this document but instead can be found in the WAGCoE final report.

Bloomfield, G. (2010). Hydrogeologic study of geothermal logging in the Perth Metropolitan Area, Western Australia. Honours thesis, School of Earth and Environmental Science, University of Western Australia.

Botman, C. (2010). Determining the geothermal properties of the Perth Basin lithology to aid geothermal energy projects. Department of Exploration Geophysics, Curtin University. Report GPH 6/10.

Botman, C., Horowitz, F., Wilkes, P., and the WAGCoE team (2011). Detailed thermal profiling and inversion for thermal conductivities and heat fluxes in the Perth metropolitan hot sedimentary aquifer play of Western Australia. In Proceedings, Thirty-Sixth Workshop on Geothermal Reservoir Engineering, Stanford University, California. SGP-TR-191.

Corbel, S., Colgan, E., Reid, L., and Wellmann, J. (2010). Building 3D geological models for groundwater and geothermal exploration. In Groundwater 2010, Canberra, Australia. International Association of Hydrogeology.

Corbel, S., Reid, L., and Ricard, L. (2011). Prefeasibility geothermal exploration workflow applied to the Fitzroy Trough, Western Australia. In Western Australian Geothermal Energy Symposium, Perth, Australia.

Corbel, S., Schilling, O., Horowitz, F., Reid, L., Sheldon, H., Timms, N., and Wilkes, P. (2012). Identification and geothermal influence of faults in the Perth Metropolitan Area, Australia. In Proceedings, Thirty-Seventh Workshop on Geothermal Reservoir Engineering, Stanford, California. SGP-TR-194.

Glasson, S. (2011). Investigation of salinity within the Yarragadee Aquifer in the Perth area. Honours thesis, School of Engineering, University of Western Australia.

Gorczyk, W., Hobbs, B., Ord, A., Gessner, K., and Gerya, T. (2010). Lithospheric architecture, heterogenities, instabilities, melting–insight form numerical modelling. In Geophysical Research Abstracts, volume 12, EGU2010– 10223, Vienna. EGU General Assembly.

Gross, L., Hornby, P., Poulet, T. and Sheldon, H.A. (2009). Solving fluid transport problems for the exploration of mineral deposits and geothermal reservoirs. In Proceedings of 4th International Conference on High Performance Scientific Computing. Submitted.

Gutbrodt, S. (2011). Thermal investigation at the M345 aquifer storage and recovery project. Technical report, CSIRO. unpublished.

Karrech, A., Poulet, T., and Regenauer-Lieb, K. (2011a). Thermo-hydro-mechanical coupling of largely transformed media. In American Geophysical Union Fall meeting, San Francisco, California.

Karrech, A., Poulet, T., and Regenauer-Lieb, K. (2011b). Thermo-hydro-mechanical coupling using logarithmic strain measures and co-rotational rates. In 4th International Conference GeoProc2011: Cross Boundaries Through THMC Integration. Perth, Australia.

Karrech, A., Poulet, T., and Regenauer-Lieb, K. (2012). Poromechanics of saturated media based on the logarithmic finite strain. Mechanics of Materials. In press.

Karrech, A., Regenauer-Lieb, K., and Poulet, T. (2010). Continuum damage mechanics of the lithosphere depending on strain-rate, temperature, and water content. In Proceedings, ICAMEM 2010, Hammamet, Tunisia.

Karrech, A., Regenauer-Lieb, K., and Poulet, T. (2011c). Continuum damage mechanics for the lithosphere. Journal of Geophysical Research, 116:B04205.

Karrech, A., Regenauer-Lieb, K., and Poulet, T. (2011d). A damaged visco-plasticity model for pressure and temperature sensitive geomaterials. International Journal of Engineering Science, 49(10):1141 – 1150.

Karrech, A., Regenauer-Lieb, K., and Poulet, T. (2011e). Frame indifferent elastoplasticity of frictional materials at finite strain. International Journal of Solids and Structures, 48(3-4):397 – 407.

Leong, J. J. (2011). Numerical modelling for flow, solute transport and heat transfer in a high-permeability sandstone. Honour's Thesis, Curtin University of Technology, Department of Geophysics. Report GPH 10/11.

Leong, J. J., Harris, B. D., and Reid, L. B. (2012). Numerical modelling for flow, solute transport, and heat transfer in a high-permeability sandstone. In Australian Society of Exploration Geophysics 22nd Conference, Brisbane, Australia.

Lissiman, S. (2011). Aquifer heat rejection and potential thermal impacts on an aquifer in Perth, Western Australia. Honours Thesis, School of Engineering, University of Western Australia.

Poulet, T. (2011). Reactive Transport in damageable geomaterials - Thermal-Hydrological-Mechanical-Chemical coupling of geological processes. PhD thesis, University of Western Australia, School of Earth and Environment.

Poulet, T., Corbel, S., and Stegherr, M. (2010a). A geothermal web catalog service for the Perth Basin. In Australian Geothermal Energy Conference, Adelaide.

Poulet, T., Fusseis, F., and Regenauer-Lieb, K. (2009). Cleaveage domains control the orientation of mylonitic shear zones at the brittle-viscous transition (Cap de Creus, NE Spain)–a combined field and numerical study. EGU General Assembly 2009.

Poulet, T., Gross, L., Georgiev, D., and Cleverley, J. (2012a). *escriptRT*: Reactive transport simulation in Python using escript. Computers and Geosciences. In press.

Poulet, T., Karrech, A., Regenauer-Lieb, K., Fisher, L., and Schaubs, P. (2011). Uranium deposit modeling using Thermal-Hydraulic-Mechanical-Chemical coupling. In 4th International Conference GeoProc2011: Cross Boundaries Through THMC Integration. Perth, Australia.

Poulet, T., Karrech, A., Regenauer-Lieb, K., Gross, L., Cleverley, J., and Georgiev, D. (2010b). Thermal-Mechanical-Hydrological-Chemical simulations using escript, Abaqus and WinGibbs. In Geomod 2010, Lisbon, Portugal.

Poulet, T., Regenauer-Lieb, K., and Karrech, A. (2010c). A unified multi-scale thermodynamical framework for coupling geomechanical and chemical simulations. Tectonophysics, 483(1-2):178 – 189.

Poulet, T., Regenauer-Lieb, K., Karrech, A., Fisher, L., and Schaubs, P. (2012b). Thermal-Hydraulic-Mechanical-Chemical coupling using *escriptRT* and Abaqus. Tectonophysics, 526-529:124 – 132.

Regenauer-Lieb, K., Chua, H., Wang, X., Horowitz, F., and Wellmann, J. (2009a). Direct heat geothermal applications in the Perth Basin of Western Australia. In Thrity-Fourth Workshop on Geothermal Reservoir Engineering, Stanford University, Stanford, California.

Regenauer-Lieb, K., Karrech, A., Chua, H. T., Poulet, T., Trefry, M., Ord, A., and Hobbs, B. (2011). Non-equilibrium thermodynamics for multi-scale THMC coupling. In 4th International Conference GeoProc2011: Cross Boundaries Through THMC Integration. Perth, Australia.

Regenauer-Lieb, K., Karrech, A., and Poulet, T. (2010). Multi-physics modeling of geothermal energy harvesting in sedimentary aquifers. In The fifth international conference on advances in mechanical engineering and mechanics.

Regenauer-Lieb, K., Karrech, A., Schrank, C., Fusseis, F., Liu, J., Gaede, O., Poulet, T., Weinberg, R., and G., R. (2009b). A novel thermodynamic framework for multi-scale data assimilation: First applications from micro CT-scans to meso-scale microstructure. In American Geophysical Union Fall Meeting, San francisco, California.

Regenauer-Lieb, K., Poulet, T., Siret, D., Fusseis, F., Liu, J., Gessner, K., Gaede, O., Morra, G., Hobbs, B., Ord, A., et al. (2009c). First steps towards modeling a multi-scale earth system. In Xing, H. (Ed.), Advances in geocomputing, Lecture Notes in Earth Sciences, 1–26. Springer Verlag.

Reid, L., Bloomfield, G., Botman, C., Ricard, L., and Wilkes, P. (2011a). A temperature investigation in Perth, Western Australia. In Middleton, M. F. and Gessner, K., editors, Western Australian Geothermal Energy Symposium, Perth, Australia.

Reid, L., Bloomfield, G., Botman, C., Ricard, L., and Wilkes, P. (2011b). Temperature regime in the perth metropolitan area: Results of temperature and gamma logging and analysis, june/july 2010. CSIRO Report EP111422, CSIRO, Perth, Australia.

Reid, L., Corbel, S., Ricard, L., Trefry, M., and Wellmann, J. (2010). Modelling hot sedimentary geothermal aquifers: A groundwater perspective. In National Groundwater Conference 2010. International Association of Hydrogeologists.

Reid, L., G., B., L.P., R., Wilkes, P., and C., B. (2011c). Geothermal logging in Perth, Western Australia. In Australian Geothermal Energy Conference, Melbourne, Australia.

Ricard, L., Corbel, S., Reid, L., and Trefry, M. (2010). Assessing sustainability of geothermal resources for Hot Sedimentary Aquifer systems. In National Groundwater Conference 2010. International Association of Hydrogeologists.

Sheldon, H. and Bloomfield, G. (2011). Salinity in the Yarragadee aquifer: Implications for convection and geothermal energy in the Perth Basin. In Middleton, M. F. and Gessner, K., editors, Western Australian Geothermal Energy Symposium, Perth, Australia.

Sheldon, H., Florio, B., Trefry, M., Reid, L., Ricard, L., and Ghori, K. (2012). The potential for convection and implications for geothermal energy in the Perth Basin, Western Australia. Hydrogeology Journal. in press.

Sheldon, H., Poulet, T., Wellmann, J., Regenauer-Lieb, K., Trefry, M., Horowitz, F., and Gessner, K. (2009). Assessing the Perth Basin geothermal opportunity: Preliminary results from simulations of heat transfer and fluid flow. Journal of Geochemical Exploration, 101(1):95.

Sheldon, H., Reid, L., Florio, B., and Kirkby, A. (2011). Convection or conduction? Interpreting temperature data from sedimentary basins. In Australian Geothermal Energy Conference, Melbourne, Australia.

Siret, D., Poulet, T., Regenauer-Lieb, K., and Connolly, J. (2009). PreMDB, a thermodynamically consistent material database as a key to geodynamic modelling. Acta Geotechnica, 4(2):107–115.

Tran, W. (2010). Mechanisms that may create convective groundwater and heat flow in the Perth Basin, Western Australia. Honours Thesis, Department of Exploration Geophsics, Curtin University. Report GPH 20/10.

Trefry, M. G., Regenauer-Lieb, K., Webb, S., Chua, H. T., Horowitz, F., Wellmann, F., Fusseis, F., Poulet, T., Sheldon., H.A., Wilkes, P., Hoskin, T., Seibert, S., Reid, L. B., Cawood, P., Reddy, S., Wilson, M., Evans, N., Timms, N., Clarke, C., Batt, G., Gaede, O., McInnes, B., Cleverly, J., Aspandiar, M., Dyskin, A., Karrech, A., Healy, D., and McWilliams, M. (2009). Capturing the benefits of Perth's hydrothermal resources. In 10th Australasian Environmental Isotope Conference & 3rd Australasian Hydrogeology Research Conference. Curtin University of Technology, Western Australia. Keynote Address.

Trefry, M. G., Ricard, L., Wilkes, P., Reid, L., Wang, X., Corbel, S., Horowitz, F. G., Webb, S., and Regenauer-Lieb, K. (2010). Preliminary prefeasibility desktop study of geothermal potential for the Telfer Province. Report to Newcrest Mining Limited, Western Australian Geothermal Centre of Excellence.

Wellmann, F. J., Horowitz, G. F., Deckert, H., and Regenauer-Lieb, K. (2010a). A proposed new method for inferred geothermal resource estimates: Heat in place density and local sustainable pumping rates. In Proceedings, European Geosciences Union General Assembly 2010.

Wellmann, F. J., Horowitz, G. F., and Regenauer-Lieb, K. (2010b). Influence of geological structures on fluid and heat flow fields. In Proceedings, Thirty-Fifth Workshop on Geothermal Reservoir Engineering SGP-TR-188, Stanford, California. Stanford University.

Wellmann, J. (2011). Uncertainties have a meaning: Quantitative interpretation of the relationship between subsurface flow and geological data quality. PhD thesis, School of Earth and Environment, University of Western Australia.

Wellmann, J., Croucher, A., and Regenauer-Lieb, K. (2011a). Python scripting libraries for subsurface fluid and heat flow simulations with TOUGH2 and Shemat. Computers and Geosciences. submitted.

Wellmann, J., Croucher, A., Reid, L., and Regenauer-Lieb, K. (2011b). Combining geological modeling and flow simulation for hypothesis testing and uncertainty quantification. In Mathematical Geosciences at the Crossroads of Theory and Practice, IAMG 2011, Salzburg, Austria. International Association of Mathematical Geosciences.

Wellmann, J., Horowitz, F., and Regenauer-Lieb, K. (2011c). Towards a quantification of uncertainties in 3-D geological models. In Mathematical Geosciences at the Crossroads of Theory and Practice, IAMG 2011, Salzburg, Austria. International Association of Mathematical Geosciences.

Wellmann, J., Horowitz, F., Ricard, L., and Regenauer-Lieb, K. (2010c). Guided geothermal exploration in hot sedimentary aquifers. In American Geophysical Union Fall Meeting Abstracts, 1170.

Wellmann, J., Horowitz, F. G., and Regenauer-Lieb, K. (2009a). Concept of an integrated workflow for geothermal exploration in Hot Sedimentary Aquifers. In Proceedings, Australian Geothermal Energy Conference, Brisbane.

Wellmann, J. and Regenauer-Lieb, K. (2012). Effect of geological data quality on uncertainties in geological models and subsurface flow fields. In Proceedings, Thirty-Seventh Workshop on Geothermal Reservoir Engineering, Stanford, California. Stanford University. SGP-TR-194.

Wellmann, J., Reid, L., Horowitz, F., and Regenauer-Lieb, K. (2011d). Geothermal resource assessment: Combining uncertainty evaluation and geothermal simulation. In Enhanced Geothermal Systems. AAPG/SEG/SPE Hedberg Research Conference, Napa, California, USA.

Wellmann, J., Reid, L., Horowitz, F., and Regenauer-Lieb, K. (2011e). Integrated workflow for geothermal resource assessment. In Middleton, M. F. and Gessner, K. (Eds.), Western Australian Geothermal Energy Symposium, Perth, Australia.

Wellmann, J. F., Croucher, A., Horowitz, F. G., and Regenauer-Lieb, K. (2009b). Integrated workflow enables geological sensitivity analysis in geothermal simulations. In Proceedings, NZ Geothermal Worksho, 26–30.

Wellmann, J. F., Gessner, K., and Klaus, R.-L. (2009c). Combination of 3-D geological modeling and geothermal simulation: a flexible workflow with GeoModeller and SHEMAT. In General Assembly of the European Geophysical Union, Vienna.

Wellmann, J. F., Horowitz, F. G., Ricard, L. P., and Regenauer-Lieb, K. (2010d). Estimates of sustainable pumping in Hot Sedimentary Aquifers: Theoretical considerations, numerical simulations and their application to resource mapping. In Proceedings, Australian Geothermal Energy Conference, Adelaide.

Wellmann, J. F., Horowitz, F. G., Schill, E., and Renegauer-Lieb, K. (2009d). Uncertainty simulation improves understanding of 3-D geological models. Tectonophysics. Submitted.

Wellmann, J. F. and Regenauer-Lieb, K. (2011). Uncertainties have a meaning: Information entropy as a quality measure for 3-D geological models. Tectonophysics.

Wellmann, J. F., Reid, B. L., and Regenauer-Lieb, K. (2011f). From outcrop to flow fields: combining geological modeling and coupled THMC simulations. In Liu, J. (Ed.), GeoPROC 2011: Cross Boundaries Through THMC Integration, 6-9 July.

White, N. (2010). Hydrothermal convection in the Perth Basin: Geothermal energy extraction. Honours Thesis, School of Civil and Resource Engineering, University of Western Australia.

Zhang, Y., Karrech, A., Schaubs, P., Regenauer-Lieb, K., Poulet, T., and Cleverley, J. (2010). Advancing the numerical simulation of rock deformation: a new thermal dynamic continuum damage mechanics approach. In Proceedings Geo-Computing 2010.

Zhang, Y., Karrech, A., Schaubs, P., Regenauer-Lieb, K., Poulet, T., and Cleverley, J. (2012). Modelling of deformation around magmatic intrusions with application to gold-related structures in the Yilgarn Craton, Western Australia. Tectonophysics, 526–529:133 – 146.

Zhao, C., Reid, L., and Regenauer-Lieb, K. (2011). Some fundamental issues in computational hydrodynamics of mineralization: A review. Journal of Geochemical Exploration, 112:21–34.

Zhao, C., Reid, L., Regenauer-Lieb, K., and Poulet, T. (2012). A porosity-gradient replacement approach for computational simulation of chemical-dissolution front propagation in fluid-saturated porous media including pore-fluid compressibility. Computational Geosciences, 1–21.